EXCITON-PHOTON DYNAMICS IN QUANTUM DOTS EMBEDDED IN PHOTONIC CAVITIES

Thomas Allcock

A thesis presented for the degree of

Doctor of Philosophy

School of Physics and Astronomy

Cardiff University

United Kingdom

December 2020

EXCITON-PHOTON DYNAMICS IN QUANTUM DOTS EMBEDDED IN PHOTONIC CAVITIES

Thomas Allcock

We develop an exact analytical approach to four-wave mixing and higher-order optical nonlinearities of a quantum dot-microcavity system. This approach allows us to analyse the non-linear response in terms of coherent transitions between rungs of the Jaynes-Cummings ladder, finding their complex amplitudes and frequencies. Increasing the pulse area of the excitation field, a transition from quantum strong coupling to coherent classical regime is observed, which manifests itself in a formation of the famous Mollow triplet, with the observation in the three-level model of a quantum dot, including a biexciton, to predict two new effects: One is the existence of a Mollow-like quintuplet, the other is a complete elimination of the four-wave-mixing optical non-linearity under certain parameter constraints. We further develop a simple and accurate approximation in the low-damping limit of the Jaynes-Cummings model of the quantum dot-microcavity system, for nonlinear response of any order in a closed analytic form, predicting the positions and widths of the spectral lines. For higher damping, we demonstrate a strong relaxation down the ladder, shown by both numerical and analytic calculation.

Acknowledgements

I would like to thank Dr Egor Muljarov for the teaching and guidance he has provided me over my time at Cardiff University. He has been an incredibly patient and kind supervisor for the entire duration of my PhD and I appreciate everything he has done for me. I hope to one day become as good a teacher and researcher as he is.

I would like to thank Professor Wolfgang Langbein for his insight and knowledge, helping me understand the greater context including the experimental side of this theoretical work.

I would like to thank my friends and family for their support, especially my mother for taking me in over the covid days this recent year.

And 展展, I can't thank you enough for sticking with me during this long journey. 爱死你

Presentations and Posters

Role of the biexciton in the optical nonlinearity of the highly excited quantum-dot cavity system Sep 2020 - Photon 2020 Conference, oral presentation (Zoom)

A Biexciton Extension to the Jaynes-cummings Model Describing the Quantum-Dot Microcavity System Nov 2020 - Cardiff University Physics Chat, oral presentation (Zoom)

A Biexciton Extension to the Jaynes-cummings Model Describing the Quantum-Dot Microcavity System Nov 2020 - Cardiff University Theory Seminar, oral presentation (Zoom)

Light scattered from a 2-level system: Mollow's Classical Triplet and the Jaynes Cummings model Mar 2019 - Cardiff University Theory Seminar, oral presentation

Quantum-to-classical transition in a highly excited quantum dot-microcavity system Sep 2018 - Photon 2018 Conference, oral presentation

Four Wave Mixing (FWM) Response of a Highly Excited Exciton-Microcavity System Sep 2019 - Cardiff University, Poster presentation

Cavity Quantum Electrodynamics: exciton-photon interaction inside a quantum dot-microcavity system Apr 2018 - Cardiff University Postgraduate Conference - oral presentation

Publications and Conferences

T. Allcock, W. Langbein and E. A. Muljarov, "Quantum-to-classical transition in a highly excited quantum dot-microcavity system" , Photon 2018, abstracts, 3 - 6 September 2018, Aston University, Birmingham, UK

T. Allcock, W. Langbein and E. A. Muljarov, "Role of the biexciton in the optical nonlinearity of the highly excited quantum-dot cavity system" , Photon 2020, abstracts, 1 - 4 September 2018.

T. Allcock, W. Langbein and E. A. Muljarov, "Quantum-to-classical transition in a highly excited quantum dot-microcavity system", to be submitted to Physical Review Letters.

T. Allcock and E. A. Muljarov, "Total FWM signal extinction in the biexciton jaynes-cummings model", in preparation.

Contents

1 Introduction

1.1 Basic concepts

This thesis concentrates purely on the interaction of three simple entities: classical light, quantum confinement of light, and quantum confinement of electrons and holes. These three entities interact in two ways. The first is the interaction between light and an optical cavity, the second is the interaction between an optical cavity and confined electron-hole pairs. This section briefly and simply describes the most important concepts relevant to this thesis, which are then built on throughout the remainder of the thesis. If the reader is inclined, articles [1–5] give an excellent background for the topics presented in this thesis.

1.1.1 Electromagnetic waves

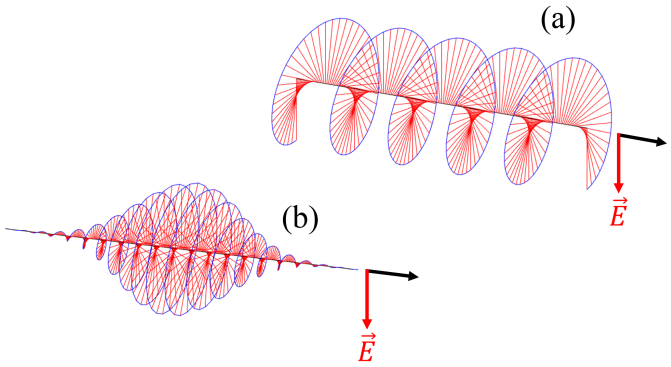

Figure 1.1: Electric field (red lines) and direction of propagation (black) of (a) Circularly polarised light, (b) Circularly polarised light pulse.

An electromagnetic wave can be fully described by its electric field, shown as red lines in Figure 1.1. It is the amplitude of the electric field which is important when we excite our system. For our system the duration of the pulse is very short as in (b) in Figure 1.1. One can imagine as the timescale of a pulse becomes very small, far shorter than the timescale of dynamics involving the rest of our system, we are able to isolate the dynamics involving these pulses from the rest of our system.

1.1.2 Confinement of light: Optical cavities

Often also called optical resonators, these objects are designed to trap light using arrangements of mirrors.

Figure 1.2: Optical cavity diagram. mirrors (green) confine light into a small region (blue).

A classical damped oscillator is any system which is able to resonate when driven at its resonant frequency, but also loses energy to the environment over time. An example would be a pendulum, that when driven (pushed) at the correct frequency will swing very high. If it is driven too fast or too slow the pendulum will not resonate and will not swing as high. If it is left undriven it will oscillate with an exponentially decreasing amplitude until there is no energy available for oscillation. The rate that energy is lost is characterised by its quality factor Q, equal to pendulum's resonant frequency Ω_c divided by its rate of energy loss to the environment γ_c.

An example of a quantum version of the classical pendulum is an optical cavity which we study in this thesis. As the pendulum is confined in space by gravity effectively pulling it towards the center of oscillation, light is confined in space by reflection of mirrors, see Figure 1.2. The same quality factor allows characterisation of how long light will remain between the mirrors until it leaks to the environment.

The model which describes confined light on the quantum scale is called a quantum harmonic oscillator. It has allowed energies of $(N+\frac{1}{2})\Omega_c$ for any natural number $N = 0, 1, 2, ...$

1.1.3 Confinement of electrons and holes: Two-level systems

Start with a bulk semiconductor which has a certain band structure with a Fermi energy between valence and conduction bands. Electrons are only allowed to be in a state with energy allowed by the band structure.

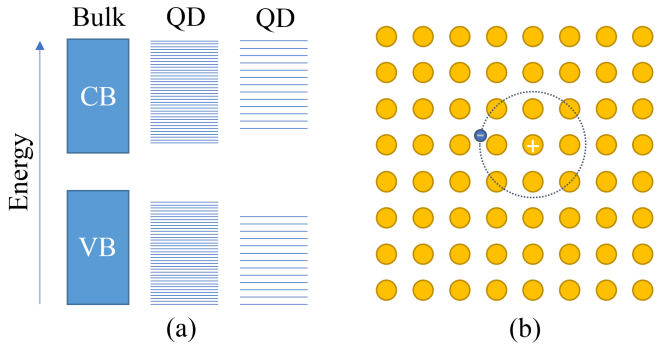

Figure 1.3: (a) Available energy levels for a bulk semiconductor valence band (VB) and conduction band (CB), larger quantum dot and smaller quantum dot. (b) Atomic lattice with one electron-hole pair.

Electrons may be popped out of the valence band if they are excited by something like light. If an electron is popped out of the semiconductor valence band to the conduction band it leaves behind a hole where the electron used to be. The two particles move freely around the semiconductor and are bound to one another. This electron-hole pair is called an exciton, see (b) in Figure 1.3.

Since compared to the unexcited bulk, this is essentially a particle-antiparticle pair with opposite charges which are attracted to each other, eventually recombining and emitting radiation into the environment.

When we confine the electron-hole pair to a small volume (all three dimensions) we call the region a quantum dot (QD), the available energies discretise in all directions and there are no longer a continuum of states available, see (a) in Figure 1.3. One result of this discretisation is the difference in energy between the highest energy valence band state and lowest energy conduction band state is increased as the electron-hole pair is confined to smaller regions. These two states become the main two states available for transition with two available energy levels, hence the name two-level system (2LS).

1.1.4 Light-cavity interaction

By controlling the amount of energy present within a cavity we can then control the next interaction between the cavity and the 2LS. We can do this by exciting the cavity in a particular way, such as with a laser. A laser pulse may for example with a very short pulse duration (much smaller than the oscillation period of the cavity) nudge the cavity into a state of higher energy. A short pulse like this puts the cavity in what is called a coherent state, which in some sense is the quantum version of a classical electromagnetic wave as its amplitude reduces closer to the single photon energy.

1.1.5 Cavity-2LS interaction

We can explain the interaction between these two systems as we would do with two coupled pendulums, which when oscillating together at their resonant frequencies produce new modes of vibration, new oscillation frequencies. It is in this way that the cavity and 2LS oscillate together producing new modes of oscillation. In quantum electrodynamics this produces what is known as a polariton, a mixed state of light and matter, which has new energy levels in comparison to the uncoupled cavity and 2LS.

g_x characterises the strength of interaction between a cavity and a 2LS and can vary almost independently. Imagine a cavity containing an electric field, we can place a 2LS in a position where the field intensity is highest, or where it is lowest. It is this positioning which allows the 2LS to couple to the electric field present in the cavity. The Purcell effect describes the improvement of a 2LS's coupling to an electric field by introducing a cavity. Eigenenergies of the cavity group together towards a single energy, increasing the number of states with similar eigenenergies to the exciton. We can effectively choose this value to match the exciton's excited

state energy, where it is called the resonant regime. The so called Purcell Factor determines the maximum value we can choose for g_x, qualitatively.

1.1.6 Four-wave mixing

Four-wave mixing (FWM) is a nonlinear technique by which two or more waves interact at the point of a nonlinearity [6, 7]. Let E,k,ω be the amplitude, wavevector and frequency of a plane wave propagating in free space. Degenerate FWM consisting of two ultrashort pulses can be explained by looking at the interference of two plane waves. The first pulse with wavevector k_1 induces first-order polarisation in the nonlinearity. The second pulse with wavevector k_2 arrives at the sample and an interference grating along the phase direction $k_2 - k_1$ is produced. A fraction of the second pulse can be self-diffract by the grating into the direction $2k_2 - k_1$. This is referred to as third-order polarisation [8]. which has an amplitude proportional to $E_1^* E_2^2$. In the same sense other mixing orders give rise to higher order diffraction, for example six-wave mixing is observed in the direction $3k_2 - 2k_1$ with an amplitude proportional to $E_1^{*2} E_2^3$.

1.2 Background

The interaction of a single fermionic 2LS with a single bosonic photon mode is described by the Jaynes-Cummings (JC) model [9–11], described in more detail later in this introduction. Adding the cavity can result in a greater coupling of the 2LS to light compared to continuous wave excitation, allowing more detailed dynamics to be uncovered before energy has dissipated away to the environment. Polariton eigenstates of the JC model form a JC ladder, with a splitting of the doublet in each rung proportional to the square root of the rung number. The splitting of these two eigenenergies Ω_1 and Ω_2 is known as Rabi splitting $|\Omega_1 - \Omega_2| = 2g$. The

polariton eigenstates are obtained by diagonalising the Hamiltonian, resulting in a list of eigenenergies. The coupling regime between a single cavity photon mode and a single 2LS describing the matter excitation, is characterised by the cavity photon–2LS coupling constant g_x, the cavity photon damping rate γ_c and the 2LS damping rate γ_x. By moving the semiconductor QD to different positions inside a cavity the coupling strength g_x can be varied, due to the Purcell effect [12]. While the transition from the ground state to the first rung is seen in the linear optical response, the strong coupling induced non-linearity, which is a hallmark of a fermionic 2LS coupling to a photon mode, is seen in higher rungs only. The observation of the higher rung splitting is defining the quantum strong coupling regime, and was shown in [8, 13] for the QD exciton, distinguishing it from the strong coupling using a bosonic 2LS such as a quantum well exciton [14, 15]. Cavity-mediated coherent coupling between three QD excitons, moving from the JC to the Tavis-Cummings ladder [16], was shown in [17].

In the strong coupling regime at resonance, the two main polariton lines have the same linewidth $(\gamma_x + \gamma_c)/2$, since they are mixed half exciton and half cavity states [18–20]. Hopfield [21–23] first predicted the strong coupling regime in solids, later on it was observed in atomic systems [24]. Studies have made lots of progress since these observations [1–3, 25, 26]. Experimentally the first confirmation of strong coupling in a semiconductor microcavity was done by Weisbuch [14].

For a long time, deep strong coupling providing a high cooperativity, $C = 2g^2/(\gamma_x\gamma_c)$ was in solid state observed only for superconducting circuits [27], with $C > 10^4$, while for excitons in QDs coupled to optical cavities, which use photon frequencies suited for long-range optical fibre communication, a cooperativity below 10 was commonplace [18, 19, 28], increased to 35 in a nanobeam cavity [29]. The main reason for this limitation was the limited photon lifetime in the cavities, due to surface state absorption of the host material GaAs for the quantum dots. Recently,

it was shown that nitration of the surface can suppress this absorption [30], opening the path to much higher cooperativities C. Alternatively, one can use an external cavity mirror and a planar structure embedding the QDs, avoiding surface states being created at the etched side walls of micropillar or photonic crystal cavities, and a cooperativity of $C = 150$ was shown recently for such a structure[31]. Both approaches open the realistic prospect to reach very high cooperativities, above 1000, in the near future.

Strong coupling in cavity quantum electrodynamics (cQED) is of both theoretical and applied interest, and is achieved in QD-cavity systems. One reason for these systems to attract the attention of researchers is the application of such systems to quantum information devices like the quantum computer. It allows us to create mixed states of light and matter [22], called polaritons, which show single photon non-linearities [32], the latter being fundamental to quantum technology. The 2LS present in the JC model allows storage of a quantum bit of information, represented using the 2-level basis of the ground state $|G\rangle$ and ground state exciton $|X\rangle$. Experiments have been conducted using superconducting quantum bits [27, 33] coupled with microwave photons, akin to the JC system studied in this thesis. In these experiments one must achieve strong coupling which experimentally is available only with a cavity with a high enough quality factor [4, 18, 28, 34]. There are various ways to design an experiment to study light-matter coupling in microcavities, such as semiconductor [8, 19], photonic crystals [28, 34] or microdisks [18]. These designs can be adapted to different applications.

1.3 Quantum Dots

A QD represents spatial electronic confinement in three dimensions. By layering two or more semiconductor materials in particular shapes, we can create QDs with

a varying bandgap energy. Some standard materials for use in creating QDs are gallium arsenide (GaAs), indium gallium arsenide (InGaAs) and aluminium gallium arsenide (AlGaAs). Properties of the QD material change greatly depending on the confinement region. In bulk semiconductors, when electrons are excited from the valence band to the conduction band, they leave a positively charged quasiparticle called a hole behind. The resulting Coulomb interaction between the excited electron in the conduction band and hole in the valence band form an exciton [35], a bound pair which can be treated as a single quasiparticle with a well defined excitation energy. The discretation of electron and hole energies inside the QD allow the well defined nature of this energy. In bulk semiconductors, excitons are free to move in any direction. It is possible to create a nanostructure which confines a particle in one direction (quantum well), two directions (quantum wire) or all three directions (QD), thanks to discontinuities which may be designed in shape at the nanoscale. In a QD, electrons and holes individually are confined in all spatial dimensions. This means the wavefunction of the electron and hole is localised in the QD and the energy is discretised similar to atoms, it is in this sense QDs are often called artificial atoms. Depending on the size of the QD, the exciton can be treated as bosonic or fermionic. The condition for this distinction is whether the QD is smaller than the Bohr radius of the exciton. If so, the exciton is considered to be in the strong confinement regime of which its ladder operators obey the fermionic anticommutator relation and Pauli exclusion principle. If not, the exciton is considered to be in the weak confinement regime and its ladder operator obeys the bosonic commutator relation. In this thesis we only consider the fermionic case, where and exciton is considered a fermionic particle bound to the QD region.

1.4 Jaynes-Cummings Model and cQED

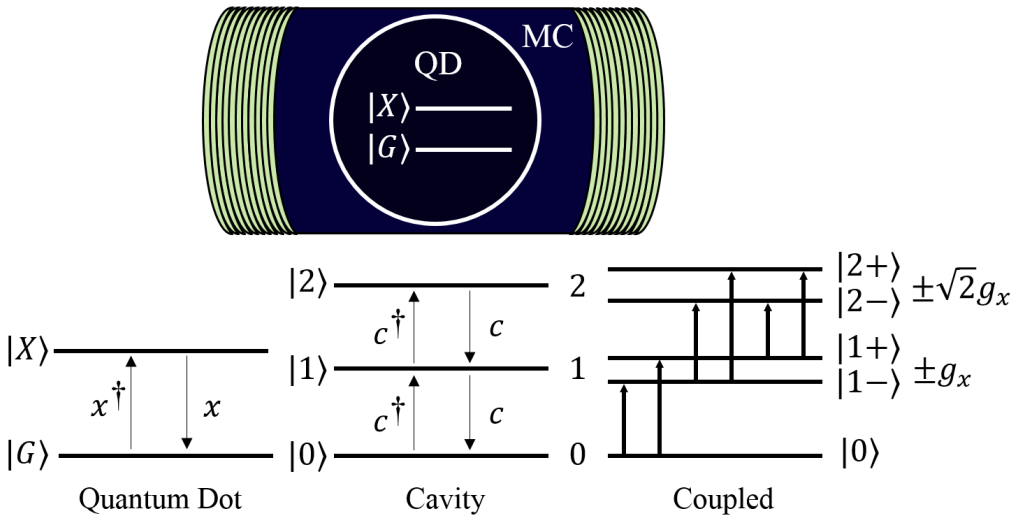

Figure 1.4: Jaynes-Cummings model for a quantum dot exciton interacting with an optical cavity mode, truncated to the lowest rung possible to observe four-wave mixing in the low-excitation regime. To observe a linear response in the low-excitation regime, one less rung of the cavity, and thus coupled system, is required.

Confining an exciton in a QD structure and embedding it into a microcavity couples the exciton to the electric field present inside the cavity, resulting in formation of a quasiparticle referred to as a microcavity polariton. This type of research is known as cQED. The general mechanics model photons being absorbed and re-emitted by the exciton, and this takes place until the cavity or QD damping releases the photon into the environment, modeled either using Lindblad dissipation or coupling to phonons, or both.

The first and perhaps standard picture of cQED is an atom interacting with a cavity field. The atom in most cases is one which can be modeled with the 2LS. The coupled model describes an interaction between a 2LS and a harmonic oscillator. When the motion of the 2LS is ignored and the rotating wave approximation is applied, the JC model provides a fully analytically solvable framework to study the

interaction [5, 9]. The JC model is the simplest quantum model which accurately describes the interaction of two sub-systems. Though it is a simple model, it has attracted a huge amount of interest from both theoretical and experimental groups.

Some theoretical predictions include: state reconstruction [36, 37], field squeezing [38–40], collapse-revivals [41], single photon states (Fock states) [42], atomic disentanglement [43–45], superposition of large amplitude coherent states (Schrödinger cats) [46, 47], nondemolition measurements [48], decoherence [49, 50], and a lot of these theoretical predictions have been realised experimentally: [51–63].

Around the time cQED was growing, another field of research appeared branched off called quantum information [64]. The carrier of quantum information, the qubit, can be encoded in either a 2LS or in a field state. In the 2LS describing a QD, the exciton may be in the absolute ground state, or in the ground exciton state. In the model of a cavity, the two lowest energy Fock states can encode the qubit $|0\rangle$ and $|1\rangle$. Applications of cQED in quantum information have also been studied experimentally [54–59, 65–74].

In this thesis, the JC model is applied to a 2LS and then generalised to a 3-level system (3LS) representing the quantum state of an exciton and biexciton in the QD, coupled to cavity photons. In the 2LS, two states represent the absolute ground state of the QD, and the ground state of an exciton bound by the QD.

The rotating wave approximation [75] allows us to neglect faster oscillating terms which appear in the more general Rabi model[76], The original JC Hamiltonian is given by

$$H = \omega_x x^\dagger x + \omega_c c^\dagger c + g(c^\dagger x + x^\dagger c)\,, \tag{1.1}$$

Here, ω_x and ω_c are the complex frequencies of the QD exciton and the cavity mode,

respectively. $c^\dagger$ and c are cavity ladder operators, or cavity photon creation and annihilation operators, the same as in a quantum harmonic oscillator, and $x^\dagger$ and x are creation and annihilation operators for the QD. ω_c and ω_x are the individual cavity and exciton frequencies of each uncoupled system, and g_x is the coupling strength between cavity and QD. While g_x is real, ω_c and ω_x are in general complex valued, the real part Ω is the frequency and the imaginary part γ is an associated decay rate.

$$\begin{aligned} \omega_c &= \Omega_c - i\gamma_c \\ \omega_x &= \Omega_x - i\gamma_x \end{aligned} \tag{1.2}$$

If we include complex frequencies as part of the JC Hamiltonian, it is no longer Hermitian, and so technically doesn't correspond to energy. Only the real parts of eigenfrequencies of H are the energy in this case.

The Lindblad operator consists of the sum of a Hamiltonian component and a dissipation component. The hamiltonian component allows energy to be transferred between rungs of the Jaynes-Cummings ladder. The dissipation term allows energy to leak permanently out of the system. By looking at the matrix elements of the Lindblad operator L, we find the diagonal block elements show coupling between inter-rung eigenstates of the ladder, and off-diagonal blocks show a one-way dissipation of energy down the rungs of the JC ladder. See Sec. B for details on elements of the Lindblad matrix.

There are two coupling regimes which are observable via the JC model dynamics. The strong and weak coupling regimes are entered by changing the value of the QD-cavity coupling constant g_x [4, 77].

For strong coupling, energy exchanged between the cavity and QD is partially reversible, and eigenstates of the system represent light-matter coupling known in literature as a dressed state or polariton [21].

By looking at the eigenvalues of the 2LS Hamiltonian, the weak and strong

coupling regimes are revealed in the square-root term $\pm\sqrt{g_x^2+\delta^2}$, in the resonant case of $\Omega_c = \Omega_x$.

$$\omega_{1,2} = \Omega_c - \frac{i}{2}(\gamma_c+\gamma_x) \pm \frac{1}{2}\sqrt{4g_x^2-(\gamma_x-\gamma_c)^2} \tag{1.3}$$

When g_x is smaller than the dampings $\frac{1}{2}|\gamma_c-\gamma_x|$, there is no longer any real splitting between each eigenstate, so they become degenerate, describing the weak coupling regime where damping terms γ_c and γ_x are larger than the coupling strength g_x. In this case, the exciton will decay significantly faster than re-absorption can occur. The exciton decay rate of irreversible emission can be enhanced by the Purcell effect [12, 19, 78]. Vice versa, when g_x is larger than the dampings $\frac{1}{2}|\gamma_c-\gamma_x|$, the real eigenstates split into two, with distinct energies Ω_1 and Ω_2, and corresponding linewidths γ_1 and γ_2. The real part of the system eigenenergies $\omega_{1,2}$ are degenerate in the resonant case, corresponding to the crossing of the exciton and photon

This work focuses on the strong coupling regime, though routines developed allow for the weak coupling regime to be studied by changing the dampings γ_c and γ_x. It is convenient to keep the exciton-cavity coupling set to 1 for numerical reasons, particularly for a highly excited cavity where many rungs of the JC ladder must be accounted for. This issue is tackled by the remainder of the thesis.

For the case of zero detuning and strong coupling, the splitting between polariton lines is $\Delta\Omega = \Omega_1 - \Omega_2$ is highly dependent on the QD-cavity coupling strength g_x. This separation, known as Rabi splitting, is straightforwardly obtained from Eq. (1.3). Moving from the linear regime to four-wave mixing polarisation, we see the same eigenstates describing the polariton doublet, with additional four polariton lines [8] which can be found by finding the eigenenergies of the second rung transitions, described in Sec. B for the 2LS and Sec. H

A review of some multi-level JC models [79] lists some interesting modifications

one can make to attempt to model a more realistic system. Models can be extended in a number of ways; by extending the Fock basis to increase the light capacity of the cavity, or adding more levels to the QD system. One attempt was made to deal with a 3LS to study six-wave mixing dynamics, but not in the high excitation regime. [80]

For the remainder of the introduction, consider an excitation of the QD-cavity system by a sequence of ultrashort optical pulses or by an extended finite wave packet of light. The master equation describing the time evolution of the density matrix (DM) representing the full set of mixed states of the QD-cavity system can be written as

$$i\dot{\rho}(t) = \left[\hat{L} + \hat{\mathcal{L}}(t)\right] \rho(t) \tag{1.4}$$

with the time-independent $\hat{L}$ and time-dependent $\hat{\mathcal{L}}(t)$ components of the Lindblad operator describing the time evolution of the density matrix $\rho(t)$.

1.5 Exciting the Jaynes-Cummings Cavity with an Ultrashort Pulse of low intensity

The JC model applied to the FWM [8, 17] accurately describes measured FWM spectra at low excitation power, corresponding to an average photon number excited below unity. Deviations between theoretical predictions and experimental data have been attributed to higher rung contributions to emitted photon spectra [81], where also some signatures of a Mollow triplet [82] have been reported, recently extended to larger photon numbers.[83]. We note that in the nonlinear response for pulsed excitation, as treated here, the Mollow triplet formation is substantially different from that observed with continous wave excitation in resonance fluorescence [84–86].

Optical cavities ideally have a large Q factor $Q = \omega_c/\delta\omega_c$ of the cavity mode, defined as the ratio of a cavity frequency ω_c to the full width at half maximum (FWHM) of the cavity mode $\delta\omega_c$ (which is the cavity damping parameter γ_c), allowing cavity photons to have a long lifetime. A light beam in this case will reflect many times between cavity mirrors, which means the linewidth (damping factor) of the cavity beam is tiny compared to the frequency of the laser. The average lifetime increases linearly with the Q-factor. Good cavities can hold photons for a long time without them leaking out into the environment. In real cavitites, the Q-factor and lifetime are limited. The photon can escape from the cavity via any number of imperfections in the system, including for example scattering by defects, phonon coupling, interaction with the crystal lattice.

We can excite a quantum-dot microcavity (QDMC) system via the cavity, allowing the cavity-QD coupling to excite the full system. In this thesis we consider pulsed excitation, approximating the shape of the pulse to an infinitesimally short delta function, a reasonable approximation based on experiments which use a pulse duration of $1ps$ [8], which compared to the timescale of dynamics of the system is very short, and so is a reasonable approximation.

The time-dependent operator $\hat{\mathcal{L}}(t)$ introduced in Eq. (1.4) is defined as

$$\hat{\mathcal{L}}(t)\rho(t) = [V(t), \rho(t)]\,, \tag{1.5}$$

where $V(t)$ is a time-dependent perturbation to the JC Hamiltonian describing the excitation of the cavity given by Eq. (1.6):

$$V(t) = -\boldsymbol{\mu} \cdot \boldsymbol{\mathcal{E}}(t)c^\dagger - \boldsymbol{\mu}^* \cdot \boldsymbol{\mathcal{E}}^*(t)c\,, \tag{1.6}$$

The general solution of Eq. (1.4) can be written as

$$\begin{aligned}\rho(t) &= T\exp\left\{-i\int_{t_0}^{t}\left[\hat{L}+\hat{\mathcal{L}}(\tau)\right]d\tau\right\}\rho(t_0)\\ &= T\prod_{j=0}^{J-1}Q_j\rho(t_0)\,,\end{aligned} \tag{1.7}$$

where T is the time-ordering operator. In the second line of Eq. (A.4), the full time evolution of the DM, between t_0 and t, is split into a time-ordered product of J operators

$$Q_j = T\exp\left\{-i\int_{t_j}^{t_{j+1}}\left[\hat{L}+\hat{\mathcal{L}}(\tau)\right]d\tau\right\}\,, \tag{1.8}$$

obtained by dividing full time interval (from t_0 to t) into J pieces, which are not necessarily equal:

$$t_0 < t_1 < \cdots < t_j < t_{j+1} < \cdots < t_J = t\,. \tag{1.9}$$

Assuming that the time steps $\Delta t_j = t_{j+1} - t_j$ are small enough, these operators may be approximated as

$$Q_j \approx T\exp\left\{-i\int_{t_j}^{t_{j+1}}\hat{L}d\tau\right\}T\exp\left\{-i\int_{t_j}^{t_{j+1}}\hat{\mathcal{L}}(\tau)d\tau\right\}\,, \tag{1.10}$$

This separates time-dependent and time-independent components of Eq. (1.4) allowing us to treat the cavity-excitation and the cavity-QD interactions individually. While the first operator in Eq. (A.7) can be written as $e^{-i\hat{L}\Delta t_j}$ due to the time-independent $\hat{L}$, which will be the subject of the next section, the second operator requires integration of the time-dependent field $\boldsymbol{\mathcal{E}}(t)$ exciting the system. The second operator in Eq. (A.7) acting on the DM can be evaluated as

$$T\exp\left\{-i\int_{t_j}^{t_{j+1}}\hat{\mathcal{L}}(\tau)d\tau\right\}\rho(t_j) = U_j\rho(t_j)U_j^{\dagger}\,, \tag{1.11}$$

where

$$U_j = T \exp\left\{-i \int_{t_j}^{t_{j+1}} V(\tau) d\tau \right\} \tag{1.12}$$

is the evolution operator due to a time-dependent interaction $V(t)$. Using the explicit form of $V(t)$, given by Eq. (1.6), which provides in particular $[V(t), V(t')] = 0$ for any different or equal times t and t', we obtain

$$U_j = e^{i(E_j c^\dagger + E_j^* c)} , \tag{1.13}$$

where E_j can be interpreted as the complex electric field amplitude at time t_j

$$E_j = \int_{t_j}^{t_{j+1}} \boldsymbol{\mu} \cdot \boldsymbol{\mathcal{E}}(\tau) d\tau . \tag{1.14}$$

Combining the results, we obtain

$$Q_j \rho(t_j) \approx e^{-i\hat{L}\Delta t_j} U_j \rho(t_j) U_j^\dagger , \tag{1.15}$$

where U_j is given by Eq. (A.10).

We find a compact way of representing this solution.

$$U(E) = e^{i(Ec^\dagger + E^* c)} = e^{-|E|^2/2} e^{iEc^\dagger} e^{iE^* c} , \tag{1.16}$$

however we cannot yet extract phase-unique components of U, which are required for calculation of N-wave mixing.

Note that the full time evolution of the DM described in more detail in Appendix. A becomes exact if the excitation field is represented by a sequence of δ pulses, given by Eq. (1.17)

$$\boldsymbol{\mu} \cdot \boldsymbol{\mathcal{E}}(t) = \sum_j E_j \delta(t - t_j) . \tag{1.17}$$

The amplitudes E_j have the meaning of the pulse areas corresponding to the time intervals Δt_j .

Let us now consider the effect of a single δ pulse on the DM, which is given by Eq. (1.16) . Dropping index j for brevity, we first transform the evolution operator:

$$\rho_+ = U\rho_- U^\dagger \tag{1.18}$$

ρ_+ is the result of applying the pulse in Eq. (1.6) to a general density matrix before the pulse ρ_-. We find that for any values of n and m ,

$$U_{nm}(E) = e^{i\varphi(n-m)} C_{nm}(|E|) \tag{1.19}$$

with $C_{nm}(|E|)$ derived for an arbitrary number of rungs in Appendix. A for any relation between n and m.

Finally, applying the operators $U(E)$ and $U^\dagger(E)$, respectively, on the left and right sides of the DM, in accordance with Appendix. A, we arrive at a general solution to applying an infinitesimal pulse with phase equal to the required N-wave mixing channel phase to the density matrix.

1.6 Master Equation and Calculation of Optical Polarisation

Here we will describe the full dynamics of the JC system using a master equation approach, with some examples at the end of this subsection.

This thesis focuses mainly on the calculation of FWM polarisation and associated spectra. Other mixing orders are also considered, including linear polarisation and N-wave mixing polarisation, a natural extension as we will see of the model developed

to describe FWM polarisation. Here we will describe the method by which this polarisation is calculated. The definition of optical polarisation is as follows:

$$P(t) = Tr\{\rho(t)c\} \tag{1.20}$$

where we have the Trace (Tr) over the time dependent density matrix $\rho(t)$ multiplied by the cavity annihilation operator c associated to the observable quantity called cavity polarisation. When we analyse the polarisation in frequency domain we find the Fourier transform of Eq. (1.20). For the quantum-dot microcavity system, we can observe either the exciton polarisation or the cavity polarisation, in which we either substitute the exciton annihilation operator x or the cavity annihilation operator c to calculate.

The evolution of the QD-cavity system between and after excitation pulses is described by the master equation

$$i\dot{\rho} = \hat{L}\rho\,, \tag{1.21}$$

which has solution expressed in Eq. (A.12):

$$\rho(t+\tau) = e^{-i\hat{L}\tau}\rho(t) \tag{1.22}$$

The action of the Lindblad operator on the DM can be conveniently expressed as

$$\hat{L}\rho = H\rho - \rho H^* + 2i\gamma_x x\rho x^\dagger + 2i\gamma_c c\rho c^\dagger \tag{1.23}$$

with terms involving the complex Hamiltonian from Eq. (1.1) and the Lindblad dissipation terms for each the 2LS and cavity. Neglecting dissipation, the Hamiltonian becomes hermitian and the eigenvalues of L become transition energies between

neighbouring rungs of the JC ladder, and no energy is able to leak out of the system or leak into the environment. If dissipation is included, eigenvalues have a real (imaginary) part corresponding to the energy (Lorenzian broadening) of each transition.

By introducing an extended basis of Fock states we can write down the density matrix organised by rung. Let $|0\rangle$ be the element of ρ representing the ground state of the JC ladder, then $|1\rangle$ and $|2\rangle$ identify the first rung states and $|3\rangle$ and $|4\rangle$ are the second rung states.

$$\begin{aligned} |0\rangle &= |G,0\rangle \\ |1\rangle = |X,0\rangle \quad |2\rangle &= |G,1\rangle \\ |3\rangle = |X,1\rangle \quad |4\rangle &= |G,2\rangle \end{aligned} \tag{1.24}$$

and the density matrixρ_{ij} is defined by the density operatorρ in this basis of states

$$\rho = \sum_{ij} \rho_{ij} |i\rangle\langle j| \tag{1.25}$$

Then the density matrix ρ isthen vectorised in this basis. By extracting only elements of ρ which either have a time derivative of zero or are zero, according to Eq. (1.21), this results in the lower block subdiagonal elements making up the vectorised density matrix ρ. For this example the vectorised density matrix represents transitions truncated to the second rung of the JC ladder, with the zeroth rung being the ground state. This gives us 6 elements in $\vec{\rho}$, with rungs separated by a horizontal line.

$$\vec{\rho} = \left[\begin{array}{c} \rho_{10} \\ \rho_{20} \\ \hline \rho_{31} \\ \rho_{32} \\ \rho_{41} \\ \rho_{42} \end{array}\right] \tag{1.26}$$

The master equation (1.21) then evolves in matrix representation

$$i\dot{\vec{\rho}} = \hat{L}\vec{\rho}, \tag{1.27}$$

where $\hat{L}$ is now a 6×6 matrix, or equivalently a block-2×2 matrix, consisting of two diagonal blocks $L_{[00]}$ and $L_{[11]}$ corresponding to inter-rung oscillations and one off-diagonal block $L_{[01]}$ corresponding to Lindblad dissipation of energy down the rungs of the JC ladder.

$$\hat{L} = \left[\begin{array}{c|c} L_{[00]} & L_{[01]} \\ \hline \hat{\mathbb{0}} & L_{[11]} \end{array}\right] \tag{1.28}$$

where $\mathbb{0}$ denotes a block of zero elements and square brackets denote block elements, as opposed to single elements. It is convenient at this point to introduce a 2×2 matrix of the N-th rung of the JC Hamiltonian in the basis of Eq. (1.24)

$$H_N = \begin{bmatrix} \omega_x + (N-1)\omega_c & \sqrt{N}g \\ \sqrt{N}g & N\omega_c \end{bmatrix}, \tag{1.29}$$

which is the same as in Eq. (1.1).

$$L_{[00]} = \begin{bmatrix} \omega_x & g_x \\ g_x & \omega_c \end{bmatrix} \tag{1.30}$$

$$L_{[11]} = \begin{bmatrix} \omega_x - \omega_c - \omega_x^* & -g_x & \sqrt{2}g_x & \cdot \\ -g_x & \omega_x + \omega_c - \omega_c^* & \cdot & \sqrt{2}g_x \\ \sqrt{2}g_x & \cdot & 2\omega_c - \omega_x^* & -g_x \\ \cdot & \sqrt{2}g_x & -g_x & 2\omega_c - \omega_c^* \end{bmatrix} \tag{1.31}$$

$$L_{[01]} = \begin{bmatrix} \cdot & 2i\gamma_c & \cdot & \cdot \\ 2i\gamma_x & \cdot & \cdot & 2\sqrt{2}i\gamma_c \end{bmatrix} \tag{1.32}$$

The diagonal blocks of $\hat{L}$ are produced by the first two terms of the Lindblad operator Eq. (1.23) and are given by the hamiltonian terms in Eq. (1.1) and the off-diagonal block

Optical polarisation given by Eq. (1.20) is then found by allowing the density matrix to evolve over time, from a state at time t, $\rho(t)$ to a time $t+\tau$, $\rho(t+\tau)$.

$$\vec{\rho}(t+\tau) = e^{-i\hat{L}\tau}\vec{\rho}(t) \tag{1.33}$$

By eigendecomposing the exponential in Eq. (1.33) we find a list of eigenvalues ω_r which are the polariton transitions in the JC model, and calculate a list of associated weights A_r using the eigenvectors U and the eigenvector inverse V of $\hat{L}$. We take the time of the final pulse to be zero, and subsequent evolution to take place over a time t. Substituting Eq. (1.33) we find an expression for the evolution of ρ at time t after the final pulse has been applied.

$$\vec{\rho}(t) = e^{-i\hat{L}t}\vec{\rho}(0) = Ue^{-i\Omega t}V\vec{\rho}(0) \tag{1.34}$$

with Ω a diagonal matrix of eigenvalues. Using Eq. (1.34) we can finally find an expression for the time dependent polarisation $P(t \geq 0)$ with zero polarisation before $t = 0$, introducing the heaviside step function $\Theta(t)$ which is defined as to 1 (0) for positive (negative) t

$$P(t) = \Theta(t)\sum_r A_r e^{-i\omega_r t} \tag{1.35}$$

where we find the transition frequency weights A_r explicitly, using Eq. (1.20).

$$A_r = \sum_{i\,j} c^T{}_i \hat{U}_{ir} \hat{V}_{rj} \vec{\rho}(0)_j \tag{1.36}$$

with c^T the transpose of a vectorised (as per basis of Eq. (1.26)) form of the cavity annihilation operator c.

The spectral domain polarisation is given by its fourier transform of Eq. (1.35).

$$\tilde{P}(\omega) = \sum_r \frac{iA_r}{\omega - \omega_r} \tag{1.37}$$

For example we have created a system which has been excited with two delta pulses, the first has a phase channel of -1, the second has phase channel +2. The 6-element density vector is excited according to Eq. (1.18) then Lindblad dynamics reveal a list of eigenfrequencies ω_r and amplitudes A_r using Eq. (1.36) with Lindblad parameters: detuning $\omega_c - \omega_x = 0$, keeping $g_x = 1$, with damping $\gamma_c = \gamma_x$ varying from g_x down to $g_x/20$. We then find the FWM Polarisation spectrum by using Eq. (1.37) (Figure 1.5).

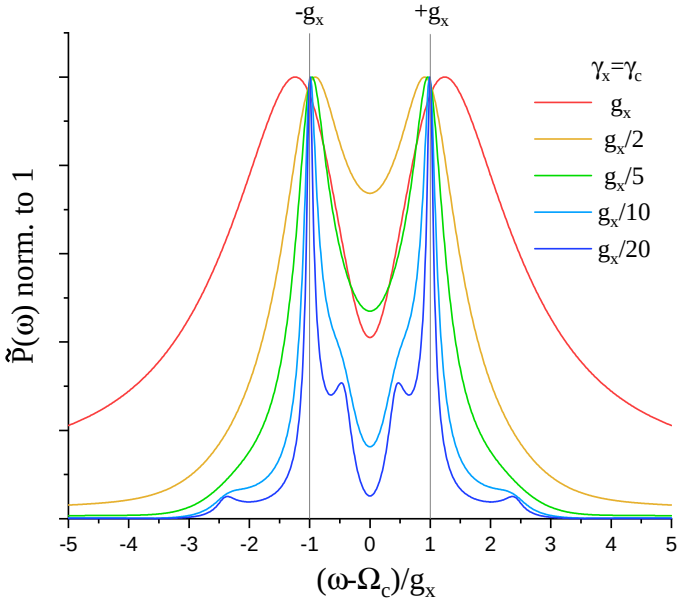

Figure 1.5: Polariton doublet transforming into the underlying six polariton lines describing low-excitation four-wave mixing polarisation.

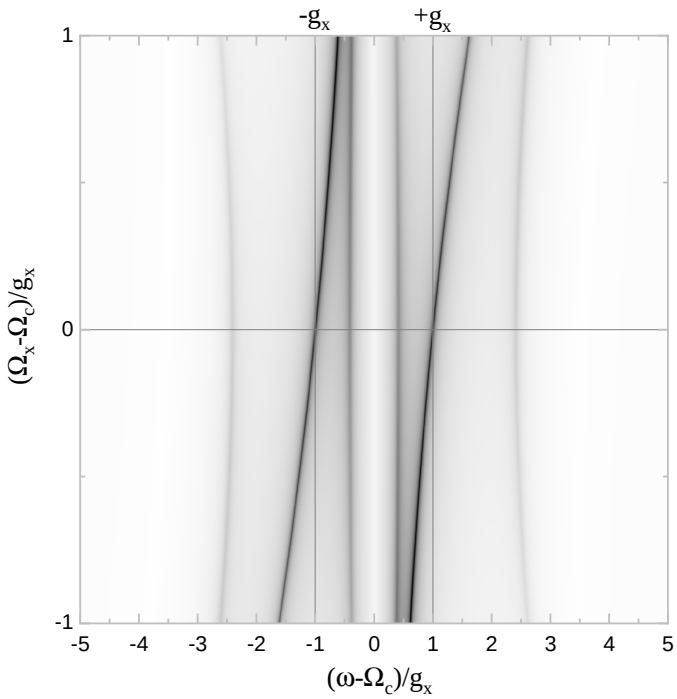

Figure 1.6: Polariton shift of a detuned system moving through the resonant state for FWM polarisation, using inverted colour scheme compared to Figure 1.6 and a gamma correction of 1/2. Detuning, in units of g_x range from -1 to 1. All other parameters the same as Figure 1.5.

Rabi doublets can be seen for each value of γ. The doublet peaks are more precisely located at $\pm g$ as broadening from neighbouring transition frequencies becomes smaller. Physically this means that as γ decreases, polaritons oscillate between $|n+\rangle$ and $|n-\rangle$ for each n for longer. As there is no allowed transition from $|1+\rangle$ to $|1-\rangle$ polaritons must first transition to the $|0\rangle$ ground state, transitioning twice, producing two bright transition lines at $\pm g$. When damping is equal to $g_x/20$ all lines clearly distinguishable. In Sec. 2 we allow the cavity excitation to increase and the brightest spectral lines are no longer caused by first rung transitions.

The polariton shift caused by a detuned system can be found by varying Ω_x and plotting the FWM polarisation along the x axis such as in Figure 1.6. Rabi splitting occurs least when detuning is minimised. This is visible in Figure 1.6 by comparing the two most intense (blackest) lines for each value of detuning.

This formalism is expanded in Sec. 2 and Sec. 3. One can use the sofware developed for this thesis to generate polarisation for any set of parameters used in the models presented, avoiding numerical constraints which inevitably appear with systems similar to the JC (and extended) Lindblad evolution dynamics.

1.7 Plan for this Thesis

We analyze here the FWM and higher-order non-linear response, which can be measured by heterodyne spectral interferometry [87].

We consider a general case of the $\mathcal{N}$-wave mixing ($\mathcal{N}$WM) cavity polarisation spectrum given by Eq. (2.19). While the formalism described in this thesis and in Sec. B and Sec. A is developed for any number of excitation pulses and arbitrary delay times between them, we focus on a degenerate $\mathcal{N}$WM, generated by two optical pulses with complex pulse areas E_1 and E_2, so that $\mathcal{N} = |\Delta N_1| + |\Delta N_2| + 1$ with $\Delta N = \Delta N_1 + \Delta N_2 = 1$. The optical response of the system carries a phase $\Phi = \Delta N_1\varphi_1 + \Delta N_2\varphi_2$ with φ the phase of each pulse's complex electric field amplitude $E = |E|e^{i\varphi}$ (the FWM corresponds to the $\Phi = 2\varphi_2 - \varphi_1$ phase channel, with $\mathcal{N} = 4$) and in the low-excitation regime is proportional to a factor $ie^{i\Phi}|E_1|^{|\Delta N_1|}|E_2|^{|\Delta N_2|}$ which we extract from all figures in Sec. 2 and Sec. 3. We assume for simplicity a zero delay between the pulses and focus on the case of an arbitrary pulse area E_1 and small E_2 ($|E_2| \ll 1$); the opposite case of small E_1 and arbitrary E_2 is treated in Sec. A. We concentrate on the zero detuning $\Omega_X = \Omega_C$ here, while results for non-zero detuning are provided in Sec. E.2)

All units presented in this thesis are of g_x (often abbreviated g), the QD exciton-cavity coupling strength. If no units are presented in a figure, assume they are in g_x. g_x is a unit which when changed, does not change the shape of any plots, and can easily be extracted from all equations with the only consequence being that all

frequencies and coupling strengths are now in units of g_x.

The external excitation pulse drives the cavity mode, leaving it in a coherent state with a Poisson distribution in the photon number, the same as the 2LS as the cavity properties have not changed.

The subsequent dynamics due to the coupling to the 2LS and the damping can be expressed as the eigenstate dynamics of the rungs of the JC ladder, which have initial amplitudes according to the eigenstate decomposition of the initial excitation of the cavity mode.

For excitation with average photon numbers much lower that one, only the first two rungs of the ladder are relevant for the FWM response, with six optical transitions fully describing the dynamics of the system, as demonstrated by good agreement with experiment [8, 17, 81]. As the excitation power increases, higher rungs become important for the QD-cavity dynamics and need to be taken into account in the modeling of high-intensity experiments [27, 81, 83].

The JC model is very well documented for predicting the behaviour of a QD-cavity system, but there is no coupling to any external environment. There is evidence that suggests phonons contribute largely to optical decoherence of the system[88–100], and thus overall dynamics, sometimes even at zero temperature [101–105]. Phonons (quasiparticles which represent quanta of thermal lattice vibrations [106].) are not considered in the dynamics in this model, and also throughout this thesis, though a basic phonon model can be added to the model code developed for this thesis, see Sec. 4 for more discussion on this.

It is useful to study the QDMC system without modeling phonons. The Jaynes-Cummings model is able to do this very well, and is exactly solvable [8]. We aim to expand on the work presented in [8], mainly to improve understanding of the transition from the low-excitation regime to the high-excitation regime.

In quantum mechanics often understanding the most simple nontrivial systems

can provide room for interpretation of more complex and realistic models. Also with simple systems analytical solutions can be found. With modern computing available, numerical solutions of system dynamics is the quickest option, but analytic solutions reveals a deeper meaning to the results and their dependence on parameters. In this Thesis, we present an exact numerical approach and analytic approximation in the low-damping limit to the nonlinear optical response of a 2-level QD-cavity system excited by an arbitrary number of photons. In particular, we calculate the FWM and higher order nonlinearities at different excitation strengths, taking into account up to 800 rungs of the JC ladder in the Lindblad dynamics of this system, and including all allowed transitions which occur between adjacent rungs. We show that the FWM spectrum consists of discrete polariton lines with a broadening increasing with the rung number. At higher excitation, these lines interfere and gradually transform the spectral profile from the lowest-rung polariton doublet towards the classical Mollow triplet [82], albeit having an additional sideband linewidth due to the distribution of photon numbers in the excitation treated here. We also present a similar method applied to an extended QD model, the 3-level biexciton model. We find a number of new interesting features of this system, including vanishing FWM polarisation and the formation of Mollow triplet-like quintuplets.

2 | Two-Level Quantum Dot Coupled to a Microcavity

This section will expand on the current understanding of the JC model describing a quantum dot coupled to a microcavity. We measure the polarisation of light exiting the cavity by exciting the system with two ultrashort pulses of arbitrary intensity. By extracting a phase from the effect of each pulse we can find N-wave mixing polarisation. We find analytic forms for all equations expressed in this section, with comparison between multiprecision numerical and analytic results.

Our parameter space includes nine quantities. In terms of dynamics we have five; the natural oscillation frequencies of a cavity photon Ω_c and a quantum dot exciton Ω_x, a coupling constant describing the strength of interaction between cavity photons and the quantum dot exciton g_b, cavity damping (coupling between the cavity and the environment) γ_c and QD decoherence rate γ_x for example due to exciton-phonon coupling and exciton radiative recombination. In terms of pulsed excitation we have four; the magnitudes of two pulses E_1 and E_2, and the phase order of the two pulses ΔN_1 and ΔN_2. We concentrate on two-pulse excitation resulting in measurement of degenerate N-wave mixing. Although the developed code supports a pulse count greater than 2, this situation is not considered in this thesis. There are also two additional parameters which are not studied but have been implemented, the delays between pulses 1 and 2, τ_{12}, and the delay between pulse 2 and the beginning of

measurement, τ_{2+}.

Owing to the analytical solutions found for this problem, we provide a detailed visualisation of this quantum-to-classical transition, tracing the individual rung contributions.

We present an analytic approximation in the low-damping limit, providing a closed-form solution in terms of elementary (in time-domain) or special functions (in frequency domain), which allows us to understand and quantify the optical nonlinearity of any order. It proves, in particular, that the position and linewidth of the spectral sideband is given, respectively, by $2Eg$ and $4g$, where E is the excitation pulse area ($|E|^2$ is the average number of cavity photons excited) and g is the QD-cavity coupling strength.

Note that the interaction of the QD exciton with a phonon environment is not included in this formalism. However, as has been recently demonstrated with the help of an asymptotically exact solution [107], the acoustic-phonon induced dephasing can be incorporated in the QD-cavity QED by simply renormalizing the QD-cavity coupling strength $g \to ge^{-S/2}$ and the exciton energy $\Omega_x \to \Omega_x + \Omega_p$, where S is the Huang-Rhys factor and Ω_p is the polaron shift. This provides a valid approximation for the cavity polarisation in the regime of g much smaller than the typical energy of interacting phonons.

2.1 System Hamiltonian and master equation

In this section we expand on Sec. 1.6 to include an arbitrary number of rungs to the 2LS, by expanding all matrices in the master equation to accommodate both a higher magnitude excitation to the cavity, and more complex dynamics via Lindblad time evolution. The pulse operator V is allowed to include as many rungs of excitation that is required to model a pulse of arbitrary strength, and the system evolves

producing new phenomena, and the complex dynamics is shown to be exactly solvable, we see a transition to the classical regime, the Mollow triplet, and explain the properties of its appearance as a function of the cavity excitation strength.

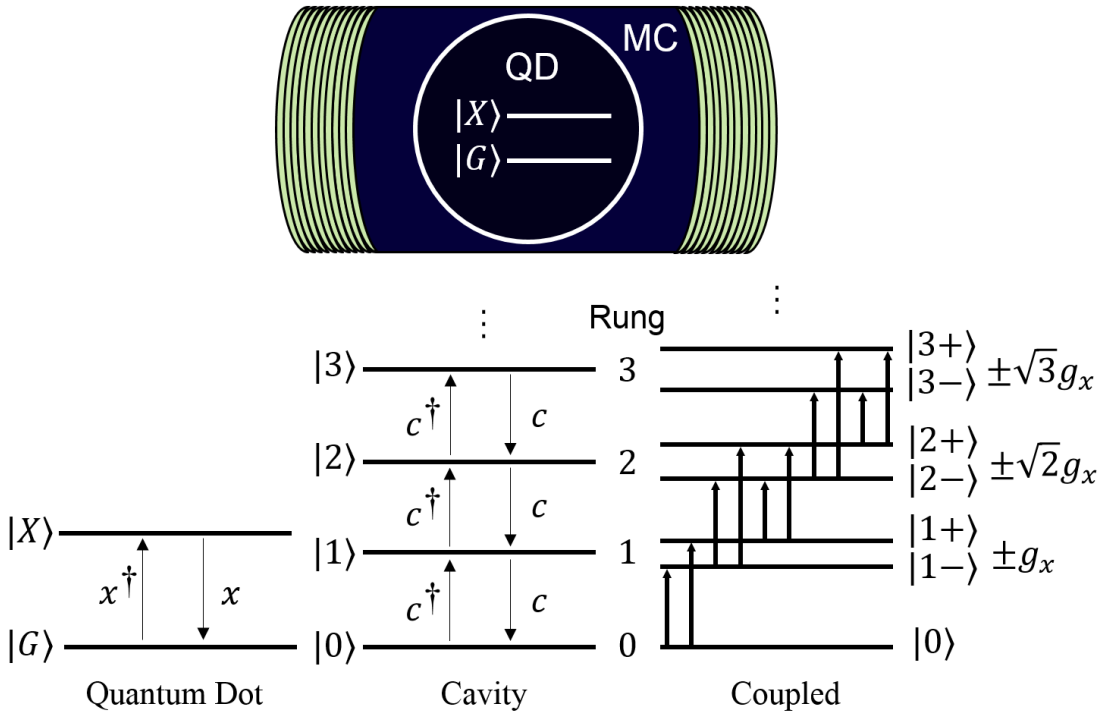

Figure 2.1: Illustration of the Jaynes-Cummings model for the QD-cavity system. For $\Omega_c = \Omega_x$, the nth rung of the JC ladder consists of mixed states $|1, n-1\rangle \pm |0, n\rangle$ with transition energy splitting $\sqrt{n}g_x$.

The QD-cavity dynamics is well described [8, 17, 108] by a master equation (taking $\hbar = 1$),

$$i\dot{\rho} = \hat{L}\rho + [V(t), \rho]\,, \tag{2.1}$$

where ρ is the DM, and the Lindblad super-operator $\hat{L}$ is given by

$$\begin{aligned}\hat{L}\rho \;\; &= [H, \rho] \;\; -i\gamma_x(x^\dagger x\rho + \rho x^\dagger x - 2x\rho x^\dagger) \\ &\quad\; -i\gamma_c(c^\dagger c\rho + \rho c^\dagger c - 2c\rho c^\dagger)\,.\end{aligned} \tag{2.2}$$

Here, H is the JC Hamiltonian of the QD-cavity systems,

$$H = \Omega_x x^\dagger x + \Omega_C c^\dagger c + g(x^\dagger c + c^\dagger x)\,, \tag{2.3}$$

$x^\dagger(c^\dagger)$ and $x(c)$ are, respectively, the creation and annihilation operators of the QD exciton (cavity mode CM), respectively, and $\omega_{x(c)} = \Omega_{x(c)} - i\gamma_{x(c)}$ are their complex eigen-frequencies. The Lindblad dissipator appears as imaginary components of $\hat{L}\rho$ scaled by damping coefficients γ_c and γ_x.

2.2 Pulsed Excitation of the QD-Cavity system

The dipole coupling of the CM to the external classical electric field $\boldsymbol{\mathcal{E}}(t)$ is described in the rotating wave approximation (consistent with the JC model) by an operator

$$V(t) = -\boldsymbol{\mu}\cdot\boldsymbol{\mathcal{E}}(t)c^\dagger - \boldsymbol{\mu}^*\cdot\boldsymbol{\mathcal{E}}^*(t)c\,, \tag{2.4}$$

in which $\boldsymbol{\mu}$ is the effective dipole moment of the CM. For the QD-cavity system excited by a sequence of ultrashort pulses, this interaction is well described by a series of δ functions:

$$\boldsymbol{\mu}\cdot\boldsymbol{\mathcal{E}}(t) = \sum_j E_j\delta(t-t_j)\,, \tag{2.5}$$

where E_j is the complex integral amplitude (i.e., the pulse area) of the pulse arriving at time t_j. Excitations by longer pulses and even finite wave packets can also be approximated with Eq. (2.5), as shown in detail in Appendix. B.

Using the form of the excitation Eq. (2.5), the evolution of the DM can be described as a time-ordered product of operators acting on the initial DM, each such operator consisting of a pulse operator $\hat{X}(E_j)$ due to pulse j and a subsequent

Lindblad dynamics during time Δt between pulses (i.e. $\Delta t \leqslant t_{j+1} - t_j$):

$$\rho(t_j + \Delta t) = e^{-i\hat{L}\Delta t}\hat{X}(E_j)\rho(t_j - 0_+)\,, \tag{2.6}$$

where 0_+ is a positive infinitesimal. The pulse operator has the following explicit form

$$\hat{X}(E)\rho = e^{i(Ec^\dagger + E^* c)}\rho e^{-i(Ec^\dagger + E^* c)}\,, \tag{2.7}$$

in which $e^{i(Ec^\dagger + E^* c)} = e^{-|E|^2/2}e^{iEc^\dagger}e^{iE^* c}$, standing on each side of the DM, is an operator transforming the cavity ground state into a Glauber coherent state [109] with the eigenvalue iE. Hence the average number of photons, which is given by the expectation value of $c^\dagger c$, is $|E|^2$ in such a coherent state. However, we need to address here the more general case of the DM not in the ground state due to the preceding pulses and a subsequent Lindblad evolution.

Photon creation and annihilation matrix elements are constructed from their operators. Here, matrices are found in the cavity basis, ignoring mixed states involving the exciton.

$$c^\dagger = \begin{bmatrix} \cdot & \cdot & \cdot & \cdot & \cdots \\ 1 & \cdot & \cdot & \cdot & \cdots \\ \cdot & \sqrt{2} & \cdot & \cdot & \cdots \\ \cdot & \cdot & \sqrt{3} & \cdot & \cdots \\ \vdots & \vdots & \vdots & \vdots & \ddots \end{bmatrix} \tag{2.8}$$

e^{iV} and e^{-iV} matrices required by Eq. (2.7) can be found using Eq. (2.15). Let V be the pulse potential operator, defined as a hollow tridiagonal matrix. $V = Ec^\dagger + E^* c$,

is the pulse strength, physically representing the electric field strength of the pulse.

$$V = \begin{bmatrix} \cdot & E^* & \cdot & \cdot & \cdots \\ E & \cdot & \sqrt{2}\,E^* & \cdot & \cdots \\ \cdot & \sqrt{2}\,E & \cdot & \sqrt{3}\,E^* & \cdots \\ \cdot & \cdot & \sqrt{3}\,E & \cdot & \cdots \\ \vdots & \vdots & \vdots & \vdots & \ddots \end{bmatrix} \tag{2.9}$$

The exponential of V is equal to the C matrix described in Eq. (2.15)

$$e^{iV} = \begin{bmatrix} C_{11} & C_{12} & C_{13} & C_{14} & \cdots \\ C_{21} & C_{22} & C_{23} & C_{24} & \cdots \\ C_{31} & C_{32} & C_{33} & C_{34} & \cdots \\ C_{41} & C_{42} & C_{43} & C_{44} & \cdots \\ \vdots & \vdots & \vdots & \vdots & \ddots \end{bmatrix} \tag{2.10}$$

And since the operator is hollow tridiagonal hermitian, the identity $\left(e^{-iV}\right)_{mn} = \left(e^{iV}\right)_{mn}(-1)^{m+n}$ holds for an infinite matrix and for truncation using limited rungs.

$$e^{-iV} = \begin{bmatrix} C_{11} & -C_{12} & C_{13} & -C_{14} & \cdots \\ -C_{21} & C_{22} & -C_{23} & C_{24} & \cdots \\ C_{31} & -C_{32} & C_{33} & -C_{34} & \cdots \\ -C_{41} & C_{42} & -C_{43} & C_{44} & \cdots \\ \vdots & \vdots & \vdots & \vdots & \ddots \end{bmatrix} \tag{2.11}$$

This pulsed excitation problem can be solved fully analytically. We introduce an extended basis of Fock states $|\nu, n\rangle$ with the occupation numbers $\nu = 0,\ 1$ for the QD exciton and $n = 0,\ 1,\ 2\ldots$ for the CM. Using this basis, the DM can be written

as

$$\rho = \sum_{\nu\nu' nn'} \rho_{nn'}^{\nu\nu'} |\nu, n\rangle\langle\nu', n'| \,, \tag{2.12}$$

so that the total optical polarisation takes the following explicit form:

$$P(t) = \mathrm{Tr}\{\rho(t)c\} = \sum_{\nu n} \rho_{n,n-1}^{\nu\nu}(t)\sqrt{n} \,. \tag{2.13}$$

Furthermore, as we show in Appendix. A , the pulse operator $\hat{X}(E)$, see Eq. (2.7), with a complex amplitude of optical excitation, $E = |E|e^{i\varphi}$, transforms the elements $\rho_{nn'}^{\nu\nu'}$ of the DM in the following way:

$$\left[\hat{X}(E)\rho\right]_{nn'}^{\nu\nu'} = \sum_{kk'} e^{i\varphi(n-k-n'+k')} C_{nk} C_{n'k'}^{*} \rho_{kk'}^{\nu\nu'} \tag{2.14}$$

with the transformation matrix taking an analytic form

$$C_{nk} = i^{n-k}|E|^{n-k}\sqrt{\frac{k!}{n!}} L_k^{n-k}(|E|^2) e^{-|E|^2/2} \,, \tag{2.15}$$

where $L_k^p(x)$ are the associated Laguerre polynomials. The phase factor in Eq. (2.14) determines the phase Φ of the optical response, which in turn determines the distance $\Delta N = \nu + n - (\nu' + n')$ between the rungs involved in the coherent dynamics, see Figure 2.1. For example, starting from a fully unexcited DM $\rho_0 = |0,0\rangle\langle 0,0|$, an optical pulse Eq. (2.7) distributes the excitation between all rungs of the JC ladder. However, focusing on a particular phase $\Phi = \varphi\Delta N$, we see that the subsequent Lindblad evolution does not couple the group of the elements of the DM, selected according to ΔN, with any other group.

To extract phases from matrix elements of Eq. (2.10) and Eq. (2.11), we find that along the diagonals lie integer powers p of the optical excitation E, with all $C_{i,i-p}$ elements having a common phase factor of $e^{ip\phi}$.

The JC Hamiltonian conserves the particle number, so that without dissipation

($\gamma_x = \gamma_c = 0$) the evolution between pulses does not alter the rung number on either side of the DM, in this way conserving ΔN. Including the disspation introduces on both sides of the DM simulteneous relaxation transitions between neighboring rungs, again not changing the distance ΔN.

With J pulses exciting the system, all phase channels can be treated independently, so that one can select a phase $\Phi = \sum_{j=1}^{J} \Delta N_j \varphi_j$ of the optical polarisation, determining the transitions between rungs present in the coherent dynamics following the pulses. These rungs of the JC ladder are separated by a distance $\sum_{j=1}^{J} \Delta N_j$. In the standard FWM polarisation, excited by a sequence of three pulses, the selected phase channel after all pulses is given by $\Phi = \varphi_2 + \varphi_3 - \varphi_1$, corresponding to $\Delta N_1 = -1$ and $\Delta N_2 = \Delta N_3 = 1$, and thus involving transitions between neighbouring rungs only. The same phase selection procedure is applicable to the evolution of the system between pulses, which does not explicitly depend on the phases, in this way determining the pulse delay dynamics.

2.3 Evolution of the system between or after pulses

The evolution of the system between pulses ($t < 0$) and after pulses ($t > 0$) can also be described by explicit analytic expressions. Introducing a vector $\vec{\rho}$ comprising all relevant elements of the DM, i.e. those involved in the coherent dynamics for the selected phase, the time evolution after pulses is given by

$$\vec{\rho}(t) = e^{-i\hat{L}t}\vec{\rho}(0_+) = \hat{U}e^{-i\hat{\Omega}t}\hat{V}\vec{\rho}(0_+)\,, \tag{2.16}$$

where matrices $\hat{U}$ and $\hat{V}$ diagonalizing the Lindblad matrix, $\hat{L} = \hat{U}\hat{\Omega}\hat{V}$, take an explicit analytic form (Appendix. B) in terms of 2×2 matrices Y_N diagonalizing the

complex Hamiltonian H_N of the N-th rung,

$$H_N = \begin{bmatrix} \omega_x + (N-1)\omega_c & \sqrt{N}g \\ \sqrt{N}g & N\omega_c \end{bmatrix} = Y_N \begin{bmatrix} \lambda_N^- & 0 \\ 0 & \lambda_N^+ \end{bmatrix} Y_N^{\mathrm{T}}\,, \tag{2.17}$$

where $\lambda_N^{\pm}$ are the complex eigenvalues of H_N. The Lindblad matrix can be written as a square block bidiagonal matrix Eq. (2.18).

$$\hat{L} = \left[\begin{array}{c|c|c|c|c} L_{[00]} & L_{[01]} & \hat{\mathbb{0}} & \hat{\mathbb{0}} & \cdots \\ \hline \hat{\mathbb{0}} & L_{[11]} & L_{[12]} & \hat{\mathbb{0}} & \cdots \\ \hline \hat{\mathbb{0}} & \hat{\mathbb{0}} & L_{[22]} & L_{[23]} & \cdots \\ \hline \hat{\mathbb{0}} & \hat{\mathbb{0}} & \hat{\mathbb{0}} & L_{[33]} & \cdots \\ \hline \vdots & \vdots & \vdots & \vdots & \ddots \end{array}\right] \tag{2.18}$$

with lines separating dynamics corresponding to different rungs of the JC ladder, and $\hat{\mathbb{0}}$ symbolises a zero block matrix. The diagonal matrix $\hat{\Omega}$ in Eq. (2.16) consists of the eigenvalues of $\hat{L}$ which are given by $\omega_r = \lambda^s_{N+\Delta N} - (\lambda^{s'}_N)^*$, with a fixed ΔN and all possible sign combinations of $s, s' = \pm$ and rung numbers N, including the case of the ground state with $\lambda_0 = 0$. Fixing ΔN is equivalent to acknowledging that the observable in question, cavity polarisation, is found using the expression in Eq. (1.20), where the operator c can be thought of as phase shifting, as it has the effect of shifting block elements of the density matrix which correspond to $\Delta N = 1$ up by one sub-block-diagonal into the main block-diagonal, where the trace over ρc then measures the correct mixing channel. The linear polarisation Eq. (2.13) and its Fourier transform take the following analytic form

$$P(t>0) = \sum_r A_r e^{-i\omega_r t}\,, \quad \tilde{P}(\omega) = \sum_r \frac{iA_r}{\omega - \omega_r} \tag{2.19}$$

with the amplitudes A_r being the products of the matrix elements of $\hat{U}$ and $\hat{V}$, according to Eqs. (2.13) and (2.16). By introducing an extended basis of fock states we can find an expression for the complex amplitudes. Let ρ have two indices, combining the four basis indices in Eq. (2.12) into Eq. (2.20).

$$\begin{aligned} |0\rangle &= |G,0\rangle \\ |1\rangle = |X,0\rangle \quad |2\rangle &= |G,1\rangle \\ |3\rangle = |X,1\rangle \quad |4\rangle &= |G,2\rangle \\ |5\rangle = |X,2\rangle \quad |6\rangle &= |G,3\rangle \\ &\dots \end{aligned} \tag{2.20}$$

Then the density matrix ρ is vectorised in this basis by extracting only elements which either have a time derivative of zero or are zero, which results in the lower block subdiagonal elements making up the vectorised density matrix $\check{\rho}$.

$$\begin{aligned} i\dot{\rho} &= L\rho \\ i\dot{\rho}_{mn} &= \sum_{ij} \hat{L}_{mn,ij}\rho_{ij} \\ i\dot{\rho}_a &= \sum_{b} \hat{L}_{ab}\check{\rho}_b \end{aligned} \tag{2.21}$$

Then diagonalising $\hat{L}$ into eigenvector matrices $\hat{U}$ and $\hat{V}$ as described in Appendix. B we arrive at the expression for A_r, each of which describes the complex weight of contribution of each eigenfrequency ω_r of $\hat{L}$.

$$A_r = \sum_{i\,j} {c^T}_i \hat{U}_{ir} \hat{V}_{rj} \rho(0_+)_j \tag{2.22}$$

with c^T denoting the matrix transpose. We can use the list of complex pairs of A_r and ω_r to produce either the observables mentioned in Eq. (2.19), or go one step further and convolve it with a spectral response function to model experimental

results.

2.4 Dynamics of the two-level system coupled to a photonic cavity when highly excited by ultra-short pulses

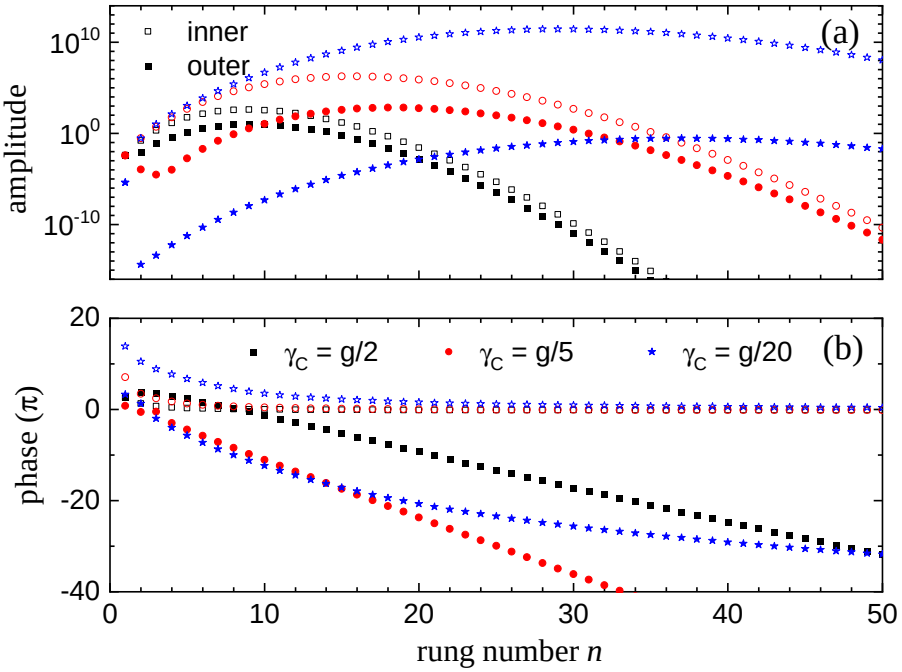

Figure 2.3: (a) Amplitude and (b) phase of $A_r^{(+)}$ [with a factor of $(-1)^n$ added] for inner (empty symbols) and outer (full symbols) transitions with positive frequencies $\mathrm{Re}(\omega_r) = \Delta_n^{o,i}$, as functions of the rung number n, for $|E_1| = 6$ and different values of γ_c as given; other parameters as in Fig. 2.2. For negative transition frequencies $A_r^{(-)} = [A_r^{(+)}]^*$.

The FWM spectrum $\tilde{P}(\omega)$ calculated for $\gamma_c = g/2$ is shown in Fig. 2.2(a) as a phase-amplitude color map for the pulse area E_1 up to $|E_1| = 10$, thus effectively exciting up 100 photons in the system. $|\tilde{P}(\omega)|$ is displayed in Fig. 2.2(c) for selected $|E_1|$, and the optical transitions between neighboring rungs which contribute to these spectra are shown in Fig. 2.2(d)-(f), in terms of the complex transition amplitudes

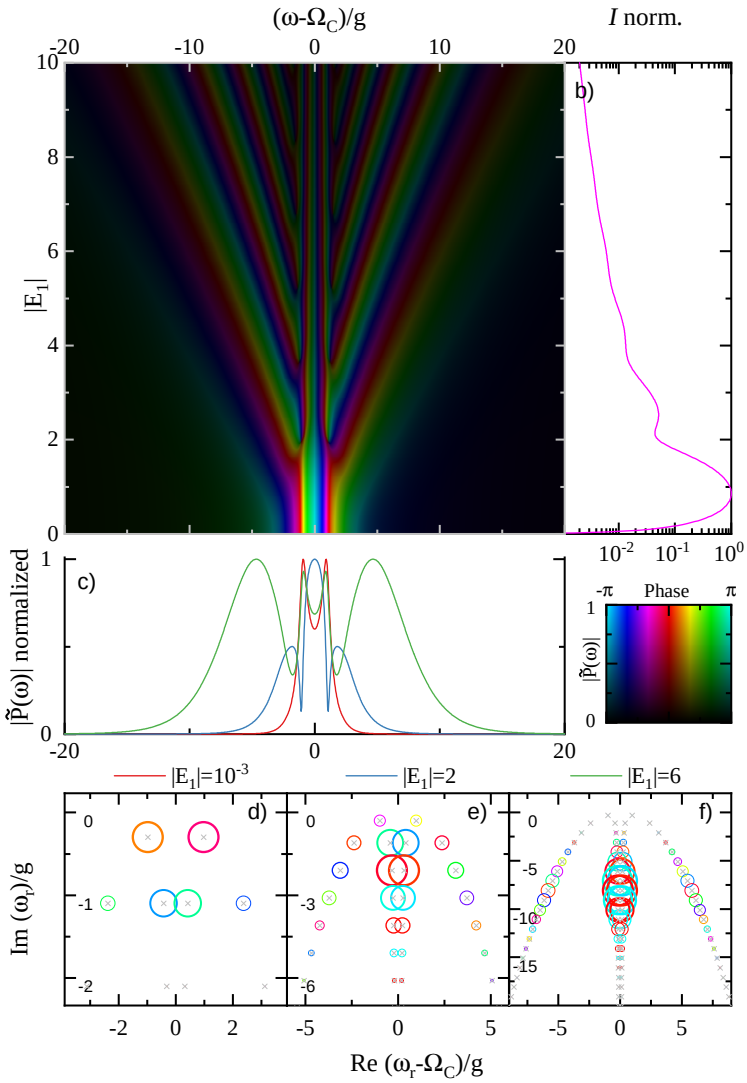

Figure 2.2: FWM response calculated for $|E_2| = 0.001$ and varying $|E_1|$, with $\Omega_x = \Omega_c$, $\gamma_C = g/2$, and $\gamma_x = g/10$. (a) FWM spectrum $\tilde{P}(\omega)$ in a color plot with the hue giving the phase (see color scale) and the brightness giving the amplitude $|\tilde{P}|^{1/4}$. (b) spectrally integrated power $I = \int |\tilde{P}(\omega)|^2 d\omega$ versus $|E_1|$. (c) $|P(\omega)|$ normalized to 1 at the maximum, for selected $|E_1|$ as labelled. (d)–(f) optical transition frequencies ω_r and their complex amplitudes A_r in $\tilde{P}(\omega)$, see Eq. (2.19), for different $|E_1|$ as given in (c). ω_r and A_r are shown, respectively, by crosses in the complex ω-plane and by circles centered at ω_r with an area proportional to $|A_r|$ and color given by the phase according to the scale in (a). See Appendix. E for complex colour map.

A_r (colored circles) and their frequencies ω_r (circle centers) (see Sec. 2.19). In the low-excitation regime ($|E_1| = 0.001$), only the first two rungs contribute, and the spectrum shows a doublet due to the lowest-rung transitions, studied in detail in [8]. For $|E_1| = 2$, the spectrum is wider, with no doublet seen, but with sidebands forming instead and a range of transitions contributing around rungs 2-4, see Fig. 2.2(e). For $|E_1| = 6$, there are clearer sidebands separated from the central peak, the doublet is seen again at the center, and higher rungs are involved in the coherent dynamics. See Appendix. E.2 for variation of parameters g_x, γ_x and γ_c.

2.4.1 Mollow triplet

Eq. (2.17) (in more detail Appendix. B) describe the transition frequencies between adjacent rungs of the JC ladder $\omega_r = \pm\Delta_n^\sigma - i(2n\gamma_c + \gamma_x)$, where $\sigma = o, i$, and n is the rung number. For each rung $n > 1$, there are two "inner" and two "outer" transitions, corresponding to $\Delta_n^o = (\sqrt{n+1} + \sqrt{n})g$ and $\Delta_n^i = (\sqrt{n+1} - \sqrt{n})g$, respectively. Neglecting relaxation, the system excited with $|E_1|^2$ photons has a dominant contribution coming from rungs with $n \sim |E_1|^2$. This implies that as E_1 increases, the spectrum can split into a central peak due to the inner transitions at $\omega \approx \pm\Delta_n^i \approx 0$, possibly with a fine structure, and two sidebands at around $\omega \approx \pm\Delta_n^o \approx \pm 2g|E_1|$ (more details in Appendix. C). Such a spectrum resembles Mollow's triplet observed in a two-level system continuously driven by a classical light [82]. Even though our QD-cavity system is excited in entirely different way, i.e. via a sequence of short pulses, the coherent excitation trapped within the cavity is akin to a classical continuous wave, provided that the number of photons is big enough and the damping is not too large, in this way supporting the analogy with Mollow's triplet.

In fact, the Rabi splitting of the sidebands and the phase range of $\tilde{P}$ in Fig. 2.2(a) grow almost linearly with E_1. However, the observed splitting is somewhat smaller

than the predicted value of $4g|E_1|$. A closer look into the complex transition amplitudes provided in Fig. 2.3 reveals a new phenomenon: A sub-Poissonian distribution peaked at a lower rung number than $|E|^2$. As damping increases, the peak of this amplitude distribution decreases, owing to the sensitive destructive interference of many transitions. This interference is so pronounced that calculating it numerically requires the use of high precision and high number of rungs - for example for $|E_1| = 10$ the results shown use 1000-bit precision and 500 rungs. Using 250 bits of precision is not enough for $P(\omega)$ to converge, but 500 is for parameters used in Figure 2.2. 1000 bits was used to totally remove the possibility of precision affecting results while varying the system parameters. The distribution is due to a relaxation of the optical excitation in the system towards lower rungs. Damping also plays a role in deciding where on the frequency axis sidebands appear, as seen in Appendix. F.1 comparing high damping to low damping results.

2.4.2 Analytic approximation

To understand the observed triplet, we develop an analytic approach to the $\mathcal{N}$WM response the limit of low damping ($\gamma_x, \gamma_c \ll g$) and large pulse area. Using Eqs. (2.14) and (2.15) we find all relevant elements of the DM after the pulses in Appendix. D:

$$\rho^{00}_{n+1,n}(0_+) = \frac{e^{-\lambda}\lambda^{n+1-m}L_m^{n+1-m}(\lambda)}{n!\sqrt{n+1}}\,, \tag{2.23}$$

where $\lambda = |E_1|^2$ and $m = \mathcal{N}/2$. In the limit of large pulse area, $\lambda \gg 1$, the Poisson distribution in Eq. (2.23) becomes Gaussian, with the mean rung number (given by the mean photon number) $\langle n\rangle = \lambda$ and mean deviation $\langle n^2 - \lambda^2\rangle = \lambda$. Around the maximum of this distribution, the Laguerre polynomials are approximated as $L_m^{n-m}(\lambda) \approx (\lambda/2)^{m/2}\, H_m(z)/m!$, where $z = (n-\lambda)/\sqrt{2\lambda}$ and $H_m(z)$ are Hermite

polynomials, and the frequencies of the inner and outer transitions as

$$\Delta_n^o \approx 2\sqrt{\lambda}g + z\sqrt{2}g\,, \qquad \Delta_n^i \approx \frac{g}{2\sqrt{\lambda}} - z\frac{g}{2\sqrt{2}\lambda}\,. \tag{2.24}$$

This allows us to replace the transition frequencies in Eq. (2.19) with $\omega_r = s\Delta_n^\sigma \approx \omega_{\sigma s} + z\Delta\omega_{\sigma s}$, where the frequencies $\omega_{\sigma s}$ and the linewidths $\Delta\omega_{\sigma s}$ are given by Eq. (2.24), and $s = \pm$. Note that the actual linewidth $\Delta\omega_{\sigma s}$ is produced by a coherent superposition of the inner or outer transitions and is thus determined by their frequency dispersion with respect to the rung number n. The coherent dynamics after pulses Eq. (2.16) can then be treated analytically, replacing $\sum_n \to \sqrt{2\lambda}\int dz$ in Eq. (2.13), which results in the following explicit form of the $\mathcal{N}$WM polarisation (see Appendix. D):

$$P_{\sigma s}(t) = \sum_{\sigma=i,o}\sum_{s=\pm}\frac{1}{2}A_\sigma^{(m)}(\Delta\omega_{\sigma s}t)^m e^{-i\omega_{\sigma s}t-(\Delta\omega_{\sigma s}t)^2/4}\,. \tag{2.25}$$

Fourier transforming Eq. (2.25) gives an analytic $\mathcal{N}$WM spectrum:

$$\tilde{P}(\omega) = \frac{(-i)^m}{4m!(\sqrt{2\lambda})^m}\left[\bar{P}(\omega) + \bar{P}^*(-\omega)\right]\,, \tag{2.26}$$

where

$$\bar{P}(\omega) = w_m\left(\frac{\omega-\sqrt{4\lambda}g}{\sqrt{2}g}\right) + 16\lambda^2 w_m\left(4\lambda\frac{\omega+g/\sqrt{4\lambda}}{\sqrt{2}g}\right)\,, \tag{2.27}$$

and $w_m(z) = (1/2)\int_0^\infty t^m e^{izt}e^{-t^2/4}dt$ is a generalized Faddeeva function, see Appendix. D for details. Here, $\lambda = |E_1|^2$ and $m = \mathcal{N}/2$. However, the same result Eqs. (2.25)–(2.27) is valid in the opposite case of small E_1 and arbitrary E_2, provided that the response is divided by λ, and $\lambda = |E_2|^2$ and $m = \mathcal{N}/2 - 1$ are used.

Figure 2.4 illustrates the analytic approximation, Eqs. (2.26) and (2.27), for

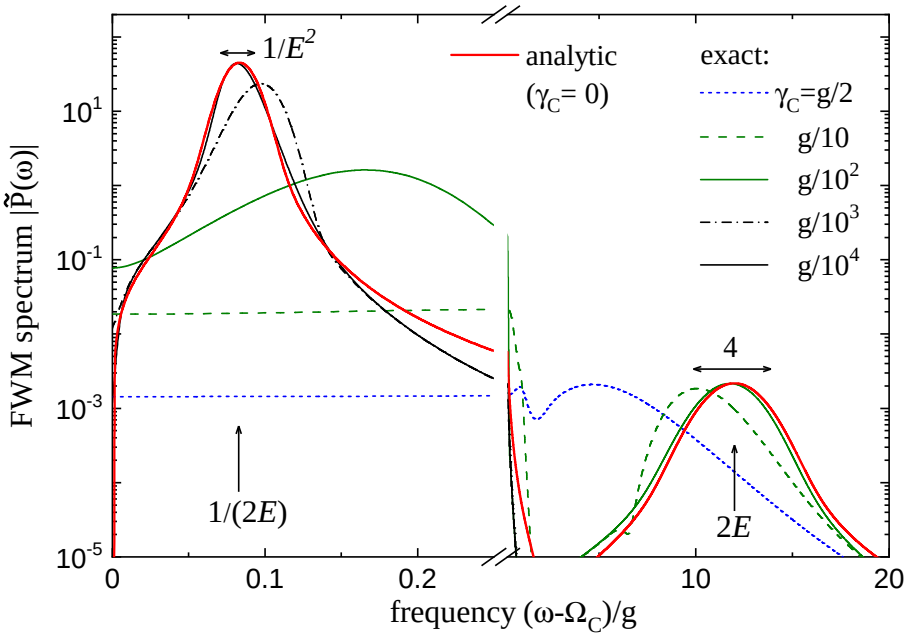

Figure 2.4: Analytic approximation Eqs. (2.26) and (2.27) (red curve) and exact FWM spectrum for different γ_c as given, for $E = \sqrt{4\lambda} = |E_1| = 6$. Vertical (horizontal) arrows show the position and FWHM of the spectral lines produced by the inner and outer transitions. Arrows indicate peak position

$|E_1| = 6$, in comparison with the full calculation at different values of γ_c, demonstrating an excellent agreement between the two in the limit of small damping. The first term in Eq. (2.27), produced by the outer transitions, describes the spectral sideband of the Mollow triplet, with a maximum at $\omega = \sqrt{4\lambda}g = 2g|E_1|$, i.e. growing linearly with the pulse area, as discussed above, and a linewidth of $\sqrt{2}g$, i.e. independent of the excitation field, as observed in the full calculation, even for a rather large damping. This linewidth in the argument of the Faddeeva function corresponds to a FWHM of about $4g$, see Appendix. D for a more detailed analysis. The inner transitions are in turn responsible for the above mentioned doublet of the central line, shown in Fig. 2.4 for the positive frequency only. Both the peak position ($g/2|E_1|$) and the FWHM ($g/|E_1|^2$) strongly depend on the pulse area, and a good agreement with the full calculation is reached at a very low damping, much lower than for the outer lines due to the small linewidth (a factor of $4|E|^2$ lower, that is

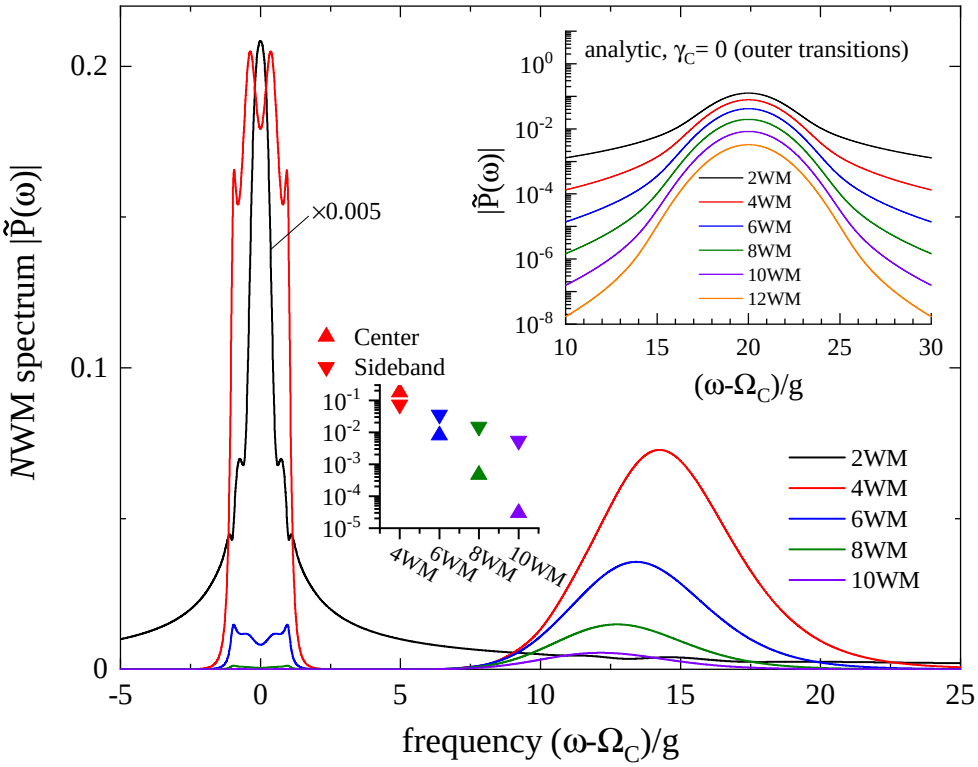

Figure 2.5: $\mathcal{N}$WM spectra $|\tilde{P}(\omega)|$ of the response detected at φ_1 ($\mathcal{N} = 2$, black), $2\varphi_2 - \varphi_1$ ($\mathcal{N} = 4$, red), $3\varphi_2 - 2\varphi_1$ ($\mathcal{N} = 6$, green), and $4\varphi_2 - 3\varphi_1$ ($\mathcal{N} = 8$, blue), for $|E_1| = 10$ and $\gamma_c = g/5$. The inset shows the sideband of the Mollow triplet for $\mathcal{N}$ up to 12, calculated using the analytic approximation Eqs. (2.26) and (2.27). All spectra are multiplied with $|E_1|^{\mathcal{N}/2}$.

144 in the figure shown).

2.4.3 NWM

We finally consider higher-order $\mathcal{N}$WM. The inset in Fig. 2.5 shows the analytic spectrum of the sideband for $\mathcal{N} = 2$, 4, 6, 8, 10, and 12 (for more results, see Appendix. D). While the FWHM almost does not change with $\mathcal{N}$, the spectral tails are getting more suppressed, which can be seen in the time domain as $t^{\mathcal{N}/2}$ rise of the polarisation at short times, see Eq. (2.25). The increase with $\mathcal{N}$ of the rise time is due to the fact that the optical non-linearity requires the excitation to be transferred from the cavity mode to the QD exciton and then back to the cavity, with the

complexity of this process increasing with $\mathcal{N}$. As a result, the 2WM spectrum (with $\mathcal{N} = 2$) has a very strong "linear" contribution from the cavity and a long tail of the central band; therefore the sideband whilst the strongest is not well seen in the full spectrum in Fig. 2.5. The Mollow sideband is prominent in the FWM spectrum, dominates over the central band in the 6WM (for the chosen parameters), and is getting weaker for the 8WM and higher non-linearities, in accordance with the analytic results. The 6WM, while infrequently studied in experiment as it requires a much higher signal-to-noise ratio, seems to be the best candidate of observing the Mollow triplet in cavity QED. In general the sideband amplitude reduces at a lower rate than the central peak amplitude as $\mathcal{N}$ increases.

2.4.4 Modeling spectrometer response

A recent article [83] published the appearance of the Mollow triplet in a 2-level system. The method used in their simulation was not the same as the method presented in this section, but a numerical brute force approach. By diagonalising the lindblad matrix using zero damping and detuning, a list of real eigenfrequencies and amplitudes describe the output of the system before any SRF is applied, then by applying a convolution with a SRF the output of a spectrometer can be predicted. In [83] the response function is defined as the sum of an exponential part and a Gaussian part. The cavity polarisation then multiplies SRF directly to model spectrometer response.

Beginning with the expression for cavity polarisation in the time domain, a sum of exponential plane waves

$$P(t) = \sum_j A_j e^{-i\omega_j t} \tag{2.28}$$

The SRF in time domain is given by [83] in the following form

$$S(t) = ae^{-\gamma t} + be^{-\delta^2 t^2} \tag{2.29}$$

with parameters a, b, δ and γ given in [110]. The combined spectrometer response is given by

$$\tilde{P}(t) = P(t)S(t) \tag{2.30}$$

Fourier transforming gives the cavity polarisation in the spectral domain. The result is a spectral function of each eigenfrequency multiplied by each amplitude

$$P(\omega) = \int_{-\infty}^{\infty} \tilde{P}(t)e^{-i\omega t}dt = \sum_j A_j P_j(\omega) \tag{2.31}$$

Then separating the result P_t into two components which represent the two parts to $S(t)$

$$P_j(\omega) = aP_j^a(\omega) + bP_j^b(\omega) \tag{2.32}$$

Part a is Lorentzian broadening, which is already present in the main 2-level model. It is equivalent here to adding a constant γ to the imaginary component of each eigenfrequency ω_j.

$$P_j^a(\omega) = \int_0^{\infty} e^{i(\omega-\omega_j)t}e^{-\gamma t}dt = \frac{i}{(\omega-\omega_j) - i\gamma} \tag{2.33}$$

Part b is unique to this SRF, representing the Fourier transform of the Gaussian curve from its center.

$$P_j^b(\omega) = \int_0^{\infty} e^{i(\omega-\omega_j)t}e^{-\delta^2 t^2}dt = \frac{1}{\delta}\omega_0\left(\frac{\omega-\omega_j}{2\delta}\right) \tag{2.34}$$

Where ω_0 is a scaled Faddeeva function, related to the Fresnel integral and the Voigt

function which is convolution of a centralised Gaussian with a Lorentzian.

$$\omega_0(z) = \frac{\sqrt{\pi}}{2} e^{-z^2} + i \cdot D(z) \tag{2.35}$$

The SRF in [83] uses $a = 8288$, $b = 7888$, $\gamma = \frac{1}{51ps}$, $\delta = \frac{1}{76ps}$. Normalising so the SRF has a value of 1 at $t = 0$ we scale by dividing $S(t)$ by $a + b$. Let $\alpha = \frac{a}{a+b}$ and $\beta = \frac{b}{a+b}$.

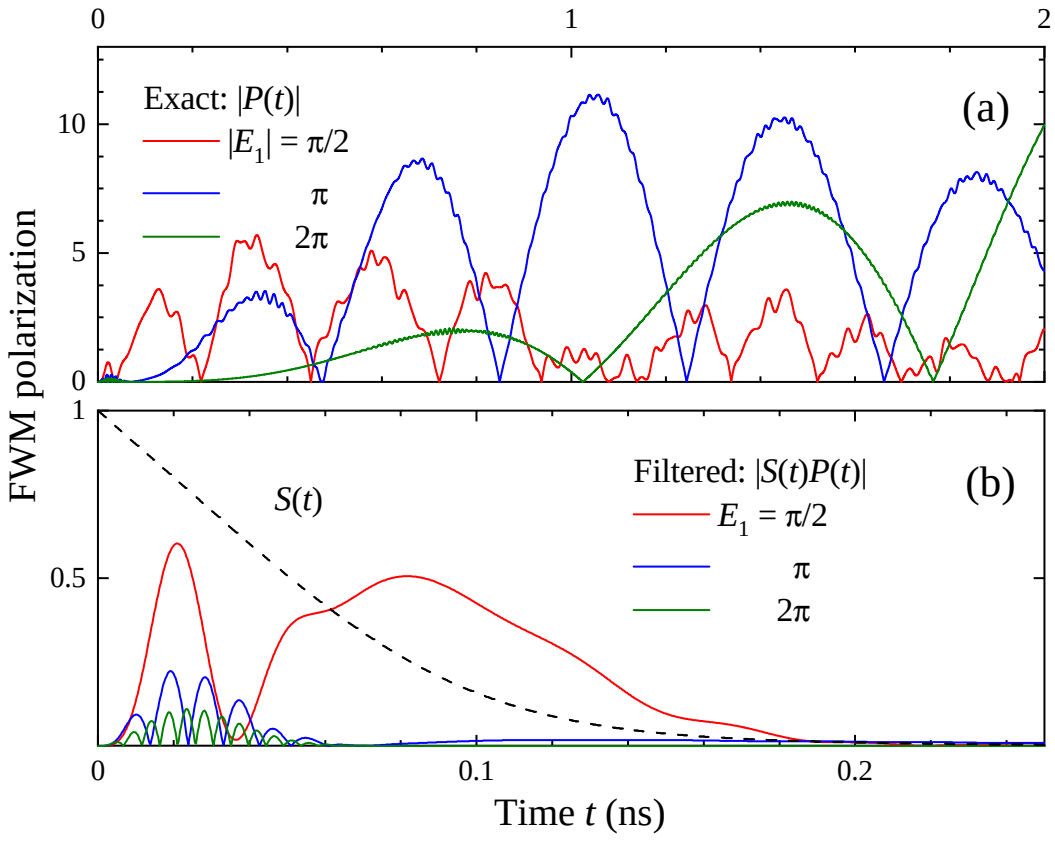

Figure 2.6: Applying the SRF $S(t)$ to $P(t)$. (a) Time domain polarisation $P(t)$ for three pulse areas for pulse 1. Dynamics present which create the sidebands seen in Figure 2.7 take place during the time frame allowed by the SRF $S(t)$ in (b)which is then applied to $P(t)$.

It is reasonable to suggest that long time dynamics are destroyed by $S(t)$ since any long wavelength information is much longer than what $S(t)$ can support, which will result in the central spectral peak being reduced in amplitude for higher values

of $|E_1|$. This is not a feature in [83], however it is present in Figure 2.7. This suggests in the article the number of rungs available in their calculation was not high enough to reduce the central peak. As even eigenfrequencies with a low amplitude can contribute to $P(\omega)$ significantly due to large numbers of large subtractions happening at higher rungs and amplitudes, it is likely their model has been truncated to too low a rung before Fourier transforming, perhaps because of the numerical precision issue we approached in Sec. 2.4.1

The FWM polarisation in spectral domain is given by

$$P(\omega) = \sum_j A_j \left[\frac{\alpha i}{(\omega - \omega_j) - i\gamma} + \frac{\beta}{\delta}\omega_0 \left(\frac{\omega - \omega_j}{2\delta} \right) \right] \tag{2.36}$$

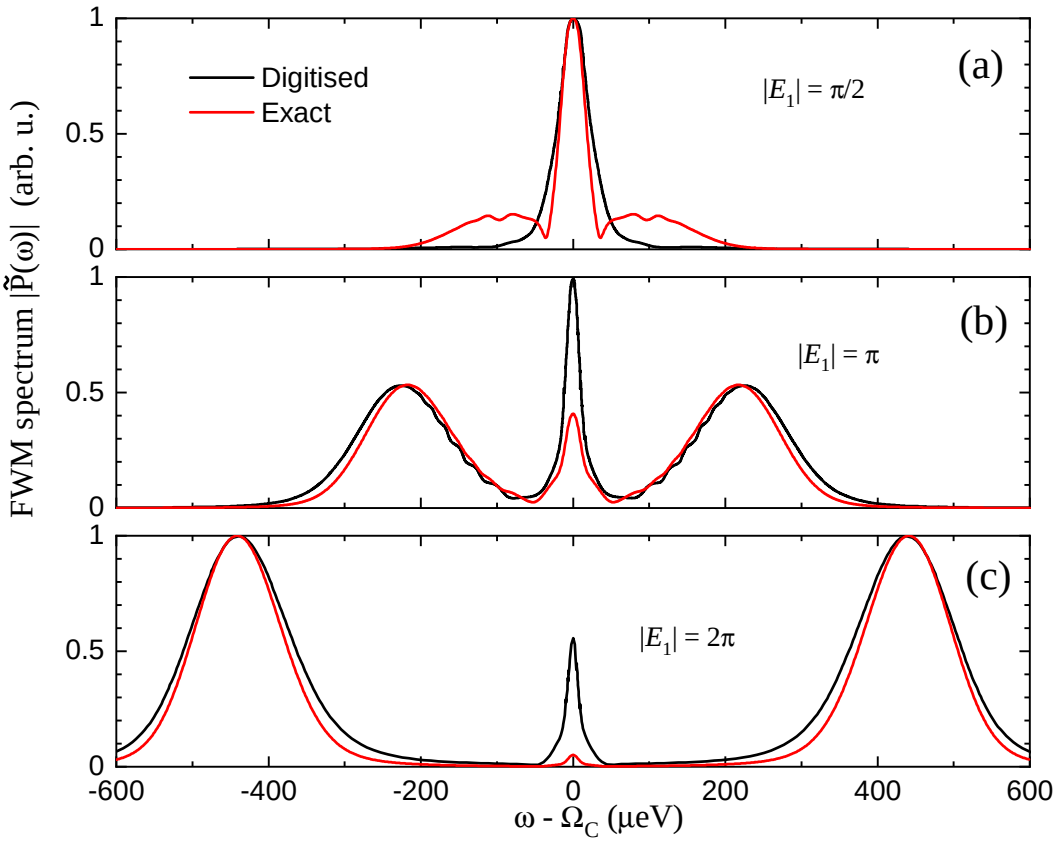

Figure 2.7: Comparison between digitised spectrum found in [83] (black) and analytic convolved spectrum of $P(t)$ described by Eq. (2.31).

The central peak at $\omega = 0$ represents slow oscillations in time domain, of which on average get longer as $|E_1|$ increases. Applying $S(t)$ results in the loss of all long wave signals, explaining the loss of the central peak at high pulse areas. Features of the sidebands are preserved better as the pulse area increases, as outer eigenfrequencies in the JC ladder only increase in frequency away from zero, allowing their oscillation to be captured for more oscillation cycles by the spectrometer.

2.4.5 Why we need multiprecision throughout calculation of NWM polarisation

During testing it has been shown that accuracy of all stages of the two-level code are highly sensitive to numerical precision. The standard double precision float standard defines the `double` to have a mantissa of 52 bits (plus one bit for negative numbers). The effective number of digits of precision D is given by its relation between bits of precision B

$$\begin{aligned} 2^B &= 10^D \\ D &= \frac{\ln(2)}{\ln(10)} B \end{aligned} \tag{2.37}$$

This gives an effective number of digits of precision of a double precision float between 15 and 16, so a guaranteed precision of 15 decimal digits. For this precision the two-level code fails to accurately diagonalise the Lindblad matrix when the number of rungs exceeds 20, capping the maximum value of E to around 4. This problem persists whether numerical diagonalisation or the analytic diagonalisation derived in the supplement is found. This alone suggests the Lindblad matrix approaches the form of a singular matrix at a large number of rungs. Upon investigation, it is apparent that L approaches singularity when it is truncated higher up the JC ladder, like the $\left[\begin{smallmatrix} 1 & 1 \\ 0 & 1 \end{smallmatrix}\right]$ matrix. There are two things which help reduce the effect of

this near-singularity. One is to extract a common factor of g from L, reducing the absolute difference between elements in the matrix by a factor of g (In the case of the heterodyne experiment in [83], $g = 35.25$, a significant increase in accuracy). The second is to use a precision higher than that available using the standard double. The code used to produce all results in this thesis uses the MPC library, an extension of the MPFR and GMP libraries for real and integer arithmetic in C. By allowing precision to vary arbitrarily, L approaching singularity is no longer an issue, as long as the precision is set high enough. For the two-level code, using 500 bits of precision (150 decimal digits) is more than enough for values of E up to 10 (up to 100 photons).

Multiprecision is also required in the final calculation of $\tilde{P}(\omega)$ for high rungs. With the appearance of the second wave of amplitudes in section Sec. 2.4, the final value of $\tilde{P}(\omega)$ requires the summation of complex numbers taking very-nearly opposite values which reduce to a number orders of magnitude lower.

2.5 Discussion of data in Appendix. F.1

This section will describe what is happening in video data produced alongside the colour diagrams in Sec. E.2. The video is essentially a parameter sweep (vary the system parameters in as wide a range as possible) for a subset of the total parameters of the 2-level QDMC model. The parameter sweep in this section includes variation of the following parameters: the

- detuning $\Omega_c - \Omega_x$ using two values, 0 and g_x.
- Pulse 1 amplitude $|E_1|$ varies continuously between 0 and 10
- Pulse 1 phase $|\Delta N_1|$ takes the value -1(FWM)
- Pulse 2 amplitude $|E_2|$ varies continuously between 0 and 10

- Pulse 2 phase $|\Delta N_2|$ takes the value 2(FWM)
- Cavity and exciton dampings γ_c and γ_x vary simultaneously, take the values g_x, $g_x/2$, $g_x/5$, $g_x/10$, $g_x/20$, $g_x/50$, and $g_x/100$.

We find good examples of the Mollow triplet and visualise the triplet's dependency on the damping parameters.

2.6 Conclusion

In conclusion, we have presented a fully analytic approach to the optical nonlinearity of any mixing order for the 2L QDMC system. The coherent transitions between rungs of the JC ladder predicted by the analytics allows full analysis of the response of the system. At high pulse areas, the Mollow triplet was observed, demonstrating a transition from quantum strong coupling to the coherent classical regime, such that it resembles a classical coherent response from continuous wave excitation. An analytic approximation to the low-damping response of the system was found, predicting the linewidths and spectral positions of sidebands given the pulse area and mixing order, as a closed form of the solution in terms of elementary functions in time domain and special functions in frequency domain. Sideband linewidths were found to be $4g$ at a spectral position of $2Eg$, independent of pulse strength. For higher damping a relaxation down the JC ladder was observed, more so for higher cavity damping, moving the triplet sidebands closer to the central peak. A comparison of the model developed in this chapter with a recent publication revealed disagreement between results of the two approaches. It may be the case that the dependence of this model on multiprecision could have affected the accuracy of their result, or perhaps it could be a truncation down to too few rungs of the Jaynes-Cummings ladder.

3 | Three-Level Quantum Dot Coupled to a Microcavity

The 3-level QDMC system is an extension of the system presented in Sec. 2, explored experimentally by other groups [80] but not in the high-excitation regime like Sec. 2. By modifying the quantum level scheme to include a biexciton state we now model a slightly more realistic QD. In this section we explore the parameter space of the 3-level extended JC model, calculating the NWM response of the QDMC system in the low and high excitation regimes.

Our parameter space includes twelve quantities. In terms of dynamics we have eight, the same five from Sec. 2 plus some extras to properly represent the biexciton; the natural oscillation frequencies of a cavity photon ω_c, the quantum dot exciton ω_x and the quantum dot biexciton ω_b, a coupling constant describing the strength of interaction between cavity photons and the quantum dot exciton g_x, and the same for the quantum dot biexciton g_b, cavity damping (coupling between the cavity and the environment) γ_c and exciton and biexciton dampings γ_x, γ_b. In terms of pulsed excitation we have the same four from Sec. 2; the magnitudes of two pulses E_1 and E_2, and the phase order of the two pulses ΔN_1 and ΔN_2. We again concentrate on two-pulse excitation resulting in measurement of degenerate N-wave mixing, There are also two additional parameters which are not studied but have been implemented in code, the delays between pulses 1 and 2 τ_{12}, and the delay between pulse 2 and

the beginning of measurement τ_{2+}.

This model collapses to the 2-level model presented in the previous chapter Sec. 2 when biexciton coupling g_b is set to zero. Physically this represents an entity which is indeed present but does not interact with any other entity within the system.

Exploring $\mathcal{N}$ dynamics in the new 3-level model in the low-excitation regime reveals that for a narrow set of parameters the FWM signal is suppressed or even vanishing, but this doesn't apply to higher order mixing. In the high-excitation regime we find the formation in frequency domain of a new quintuplet, similar to the mollow triplet where an additional pair of sidebands which peak at twice the frequency difference compared to the triplet studied in Sec. 2. This quintuplet is also dependent on the ratio of biexciton-cavity and exciton-cavity coupling.

3.1 Extending the 2-level QD model to 3-level - Adding the biexciton state

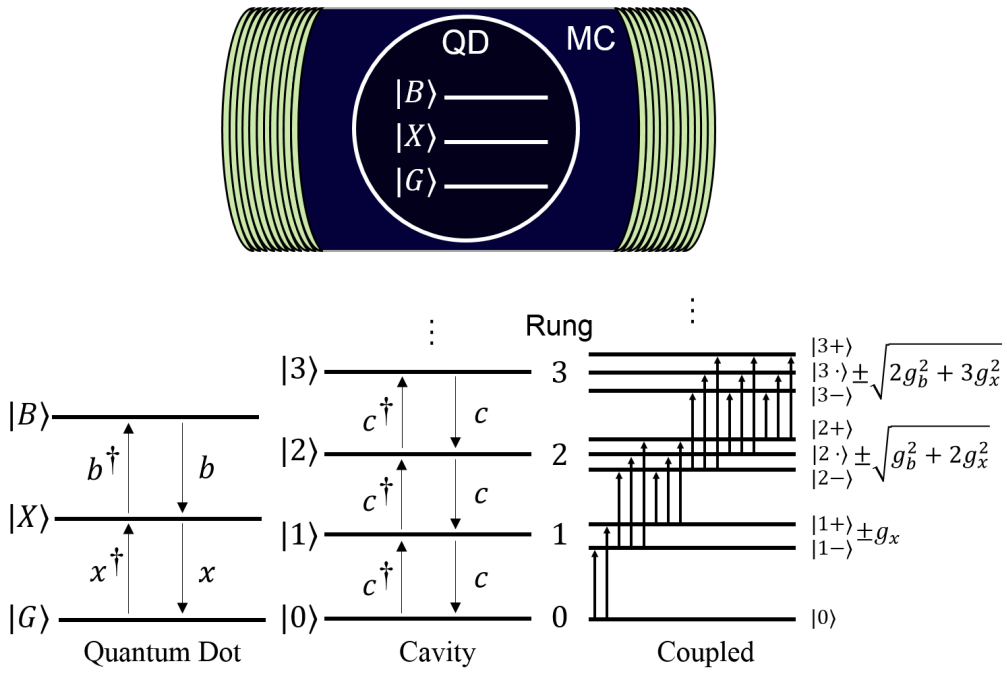

Figure 3.1: Diagram of full basis of states of a 3-level QD coupled to an optical cavity. Allowed transitions through Lindblad dynamics shown with arrows. 17 transitions are split 2:6:9 over first 3 rungs of the modified Jaynes-Cummings ladder. Each rung beyond 1 has 3 eigenenergies.

The basis in Figure 3.1 is described as the combination of the cavity basis, which consists of a Fock basis of states $|n\rangle$ representing an excited cavity mode containing n cavity photons, and the QD basis has 3 states: the ground state with no excitons present $|G\rangle$, the first excited state with a single exciton present $|X\rangle$ and the state representing a biexciton $|B\rangle$. The coupled eigenstates from Figure 3.1 use a combined basis, the outer product of the QD and cavity bases, as was done in Eq. (2.12), then

combined in Eq. (2.20) like the 2-level QD model.

$$\begin{aligned} & & & |0\rangle = |G,0\rangle \\ & & |1\rangle = |X,0\rangle \quad & |2\rangle = |G,1\rangle \\ |3\rangle = |B,0\rangle \quad & |4\rangle = |X,1\rangle \quad & |5\rangle = |G,2\rangle \\ |6\rangle = |B,1\rangle \quad & |7\rangle = |X,2\rangle \quad & |8\rangle = |G,3\rangle \\ \ldots & & \end{aligned} \tag{3.1}$$

As the 3-level QD formalism is numerically substantially more complex than the 2-level QD's, it was decided that using a quicker numerical approach rather than a fully analytic approach in Sec. 2 would benefit this thesis. The succeeding sections of this chapter use the basis of Eq. (3.1) to calculate matrix elements of all operators present in Eq. (3.2)

3.2 System Hamiltonian and relation to the 2-level QDMC model

The Hamiltonian for the 3-level QDMC system is given in Eq. (3.2)

$$H = \omega_c c^\dagger c + \omega_x x^\dagger x + \omega_b b^\dagger b + g_x(x^\dagger c + c^\dagger x) + g_b(b^\dagger c + c^\dagger b) \tag{3.2}$$

where ω_c, ω_x and ω_b are the complex MC, QD exciton and QD biexciton frequencies, and g_x and g_b are constants which correspond to exciton and biexciton coupling to the MC. ω_c, ω_x, ω_b represent complex frequencies using real and imaginary parts, the same as Sec. 2. The real part determines the energy of eigenstates, the imaginary part determines the rate at which the state will decay into a rung of lower energy (when considering Lindblad damping in later sections) and energy leaking to the environment, for example the $|B\rangle$ state will decay over time into the $|X\rangle$ state and

the n^{th} cavity mode $|n\rangle$ will decay to $< n^{th}$ modes.

Creation and annihilation operators have been defined separately for the exciton ($x^\dagger$, x) and biexciton ($b^\dagger$, b) states in the 3-level ladder. Let operators $x^\dagger$ and $b^\dagger$ allow states $|X\rangle$ and $|B\rangle$ to be populated from the ground state $|G\rangle$ in the QD basis by the definitions $x^\dagger = |X\rangle\langle G|$ and $b^\dagger = |B\rangle\langle X|$. Dots in matrices replace zeros, for aesthetics.

$$x^\dagger = \begin{bmatrix} \cdot & \cdot & \cdot \\ 1 & \cdot & \cdot \\ \cdot & \cdot & \cdot \end{bmatrix} \qquad b^\dagger = \begin{bmatrix} \cdot & \cdot & \cdot \\ \cdot & \cdot & \cdot \\ \cdot & 1 & \cdot \end{bmatrix} \tag{3.3}$$

In the full basis described in Figure 3.1, $x^\dagger = |X,n\rangle\langle G,n|$ and $b^\dagger = |B,n\rangle\langle X,n|$ are combined into full basis indices: $x^\dagger = |1\rangle\langle 0| + |3n+4\rangle\langle 3n+2|, n \geq 1$ and $b^\dagger = |3n+3\rangle\langle 3n+1|, n \geq 1$.

$$x^\dagger = \left[\begin{array}{c|cc|ccc|ccc} \cdot & \cdot & \cdot & \cdot & \cdot & \cdot & \cdot & \cdot & \cdot \\ \hline 1 & \cdot & \cdot & \cdot & \cdot & \cdot & \cdot & \cdot & \cdot \\ \cdot & \cdot & \cdot & \cdot & \cdot & \cdot & \cdot & \cdot & \cdot \\ \hline \cdot & \cdot & \cdot & \cdot & \cdot & \cdot & \cdot & \cdot & \cdot \\ \cdot & \cdot & 1 & \cdot & \cdot & \cdot & \cdot & \cdot & \cdot \\ \cdot & \cdot & \cdot & \cdot & \cdot & \cdot & \cdot & \cdot & \cdot \\ \hline \cdot & \cdot & \cdot & \cdot & \cdot & \cdot & \cdot & \cdot & \cdot \\ \cdot & \cdot & \cdot & \cdot & \cdot & 1 & \cdot & \cdot & \cdot \\ \cdot & \cdot & \cdot & \cdot & \cdot & \cdot & \cdot & \cdot & \cdot \end{array}\right] \qquad b^\dagger = \left[\begin{array}{c|cc|ccc|ccc} \cdot & \cdot & \cdot & \cdot & \cdot & \cdot & \cdot & \cdot & \cdot \\ \hline \cdot & \cdot & \cdot & \cdot & \cdot & \cdot & \cdot & \cdot & \cdot \\ \cdot & \cdot & \cdot & \cdot & \cdot & \cdot & \cdot & \cdot & \cdot \\ \hline \cdot & 1 & \cdot & \cdot & \cdot & \cdot & \cdot & \cdot & \cdot \\ \cdot & \cdot & \cdot & \cdot & \cdot & \cdot & \cdot & \cdot & \cdot \\ \cdot & \cdot & \cdot & \cdot & \cdot & \cdot & \cdot & \cdot & \cdot \\ \hline \cdot & \cdot & \cdot & \cdot & 1 & \cdot & \cdot & \cdot & \cdot \\ \cdot & \cdot & \cdot & \cdot & \cdot & \cdot & \cdot & \cdot & \cdot \\ \cdot & \cdot & \cdot & \cdot & \cdot & \cdot & \cdot & \cdot & \cdot \end{array}\right] \tag{3.4}$$

The Hamiltonian matrix Eq. (3.5) appears as the 2-level Hamiltonian matrix with

diagonal blocks for rungs $n \geq 2$ expanded to 3×3 blocks.

$$H = \left[\begin{array}{c|cc|ccc|ccc} \cdot & \cdot & \cdot & \cdot & \cdot & \cdot & \cdot & \cdot & \cdot \\ \hline \cdot & \omega_x & g_x & \cdot & \cdot & \cdot & \cdot & \cdot & \cdot \\ \cdot & g_x & \omega_c & \cdot & \cdot & \cdot & \cdot & \cdot & \cdot \\ \hline \cdot & \cdot & \cdot & \omega_b & g_b & \cdot & \cdot & \cdot & \cdot \\ \cdot & \cdot & \cdot & g_b & \omega_c + \omega_x & \sqrt{2}\, g_x & \cdot & \cdot & \cdot \\ \cdot & \cdot & \cdot & \cdot & \sqrt{2}\, g_x & 2\,\omega_c & \cdot & \cdot & \cdot \\ \hline \cdot & \cdot & \cdot & \cdot & \cdot & \cdot & \omega_b + \omega_c & \sqrt{2}\, g_b & \cdot \\ \cdot & \cdot & \cdot & \cdot & \cdot & \cdot & \sqrt{2}\, g_b & 2\,\omega_c + \omega_x & \sqrt{3}\, g_x \\ \cdot & \cdot & \cdot & \cdot & \cdot & \cdot & \cdot & \sqrt{3}\, g_x & 3\,\omega_c \end{array}\right] \tag{3.5}$$

H is a block diagonal matrix with the nth rung block defined as H_n

$$H_n = \begin{bmatrix} (n-2)\omega_c + \omega_b & \sqrt{n-1}g_b & \cdot \\ \sqrt{n-1}g_b & (n-1)\omega_c + \omega_x & \sqrt{n}g_x \\ \cdot & \sqrt{n}g_x & n\omega_c \end{bmatrix} \tag{3.6}$$

and can be diagonalised, revealing the energy levels of this 3-level system Appendix. H. Numerically this is trivial but does not compress into a nice expression. In this special case of zero detuning, $2\omega_c = 2\omega_x = \omega_b$ this matrix is simply a tridiagonal matrix of the form H_a

$$H_n = \begin{bmatrix} r & p & \cdot \\ p & r & q \\ \cdot & q & r \end{bmatrix} \qquad \textit{with} \qquad \begin{array}{c} p = g_b\sqrt{n-1} \\ q = g_x\sqrt{n} \\ r = n\,\omega_c \end{array} \tag{3.7}$$

which has eigenvalues

$$\begin{aligned} r &= n\omega_c \\ r + \sqrt{p^2 + q^2} &= n\,\omega_c + \sqrt{[n-1]\ {g_b}^2 + n\,{g_x}^2} \\ r - \sqrt{p^2 + q^2} &= n\,\omega_c - \sqrt{[n-1]\ {g_b}^2 + n\,{g_x}^2} \end{aligned} \tag{3.8}$$

resulting in the splitting stated in Figure 3.1. If the biexciton coupling is set to zero (effectively recreating the 2-level system), two eigenvalues reveal the eigenvalues of the 2-level nth rung Hamiltonian

$$\begin{aligned} r + p &= n\,\omega_c + g_x\sqrt{n} \\ r - p &= n\,\omega_c - g_x\sqrt{n} \end{aligned} \tag{3.9}$$

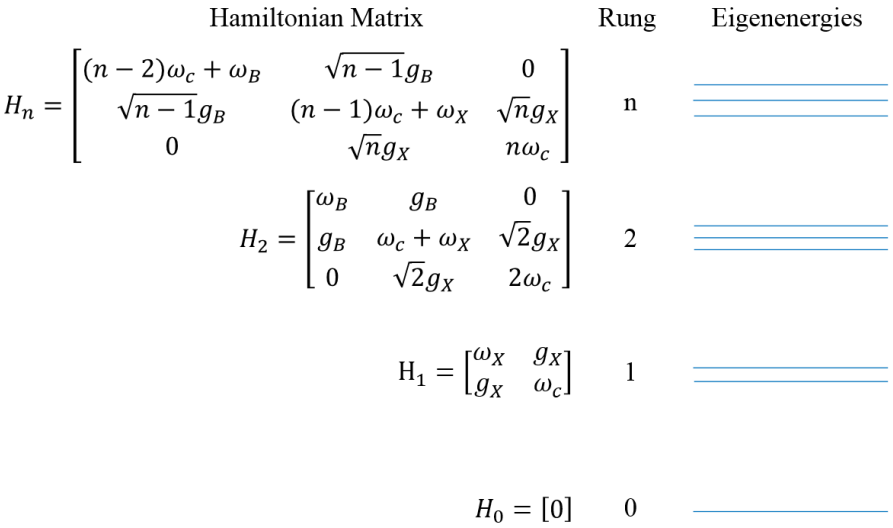

Figure 3.2: Diagram of energies of a simplified coupled 3-level biexciton cavity hamiltonian.

3.3 Pulsed excitation of the 3-level QD model

The pulse operator $\hat{X}$ from the 2-level QDMC model is maintained here, as there is no difference between cavities in both models. For this partially numerical project,

the full representation of the pulse matrix component e^{iV} in the full basis is found, which multiplies the density matrix as per Eq. (3.10) ensuring only the elements with the desired multiple of the pulse phase $arg(E)$ are found. See Appendix. A for details, the matrix C does not change from the previous chapter.

$$\rho_+ = \hat{X}(E)\rho_- = e^{-iV}\rho_- e^{iV} \tag{3.10}$$

$$e^{iV} = \left[\begin{array}{ccc|ccc|ccc|c} C_{11} & \cdot & C_{12} & \cdot & \cdot & C_{13} & \cdot & \cdot & C_{14} & \cdots \\ \hline \cdot & C_{11} & \cdot & \cdot & C_{12} & \cdot & \cdot & C_{13} & \cdot & \\ C_{21} & \cdot & C_{22} & \cdot & \cdot & C_{23} & \cdot & \cdot & C_{24} & \cdots \\ \hline \cdot & \cdot & \cdot & C_{11} & \cdot & \cdot & C_{12} & \cdot & \cdot & \\ \cdot & C_{21} & \cdot & \cdot & C_{22} & \cdot & \cdot & C_{23} & \cdot & \\ C_{31} & \cdot & C_{32} & \cdot & \cdot & C_{33} & \cdot & \cdot & C_{34} & \cdots \\ \hline \cdot & \cdot & \cdot & C_{21} & \cdot & \cdot & C_{22} & \cdot & \cdot & \\ \cdot & C_{31} & \cdot & \cdot & C_{32} & \cdot & \cdot & C_{33} & \cdot & \\ C_{41} & \cdot & C_{42} & \cdot & \cdot & C_{43} & \cdot & \cdot & C_{44} & \cdots \\ \hline \vdots & & \vdots & & & \vdots & & & \vdots & \ddots \end{array}\right] \tag{3.11}$$

e^{-iV} is as e^{iV} but with $(e^{iV})_{ij}$ negated when $i+j$ is odd.

3.4 Three-level dynamics in the low excitation regime

One natural progression is to include more states for the quantum dot to enter during Lindblad dynamics. A real QD has the possibility to have multiple excited states including charged and multiexciton states, one of these states is the biexciton. The biexciton model used in this section is one which assumes the cavity pulses are of equal polarisation and phase, approximating a four-level system described in [111]. More generally, biexcitons form in two separate ways involving the order of quantum dot excitation from the cavity, where the two pulses have different polarisations.

Using the low-energy third-order approximation to the low-excitation (E is small) 2-pulse density matrix

$$\rho^{(3)} = \left[\begin{array}{c|cc|ccc} \cdot & \cdot & \cdot & \cdot & \cdot & \cdot \\ \hline 0 & \cdot & \cdot & \cdot & \cdot & \cdot \\ -2\,\rho_{02}^{(1)} & \cdot & \cdot & \cdot & \cdot & \cdot \\ \hline \cdot & 0 & 0 & \cdot & \cdot & \cdot \\ \cdot & 0 & \sqrt{2}\,\rho_{01}^{(1)} & \cdot & \cdot & \cdot \\ \cdot & 0 & \sqrt{2}\,\rho_{02}^{(1)} & \cdot & \cdot & \cdot \end{array}\right] \tag{3.12}$$

where $\rho_{01}^{(1)}$ and $\rho_{02}^{(1)}$ are mixed states found by approximating the first pulse as low-energy , for this reason they have values of 0 and -1 as previously calculated in the 2-level model [8]. Dots represent states which will not be present in the Lindblad dynamics after vectorisation, and are zero. Only the 8 states represented with numerical values will remain after vectorisation. The expressions for $L_{[00]}$, $L_{[11]}$ and $L_{[01]}$ are similar to 2-level from Eq. (3.20), including two more available mixed states from the vectorisation process, $|3\rangle\langle 1|$ and $|3\rangle\langle 2|$.

Energy loss to the environment is modeled by damping occupied states over time in the master equation. Damping is calculated using the same Lindblad damping operator from Sec. 2, but now it applies additionally to the biexciton via an additional $\mathcal{D}$ taking γ_b as an input. The Lindblad operator in 3-level is defined as

$$L = H\rho - \rho H^* + 2i\gamma_c c\rho c^\dagger + 2i\gamma_x x\rho x^\dagger + 2i\gamma_b b\rho b^\dagger$$

$$L = \left[\begin{array}{cc|cccccc} \omega_x & g_x & \cdot & \cdot & \cdot & 2i\gamma_c & \cdot & \cdot \\ g_x & \omega_c & \cdot & \cdot & 2i\gamma_x & \cdot & \cdot & 2\sqrt{2}i\,\gamma_c \\ \hline \cdot & \cdot & \omega_b - \omega_x^* & -g_x & g_b & \cdot & \cdot & \cdot \\ \cdot & \cdot & -g_x & \omega_b - \omega_c^* & \cdot & g_b & \cdot & \cdot \\ \cdot & \cdot & g_b & \cdot & \omega_x + \omega_c - \omega_x^* & -g_x & \sqrt{2}\,g_x & \cdot \\ \cdot & \cdot & \cdot & g_b & -g_x & \omega_x + \omega_c - \omega_c^* & \cdot & \sqrt{2}\,g_x \\ \cdot & \cdot & \cdot & \cdot & \sqrt{2}\,g_x & \cdot & 2\omega_c - \omega_x^* & -g_x \\ \cdot & \cdot & \cdot & \cdot & \cdot & \sqrt{2}\,g_x & -g_x & 2\omega_c - \omega_c^* \end{array}\right] \tag{3.13}$$

This Lindblad operator is diagonalised to find the transition energies (eigenvalues Ω_n) and transition states (eigenvectors R_n). There are 8 transition energies at the low-energy approximation, compared to 6 in 2-level. Considering a simplified case using the following assumptions: $\gamma = 0$, $2\omega_c = 2\omega_x = \omega_b$. After simplifying L by subtracting $w_c I$ and dividing by g_x there remains

$$\frac{L - \omega_c I}{g_x} = \left[\begin{array}{cc|cccccc} \cdot & 1 & \cdot & \cdot & \cdot & \cdot & \cdot & \cdot \\ 1 & \cdot & \cdot & \cdot & \cdot & \cdot & \cdot & \cdot \\ \hline \cdot & \cdot & \cdot & -1 & s & \cdot & \cdot & \cdot \\ \cdot & \cdot & -1 & \cdot & \cdot & s & \cdot & \cdot \\ \cdot & \cdot & s & \cdot & \cdot & -1 & \sqrt{2} & \cdot \\ \cdot & \cdot & \cdot & s & -1 & \cdot & \cdot & \sqrt{2} \\ \cdot & \cdot & \cdot & \cdot & \sqrt{2} & \cdot & \cdot & -1 \\ \cdot & \cdot & \cdot & \cdot & \cdot & \sqrt{2} & -1 & \cdot \end{array}\right] \tag{3.14}$$

with $s = g_b/g_x$. This matrix decomposes into a matrix of eigenvalues and eigenvectors $L = R\,\Omega\,R^{-1}$

$$R = \left[\begin{array}{cc|cccccc} 1 & -1 & \cdot & \cdot & \cdot & \cdot & \cdot & \cdot \\ 1 & 1 & \cdot & \cdot & \cdot & \cdot & \cdot & \cdot \\ \hline \cdot & \cdot & -\frac{\sqrt{2}}{s} & \frac{\sqrt{2}}{s} & \frac{\sqrt{2}\,s}{2} & -\frac{\sqrt{2}\,s}{2} & \frac{\sqrt{2}\,s}{2} & -\frac{\sqrt{2}\,s}{2} \\ \cdot & \cdot & -\frac{\sqrt{2}}{s} & -\frac{\sqrt{2}}{s} & \frac{\sqrt{2}\,s}{2} & \frac{\sqrt{2}\,s}{2} & \frac{\sqrt{2}\,s}{2} & \frac{\sqrt{2}\,s}{2} \\ \cdot & \cdot & \cdot & \cdot & -\frac{d\sqrt{2}}{2} & \frac{d\sqrt{2}}{2} & \frac{d\sqrt{2}}{2} & -\frac{d\sqrt{2}}{2} \\ \cdot & \cdot & \cdot & \cdot & -\frac{d\sqrt{2}}{2} & -\frac{d\sqrt{2}}{2} & \frac{d\sqrt{2}}{2} & \frac{d\sqrt{2}}{2} \\ \cdot & \cdot & 1 & -1 & 1 & -1 & 1 & -1 \\ \cdot & \cdot & 1 & 1 & 1 & 1 & 1 & 1 \end{array}\right] \qquad \Omega = \begin{bmatrix} 1 \\ -1 \\ -1 \\ 1 \\ -d-1 \\ -d+1 \\ d-1 \\ d+1 \end{bmatrix} \tag{3.15}$$

where auxiliary variables $d = \sqrt{s^2+2}$, $a = \frac{1}{\sqrt{s^2+2}}$.

$$R^{-1} = \left[\begin{array}{cc|cccccc} \frac{1}{2} & \frac{1}{2} & \cdot & \cdot & \cdot & \cdot & \cdot & \cdot \\ -\frac{1}{2} & \frac{1}{2} & \cdot & \cdot & \cdot & \cdot & \cdot & \cdot \\ \hline \cdot & \cdot & -\frac{\sqrt{2}\,a\,s}{2} & -\frac{\sqrt{2}\,a\,s}{2} & \cdot & \cdot & \frac{a\,s^2}{2} & \frac{a\,s^2}{2} \\ \cdot & \cdot & \frac{\sqrt{2}\,a\,s}{2} & -\frac{\sqrt{2}\,a\,s}{2} & \cdot & \cdot & -\frac{a\,s^2}{2} & \frac{a\,s^2}{2} \\ \cdot & \cdot & \frac{\sqrt{2}\,a\,s}{4} & \frac{\sqrt{2}\,a\,s}{4} & -\frac{\sqrt{2}\,a}{4} & -\frac{\sqrt{2}\,a}{4} & \frac{a}{2} & \frac{a}{2} \\ \cdot & \cdot & -\frac{\sqrt{2}\,a\,s}{4} & \frac{\sqrt{2}\,a\,s}{4} & \frac{\sqrt{2}\,a}{4} & -\frac{\sqrt{2}\,a}{4} & -\frac{a}{2} & \frac{a}{2} \\ \cdot & \cdot & \frac{\sqrt{2}\,a\,s}{4} & \frac{\sqrt{2}\,a\,s}{4} & \frac{\sqrt{2}\,a}{4} & \frac{\sqrt{2}\,a}{4} & \frac{a}{2} & \frac{a}{2} \\ \cdot & \cdot & -\frac{\sqrt{2}\,a\,s}{4} & \frac{\sqrt{2}\,a\,s}{4} & -\frac{\sqrt{2}\,a}{4} & \frac{\sqrt{2}\,a}{4} & -\frac{a}{2} & \frac{a}{2} \end{array}\right] \tag{3.16}$$

Applying (2.19) and reversing the simplifications made in Eq. (3.14) we find 3-level

expressions for A and Ω

$$\Omega = \omega_c \vec{1} + g_x \begin{bmatrix} 1 \\ -1 \\ -1 \\ 1 \\ -\sqrt{D}-1 \\ -\sqrt{D}+1 \\ \sqrt{D}-1 \\ \sqrt{D}+1 \end{bmatrix} \quad \text{and} \quad A = \begin{bmatrix} 1 \\ 1 \\ -\frac{s^2}{D} \\ -\frac{s^2}{D} \\ \frac{\sqrt{D}-2}{2D} \\ -\frac{\sqrt{D}+2}{2D} \\ -\frac{\sqrt{D}+2}{2D} \\ \frac{\sqrt{D}-2}{2D} \end{bmatrix} \tag{3.17}$$

with $D = s^2 + 2$. When comparing to the simplified 2-level result, we must set the value of g_b to 0, as there is no coupling to a biexciton in 2-level. This implies that in Eq. (3.15) $d = 0$ and in Eq. (3.16) $p = \sqrt{2}$. Considering the simplifications made to L , the resultant simplified A and Ω match the 2-level result, and the additional amplitudes introduced in 3-level formulation are found to be zero. The 2-level result is:

$$\Omega = \omega_c \vec{1} + g_x \begin{bmatrix} 1 \\ -1 \\ -1 \\ 1 \\ -\sqrt{2}-1 \\ -\sqrt{2}+1 \\ \sqrt{2}-1 \\ \sqrt{2}+1 \end{bmatrix} \quad A = \begin{bmatrix} 1 \\ 1 \\ . \\ . \\ \frac{\sqrt{2}-2}{4} \\ -\frac{\sqrt{2}+2}{4} \\ -\frac{\sqrt{2}+2}{4} \\ \frac{\sqrt{2}-2}{4} \end{bmatrix} \tag{3.18}$$

In agreement with [8].

3.5 Extinction of the FWM signal

Inside the 3-level low-excitation solution Eq. (3.17) there is an interesting effect when the biexciton coupling is equal to $\sqrt{2}$ times the exciton coupling, setting $s = g_b/g_x = \sqrt{2}$ therefore $s^2 = 2$ and $D = 4$. This gives eigenvalues and amplitudes A_n with j an index running from 0 to 7 in order down the vector in Eq. (3.19):

$$\Omega = \omega_c \vec{1} + g_x \begin{bmatrix} 1 \\ -1 \\ -1 \\ 1 \\ -3 \\ -1 \\ 1 \\ 3 \end{bmatrix} \qquad \text{and} \qquad A = \begin{bmatrix} 1 \\ 1 \\ -1/2 \\ -1/2 \\ \cdot \\ -1/2 \\ -1/2 \\ \cdot \end{bmatrix} \tag{3.19}$$

When we sum the amplitudes of identical frequencies, FWM signal vanishes. $\Omega_{1,2,5} = \omega_c - g_x$ of which the sum of the amplitudes is $1 - 1/2 - 1/2 = 0$, and $\Omega_{0,3,6} = \omega_c + g_x$ of which the sum of the amplitudes is $1 - 1/2 - 1/2 = 0$, and the remaining two amplitudes are 0, therefore $P_{FWM}(t)$ and $P_{FWM}(\omega)$ both vanish.

This is a special case, as Figure 3.3 also demonstrates.

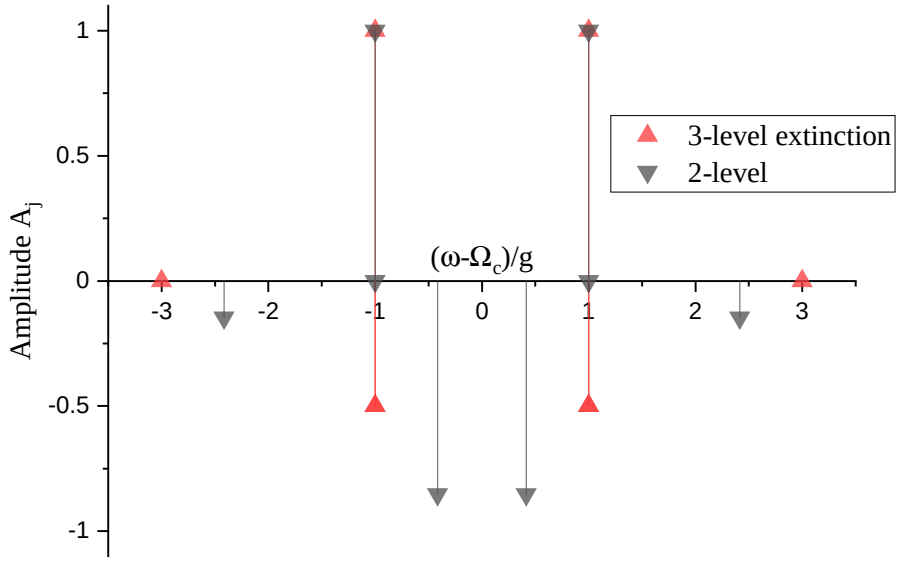

Figure 3.3: Delta function plot of $\tilde{P}(\omega)$ using the values of Ω and A in Eq. (3.19) (grey) and comparing to 2-level ($g_b = 0$) (red). The grey points at $\omega = \pm g$ are two points of the same value.

When considering the full low-excitation system with damping, we find this effect shows up more remarkably. By varying the biexciton damping parameter g_b, it is easy to see the extinction exists even in a damped system, but only when the cavity damping is zero, otherwise the extinction becomes non-zero, but still orders of magnitude lower than nominal.

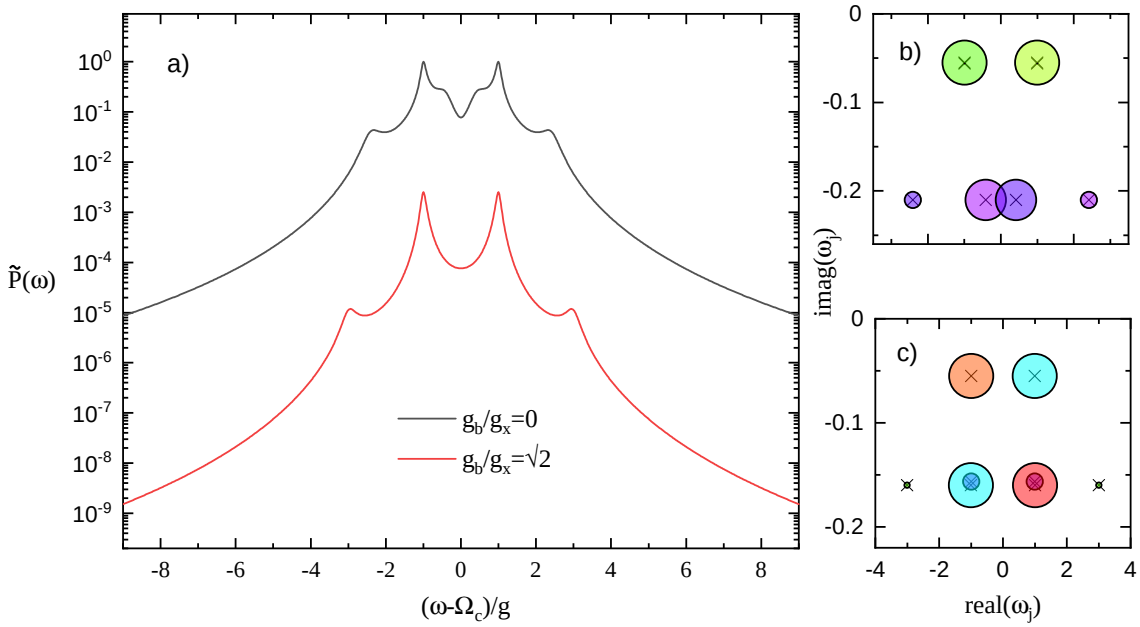

Figure 3.4: FWM polarisation plotted against frequency using the same system parameters as Figure 3.3 but with damping included. $\omega_b = 2\omega_x = 2\omega_c$, $g_b = \sqrt{2}g_x$, $\gamma_c = 0.01$, $\gamma_x = 0.001$, $\gamma_b = 0.0001$. a) Reduction in FWM signal when $g_b = \sqrt{2}g_x$. The reduction is by 400 times for this set of parameters. b) is a bubble plot of complex amplitudes for each frequency of the $g_b = 0$ curve. c) is as b) but for $(g_b = \sqrt{2})$.

Upon investigation, it is apparent that a number of rules must be obeyed to produce the extinction, which apply to all real and imaginary components: $g_b = \sqrt{2}g_x$, $\omega_b = 2\omega_x = 2\omega_c$. This is made more clear in Figure 3.5

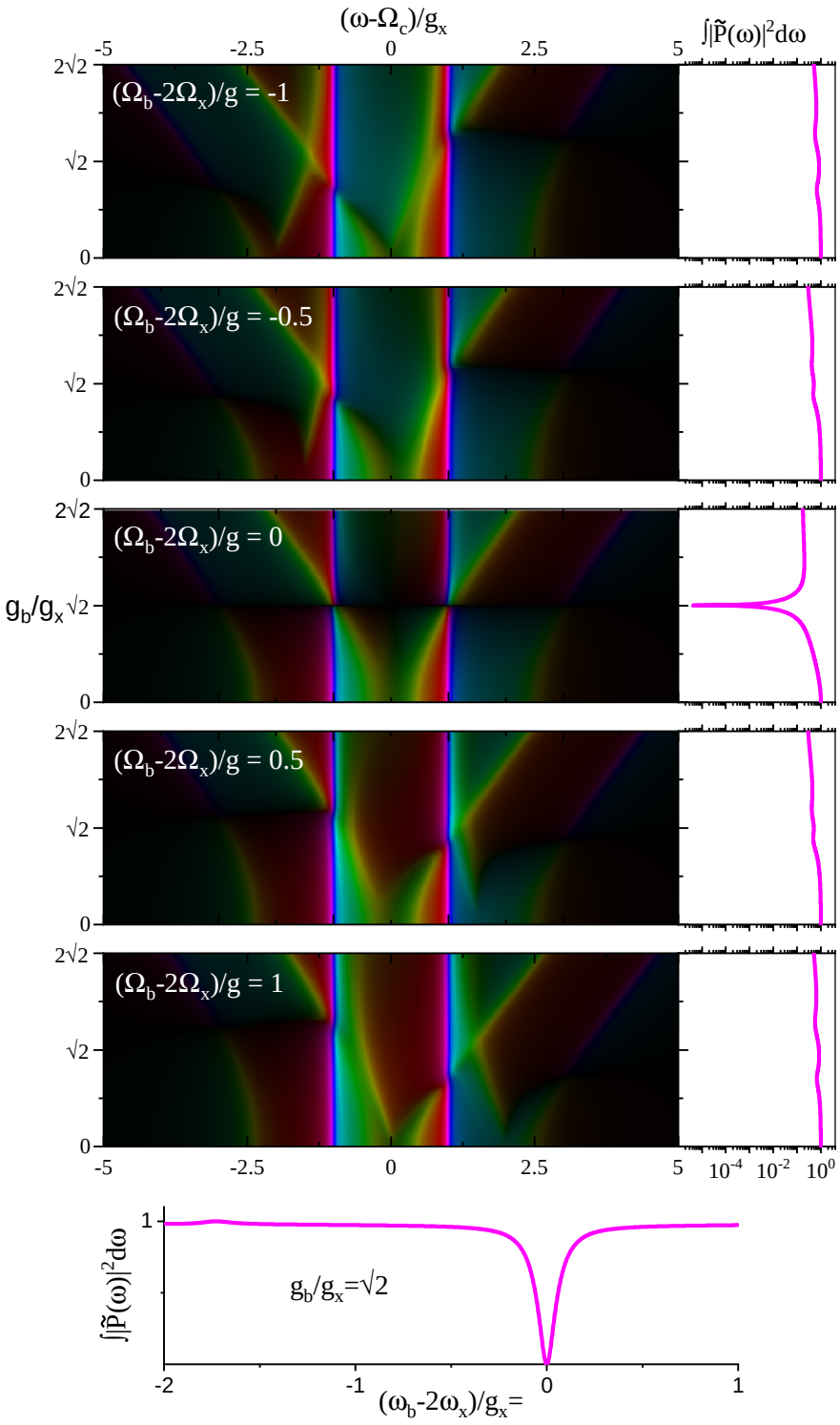

Figure 3.5: Varying biexciton coupling ratio g_b/g_x over the x axis, $|\tilde{P}(\omega)|$ is the gamma $1/2$ corrected pixel intensity of each of the five images and the phase of $\tilde{P}(\omega)$ is the pixel hue, with red being zero phase. Damping set to $\gamma_{c,x,b} = 0.1, 0.001, 0.0001$. Here as the parameters reach those required for polarisation extinction, it is visible that the polarisation is reduced by orders of magnitude at that point. The lower panel shows the extinction condition met varying ω_b instead.

Changing g_b like this is quite unrealistic. For such big detuning the JC model doesn't work well, it's not suited for this system. This does mean however that slight changes to detuning will not affect ability to measure the vanishing signal, it will be more likely to be sensitive to changes in g_b. It appears in Figure 3.4 that the energy gaps are comparable, whereas in real systems this difference is many orders of magnitude.

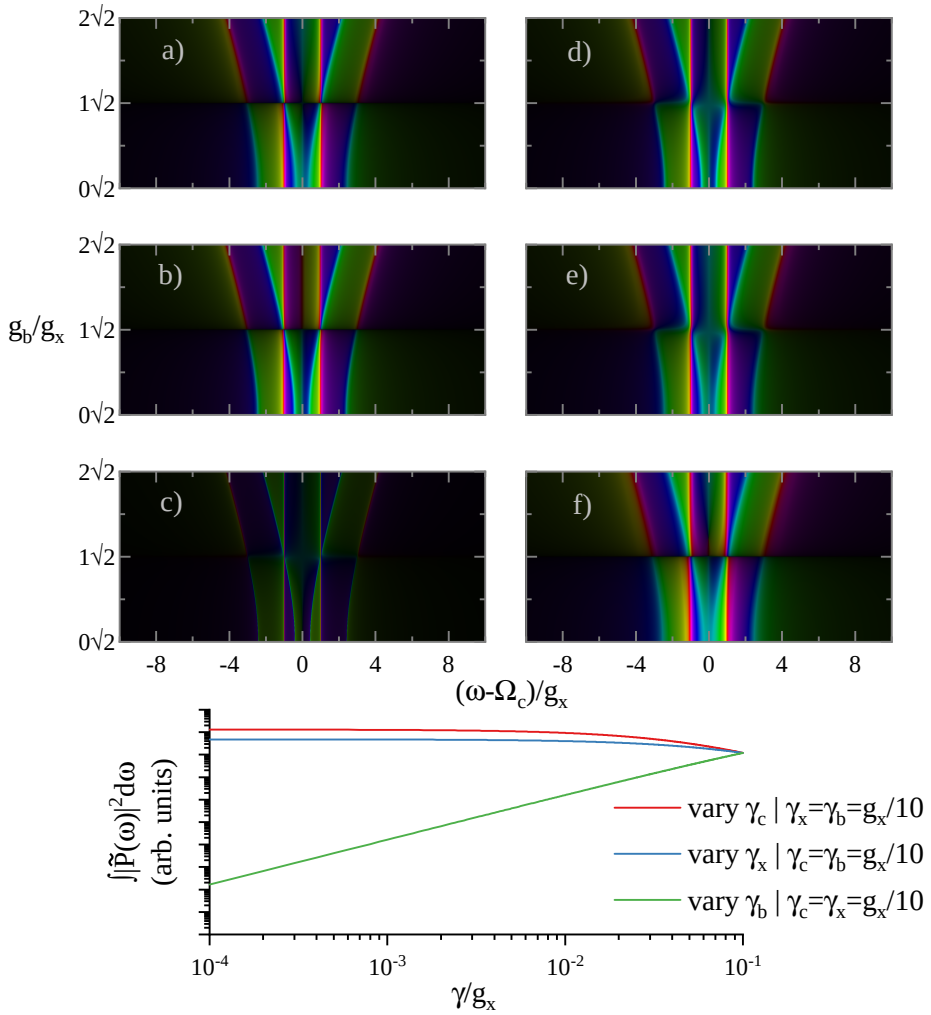

Figure 3.6: $\tilde{P}(\omega)$ Using h (l) to denote high (low) damping for the cavity, exciton and biexciton parameters $\gamma_{c,x,b}$, for example: high γ_c and low γ_x and γ_b is labeled hll. From a) to f), plots of hll, lhl, llh, lhh, hlh, hhl. c) is darker because bright peaks are more sharp due to low cavity and exciton damping at the same time. Here it is clear that the biexciton damping controls the clarity of extinction. Below: Integrated power, vary a single damping parameter.

We can tell from Figure 3.6 that both the values of g_b/g_x and ω_b/ω_c contribute to the vanishing of the FWM signal, though not to the same degree. Since experimental values of g_b and g_x are around four orders of magnitude smaller than ω_c, the range of energy values which allow suppression of FWM signal represented by coupling parameters is far smaller than that represented by the cavity frequency. It is clear that the damping parameter which controls this effect the most is γ_b, reducing $\tilde{P}(\omega)$ by two orders of magnitude for every order of magnitude γ_b reduces by, so there is likely some underlying square relationship between γ_b and the integrated power. The other damping parameters γ_c and γ_x do not reduce $\tilde{P}(\omega)$.

3.6 Three-level dynamics in the high excitation regime

In this model it's possible to change the amplitude of each pulse field, and the effects of high excitation up the rungs of the 3-level ladder can be observed, and compare the transition to the classical regime to the two-level quantum dot model. To allow Lindblad dynamics to occur over an arbitrary number of rungs, the Lindblad operator can be written in the same way as the 2-level Lindblad matrix.

$$L = \left[\begin{array}{c|c|c|c|c} L_{[00]} & L_{[12]} & \hat{\mathbb{0}} & \hat{\mathbb{0}} & \cdots \\ \hline \hat{\mathbb{0}} & L_{[11]} & L_{[23]} & \hat{\mathbb{0}} & \cdots \\ \hline \hat{\mathbb{0}} & \hat{\mathbb{0}} & L_{[22]} & L_{[34]} & \cdots \\ \hline \hat{\mathbb{0}} & \hat{\mathbb{0}} & \hat{\mathbb{0}} & L_{[33]} & \cdots \\ \hline \vdots & \vdots & \vdots & \vdots & \ddots \end{array}\right] \tag{3.20}$$

The Lindblad operator's intra-ladder transitions $L_{[nn]}$ can be written in terms of rungs of the Hamiltonian, introducing matrices F_n and G_n from the 2-level diago-

nalisation formalism Appendix. B $L_n = G_n - F_n^*$

$$F_n = \begin{bmatrix} H_{n-1} & \hat{\mathbb{0}} & \hat{\mathbb{0}} \\ \hat{\mathbb{0}} & H_{n-1} & \hat{\mathbb{0}} \\ \hat{\mathbb{0}} & \hat{\mathbb{0}} & H_{n-1} \end{bmatrix} \qquad G_n = \begin{bmatrix} I(H_n)_{00} & I(H_n)_{01} & I(H_n)_{02} \\ I(H_n)_{10} & I(H_n)_{11} & I(H_n)_{12} \\ I(H_n)_{20} & I(H_n)_{21} & I(H_n)_{22} \end{bmatrix} \tag{3.21}$$

After modifying the 2-level Hamiltonian the Lindblad matrix has a new form. The new block diagonals $L_{[nn]}$ at rung $n \geq 2$ ($L_{[11]}$ and $L_{[22]}$ given in Eq. (3.13)) can be written in general as

$$L_{[nn]}(n \geq 2) = IW_n + \begin{bmatrix} A_n & B_n & \hat{\mathbb{0}}_3 \\ B_n & A_n & C_n \\ \hat{\mathbb{0}}_3 & C_n & A_n \end{bmatrix}$$

$$W_n = \begin{bmatrix} b - b^* + (n-2)c - (n-3)c^* \\ b - x^* + (n-2)c - (n-2)c^* \\ b + (n-2)c - (n-1)c^* \\ x - b^* + (n-1)c - (n-3)c^* \\ x - x^* + (n-1)c - (n-2)c^* \\ x + (n-1)c - (n-1)c^* \\ -b^* + nc - (n-3)c^* \\ -x^* + nc - (n-2)c^* \\ nc - (n-1)c^* \end{bmatrix} \tag{3.22}$$

$$A_n = \begin{bmatrix} \cdot & -\sqrt{n-1}g_b & \cdot \\ -\sqrt{n-1} & \cdot & -\sqrt{n}g_x \\ \cdot & -\sqrt{n}g_x & \cdot \end{bmatrix} \qquad \begin{aligned} B_n &= I_3\sqrt{n}g_b \\ C_n &= I_3\sqrt{n+1}g_x \end{aligned}$$

and the upper off-diagonal block elements $L_{[n,n+1]}$ at rung $n \geq 0$ are

$$L_{[01]} = 2i \begin{bmatrix} \cdot & \cdot & \cdot & \gamma_c & \cdot & \cdot \\ \cdot & \cdot & \gamma_x & \cdot & \cdot & \sqrt{2}\,\gamma_c \end{bmatrix} \tag{3.23}$$

$$L_{[12]} = 2i \begin{bmatrix} \cdot & \gamma_c & \cdot & \cdot & \cdot & \cdot & \cdot & \cdot & \cdot \\ \cdot & \cdot & \sqrt{2}\,\gamma_c & \cdot & \cdot & \cdot & \cdot & \cdot & \cdot \\ \gamma_b & \cdot & \cdot & \cdot & \sqrt{2}\,\gamma_c & \cdot & \cdot & \cdot & \cdot \\ \cdot & \cdot & \cdot & \cdot & \cdot & 2\,\gamma_c & \cdot & \cdot & \cdot \\ \cdot & \cdot & \cdot & \cdot & \cdot & \cdot & \sqrt{3}\,\gamma_c & \cdot & \cdot \\ \cdot & \cdot & \cdot & \cdot & \gamma_x & \cdot & \cdot & \cdot & \sqrt{6}\,\gamma_c \end{bmatrix} \tag{3.24}$$

$$L_{[n,n+1]}\,, n \geq 2 = \\ 2i \begin{bmatrix} \Gamma_{0,-1} & \cdot & \cdot & \cdot & \cdot & \cdot & \cdot & \cdot & \cdot \\ \cdot & \Gamma_{0,0} & \cdot & \cdot & \cdot & \cdot & \cdot & \cdot & \cdot \\ \cdot & \cdot & \Gamma_{0,1} & \cdot & \cdot & \cdot & \cdot & \cdot & \cdot \\ \cdot & \cdot & \cdot & \Gamma_{1,-1} & \cdot & \cdot & \cdot & \cdot & \cdot \\ \gamma_b & \cdot & \cdot & \cdot & \Gamma_{1,0} & \cdot & \cdot & \cdot & \cdot \\ \cdot & \cdot & \cdot & \cdot & \cdot & \Gamma_{1,1} & \cdot & \cdot & \\ \cdot & \cdot & \cdot & \cdot & \cdot & \cdot & \Gamma_{2,-1} & \cdot & \cdot \\ \cdot & \cdot & \cdot & \cdot & \cdot & \cdot & \cdot & \Gamma_{2,0} & \cdot \\ \cdot & \cdot & \cdot & \cdot & \gamma_x & \cdot & \cdot & \cdot & \Gamma_{2,1} \end{bmatrix} \tag{3.25}$$

$$\text{with} \qquad \Gamma_{i,j} = \sqrt{(n+i)(n+j)}\gamma_c$$

All other block diagonal elements remain equal to the zero matrix.

L is diagonalised in the same way as 2-level, using the now larger block elements, first diagonalising each of F_n and G_n through diagaonalisation of H_n. See Appendix. H for eigenvalues of Eq. (3.6). For most applications numerical diago-

nalisation is sufficient, though per-rung investigations are not possible as frequency ordering by rung is lost. If the detuning is low enough however, ordering the list of eigenvalues by imaginary part puts them in rung order, increasing in rung when ordering decreasing by imaginary part.

In our model we can change the strength of each of the two pulses as with the two-level QDMC model, so we can find out what happens when a large number of three-level rungs are excited and see if there is a difference between the transition to the classical regime of two and three-level models. Figure 3.7 shows the quantum to classical transition shows a different shape. For a more complete set of High-Excitation regime data see Appendix. E.3. We calculate the four-wave mixing response of the system as a function of the excitation magnitude E, going up to 115 rungs of the three-level ladder (much less compared to 2-level QDMC calculations to compensate for increased numerical complexity, see Appendix. G.2.1 for time order and suggested rung truncation based on manual search for convergence over increasing rung number). To see all rows of data plotted in video form see Appendix. F

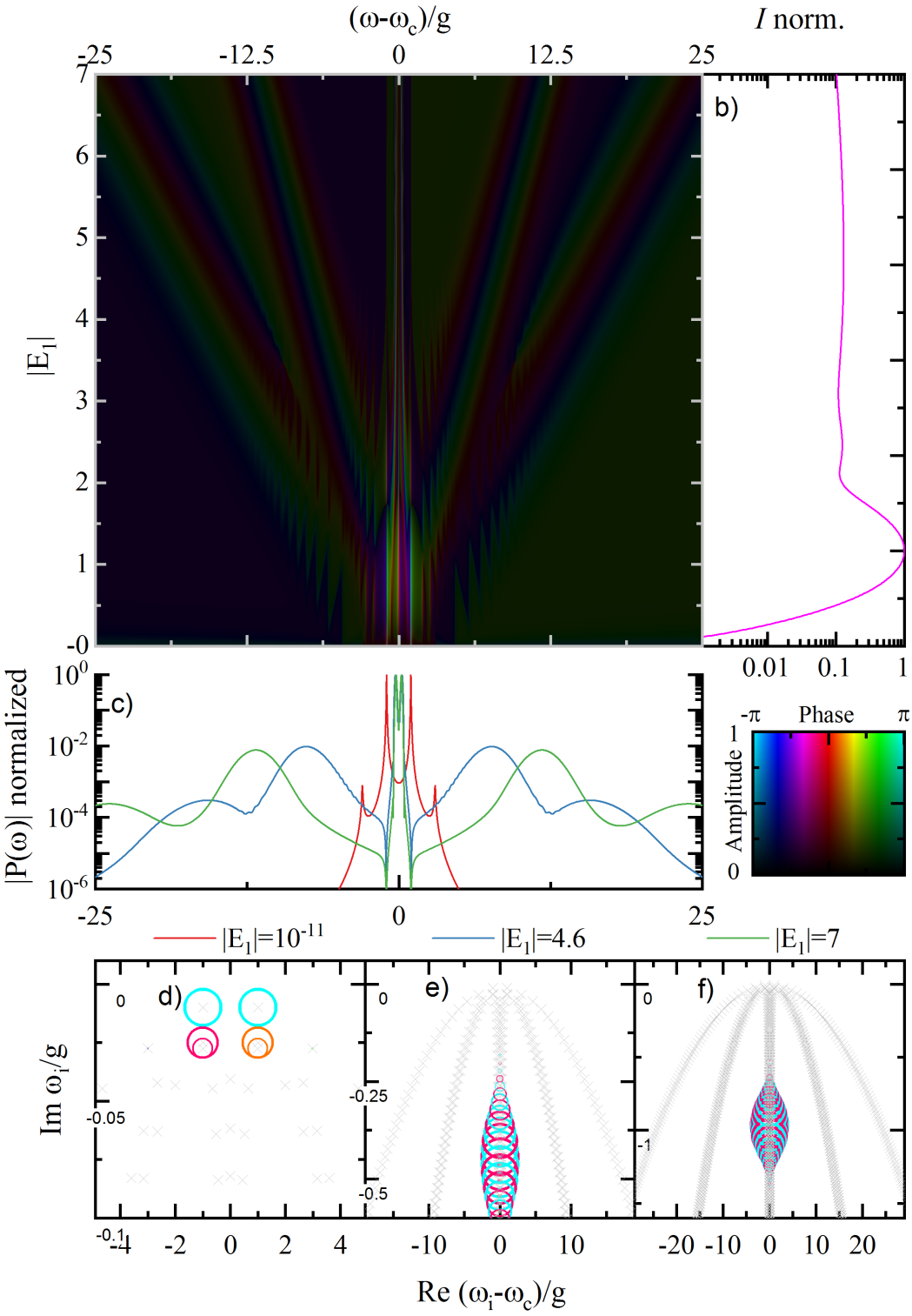

Figure 3.7: Four wave mixing response of the 3-level QDMC system. Plot configuration same as Figure 2.2. E_l changing, $\delta = 0$, $\gamma_c = \gamma_x = g/100$, $g_b/g_x = \sqrt{2}$.

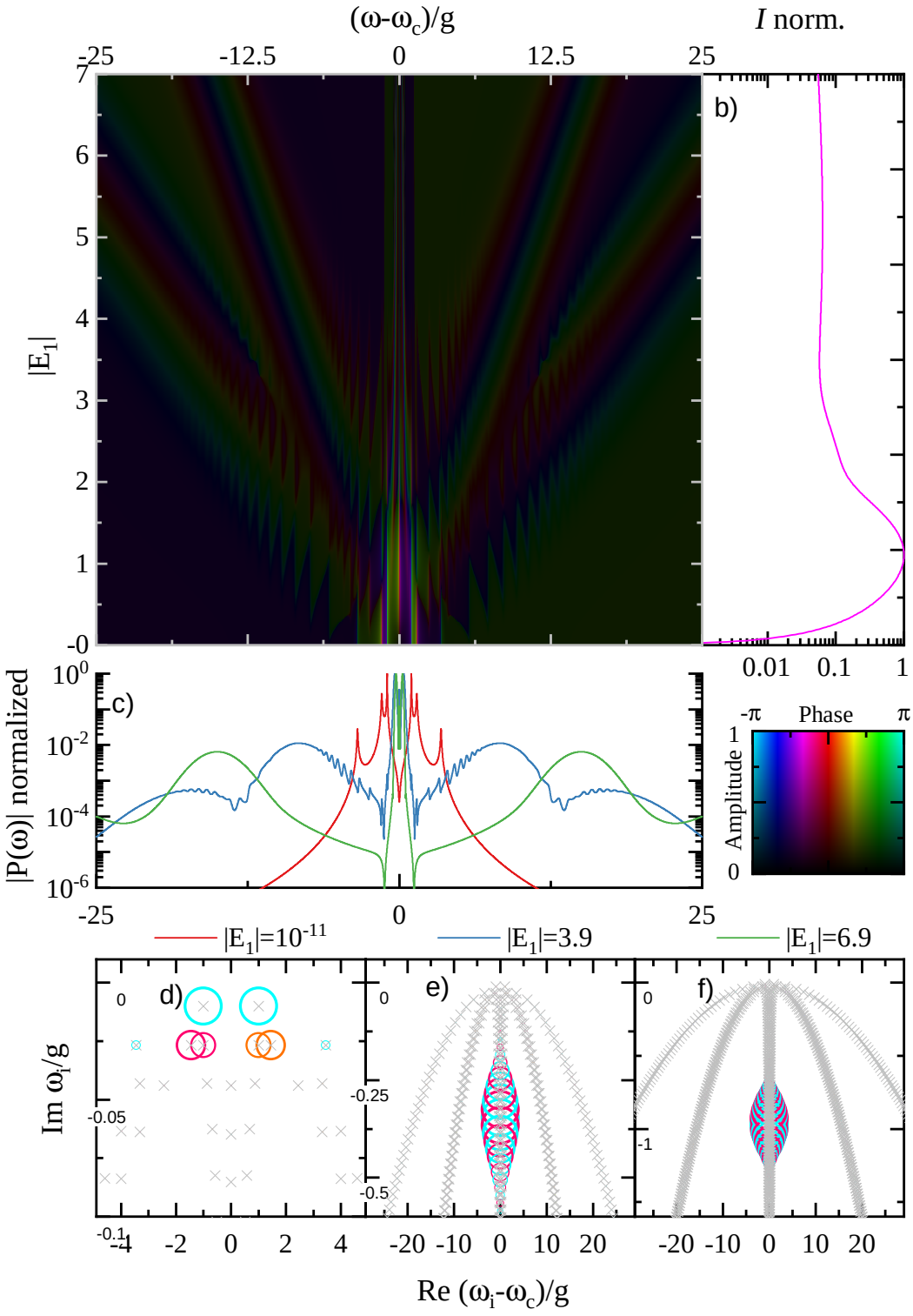

Figure 3.8: As Figure 3.7 with E_1 changing, $\delta = 0$, $\gamma_c = \gamma_x = g/100$, $g_b/g_x = 2$.

There are two interesting things happening here, depending on the parameters

chosen. For one, the signal no longer vanishes as E increases (Figure 3.9).

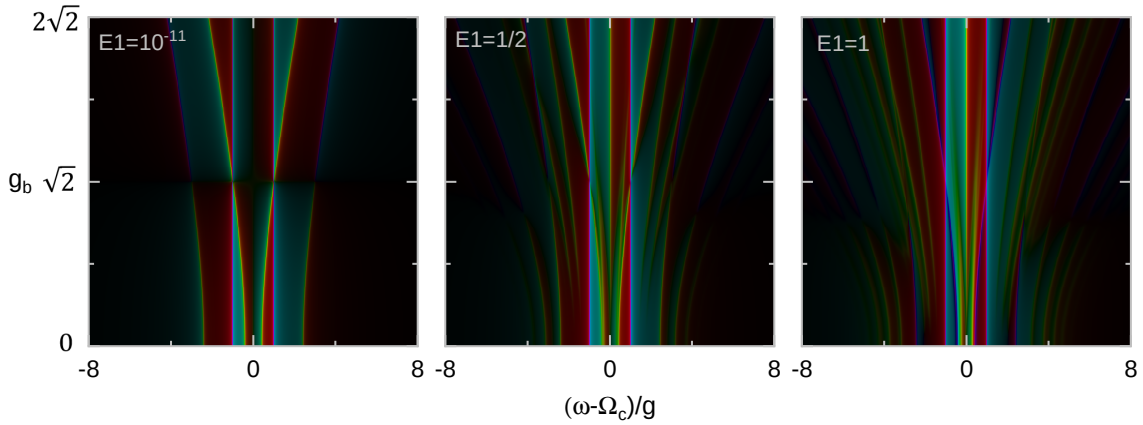

Figure 3.9: Biexciton transition plot for increasing pulse area. Each plot shows biexciton coupling g_b increasing along the y axis.

We see that as the pulse area increases even slightly the extinction property is lost.

The second is the formation of the mollow triplet, only this time there are five peaks instead of three using the two-level model. This can be explained by looking at the eigenvalues of H between neighbouring rungs.

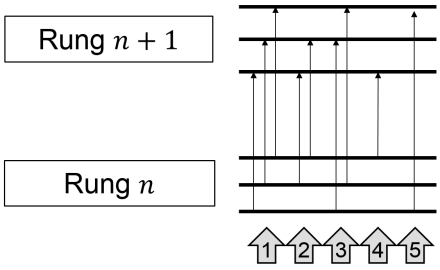

Figure 3.10: Neighbouring rungs in the three-level QDMC system produce 5 groups of similar transitions.

Qualitatively it's easy to see that by grouping the transitions that have similar energy together between neighbouring tungs, there are five groups of frequencies contributing to the spectrum instead of 3 in the two-level model. The parameter space has not yet been fully explored but there is reason to suggest there could be a

set of parameters which allow a quintuplet to form with all peaks with similar peak amplitudes.

3.7 N-wave mixing response of the 3-Level system in the low excitation regime

Our model allows the selection of phase channel used during pulsed excitation in Eq. (2.14). Extracting a different phase from each of the two pulses, as long as the phase channels sum to +1, N-wave mixing reponse of the three-level QDMC system can be found. By exploring the parameter space including N as a parameter we find that four-wave mixing is unique. It is the only mixing channel which allows the vanishing of P in time or spectral domain. At higher order mixing (Figure 3.11) the power actually peaks compared to vanishing under the same Lindblad parameters, which is quite unexpected. For a visualisation of this parameter space see Appendix. F.

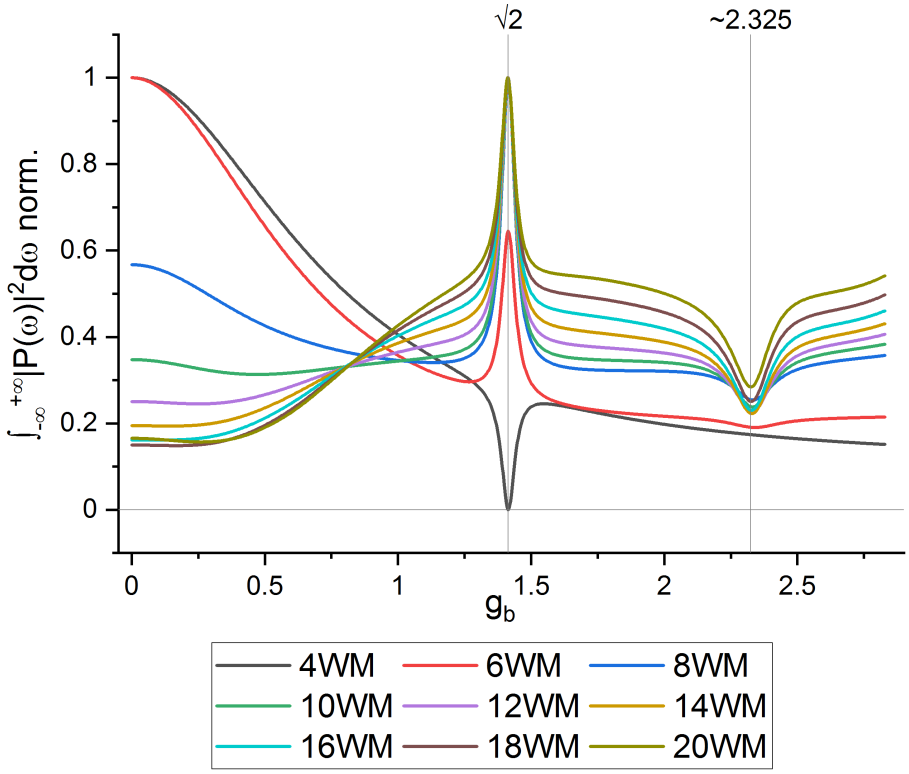

Figure 3.11: Normalised integrated power at varying ratios of g_b to g_x. Peak at $g_b = \sqrt{2}$ for four-wave mixing (FWM) is not carried through when looking at higher order mixing.

The reason for the anti-peak at 2.325 is not yet known. This will be a topic of inquiry for a future paper.

3.8 Discussion of data in Appendix. F.2

This section will describe what is happening in video data produced alongside and in addition to the colour diagrams in Sec. 3.6 and Appendix. E.3. The parameter sweep in the "High excitation" video includes variation of the following parameters:

- Pulse 1 amplitude $|E_1|$ varies continuously between 0 and 10
- Pulse 1 phase $|\Delta N_1|$ takes the values -1(FWM), -2(SWM) and 0(2WM)
- Pulse 2 amplitude $|E_2|$ varies continuously between 0 and 10

- Pulse 2 phase $|\Delta N_2|$ takes the values 2(FWM), 3(SWM) and 1(2WM)
- Cavity, exciton and biexciton dampings γ_c, γ_x and γ_b vary simultaneously, take the values g_x, $g_x/5$, $g_x/100$ and $g_x/10000$.
- Biexciton-exciton-cavity coupling ratio (BECR) g_b/g_x, takes the values 1, $\sqrt{2}$ and 2.

We find good examples of the Mollow-like quintuplet and visualise its shape and position depending on the BEC ratio, and also in the very low damping limit we see the structure of the density matrix in Appendix. A appear overlayed at the quintuplet sidebands.

The parameter sweep used in the "Low excitation" video are the preceeding data for Figure 3.11, which consists of:

- Pulse 1 phase $|\Delta N_1|$ takes the values -1(FWM), -2(SWM) and 0(2WM)
- Pulse 2 phase $|\Delta N_2|$ takes the values 2(FWM), 3(SWM) and 1(2WM)
- Biexciton-exciton-cavity coupling ratio g_b/g_x, varies continuously between 0 and $2\sqrt{2}$

We see the integrated power spectrum transition between a relatively high power suddenly dropping to zero once the conditions $2\omega_c = 2\omega_x = \omega_b$ and $g_b/g_x = \sqrt{2}$ are met, but only for the FWM polarisation, not for any higher order mixing. Also we see that even though the system is in the low-excitation regime the number of transitions which describe the dynamics grows with higher order non-linearity.

3.9 Conclusion

When adding an extra fermionic level to the quantum dot representing a biexciton, there are a special set of parameters which cause the four-wave mixing response

of the quantum-dot microcavity system to vanish, or at least reduce by orders of magnitude depending on damping parameters. This special case only occurs in the low excitation regime of the four-wave mixing when the biexciton energy is twice the exciton energy, and biexciton coupling to the microcavity is $\sqrt{2}$ times the coupling between the exciton and microcavity.

A Mollow-like quintuplet has been found to exist providing damping is low enough and excitation strength is high enough. The triplet appears to have the same peaks at $\omega - \omega_c = \pm 2Eg$ as found in the analytics presented in Sec. 2 along with two additional peaks at $\omega - \omega_c = \pm 4Eg$, also somewhat controlled by the ratio of g_b/g_x. As it increases, this ratio appears to increase the difference between sideband peak frequency and the central peak. The reason for this will be a topic of a future study. One reason may be because as the QD component increases in complexity there are in general more energies which, at high rung number, will produce more peaks. It is in this sense that perhaps the quintuplet here is simply an intermediate stage between a bulk-like band structure and the 2LS band structure.

4 | Conclusions and Future Outlook

Even for a simple model like the JC model, an enourmous range of interesting phenomena have been discovered since its birth in the 60s [9].

This thesis discusses only a few models, and is by no means a complete study of quantum dot microcavity systems. The only limitation is what one can imagine the system could be. New and interesting models are appearing all the time, with the potential to be studied as an extension of that discussed in this thesis.

The beauty of our model lies in the generality of the formalism. There are a bunch of additional elements which can be added to the Hamiltonian of the quantum dot microcavity system which doesn't require much of the numerical innerworkings to be changed. Code developed for this thesis may be applied to many different configurations of JC systems. As the project grows in complexity, maintaining serialisation, generality and flexibility between selection of system parameters, this program can potentially scale extremely well. There are still a number of parameters which are available for use in our developed code, but have not yet been studied. The sweep over the current parameter space for the 2-level and 3-level model is still yet to be done as the full space of parameters is very large, even for the 2-level model.

There are a number of possible changes to our quantum dot microcavity model which are still not studied in literature in the regimes presented in this thesis, which is exciting for the future of the work we have completed here:

- Extend the quantum dot model further to include the 4-level model [111]
- Extensions of the quantum dot model which describe new quasiparticles such as trions
- Dicke model or Tavis-Cummings model [16, 17] describing the coupling of a cavity mode with multiple 2-level systems
- Incorporate coupling between the quantum dot and a phonon bath, more accurately modeling dissipation to the environment compared to Lindblad dissipation only. There is a simple expression for this which involves a modification of the coupling constant g_x in the 2-level system [107].
- Change the observable from cavity polarisation to something else. This is a trivial implementation which has not been investigated in this thesis. A simple swap of operators from c to something else in the final vectorised expression for the transition eigenfrequency amplitudes A_r will do this. An example would be the absorption spectrum of the cavity or QD (using $c^\dagger c$ or $x^\dagger x$).
- Not assuming the cavity excitation is infinitesimal in time scale, giving each pulse a width and the shape of perhaps a gaussian, and comparing to the ultrashort pulse approach. This would take more time to develop, as the current code is not equipped to do this.

There also exists the possibility of changing the quantum system being pulsed, by replacing the quantum dot with a quantum well or wire.

We would like to publish our results on the 3-level quantum dot, including polarisation extinction and the quintuplet found in FWM results.

So far the N-wave mixing dynamics in the high excitation regime have not been explored. One issue is numerical complexity. Exciting the 2-level system density matrix with a pulse equivalent to 100 photons requires a few minutes to calculate

using multiprecision. The same problem in 3-level numerically (as analytics haven't been found for this model's dynamics) takes around 11 times longer for the same cavity excitation. One way to get around this is to find an analytic solution to the 3-level master equation, which is possible since the eigenvalues already have an exact form.

A test which would be interesting to perform is to do what was done in the 2-level quantum dot microcavity system, but don't apply the rotating wave approximation, then do a parameter sweep to find in what parameter space the rotating wave approximation is valid.

Investigation into the weak coupling regime was ignored in this thesis. It is not a regime which is of as much interest compared to the applications of the strong coupling regime, but it is simple to model using the current version of code, by simiply increasing the value of γ_c or γ_x in the two-level system. An analysis for the 3-level system has not been done, and it is not known if it posesses the same weak and strong coupling regimes as 2-level.

A slightly more farfetched prospect is the idea of having some of the system parameters time-dependent. Time-dependent exciton-cavity detuning has already been studied [112]

Lastly an area which would be interesting to develop is data visualisation. We have come up with interesting ways to present a large amount of data in this thesis, including videos. Often, a good visualisation or presentation of data can be as important as the data itself.

Bibliography

[1] M S Skolnick, T A Fisher, and D M Whittaker. "Strong coupling phenomena in quantum microcavity structures". Semiconductor Science and Technology 13.7 (July 1998), pp. 645–669. DOI: 10.1088/0268-1242/13/7/003.

[2] G. Khitrova et al. "Nonlinear optics of normal-mode-coupling semiconductor microcavities". Rev. Mod. Phys. 71 (5 Oct. 1999), pp. 1591–1639. DOI: 10.1103/RevModPhys.71.1591.

[3] A. Kavokin. "Exciton-polaritons in microcavities: present and future". Applied Physics A 89.2 (June 2007), pp. 241–246. DOI: 10.1007/s00339-007-4145-z.

[4] G. Khitrova et al. "Vacuum Rabi splitting in semiconductors". Nature Physics 2.2 (Feb. 2006), pp. 81–90. DOI: 10.1038/nphys227.

[5] Bruce W. Shore and Peter L. Knight. "The Jaynes-Cummings Model". Journal of Modern Opt 40.7 (July 1993), pp. 1195–1238. DOI: 10.1080/09500349314551321.

[6] Ilse Aben et al. "Polarization effects in resonant four-wave-mixing processes". Molecular Physics 76.3 (June 1992), pp. 591–608. DOI: 10.1080/00268979200101551.

[7] Qiang Lin and Govind P. Agrawal. "Vector theory of four-wave mixing: polarization effects in fiber-optic parametric amplifiers". J. Opt. Soc. Am. B 21.6 (June 2004), pp. 1216–1224. DOI: 10.1364/JOSAB.21.001216.

[8] J. Kasprzak et al. "Up on the Jaynes–Cummings ladder of a quantum-dot/microcavity system". Nature Materials 9.4 (Mar. 2010), pp. 304–308. DOI: 10.1038/nmat2717.

[9] E. T. Jaynes and F. W. Cummings. "Comparison of quantum and semiclassical radiation theories with application to the beam maser". Proceedings of the IEEE 51.1 (1963), pp. 89–109. DOI: 10.1109/PROC.1963.1664.

[10] Fabrice P. Laussy et al. "Statistics of excitons in quantum dots and their effect on the optical emission spectra of microcavities". Phys. Rev. B 73 (11 Mar. 2006), p. 115343. DOI: 10.1103/PhysRevB.73.115343.

[11] Elena del Valle, Fabrice P. Laussy, and Carlos Tejedor. "Luminescence spectra of quantum dots in microcavities. II. Fermions". Phys. Rev. B 79 (23 June 2009), p. 235326. DOI: 10.1103/PhysRevB.79.235326.

[12] E. M. Purcell. "Spontaneous Emission Probabilities at Radio Frequencies" (1995), pp. 839–839. DOI: 10.1007/978-1-4615-1963-8_40.

[13] Andrei Faraon et al. "Coherent generation of non-classical light on a chip via photon-induced tunnelling and blockade". Nat. Phys. 4.11 (Nov. 2008), pp. 859–863. DOI: 10.1038/nphys1078.

[14] C. Weisbuch et al. "Observation of the Coupled Exciton-Photon Mode Splitting in a Semiconductor Quantum Microcavity". Phys. Rev. Lett. 69 (1992), p. 3314.

[15] J. R. Jensen et al. "Ultranarrow polaritons in a semiconductor microcavity". Applied Physics Letters 76.22 (May 2000), pp. 3262–3264. DOI: 10.1063/1.126601.

[16] Michael Tavis and Frederick W. Cummings. "Exact Solution for an N-Molecule—Radiation-Field Hamiltonian". Phys. Rev. 170 (2 June 1968), pp. 379–384. DOI: 10.1103/PhysRev.170.379.

[17] F. Albert et al. "Microcavity controlled coupling of excitonic qubits". Nature Communications 4.1 (Apr. 2013). DOI: 10.1038/ncomms2764.

[18] E. Peter et al. "Exciton-Photon Strong-Coupling Regime for a Single Quantum Dot Embedded in a Microcavity". Phys. Rev. Lett. 95 (6 Aug. 2005), p. 067401. DOI: 10.1103/PhysRevLett.95.067401.

[19] J. P. Reithmaier et al. "Strong coupling in a single quantum dot–semiconductor microcavity system". Nature 432.7014 (Nov. 2004), pp. 197–200. DOI: 10.1038/nature02969.

[20] Ryuichi Ohta et al. "Strong coupling between a photonic crystal nanobeam cavity and a single quantum dot". Applied Physics Letters 98.17 (Apr. 2011), p. 173104. DOI: 10.1063/1.3579535.

[21] J. J. Hopfield. "Theory of the Contribution of Excitons to the Complex Dielectric Constant of Crystals". Phys. Rev. 112 (5 Dec. 1958), pp. 1555–1567. DOI: 10.1103/PhysRev.112.1555.

[22] J. J. Hopfield and D. G. Thomas. "Polariton Absorption Lines". Phys. Rev. Lett. 15 (1 July 1965), pp. 22–25. DOI: 10.1103/PhysRevLett.15.22.

[23] J. J. Hopfield. "Resonant Scattering of Polaritons as Composite Particles". Phys. Rev. 182 (3 June 1969), pp. 945–952. DOI: 10.1103/PhysRev.182.945.

[24] Y. Kaluzny et al. "Observation of Self-Induced Rabi Oscillations in Two-Level Atoms Excited Inside a Resonant Cavity: The Ringing Regime of Superradiance". Phys. Rev. Lett. 51 (13 Sept. 1983), pp. 1175–1178. DOI: 10.1103/PhysRevLett.51.1175.

[25] Alexey Kavokin. "Exciton-polaritons in microcavities: Recent discoveries and perspectives". physica status solidi (b) 247.8 (June 2010), pp. 1898–1906. DOI: 10.1002/pssb.200983955.

[26] Hui Deng, Hartmut Haug, and Yoshihisa Yamamoto. "Exciton-polariton Bose-Einstein condensation". Rev. Mod. Phys. 82 (2 May 2010), pp. 1489–1537. DOI: 10.1103/RevModPhys.82.1489.

[27] J. M. Fink et al. "Climbing the Jaynes-Cummings ladder and observing its nonlinearity in a cavity QED system". Nature 454.7202 (2008), pp. 315–318. DOI: 10.1038/nature07112.

[28] T. Yoshie et al. "Vacuum Rabi splitting with a single quantum dot in a photonic crystal nanocavity". Nature 432.7014 (Nov. 2004), pp. 200–203. DOI: 10.1038/nature03119.

[29] Ryuichi Ohta et al. "Strong coupling between a photonic crystal nanobeam cavity and a single quantum dot". Appl. Phys. Lett. 98.17, 173104 (2011), p. 173104. DOI: 10.1063/1.3579535.

[30] Biswarup Guha et al. "Surface-enhanced gallium arsenide photonic resonator with quality factor of $6 \times 10\hat{6}$". Optica 4.2 (Feb. 2017), p. 218. DOI: 10.1364/OPTICA.4.000218.

[31] Daniel Najer et al. "A gated quantum dot strongly coupled to an optical microcavity". Nature 575.7784 (Oct. 2019), pp. 622–627. DOI: 10.1038/s41586-019-1709-y.

[32] K. M. Birnbaum et al. "Photon blockade in an optical cavity with one trapped atom". Nature 436.7047 (July 2005), pp. 87–90. DOI: 10.1038/nature03804.

[33] R. J. Schoelkopf and S. M. Girvin. "Wiring up quantum systems". Nature 451.7179 (Feb. 2008), pp. 664–669. DOI: 10.1038/451664a.

[34] K. Hennessy et al. "Quantum nature of a strongly coupled single quantum dot–cavity system". Nature 445.7130 (Jan. 2007), pp. 896–899. DOI: 10.1038/nature05586.

[35] R. S. Knox. "Introduction to Exciton Physics" (1983), pp. 183–245. DOI: 10.1007/978-1-4684-8878-4_5.

[36] C. T. Bodendorf et al. "Quantum-state reconstruction in the one-atom maser". Phys. Rev. A 57 (2 Feb. 1998), pp. 1371–1378. DOI: 10.1103/PhysRevA.57.1371.

[37] M. S. Kim et al. "Scheme for direct observation of the Wigner characteristic function in cavity QED". Phys. Rev. A 58 (1 July 1998), R65–R68. DOI: 10.1103/PhysRevA.58.R65.

[38] P. Meystre and M.S. Zubairy. "Squeezed states in the Jaynes-Cummings model". Physics Letters A 89.8 (June 1982), pp. 390–392. DOI: 10.1016/0375-9601(82)90330-9.

[39] A. Heidmann, J. M. Raimond, and S. Reynaud. "Squeezing in a Rydberg Atom Maser". Phys. Rev. Lett. 54 (4 Jan. 1985), pp. 326–328. DOI: 10.1103/PhysRevLett.54.326.

[40] J. R. Kuklinski and J. L. Madajczyk. "Strong squeezing in the Jaynes-Cummings model". Phys. Rev. A 37 (8 Apr. 1988), pp. 3175–3178. DOI: 10.1103/PhysRevA.37.3175.

[41] J. H. Eberly, N. B. Narozhny, and J. J. Sanchez-Mondragon. "Periodic Spontaneous Collapse and Revival in a Simple Quantum Model". Phys. Rev. Lett. 44 (20 May 1980), pp. 1323–1326. DOI: 10.1103/PhysRevLett.44.1323.

[42] M. França Santos, E. Solano, and R. L. de Matos Filho. "Conditional Large Fock State Preparation and Field State Reconstruction in Cavity QED". Phys. Rev. Lett. 87 (9 Aug. 2001), p. 093601. DOI: 10.1103/PhysRevLett.87.093601.

[43] Julio Gea-Banacloche. "Collapse and revival of the state vector in the Jaynes-Cummings model: An example of state preparation by a quantum apparatus". Phys. Rev. Lett. 65 (27 Dec. 1990), pp. 3385–3388. DOI: 10.1103/PhysRevLett.65.3385.

[44] Simon J. D. Phoenix and P. L. Knight. "Establishment of an entangled atom-field state in the Jaynes-Cummings model". Phys. Rev. A 44 (9 Nov. 1991), pp. 6023–6029. DOI: 10.1103/PhysRevA.44.6023.

[45] Simon J. D. Phoenix and P. L. Knight. "Comment on "Collapse and revival of the state vector in the Jaynes-Cummings model: An example of state preparation by a quantum apparatus"". Phys. Rev. Lett. 66 (21 May 1991), pp. 2833–2833. DOI: 10.1103/PhysRevLett.66.2833.

[46] J.-M. Raimond and S. Haroche. "Atoms and Cavities: The Birth of a Schrödinger Cat of the Radiation Field" (1999). Ed. by Toshimitsu Asakura, pp. 40–53. DOI: 10.1007/978-3-540-48886-6_4.

[47] V. Bužek et al. "Schrödinger-cat states in the resonant Jaynes-Cummings model: Collapse and revival of oscillations of the photon-number distribution". Phys. Rev. A 45 (11 June 1992), pp. 8190–8203. DOI: 10.1103/PhysRevA.45.8190.

[48] P. J. Bardroff, E. Mayr, and W. P. Schleich. "Quantum state endoscopy: Measurement of the quantum state in a cavity". Phys. Rev. A 51 (6 June 1995), pp. 4963–4966. DOI: 10.1103/PhysRevA.51.4963.

[49] D. F. Walls and G. J. Milburn. "Effect of dissipation on quantum coherence". Phys. Rev. A 31 (4 Apr. 1985), pp. 2403–2408. DOI: 10.1103/PhysRevA.31.2403.

[50] G. S. Agarwal, M. O. Scully, and H. Walther. "Inhibition of Decoherence due to Decay in a Continuum". Phys. Rev. Lett. 86 (19 May 2001), pp. 4271–4274. DOI: 10.1103/PhysRevLett.86.4271.

[51] Gerhard Rempe, Herbert Walther, and Norbert Klein. "Observation of quantum collapse and revival in a one-atom maser". Phys. Rev. Lett. 58 (4 Jan. 1987), pp. 353–356. DOI: 10.1103/PhysRevLett.58.353.

[52] A. Auffeves et al. "Entanglement of a Mesoscopic Field with an Atom Induced by Photon Graininess in a Cavity". Phys. Rev. Lett. 91 (23 Dec. 2003), p. 230405. DOI: 10.1103/PhysRevLett.91.230405.

[53] C. J. Hood. "The Atom-Cavity Microscope: Single Atoms Bound in Orbit by Single Photons". Science 287.5457 (Feb. 2000), pp. 1447–1453. DOI: 10.1126/science.287.5457.1447.

[54] M. Brune et al. "Quantum Rabi Oscillation: A Direct Test of Field Quantization in a Cavity". Phys. Rev. Lett. 76 (11 Mar. 1996), pp. 1800–1803. DOI: 10.1103/PhysRevLett.76.1800.

[55] M. Brune et al. "From Lamb shift to light shifts: Vacuum and subphoton cavity fields measured by atomic phase sensitive detection". Phys. Rev. Lett. 72 (21 May 1994), pp. 3339–3342. DOI: 10.1103/PhysRevLett.72.3339.

[56] Simon Brattke, Benjamin T. H. Varcoe, and Herbert Walther. "Generation of Photon Number States on Demand via Cavity Quantum Electrodynamics". Phys. Rev. Lett. 86 (16 Apr. 2001), pp. 3534–3537. DOI: 10.1103/PhysRevLett.86.3534.

[57] G. Nogues et al. "Seeing a single photon without destroying it". Nature 400.6741 (July 1999), pp. 239–242. DOI: 10.1038/22275.

[58] P. Bertet et al. "Generating and Probing a Two-Photon Fock State with a Single Atom in a Cavity". Phys. Rev. Lett. 88 (14 Mar. 2002), p. 143601. DOI: 10.1103/PhysRevLett.88.143601.

[59] B. T. H. Varcoe et al. "Preparing pure photon number states of the radiation field". Nature 403.6771 (Feb. 2000), pp. 743–746. DOI: 10.1038/35001526.

[60] M. Brune et al. "Observing the Progressive Decoherence of the "Meter" in a Quantum Measurement". Phys. Rev. Lett. 77 (24 Dec. 1996), pp. 4887–4890. DOI: 10.1103/PhysRevLett.77.4887.

[61] J. M. Raimond, M. Brune, and S. Haroche. "Reversible Decoherence of a Mesoscopic Superposition of Field States". Phys. Rev. Lett. 79 (11 Sept. 1997), pp. 1964–1967. DOI: 10.1103/PhysRevLett.79.1964.

[62] Simon Brattke, Ben T. H. Varcoe, and Herbert Walther. "Preparing Fock states in the micromaser". Opt. Express 8.2 (Jan. 2001), pp. 131–144. DOI: 10.1364/OE.8.000131.

[63] G. Rempe, F. Schmidt-Kaler, and H. Walther. "Observation of sub-Poissonian photon statistics in a micromaser". Phys. Rev. Lett. 64 (23 June 1990), pp. 2783–2786. DOI: 10.1103/PhysRevLett.64.2783.

[64] Michael A. Nielsen, Isaac Chuang, and Lov K. Grover. "Quantum Computation and Quantum Information". American Journal of Physics 70.5 (May 2002), pp. 558–559. DOI: 10.1119/1.1463744.

[65] J. M. Raimond, M. Brune, and S. Haroche. "Manipulating quantum entanglement with atoms and photons in a cavity". Rev. Mod. Phys. 73 (3 Aug. 2001), pp. 565–582. DOI: 10.1103/RevModPhys.73.565.

[66] A. Rauschenbeutel et al. "Coherent Operation of a Tunable Quantum Phase Gate in Cavity QED". Phys. Rev. Lett. 83 (24 Dec. 1999), pp. 5166–5169. DOI: 10.1103/PhysRevLett.83.5166.

[67] X. Maıtre et al. “Quantum Memory with a Single Photon in a Cavity”. Phys. Rev. Lett. 79 (4 July 1997), pp. 769–772. DOI: 10.1103/PhysRevLett.79.769.

[68] C. Wagner et al. “Phase diffusion, entangled states, and quantum measurements in the micromaser”. Phys. Rev. A 47 (6 June 1993), pp. 5068–5079. DOI: 10.1103/PhysRevA.47.5068.

[69] A. Rauschenbeutel. “Step-by-Step Engineered Multiparticle Entanglement”. Science 288.5473 (June 2000), pp. 2024–2028. DOI: 10.1126/science.288.5473.2024.

[70] H. Walther. “Experiments on cavity quantum electrodynamics”. Physics Reports 219.3 (1992), pp. 263–281. DOI: https://doi.org/10.1016/0370-1573(92)90142-M.

[71] J. I. Cirac et al. “Quantum State Transfer and Entanglement Distribution among Distant Nodes in a Quantum Network”. Phys. Rev. Lett. 78 (16 Apr. 1997), pp. 3221–3224. DOI: 10.1103/PhysRevLett.78.3221.

[72] E. Hagley et al. “Generation of Einstein-Podolsky-Rosen Pairs of Atoms”. Phys. Rev. Lett. 79 (1 July 1997), pp. 1–5. DOI: 10.1103/PhysRevLett.79.1.

[73] A. Rauschenbeutel et al. “Controlled entanglement of two field modes in a cavity quantum electrodynamics experiment”. Phys. Rev. A 64 (5 Oct. 2001), p. 050301. DOI: 10.1103/PhysRevA.64.050301.

[74] Berthold-Georg Englert and Herbert Walther. “Preparing a GHZ state, or an EPR state, with the one-atom maser”. Optics Communications 179.1 (2000), pp. 283–288. DOI: https://doi.org/10.1016/S0030-4018(99)00728-2.

[75] James E. Bayfield. Quantum Evolution: An Introduction to Time-Dependent Quantum Mec 1999.

[76] Qiongtao Xie et al. "The quantum Rabi model: solution and dynamics". Journal of Physics A: Mathematical and Theoretical 50.11 (Feb. 2017), p. 113001. DOI: 10.1088/1751-8121/aa5a65.

[77] Pierre Meystre and Murray Sargent, eds. Elements of Quantum Optics. Springer Berlin Heidelberg, 2007. DOI: 10.1007/978-3-540-74211-1.

[78] Kartik Srinivasan et al. "Cavity Q, mode volume, and lasing threshold in small diameter AlGaAs microdisks with embedded quantum dots". Opt. Express 14.3 (Feb. 2006), pp. 1094–1105. DOI: 10.1364/OE.14.001094.

[79] A. Messina, S. Maniscalco, and A. Napoli. "Interaction of bimodal fields with few-level atoms in cavities and traps". Journal of Modern Optics 50.1 (Jan. 2003), pp. 1–49. DOI: 10.1080/09500340308234530.

[80] H. Tahara et al. "Generation of undamped exciton-biexciton beats in InAs quantum dots using six-wave mixing". Phys. Rev. B 89 (19 May 2014), p. 195306. DOI: 10.1103/PhysRevB.89.195306.

[81] J Kasprzak et al. "Coherence dynamics and quantum-to-classical crossover in an exciton–cavity system in the quantum strong coupling regime". New Journal of Physics 15.4 (Apr. 2013), p. 045013. DOI: 10.1088/1367-2630/15/4/045013.

[82] B. R. Mollow. "Power Spectrum of Light Scattered by Two-Level Systems". Physical Review 188.5 (Dec. 1969), pp. 1969–1975. DOI: 10.1103/physrev.188.1969.

[83] Daniel Groll et al. "Four-wave mixing dynamics of a strongly coupled quantum-dot–microcavity system driven by up to 20 photons". Phys. Rev. B 101 (24 June 2020), p. 245301. DOI: 10.1103/PhysRevB.101.245301.

[84] S. Ates et al. "Post-Selected Indistinguishable Photons from the Resonance Fluorescence of a Single Quantum Dot in a Microcavity". Phys. Rev. Lett. 103 (16 Oct. 2009), p. 167402. DOI: 10.1103/PhysRevLett.103.167402.

[85] A. Nick Vamivakas et al. “Spin-resolved quantum-dot resonance fluorescence”. Nature Physics 5 (Dec. 2009), p. 925. DOI: 10.1038/nphys1459.

[86] E. B. Flagg et al. “Resonantly driven coherent oscillations in a solid-state quantum emitter”. Nature Physics 5.3 (Jan. 2009), pp. 203–207. DOI: 10.1038/nphys1184.

[87] Wolfgang Langbein and Brian Patton. “Heterodyne spectral interferometry for multidimensional nonlinear spectroscopy of individual quantum systems”. Optics Letters 31.8 (Apr. 2006), p. 1151. DOI: 10.1364/ol.31.001151.

[88] I. Wilson-Rae and A. Imamo ğlu. “Quantum dot cavity-QED in the presence of strong electron-phonon interactions”. Phys. Rev. B 65 (23 May 2002), p. 235311. DOI: 10.1103/PhysRevB.65.235311.

[89] P. Kaer et al. “Non-Markovian Model of Photon-Assisted Dephasing by Electron-Phonon Interactions in a Coupled Quantum-Dot–Cavity System”. Phys. Rev. Lett. 104 (15 Apr. 2010), p. 157401. DOI: 10.1103/PhysRevLett.104.157401.

[90] Ulrich Hohenester. “Cavity quantum electrodynamics with semiconductor quantum dots: Role of phonon-assisted cavity feeding”. Phys. Rev. B 81 (15 Apr. 2010), p. 155303. DOI: 10.1103/PhysRevB.81.155303.

[91] C. Roy and S. Hughes. “Phonon-Dressed Mollow Triplet in the Regime of Cavity Quantum Electrodynamics: Excitation-Induced Dephasing and Non-perturbative Cavity Feeding Effects”. Phys. Rev. Lett. 106 (24 June 2011), p. 247403. DOI: 10.1103/PhysRevLett.106.247403.

[92] M. Glässl et al. “Interaction of a quantum-dot cavity system with acoustic phonons: Stronger light-matter coupling can reduce the visibility of strong coupling effects”. Phys. Rev. B 86 (3 July 2012), p. 035319. DOI: 10.1103/PhysRevB.86.035319.

[93] Ahsan Nazir and Dara P S McCutcheon. "Modelling exciton–phonon interactions in optically driven quantum dots". Journal of Physics: Condensed Matter 28.10 (Feb. 2016), p. 103002. DOI: 10.1088/0953-8984/28/10/103002.

[94] Davoud G Nahri, Faisal H A Mathkoor, and C H Raymond Ooi. "Real-time path-integral approach for dissipative quantum dot-cavity quantum electrodynamics: impure dephasing-induced effects (2017 J. Phys.: Condens. Matter 29 055701)". Journal of Physics: Condensed Matter 30.1 (Dec. 2017), p. 019501. DOI: 10.1088/1361-648x/aa9b00.

[95] Gaston Hornecker, Alexia Auffèves, and Thomas Grange. "Influence of phonons on solid-state cavity-QED investigated using nonequilibrium Green's functions". Phys. Rev. B 95 (3 Jan. 2017), p. 035404. DOI: 10.1103/PhysRevB.95.035404.

[96] Ulrich Hohenester et al. "Phonon-assisted transitions from quantum dot excitons to cavity photons". Phys. Rev. B 80 (20 Nov. 2009), p. 201311. DOI: 10.1103/PhysRevB.80.201311.

[97] M. Calic et al. "Phonon-Mediated Coupling of InGaAs/GaAs Quantum-Dot Excitons to Photonic Crystal Cavities". Phys. Rev. Lett. 106 (22 June 2011), p. 227402. DOI: 10.1103/PhysRevLett.106.227402.

[98] Daniel Valente et al. "Frequency cavity pulling induced by a single semiconductor quantum dot". Phys. Rev. B 89 (4 Jan. 2014), p. 041302. DOI: 10.1103/PhysRevB.89.041302.

[99] Simone Luca Portalupi et al. "Bright Phonon-Tuned Single-Photon Source". Nano Letters 15.10 (Sept. 2015), pp. 6290–6294. DOI: 10.1021/acs.nanolett.5b00876.

[100] Kai Müller et al. "Ultrafast Polariton-Phonon Dynamics of Strongly Coupled Quantum Dot-Nanocavity Systems". Phys. Rev. X 5 (3 July 2015), p. 031006. DOI: 10.1103/PhysRevX.5.031006.

[101] P. Borri et al. "Ultralong Dephasing Time in InGaAs Quantum Dots". Phys. Rev. Lett. 87 (15 Sept. 2001), p. 157401. DOI: 10.1103/PhysRevLett.87.157401.

[102] B. Krummheuer, V. M. Axt, and T. Kuhn. "Theory of pure dephasing and the resulting absorption line shape in semiconductor quantum dots". Phys. Rev. B 65 (19 May 2002), p. 195313. DOI: 10.1103/PhysRevB.65.195313.

[103] L. Besombes et al. "Acoustic phonon broadening mechanism in single quantum dot emission". Phys. Rev. B 63 (15 Mar. 2001), p. 155307. DOI: 10.1103/PhysRevB.63.155307.

[104] E. A. Muljarov and R. Zimmermann. "Dephasing in Quantum Dots: Quadratic Coupling to Acoustic Phonons". Phys. Rev. Lett. 93 (23 Nov. 2004), p. 237401. DOI: 10.1103/PhysRevLett.93.237401.

[105] E. A. Muljarov, T. Takagahara, and R. Zimmermann. "Phonon-Induced Exciton Dephasing in Quantum Dot Molecules". Phys. Rev. Lett. 95 (17 Oct. 2005), p. 177405. DOI: 10.1103/PhysRevLett.95.177405.

[106] J. Frenkel. "On the Transformation of light into Heat in Solids. I". Phys. Rev. 37 (1 Jan. 1931), pp. 17–44. DOI: 10.1103/PhysRev.37.17.

[107] A. Morreau and E. A. Muljarov. "Phonon-induced dephasing in quantum-dot–cavity QED". Phys. Rev. B 100 (11 Sept. 2019), p. 115309. DOI: 10.1103/PhysRevB.100.115309.

[108] Howard M. Wiseman and Gerard J. Milburn. Quantum Measurement and Control. Cambridge University Press, 2009. DOI: 10.1017/cbo9780511813948.

[109] Roy J. Glauber. "Coherent and Incoherent States of the Radiation Field". Physical Review 131.6 (Sept. 1963), pp. 2766–2788. DOI: 10.1103/physrev.131.2766.

[110] Tomasz Jakubczyk et al. "Impact of Phonons on Dephasing of Individual Excitons in Deterministic Quantum Dot Microlenses". ACS Photonics 3.12 (Nov. 2016), pp. 2461–2466. DOI: 10.1021/acsphotonics.6b00707.

[111] Q. Mermillod et al. "Dynamics of excitons in individual InAs quantum dots revealed in four-wave mixing spectroscopy". Optica 3.4 (Apr. 2016), pp. 377–384. DOI: 10.1364/OPTICA.3.000377.

[112] I. Cohen, N. Aharon, and A. Retzker. "Continuous dynamical decoupling utilizing time-dependent detuning". Fortschritte der Physik 65.6-8 (Nov. 2016), p. 1600071. DOI: 10.1002/prop.201600071.

[113] Masuo Suzuki. "Generalized Trotter's formula and systematic approximants of exponential operators and inner derivations with applications to many-body problems". Communications in Mathematical Physics 51.2 (1976), pp. 183–190. DOI: 10.1007/BF01609348.

[114] I. S. Gradshtein and I. M. Ryzhik. Table of Integrals, Series, and Products. Academic Press, New York, 1965.

List of Figures

A | The effect of a pulsed optical excitation on the density matrix of a QD-cavity system: Analytic solution

Let us consider an excitation of the QD-cavity system by a sequence of ultrashort optical pulses or by an extended finite wave packet of light. The master equation (1) describing the time evolution of the density matrix (DM) can be written as

$$i\dot{\rho}(t) = \left[\hat{L} + \hat{\mathcal{L}}(t)\right] \rho(t) \tag{A.1}$$

with time-independent Lindblad operator L defined by Eq. (1.23) and a time-dependent operator $\hat{\mathcal{L}}(t)$ defined as

$$\hat{\mathcal{L}}(t)\rho(t) = [V(t), \rho(t)]\,, \tag{A.2}$$

where $V(t)$ is given by Eq.(4):

$$V(t) = -\boldsymbol{\mu} \cdot \boldsymbol{\mathcal{E}}(t)c^{\dagger} - \boldsymbol{\mu}^{*} \cdot \boldsymbol{\mathcal{E}}^{*}(t)c\,, \tag{A.3}$$

The formal solution of Eq. (A.1) can be written as

$$\begin{aligned}\rho(t) &= T\exp\left\{-i\int_{t_0}^{t}\left[\hat{L}+\hat{\mathcal{L}}(\tau)\right]d\tau\right\}\rho(t_0)\\ &= T\prod_{j=0}^{J-1}Q_j\rho(t_0)\,,\end{aligned} \tag{A.4}$$

where T is the standard time-ordering opertor. In the second line of Eq. (A.4), the full time evolution of the DM, between t_0 and t, is split into a time-ordered product of J operators

$$Q_j = T\exp\left\{-i\int_{t_j}^{t_{j+1}}\left[\hat{L}+\hat{\mathcal{L}}(\tau)\right]d\tau\right\}\,, \tag{A.5}$$

obtained by dividing full time interval (from t_0 to t) into J pieces, which are not necessarily equal:

$$t_0 < t_1 < \cdots < t_j < t_{j+1} < \cdots < t_J = t\,. \tag{A.6}$$

Assuming that the time steps $\Delta t_j = t_{j+1} - t_j$ are small enough, these operators may be approximated as

$$Q_j \approx T\exp\left\{-i\int_{t_j}^{t_{j+1}}\hat{L}d\tau\right\}T\exp\left\{-i\int_{t_j}^{t_{j+1}}\hat{\mathcal{L}}(\tau)d\tau\right\}\,, \tag{A.7}$$

with the error proportional to $(\Delta t_j)^2$ [113]. While the first operator in Eq. (A.7) can be written as $e^{-i\hat{L}\Delta t_j}$ due to the time-independent $\hat{L}$, the second operator requires integration of the time-dependent field $\boldsymbol{\mathcal{E}}(t)$ exciting the system. As it immediately follows from its definition Eq. (A.2), the action of the second operator in Eq. (A.7) on the DM can be evaluated as

$$T\exp\left\{-i\int_{t_j}^{t_{j+1}}\hat{\mathcal{L}}(\tau)d\tau\right\}\rho(t_j) = U_j\rho(t_j)U_j^{\dagger}\,, \tag{A.8}$$

where

$$U_j = T \exp\left\{-i \int_{t_j}^{t_{j+1}} V(\tau) d\tau\right\} \tag{A.9}$$

is the standard evolution operator due to a time-dependent interaction $V(t)$. Using the explicit form of $V(t)$, given by Eq. (A.3), which provides in particular $[V(t), V(t')] = 0$ for any different or equal times t and t', we obtain

$$U_j = e^{i(E_j c^\dagger + E_j^* c)}\,, \tag{A.10}$$

where

$$E_j = \int_{t_j}^{t_{j+1}} \boldsymbol{\mu} \cdot \boldsymbol{\mathcal{E}}(\tau) d\tau\,. \tag{A.11}$$

Combining the results, we obtain

$$Q_j \rho(t_j) \approx e^{-i\hat{L}\Delta t_j} U_j \rho(t_j) U_j^\dagger\,, \tag{A.12}$$

‘ where U_j is given by Eq. (A.10).

Note that the full time evolution of the DM described by Eqs. (A.4) and (A.10)–(A.12) becomes exact if the excitation field is represented by a sequence of δ pulses, given by Eq. (5):

$$\boldsymbol{\mu} \cdot \boldsymbol{\mathcal{E}}(t) = \sum_j E_j \delta(t - t_j)\,. \tag{A.13}$$

In fact, Eq. (A.13) is equivalent to the rectangular rule of numerical integration of finite wave packet:

$$\int_{-\infty}^{\infty} \boldsymbol{\mu} \cdot \boldsymbol{\mathcal{E}}(t) dt = \sum_j E_j = \sum_j \boldsymbol{\mu} \cdot \boldsymbol{\mathcal{E}}(t_j) \Delta t_j\,. \tag{A.14}$$

Obviously, the amplitudes E_j have the meaning of the pulse areas corresponding to the time intervals Δt_j .

Let us now consider the effect of a single δ pulse on the DM, which is given by Eq. (A.8) . Dropping index j for brevity, we first transform the evolution operator:

$$U(E) = e^{i(Ec^\dagger + E^* c)} = e^{-|E|^2/2} e^{iEc^\dagger} e^{iE^* c}\,, \tag{A.15}$$

using the fact [113] that $e^{A+B} = e^A e^B e^C$, if $C = -\frac{1}{2}[A,B]$ commutes with both operators A and B, which is true in the present case. When acting on the ground state $|0\rangle$ of the optical cavity (with a single cavity mode), this operator generates a Glauber coherent states $|\alpha\rangle$ with the eigenvalue $\alpha = iE$. In fact,

$$|\alpha\rangle = U(E)|0\rangle = e^{-|E|^2/2} e^{iEc^\dagger}|0\rangle = e^{-|E|^2/2} \sum_{n=0}^{\infty} \frac{(iE)^n (c^\dagger)^n}{n!}|0\rangle = e^{-|E|^2/2} \sum_{n=0}^{\infty} \frac{(iE)^n}{\sqrt{n!}}|n\rangle\,, \tag{A.16}$$

so that

$$c|\alpha\rangle = e^{-|E|^2/2} \sum_{n=1}^{\infty} \frac{(iE)^n \sqrt{n}}{\sqrt{n!}}|n-1\rangle = e^{-|E|^2/2} \sum_{n=0}^{\infty} \frac{(iE)^{n+1}}{\sqrt{n!}}|n\rangle = iE|\alpha\rangle\,. \tag{A.17}$$

This result is useful if the system is fully unexcited before the δ pulse, so that the density matrix before the excitation is given by $|0\rangle\langle 0|$. In general, this is not the case, and the density matrix before the pulsed excitation is given by the general Eq. (2.12), or Eq. (B.4) in Appendix. B below. We therefore need to find out what is the effect of a δ pulse on an arbitrary state $|m\rangle$ of the cavity. This is given by a matrix $U_{nm}(E)$ defined by

$$U(E)|m\rangle = \sum_{n=0}^{\infty} |n\rangle U_{nm}(E) \tag{A.18}$$

and taking the following form:

$$\begin{aligned} U_{nm}(E) = \langle n|U(E)|m\rangle &= e^{-|E|^2/2}\sum_{k=0}^{\infty}\langle n|e^{iEc^\dagger}|k\rangle\langle k|e^{iE^*c}|m\rangle \\ &= e^{-|E|^2/2}\sum_{k=0}^{l}\frac{(iE)^{n-k}}{(n-k)!}\sqrt{\frac{n!}{k!}}\frac{(iE^*)^{m-k}}{(m-k)!}\sqrt{\frac{m!}{k!}}\,, \end{aligned} \tag{A.19}$$

where $l = \min(n, m)$. Introducing the phase φ of the excitation pulse, via $E = |E|e^{i\varphi}$, Eq. (A.19) becomes

$$U_{nm}(E) = i^{n-m}e^{i\varphi(n-m)}|E|^{n-m}\sqrt{\frac{m!}{n!}}e^{-|E|^2/2}\sum_{k=0}^{m}\frac{(-|E|^2)^{m-k}n!}{(n-k)!(m-k)!k!} \tag{A.20}$$

for $n \geqslant m$, and

$$U_{nm}(E) = i^{m-n}e^{i\varphi(n-m)}|E|^{m-n}\sqrt{\frac{n!}{m!}}e^{-|E|^2/2}\sum_{k=0}^{n}\frac{(-|E|^2)^{n-k}m!}{(n-k)!(m-k)!k!} \tag{A.21}$$

for $n \leqslant m$. Comparing the series in Eqs. (A.20) and (A.21) with the associated Laguerre polynomials [114], given by a series

$$L_p^\alpha(x) = \sum_{j=0}^{p}\frac{(-x)^j(p+\alpha)!}{(p-j)!(\alpha+j)!j!} \tag{A.22}$$

for $p \geqslant 0$, we find that for any values of n and m,

$$U_{nm}(E) = e^{i\varphi(n-m)}C_{nm}(|E|) \tag{A.23}$$

with $C_{nm}(|E|)$ given by Eq. (11) in terms of the Laguerre polynomials:

$$C_{nm}(|E|) = i^\alpha|E|^\alpha\sqrt{\frac{p!}{(p+\alpha)!}}L_p^\alpha(|E|^2)e^{-|E|^2/2}\,, \tag{A.24}$$

where $\alpha = |n - m|$ and $p = \min(n, m)$. Using the property

$$L_m^{n-m}(x) = L_n^{m-n}(x)\frac{n!}{m!}(-x)^{m-n}\,, \tag{A.25}$$

Eq. (A.24) can also be written more explicitly as

$$C_{nm}(|E|) = i^{n-m}|E|^{n-m}\sqrt{\frac{m!}{n!}}L_m^{n-m}(|E|^2)e^{-|E|^2/2}\,, \tag{A.26}$$

for any relation between n and m.

Finally, applying the operators $U(E)$ and $U^\dagger(E)$, respectively, on the left and right sides of the DM, in accordance with Eq. (A.8) or Eq. (A.7), we arrive at Eq. (2.14) of the main text.

B | Analytic Diagonalisation of the Lindblad Operator for the QD-cavity system

The evolution of the QD-cavity system between and after excitation pulses is described by the mater equation

$$i\dot{\rho} = \hat{L}\rho\,. \tag{B.1}$$

The action of the Lindblad operator on the DM can be conveniently expressed as

$$\hat{L}\rho = H\rho - \rho H^* + 2i\gamma_x x\rho x^\dagger + 2i\gamma_c c\rho c^\dagger \tag{B.2}$$

where the Jaynes-Cummings (JC) Hamiltonian and its complex conjugate are, respectively, given by

$$\begin{aligned} H &= \omega_X x^\dagger x + \omega_c c^\dagger c + g(c^\dagger x + x^\dagger c)\,, \\ H^* &= \omega_x^* x^\dagger x + \omega_c^* c^\dagger c + g(c^\dagger x + x^\dagger c)\,. \end{aligned} \tag{B.3}$$

Here, $\omega_x = \Omega_x - i\gamma_x$ and $\omega_c = \Omega_c - i\gamma_c$ are the complex frequencies of the QD exciton and the cavity mode, respectively. Note that Eq. (B.2) is equivalent to Eq. (2).

In the extended basis of Fock states of the QD-cavity system, the full DM is

given by Eq. (8):

$$\rho = \sum_{\nu\nu' nn'} \rho_{nn'}^{\nu\nu'} |\nu, n\rangle\langle\nu', n'| \,, \tag{B.4}$$

where ν and ν' refer to the exciton and n and n' to the cavity indices. Let us consider a group of elements of the DM responsible for the coherence between rungs $N+\Delta N$ and N of the JC ladder, where ΔN is the separation between rungs. These are the elements with

$$\nu + n = N + \Delta N \equiv N_1 \quad \text{and} \quad \nu' + n' = N \tag{B.5}$$

in Eq. (B.4). The corresponding part of the full DM is given by

$$\begin{aligned} \rho(N_1; N) \;=\; & \rho_1^{(N)} |1, N_1 - 1\rangle\langle 1, N - 1| \\ & + \rho_2^{(N)} |1, N_1 - 1\rangle\langle 0, N| \\ & + \rho_3^{(N)} |0, N_1\rangle\langle 1, N - 1| \\ & + \rho_4^{(N)} |0, N_1\rangle\langle 0, N| \,, \end{aligned} \tag{B.6}$$

which reduces for the ground state ($N = 0$ or $N_1 = 0$) to only two elements. Taking $\Delta N > 0$ for definiteness everywhere below, we have in particular

$$\begin{aligned} \rho(\Delta N; 0) \;=\; & \rho_1^{(0)} |1, \Delta N - 1\rangle\langle 0, 0| \\ & + \rho_2^{(0)} |0, \Delta N\rangle\langle 0, 0| \,. \end{aligned} \tag{B.7}$$

Note that we have introduced in Eqs. (B.6) and (B.7) new notations for the elements of the DM, compared to Eq. (B.4). For example, $\rho_1^{(N)} = \rho_{N_1-1,N-1}^{11}$. We further use these new notation, in order to form a vector $\vec{\rho}$ consisting of the elements of the DM

which appear in Eqs. (B.6) and (B.7), for all rungs and a fixed ΔN:

$$\vec{\rho} = \left[\begin{array}{c} \vec{\rho}^{(0)} \\ \hline \vec{\rho}^{(1)} \\ \hline \vec{\rho}^{(2)} \\ \hline \vdots \end{array}\right], \quad \text{where} \quad \vec{\rho}^{(0)} = \begin{bmatrix} \rho_1^{(0)} \\ \rho_2^{(0)} \end{bmatrix}, \quad \vec{\rho}^{(N)} = \begin{bmatrix} \rho_1^{(N)} \\ \rho_2^{(N)} \\ \rho_3^{(N)} \\ \rho_4^{(N)} \end{bmatrix}. \tag{B.8}$$

The master equation (B.1) then takes the following matrix form

$$i\dot{\vec{\rho}} = \hat{L}\vec{\rho}, \tag{B.9}$$

where $\hat{L}$ is now a matrix consisting of the following blocks:

$$\hat{L} = \left[\begin{array}{c|c|c|c} L_{[00]} & M_{[01]} & \mathbb{0} & \dots \\ \hline \mathbb{0} & L_{[11]} & M_{[12]} & \dots \\ \hline \mathbb{0} & \mathbb{0} & L_{[22]} & \dots \\ \hline \vdots & \vdots & \vdots & \ddots \end{array}\right] \tag{B.10}$$

where $\mathbb{0}$ denotes blocks of zero elements. It is convenient at this point to introduce a 2×2 matrix of the N-th rung of the JC Hamiltonian,

$$H_N = \begin{bmatrix} \omega_x + (N-1)\omega_c & \sqrt{N}g \\ \sqrt{N}g & N\omega_c \end{bmatrix}, \tag{B.11}$$

which is the same as in Eq. (13). The diagonal blocks of $\hat{L}$ are produced by the first two terms of the Lindblad operator Eq. (B.2) and are given by

$$L_{[00]} = H_{\Delta N}\,, \tag{B.12}$$

$$L_{[NN]} = G_{N_1} - F_N^* \quad (N_1 = N + \Delta N\,,\ N > 0)\,, \tag{B.13}$$

where

$$G_N = \begin{bmatrix} \omega_x + (N-1)\omega_c & 0 & \sqrt{N}g & 0 \\ 0 & \omega_x + (N-1)\omega_c & 0 & \sqrt{N}g \\ \sqrt{N}g & 0 & N\omega_c & 0 \\ 0 & \sqrt{N}g & 0 & N\omega_c \end{bmatrix} \tag{B.14}$$

consists of the four elements of H_N, contributing twice, one time distributed over the first and third rows and columns of G_N, the other over the second and fourth rows and columns. The other matrix, F_N^*, is the complex conjugate of

$$F_N = \begin{bmatrix} H_N & \mathbb{0} \\ \mathbb{0} & H_N \end{bmatrix}, \tag{B.15}$$

which in turn consists of 2×2 diagonal blocks H_N, given by Eq. (B.11), and 2×2 zero matrices $\mathbb{0}$ occupying its off-diagonal blocks. The off-diagonal blocks of $\hat{L}$ are due to the last two terms of the Lindblad operator Eq. (B.2) and take the following form:

$$\begin{aligned} L_{[01]} &= \begin{bmatrix} 0 & 2i\gamma_c\sqrt{\Delta N} & 0 & 0 \\ 2i\gamma_x & 0 & 0 & 2i\gamma_c\sqrt{\Delta N + 1} \end{bmatrix}, \\ L_{[N,N+1]} &= \begin{bmatrix} 2i\gamma_c\sqrt{N_1 N} & 0 & 0 & 0 \\ 0 & 2i\gamma_c\sqrt{N_1(N+1)} & 0 & 0 \\ 0 & 0 & 2i\gamma_c\sqrt{(N_1+1)N} & 0 \\ 2i\gamma_x & 0 & 0 & 2i\gamma_c\sqrt{(N_1+1)(N+1)} \end{bmatrix}, \end{aligned} \tag{B.16}$$

where again $N_1 = N + \Delta N$.

An analytic diagonalisation of the matrix $\hat{L}$ presented below is based on the eigenvalues and eigenvectors of the Hamiltonian matrix H_N of the N-th rung of the JC ladder, which is given by Eq. (B.11). This 2×2 matrix, playing the role of a

building block for the diagonalisation of $\hat{L}$, diagonalizes itself as follows:

$$H_N Y_N = Y_N \Lambda_N \,, \tag{B.17}$$

where the transformation matrix Y_N and the eigenvalue matrix Λ_N are given by

$$Y_N = \begin{bmatrix} \alpha_N & \beta_N \\ -\beta_N & \alpha_N \end{bmatrix} \quad \text{and} \quad \Lambda_N = \begin{bmatrix} \lambda_N^- & 0 \\ 0 & \lambda_N^+ \end{bmatrix}, \tag{B.18}$$

respectively, with

$$\lambda_N^\pm = N\omega_c + \delta/2 \pm \Delta_N \,, \tag{B.19}$$

$$\alpha_N = \frac{\Delta_N - \delta/2}{\gamma_N^-} = \frac{\sqrt{N}g}{\gamma_N^+} \,, \qquad \beta_N = \frac{\sqrt{N}g}{\gamma_N^-} = \frac{\Delta_N + \delta/2}{\gamma_N^+} \,, \tag{B.20}$$

$$\Delta_N = \sqrt{(\delta/2)^2 + Ng^2} \,, \qquad \gamma_N^\pm = \sqrt{(\Delta_N \pm \delta/2)^2 + Ng^2} \,, \tag{B.21}$$

$$\delta = \omega_x - \omega_c \,. \tag{B.22}$$

Here δ is the complex frequency detuning, and constants $\gamma_N^\pm$ are normalizing the eigenvectors of H_N in such a way that

$$\alpha_N^2 + \beta_N^2 = 1 \,. \tag{B.23}$$

Note that Δ_N and $\gamma_N^\pm$ are also complex-valued and expressed by Eq. (B.21) in terms of square roots, each having two values, or two branches. The choice of the sign (i.e. the square root branch) can be arbitrary in each case. However, this choice has to be used consistently in all the equations containing Δ_N and $\gamma_N^\pm$, with the sign of Δ_N being independent from those of $\gamma_N^\pm$, while the signs of γ_N^+ and γ_N^- are linked together (however, only one of these two constants, either γ_N^+ or γ_N^-, is required in calculations). Owing to the normalisation Eq. (B.23), the transformation matrix Y_N

is orthogonal, i.e.

$$Y_N^{-1} = Y_N^{\mathrm{T}}\,, \tag{B.24}$$

where Y_N^{T} is the transpose of Y_N, so that Eq. (B.17) can also be written as $Y_N^{\mathrm{T}} H_N Y_N = \Lambda_N$.

The diagonal block $L_{[00]}$ of the Lindblad matrix $\hat{L}$, which is given by Eq. (B.12), is identical to $H_{\Delta N}$ and is thus diagonalized by $Y_{\Delta N}$:

$$Y_{\Delta N}^{\mathrm{T}} L_0 Y_{\Delta N} = \Omega_0 = \begin{bmatrix} \lambda_{\Delta N}^{-} & 0 \\ 0 & \lambda_{\Delta N}^{+} \end{bmatrix}. \tag{B.25}$$

To diagonalize any other diagonal block L_N with $N > 0$, which is given by Eq. (B.13), we introduce two 4×4 matrices

$$A_N = \begin{bmatrix} \alpha_N & 0 & \beta_N & 0 \\ 0 & \alpha_N & 0 & \beta_N \\ -\beta_N & 0 & \alpha_N & 0 \\ 0 & -\beta_N & 0 & \alpha_N \end{bmatrix}, \quad B_N = \begin{bmatrix} \alpha_N & \beta_N & 0 & 0 \\ -\beta_N & \alpha_N & 0 & 0 \\ 0 & 0 & \alpha_N & \beta_N \\ 0 & 0 & -\beta_N & \alpha_N \end{bmatrix}. \tag{B.26}$$

Clearly, matrix B_N is block-diagonal, consisting of two identical blocks of Y_N. Matrix A_N can be obtained from B_N by simultaneous swapping the 2nd and 3rd rows and columns. Note that exactly the same link exists between matrices G_N and F_N contributing to L_N and consisting of zero elements and the elements of H_N, see Eqs. (B.14) and (B.15). Consequently, matrices A_N and B_N are orthogonal, i.e. $A_N^{-1} = A_N^{\mathrm{T}}$ and $B_N^{-1} = B_N^{\mathrm{T}}$, and diagonalise matrices G_N and F_N, respectively. At the same time, owing to the structure of these matrices, the following commutation relations hold:

$$[A_{N_1}, B_N^*] = [A_{N_1}, F_N^*] = [G_{N_1}, B_N^*] = 0\,. \tag{B.27}$$

Owing to the above properties, matrix

$$S_N = A_{N_1} B_N^* \tag{B.28}$$

is also orthogonal, $S_N^{-1} = S_N^{\mathrm{T}}$, and diagonalizes $L_{[NN]}$, a diagonal block of the Lindblad matrix $\hat{L}$:

$$S_N^{\mathrm{T}} L_{[NN]} S_N = \Omega_N \,. \tag{B.29}$$

In fact, matrix B_N^* diagonalized F_N^* while keeping G_{N_1} untouched, due to Eq. (B.27). Similarly, A_n diagonalizes G_{N_1} while keeping F_N^* untouched. The diagonal matrix Ω_N of the eigenvalues of $L_{[NN]}$ then takes the form:

$$\Omega_N = \begin{bmatrix} \lambda_{N_1}^- - \lambda_N^{-*} & 0 & 0 & 0 \\ 0 & \lambda_{N_1}^- - \lambda_N^{+*} & 0 & 0 \\ 0 & 0 & \lambda_{N_1}^+ - \lambda_N^{-*} & 0 \\ 0 & 0 & 0 & \lambda_{N_1}^+ - \lambda_N^{+*} \end{bmatrix}, \tag{B.30}$$

where $\lambda_N^{\pm}$ are given by Eq. (B.19). The eigenvalues Ω_N are considered in more detail in Sec. C, where special cases of large and zero detuning, and of large rung number N are also analyzed.

Let us now diagonalise the full matrix $\hat{L}$, finding matrices $\hat{U}$ and $\hat{V}$ of right and left eigenvectors, respectively:

$$\hat{L}\hat{U} = \hat{U}\hat{\Omega}\,, \qquad \hat{V}\hat{L} = \hat{\Omega}\hat{V}\,. \tag{B.31}$$

Due to the block form of $\hat{L}$, the diagonal matrix $\hat{\Omega}$ consists of the eigenvalue matrices

Ω_N found above, and $\hat{U}$ and $\hat{V}$ are block-triangular matrices:

$$\hat{\Omega} = \left[\begin{array}{c|c|c|c} \Omega_0 & \mathbb{0} & \mathbb{0} & \dots \\ \hline \mathbb{0} & \Omega_1 & \mathbb{0} & \dots \\ \hline \mathbb{0} & \mathbb{0} & \Omega_2 & \dots \\ \hline \vdots & \vdots & \vdots & \ddots \end{array}\right], \hat{U} = \left[\begin{array}{c|c|c|c} U_{[00]} & U_{[01]} & U_{[02]} & \dots \\ \hline \mathbb{0} & U_{[11]} & U_{[12]} & \dots \\ \hline \mathbb{0} & \mathbb{0} & U_{[22]} & \dots \\ \hline \vdots & \vdots & \vdots & \ddots \end{array}\right], \hat{V} = \left[\begin{array}{c|c|c|c} V_{[00]} & V_{[01]} & V_{[02]} & \dots \\ \hline \mathbb{0} & V_{[11]} & V_{[12]} & \dots \\ \hline \mathbb{0} & \mathbb{0} & V_{[22]} & \dots \\ \hline \vdots & \vdots & \vdots & \ddots \end{array}\right]. \tag{B.32}$$

Here, Ω_0, $U_{[00]}$ and $V_{[00]}$ are 2×2 blocks, $U_{[0N]}$ and $V_{[0N]}$ with $N > 0$ are 2×4 blocks, and $U_{[NK]}$ and $V_{[NK]}$ with both N, $K > 0$ are 4×4 matrices. Substituting $\hat{U}$ and $\hat{V}$ into the eigenvalue equations (B.31), we find series of recursive relations for all blocks $U_{[NK]}$ and $V_{[NK]}$ and explicit analytic expressions for their elements.

Let us first consider the right eigenvectors $\hat{U}$. Substituting $\hat{\Omega}$ and $\hat{U}$ from Eq. (B.32) and $\hat{L}$ from Eq. (B.10) into the first eigenvalue equation (B.31), we obtain for any fixed N, a matrix equation

$$L_{[NN]}U_{[NN]} = U_{[NN]}\Omega_N\,, \tag{B.33}$$

from what follows that $U_{[NN]} = S_N$, having an explicit form given by Eqs. (B.26) and (B.28). For any $0 \leqslant K < N$, we then find a matrix equation linking $U_{[K,N]}$ to $U_{[K+1,N]}$:

$$L_{[KK]}U_{[KN]} + L_{[K,K+1]}U_{[K+1,N]} = U_{[KN]}\Omega_N\,. \tag{B.34}$$

Multiplying this equation from the left with S_K^{T}, and using the fact that $S_K^{\mathrm{T}}L_K = \Omega_K S_K^{\mathrm{T}}$, we obtain

$$\Omega_K\tilde{U}_{[KN]} + \tilde{L}_{[K,K+1]}\tilde{U}_{[K+1,N]} = \tilde{U}_{[KN]}\Omega_N\,, \tag{B.35}$$

where

$$\tilde{U}_{[KN]} = S_K^{\mathrm{T}}U_{[KN]}\,, \quad \tilde{L}_{[K,K+1]} = S_K^{\mathrm{T}}L_{[K,K+1]}S_{K+1}\,. \tag{B.36}$$

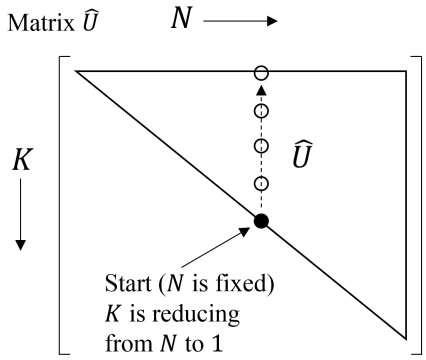

Figure B.1: Scheme illustrating the algorithm of the analytic calculation of matrix $\hat{U}$ of right eigenvectors. The diagonal blocks of $\hat{U}$ are found by iterating over N which changes from 0 to ∞. Nonzero off-diagonal blocks are found by fixing N and iterating over K which changes from the diagonal value $K = N$ to $K = 0$.

As Ω_K is a diagonal matrix, Eq. (B.35) results in the following explicit form of the matrix elements of $\tilde{U}_{[KN]}$:

$$(\tilde{U}_{[KN]})_{ij} = \frac{(\tilde{L}_{[K,K+1]}\tilde{U}_{[K+1,N]})_{ij}}{(\Omega_N)_{jj} - (\Omega_K)_{ii}} \,. \tag{B.37}$$

For each N, we use $\tilde{U}_{[NN]} = S_N^{\mathrm{T}} U_{[NN]} = S_N^{\mathrm{T}} S_N = \mathbb{1}$ (here $\mathbb{1}$ is the identity matrix) as a start point and calculate all $\tilde{U}_{[KN]}$ from the Eq. (B.37) sequentially, for $K = N-1, N-2, ..., 0$. Note that the index i (j), labelling the matrix elements, takes the values of 1 or 2 for $K = 0$ ($N = 0$) and $1, 2, 3$ or 4 for $K > 0$ ($N > 0$), due to the sizes of the corresponding blocks.

Finally the blocks of the right eigenvector matrix $\hat{U}$ are found from the matrix multiplication

$$U_{[KN]} = S_K \tilde{U}_{[KN]} \,, \tag{B.38}$$

which is the inverse transformation, compared to Eq. (B.36). Figure B.1 illustrates the above algorithm.

The procedure of finding the left eigenvector matrix $\hat{V}$ is very similar. We first

obtain matrix equations for the diagonal blocks of $\hat{V}$:

$$V_{[NN]}L_N = \Omega_N V_{[NN]}\,, \tag{B.39}$$

concluding that $V_{[NN]} = S_N^{\mathrm{T}}$. Then for any $K > N$, we have

$$V_{[NK]}L_K + V_{[N,K-1]}L_{[K-1,K]} = \Omega_N V_{[NK]}\,. \tag{B.40}$$

Multiplying this equation with matrix S_K from the right, and using the fact that $L_{[KK]}S_K = S_K\Omega_K$, we find

$$\tilde{V}_{[NK]}\Omega_K + \tilde{V}_{[N,K-1]}\tilde{L}_{[K-1,K]} = \Omega_N \tilde{V}_{[NK]}\,, \tag{B.41}$$

where

$$\tilde{V}_{[NK]} = V_{[NK]}S_K\,, \tag{B.42}$$

and $\tilde{L}_{[K-1,K]}$ is defined in Eq. (B.36). This again allows us to obtain an explicit form of the matrix elements:

$$(\tilde{V}_{[NK]})_{ij} = \frac{(\tilde{V}_{[N,K-1]}\tilde{L}_{[K-1,K]})_{ij}}{(\Omega_N)_{ii} - (\Omega_K)_{jj}}\,. \tag{B.43}$$

For a given fixed N, one can generate sequentially, starting from $\tilde{V}_{[NN]} = \mathbb{1}$ and using Eq. (B.43), all the matrices $\tilde{V}_{[NK]}$ for $K = N+1, N+2, \ldots$. Matrices $V_{[NK]}$ can then be found, using the inverse transformation, as

$$V_{[NK]} = \tilde{V}_{[NK]}S_K^{\mathrm{T}}\,. \tag{B.44}$$

This algorithm of reconstructing the full matrix $\hat{V}$ is illustrated by Figure B.2.

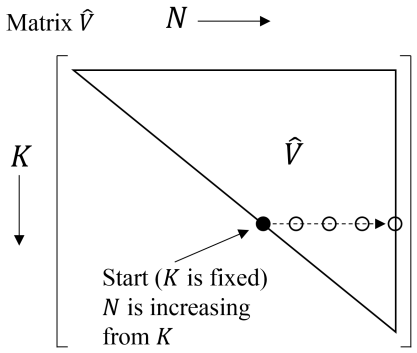

Figure B.2: As Fig. B.1 but for matrix $\hat{V}$ of left eigenvectors.

Note that the left and right eigenvectors are orthogonal:

$$\hat{V}\hat{U} = \hat{U}\hat{V} = \hat{\mathbb{1}} \tag{B.45}$$

which results in particular in the following relations ($N' \geqslant N$):

$$\sum_{K=N}^{N'} V_{[NK]}U_{[KN']} = \sum_{K=N}^{N'} U_{[NK]}V_{[KN']} = \mathbb{1}\delta_{NN'}\,, \tag{B.46}$$

where $\mathbb{1}$ is the identity matrix and $\delta_{[NN']}$ is the Kronecker delta. Equation (B.46) can also be written as

$$\sum_{K=N}^{N'} \tilde{V}_{[NK]}\tilde{U}_{[KN']} = \sum_{K=N}^{N'} \tilde{U}_{[NK]}\tilde{V}_{[KN']} = \mathbb{1}\delta_{NN'}\,. \tag{B.47}$$

Let us finally illustrate the analytic diagonalisation presented above on a 6×6 Lindblad matrix corresponding to the lowest order of the standard FWM polarisation treated in [8]:

$$\hat{L} = \left[\begin{array}{c|c} L_{[00]} & L_{[01]} \\ \hline \mathbb{0} & L_{[11]} \end{array}\right], \quad \hat{U} = \left[\begin{array}{c|c} S_0 & U_{[01]} \\ \hline \mathbb{0} & S_1 \end{array}\right], \quad \hat{V} = \left[\begin{array}{c|c} S_0^{\mathrm{T}} & V_{[01]} \\ \hline \mathbb{0} & S_1^{\mathrm{T}} \end{array}\right]. \tag{B.48}$$

We find $U_{[01]} = S_0 \tilde{U}_{[01]}$ and $V_{[01]} = \tilde{V}_{[01]} S_2^{\mathrm{T}}$, where

$$(\tilde{U}_{[01]})_{ij} = \frac{(\tilde{L}_{[01]})_{ij}}{(\Omega_1)_{jj} - (\Omega_0)_{ii}}\,, \tag{B.49}$$

$$(\tilde{V}_{[01]})_{ij} = \frac{(\tilde{L}_{[01]})_{ij}}{(\Omega_0)_{ii} - (\Omega_1)_{jj}} = -(\tilde{U}_{[01]})_{ij}\,, \tag{B.50}$$

and $\tilde{L}_{[01]} = S_0^{\mathrm{T}} L_{[01]} S_1$. The orthogonality of $\hat{V}$ and $\hat{U}$ then takes the form:

$$\hat{U}\hat{V} = \left[\begin{array}{c|c} S_0 & U_{[01]} \\ \hline \mathbb{0} & S_1 \end{array}\right] \left[\begin{array}{c|c} S_0^{\mathrm{T}} & V_{[01]} \\ \hline \mathbb{0} & S_1^{\mathrm{T}} \end{array}\right] = \left[\begin{array}{c|c} S_0 S_0^{\mathrm{T}} & S_0 V_{[01]} + U_{01} S_1^{\mathrm{T}} \\ \hline \mathbb{0} & S_1 S_1^{\mathrm{T}} \end{array}\right] = \hat{\mathbb{1}}\,, \tag{B.51}$$

since

$$S_0 V_{[01]} + U_{[01]} S_1^{\mathrm{T}} = S_0 \tilde{V}_{[01]} S_1^{\mathrm{T}} + S_0 \tilde{U}_{[01]} S_1^{\mathrm{T}} = S_0 (\tilde{V}_{[01]} + \tilde{U}_{[01]}) S_1^{\mathrm{T}} = \mathbb{0}\,, \tag{B.52}$$

due to Eq. (B.50) .

C | Transition frequencies of the 2-level QDMC system

By fixing the distance ΔN between rungs of the JC ladder, contributing to the left and right parts of the DM, we isolate a specific component of the coherent dynamics of the QD-cavity system corresponding to a selected phase combination of the optical pulses exciting the system. The time dependence of this polarisation is given by Eq. (16) which contains the transition frequencies ω_r between rungs. These frequencies are the eigenvalues of the reduced Lindblad matrix $\hat{L}$, isolated from the full Lindblad operator by fixing the ΔN. The eigenvalues are given by the diagonal matrix $\hat{\Omega}$, Eq. (B.32), which consists of blocks Ω_N described by Eqs. (B.25) and (B.30). For $N > 0$, these diagonal blocks can be written as

$$\Omega_N = (\bar{\Omega} - i\gamma_N)\mathbb{1} + \begin{bmatrix} -\Delta_N^i & 0 & 0 & 0 \\ 0 & -\Delta_N^o & 0 & 0 \\ 0 & 0 & \Delta_N^o & 0 \\ 0 & 0 & 0 & \Delta_N^i \end{bmatrix}, \tag{C.1}$$

where

$$\Delta_N^{o,i} = \sqrt{(\delta/2)^2 + (N + \Delta N)g^2} \pm \sqrt{(\delta^*/2)^2 + Ng^2}\,. \tag{C.2}$$

The complex frequencies of all four transition, which occur between the two pairs of quantum levels of rungs N and $N + \Delta N$, have the same dominant contribution

described by the first term of Eq. (C.1). It consists of the average frequency distance between the rungs,

$$\bar{\Omega} = \Delta N \Omega_c \,, \tag{C.3}$$

which is obviously the same for all pairs of rungs separated by ΔN, and the average damping,

$$\gamma_N = (2N + \Delta N - 1)\gamma_c + \gamma_x \,, \tag{C.4}$$

showing a linear increase with N, as the dampings of both rungs participating in the coherent dynamics add up.

The second term in Eq. (C.1) describes a fine structure of the transitions, given by the splittings $\Delta_N^{o,i}$, which depend on the detuning $\delta = \omega_x - \omega_c$, the coupling constant g, and the rung number N. Below we analyze this fine structure in more detail, providing simple asymptotic expressions for special cases of (i) large and (ii) small or zero detuning, in the latter case paying attention to the limit of large N.

(i) Large detuning: $|\delta/2| \gg \sqrt{N_1}g$, $\sqrt{N}g$ (where $N_1 = N + \Delta N$). From Eq. (C.2) we find

$$\Delta_N^{o,i} \approx \frac{\delta \pm \delta^*}{2} + g^2 \left(\frac{N_1}{\delta} \pm \frac{N}{\delta^*} \right) , \tag{C.5}$$

so that

$$\Delta_N^o \approx \Delta\Omega + g^2 \frac{(2N + \Delta N)\Delta\Omega + i\Delta N \Delta\gamma}{(\Delta\Omega)^2 + (\Delta\gamma)^2} \,, \tag{C.6}$$

$$\Delta_N^i \approx -i\Delta\gamma + g^2 \frac{\Delta N \Delta\Omega + i(2N + \Delta N)\Delta\gamma}{(\Delta\Omega)^2 + (\Delta\gamma)^2} \,, \tag{C.7}$$

where the complex detuning $\delta = \Delta\Omega - i\Delta\gamma$ is split into the real and imaginary parts, given by $\Delta\Omega = \Omega_x - \Omega_c$ and $\Delta\gamma = \gamma_x - \gamma_c$, respectively. Furthermore, for $|\Delta\Omega| \gg |\Delta\gamma|$, the above equations simplify to

$$\Delta_N^o \approx \Delta\Omega + g^2 \frac{2N + \Delta N}{|\delta|} \quad \text{and} \quad \Delta_N^i \approx -i\Delta\gamma + g^2 \frac{\Delta N}{|\delta|} \,, \tag{C.8}$$

giving approximate frequencies $\pm\Delta_N^o$ and $\pm\Delta_N^i$ of, respectively, "outer" and "inner" transition doublets, to be considered on top of the same for all four transitions lead frequency and damping described by Eqs. (C.3) and (C.4), respectively. We see that the splitting between the outer transitions is dominated by $2\Delta\Omega$, with a smaller correction on top of it, which is proportional to g^2 and is growing linearly with N. At the same time, the inner transitions have a small splitting $2g^2\Delta N/|\delta|$, which is independent of N. The damping of the outer transitions is the same and is given by γ_N. For the inner doublet, the dampings are different: $\gamma_N \pm \Delta\gamma$, making the lower-frequency inner transition broader than the upper one, if $\gamma_x < \gamma_c$ ($\Delta\gamma < 0$).

(ii) Small detuning: $\delta/2 \ll \sqrt{N_1}g$, $\sqrt{N}g$. In this case, we find from Eq. (C.2):

$$\Delta_N^{o,i} \approx \left(\sqrt{N_1} \pm \sqrt{N}\right) g + \frac{\delta^2}{8N_1 g^2} \pm \frac{\delta^{*2}}{8Ng^2}\,. \tag{C.9}$$

Assuming $N \gg \Delta N$, this result further simplifies to

$$\Delta_N^o \approx \left(\sqrt{N_1} + \sqrt{N}\right) g \approx 2\sqrt{N}g + \frac{\Delta N}{2N} g\,, \tag{C.10}$$

$$\Delta_N^i \approx \frac{\Delta N}{2\sqrt{N}} g - i\frac{\Delta\Omega\Delta\gamma}{2\sqrt{N}g^2}\,. \tag{C.11}$$

Finally, for zero detuning, $\Omega_x = \Omega_c$, we obtain, to the lead order,

$$\Delta_N^o \approx 2\sqrt{N}g \quad \text{and} \quad \Delta_N^i \approx \frac{\Delta N}{2\sqrt{N}} g\,, \tag{C.12}$$

from where we find also the change of the transition frequencies with rung number N:

$$\Delta_{N+1}^o - \Delta_N^o \approx \frac{g}{\sqrt{N}} \quad \text{and} \quad \Delta_{N+1}^i - \Delta_N^i \approx -\frac{\Delta N g}{4N\sqrt{N}}\,, \tag{C.13}$$

respectively, for the outer and inner doublets.

D | Degenerate $\mathcal{N}$-wave mixing in the low-damping limit

In this section, we consider all possible phase channels in the optical polarisation when the system is excited by two laser pulses of arbitrary strength. We focus on the situation when both pulses arrive simultaneously (i.e. the time delay is zero) and call the optical response on this excitation *degenerate* $\mathcal{N}$-wave mixing ($\mathcal{N}$WM) polarisation, where $\mathcal{N}$ determines the detected phase channel. We first treat rigorously the change of the DM due to the pulsed excitation, concentrating on two important special cases when the pulse area of one of the two pulses is sufficiently small and can thus be accounted for in the lowest order while the pulse area of the other pulse can be arbitrarily large. Then we consider the coherent dynamics after the pulses in the limit of small exciton and cavity dampings, so that the off-diagonal blocks of the Lindblad matrix can be neglected. Finally, we treat analytically the limit of a large average number of photons n_{ph} excited in the cavity, $n_{\mathrm{ph}} \gg 1$, corresponding to a large pulse area of one of the pulses, which allows us to develop a closed-form solution for the $\mathcal{N}$WM polarisation both in time and frequency domain.

D.1 Two-pulse excitation

The so-called $\mathcal{N}$WM mentioned above describes a mixing $\mathcal{N}$ effective or real waves which produce an optical response of the systems with a phase

$$\Phi = \Delta N_1 \varphi_1 + \Delta N_2 \varphi_2 \,, \tag{D.1}$$

where $\varphi_j = \arg(E_j)$ and

$$|\Delta N_1| + |\Delta N_2| + 1 = \mathcal{N} \,. \tag{D.2}$$

For example, the standard FWM corresponds to $\Delta N_1 = -1$ and $\Delta N_2 = 2$; therefore $\mathcal{N} = 4$ and $\Phi = 2\varphi_2 - \varphi_1$.

Starting from the DM of a fully relaxed system before the excitation,

$$\rho(0_-) = |0\rangle\langle 0| \,, \tag{D.3}$$

where $|0\rangle$ is the absolute ground state and 0_- is a negative infinitesimal, we consider below the effect on the DM of the two pulses both arriving at $t = 0$ and having pulse areas E_1 and E_2, focusing on the two special cases, as mentioned above.

Case 1: E_1 is small, E_2 is arbitrary.

While we are assuming that the pulses arrive simultaneously at $t = 0$, it is convenient to consider first the effect of the smaller pulse. Using the general Eq. (10) with the QD exciton indices dropped for brevity and the unexcited DM in the form of Eq. (D.3), the DM straight after the first pulse takes the form:

$$\rho_{kk'}(0) = \left[\hat{X}(E_1)\rho(0_-)\right]_{kk'} = e^{i\varphi_1(k-k')} C_{k0} C^*_{k'0} \,. \tag{D.4}$$

From Eq. (D.1) it follows that $k-k' = \Delta N_1$. Then, concentrating on the lowest-order response, we find the following two options for k and k':

$$\begin{aligned} &(i) \quad k = \Delta N_1 \quad \text{and} \quad k' = 0 \qquad\quad \text{for} \quad \Delta N_1 \geqslant 0\,, \\ &(ii) \quad k = 0 \qquad\quad \text{and} \quad k' = -\Delta N_1 \quad \text{for} \quad \Delta N_1 \leqslant 0\,. \end{aligned} \tag{D.5}$$

Since the pulse area E_2 of the second pulse can be arbitrarily large, we take into account its effect rigorously in all orders, which results in the following DM after the pulses:

$$\rho_{nn'}(0_+) = \Big[\hat{X}(E_2)\rho(0)\Big]_{nn'} = e^{i\varphi_2(n-n'-\Delta N_1)} C_{nk} C^*_{n'k'} \rho_{kk'}(0) = e^{i\Phi} C_{nk} C^*_{n'k'} C_{k0} C^*_{k'0}\,, \tag{D.6}$$

according to Eq. (10). From Eq. (D.1) we find

$$n - n' = \Delta N_1 + \Delta N_2 = \Delta N\,, \tag{D.7}$$

and then from Eq. (11) obtain

$$\rho_{n+\Delta N,n}(0_+) = e^{i\Phi} i^{\Delta N} |E_1|^{|\Delta N_1|} |E_2|^{|\Delta N_2|} R_n\,, \tag{D.8}$$

where

$$R_n = \frac{\lambda^n e^{-\lambda}}{\sqrt{n!(n+\Delta N)!}} \tilde{R}_n \tag{D.9}$$

with $\lambda = |E_1|$ and

$$\tilde{R}_n = \begin{cases} \lambda^m L^{n+\Delta N_2}_{\Delta N_1}(\lambda) & \text{for} \quad \Delta N_1 \geqslant 0\,, \\ \lambda^{m+\Delta N_1} L^{n+\Delta N_2}_{-\Delta N_1}(\lambda) & \text{for} \quad \Delta N_1 \leqslant 0\,. \end{cases} \tag{D.10}$$

Here $L_p^k(x)$ are the Laguerre polynomials, and

$$m = \begin{cases} 0 & \text{for} \quad \Delta N_2 \geqslant 0\,, \\ \\ \Delta N_2 & \text{for} \quad \Delta N_2 \leqslant 0\,. \end{cases} \tag{D.11}$$

For $\mathcal{N}$WM, we have in particular $\Delta N_1 = 1 - \mathcal{N}/2$ and $\Delta N_2 = \mathcal{N}/2$, so that $\Delta N = 1$, in accordance with Eq. (D.2), and Eqs. (D.8)–(D.11) reduce to

$$\rho_{n+1,n}(0_+) = e^{i\Phi} i |E_1|^{|\Delta N_1|} |E_2|^{|\Delta N_2|} R_n\,, \tag{D.12}$$

where

$$R_n = \frac{\lambda^n e^{-\lambda}}{n!\sqrt{n+1}} \tilde{R}_n \tag{D.13}$$

and

$$\tilde{R}_n = \lambda^{1-\mathcal{N}/2} L_{\mathcal{N}/2-1}^{n+1-\mathcal{N}/2}(\lambda)\,. \tag{D.14}$$

The last equation becomes simply

$$\tilde{R}_n = \frac{1}{\lambda} L_1^{n-1}(\lambda) \tag{D.15}$$

for the standard FWM, in which case $\mathcal{N} = 4$, $\Delta N_1 = -1$, and $\Delta N_2 = 2$.

Case 2: E_2 is small, E_1 is arbitrary.

To address this case we use the fact that for simultaneous pulses, the pulse operators $\hat{X}(E_1)$ and $\hat{X}(E_2)$ commute:

$$\hat{X}(E_1)\hat{X}(E_2)\rho = \hat{X}(E_2)\hat{X}(E_1)\rho\,. \tag{D.16}$$

This is easy to see from the definition of $\hat{X}(E)$, Eq. (7), and the fact that the commutator $[E_1 c^\dagger + E_1^* c, E_2 c^\dagger + E_2^* c] = E_1^* E_2 - E_1 E_2^*$ is a constant. Therefore, the result obtained for the *Case 1*, given by Eqs. (D.8)–(D.11), can be used for *Case 2* by swapping $E_1 \leftrightarrow E_2$ and $\Delta N_1 \leftrightarrow \Delta N_2$. Then the DM after the pulses is described by the same Eqs. (D.8) and (D.9) with $\lambda = |E_1|^2$ and $\tilde{R}_n$ now given by

$$\tilde{R}_n = \begin{cases} \lambda^m L_{\Delta N_2}^{n+\Delta N_1}(\lambda) & \text{for} \quad \Delta N_2 \geqslant 0\,, \\ \lambda^{m+\Delta N_2} L_{-\Delta N_2}^{n+\Delta N_1}(\lambda) & \text{for} \quad \Delta N_2 \leqslant 0\,, \end{cases} \tag{D.17}$$

where

$$m = \begin{cases} 0 & \text{for} \quad \Delta N_1 \geqslant 0\,, \\ \Delta N_1 & \text{for} \quad \Delta N_1 \leqslant 0\,. \end{cases} \tag{D.18}$$

Again, for $\mathcal{N}$WM, Eqs. (D.12) and (D.13) remain the same as in *Case 1*, while Eqs. (D.17) and (D.18) simplify to

$$\tilde{R}_n = \lambda^{1-\mathcal{N}/2} L_{\mathcal{N}/2}^{n+1-\mathcal{N}/2}(\lambda)\,, \tag{D.19}$$

which reduces to

$$\tilde{R}_n = \frac{1}{\lambda} L_2^{n-1}(\lambda) \tag{D.20}$$

for the standard FWM with $\Delta N_1 = -1$ and $\Delta N_2 = 2$.

Note that in the $\mathcal{N}$WM, the difference between the two *Cases* is only in the lower index of the Laguerre polynomials; compare Eqs. (D.14) and (D.19) and similarly Eqs. (D.15) and (D.20).

D.2 Coherent dynamics after the pulses

Now, omitting the factor

$$e^{i\Phi} i^{\Delta N} |E_1|^{|\Delta N_1|} |E_2|^{|\Delta N_2|} \tag{D.21}$$

in Eq. (D.8), which is common for all elements of the DM, we present the initial DM straight after the pulses in the vector form:

$$\vec{\rho}^{(0)}(0_+) = \begin{bmatrix} 0 \\ \\ R_0 \end{bmatrix}, \quad \vec{\rho}^{(n)}(0_+) = \begin{bmatrix} 0 \\ 0 \\ 0 \\ R_n \end{bmatrix}, \tag{D.22}$$

where now the exciton components are restored; for definition of the basis, see Eqs. (B.6)–(B.8) in Appendix. B.

In the limit of small damping of both the QD exciton and the cavity mode, $\gamma_x, \gamma_c \ll g$, one can neglect the off-diagonal blocks $M_{n,n+1}$ of the Lindblad matrix $\hat{L}$, see Eq. (B.16). The remaining diagonal blocks of $\hat{L}$ are diagonalized according to Eq. (B.29)

$$L_n = S_n \Omega_n S_n^{\mathrm{T}}, \tag{D.23}$$

where matrices S_n and Ω_n are given, respectively, by Eqs. (B.28) and (B.30). The time evolution is then described as

$$\vec{\rho}^{(n)}(t) = e^{-iL_n t}\vec{\rho}^{(n)}(0_+) = S_n e^{-i\Omega_n t} S_n^{\mathrm{T}} \vec{\rho}^{(n)}(0_+)\,. \tag{D.24}$$

Using the general form Eq. (8) of the optical polarisation, we find

$$P(t) = \sum_{n=0}^{\infty} \vec{c}^{(n)} \cdot \vec{\rho}^{(n)}(t) \tag{D.25}$$

where $\vec{c}^{(n)}$ is the vector representation of the photon annihilation operator c:

$$\vec{c}^{(0)} = \begin{bmatrix} 0 \\ 1 \end{bmatrix}, \quad \vec{c}^{(n)} = \begin{bmatrix} \sqrt{n} \\ 0 \\ 0 \\ \sqrt{n+1} \end{bmatrix}, \tag{D.26}$$

in accordance with the basis defined in Eqs. (B.6) and (B.7). Now, using the explicit form of the matrices S_n and Ω_n provided in Eqs. (B.26) and (B.28), and Eqs. (C.1) and (C.2), respectively, we find

$$P(t) = e^{-i\bar{\Omega}t} + \sum_{\sigma=i,o} \sum_{s=\pm} P_{\sigma s}(t)\,, \tag{D.27}$$

where

$$P_{\sigma s}(t) = \sum_{n=0}^{\infty} R_n C_n^{\sigma s} e^{-i(s\Delta_n^{\sigma} - i\gamma_n)t}\,. \tag{D.28}$$

The frequencies Δ_n^i and Δ_n^o of, respectively, the inner and outer transitions are given by Eq. (C.2), and the damping γ_n by Eq. (C.4). Using the matrices A_{n+1} and B_n^*, Eq. (B.26), forming the transformation matrix S_n, we find the coefficients $C_n^{\sigma s}$ for an arbitrary detuning δ:

$$\begin{aligned}
C_n^{i+} &= \alpha_n^* \alpha_{n+1} \left(\alpha_n^* \alpha_{n+1} \sqrt{n+1} + \beta_n^* \beta_{n+1} \sqrt{n} \right), \\
C_n^{i-} &= \beta_n^* \beta_{n+1} \left(\beta_n^* \beta_{n+1} \sqrt{n+1} + \alpha_n^* \alpha_{n+1} \sqrt{n} \right), \\
C_n^{o+} &= \beta_n^* \alpha_{n+1} \left(\beta_n^* \alpha_{n+1} \sqrt{n+1} - \alpha_n^* \beta_{n+1} \sqrt{n} \right), \\
C_n^{o-} &= \alpha_n^* \beta_{n+1} \left(\alpha_n^* \beta_{n+1} \sqrt{n+1} - \beta_n^* \alpha_{n+1} \sqrt{n} \right).
\end{aligned} \tag{D.29}$$

For a detuning much smaller than the energy splitting of the n-th rung, $\delta \ll \sqrt{n} g$, which is relevant to the case of large excitation pulse area treated below, they take

an approximate form:

$$\begin{aligned} C_n^{i\pm} &= \frac{1}{4}\left(\sqrt{n+1}+\sqrt{n}\right), \\ C_n^{o\pm} &= \frac{1}{4}\left(\sqrt{n+1}-\sqrt{n}\right) \end{aligned} \tag{D.30}$$

for $n \geqslant 1$, and $C_0^{i+} = C_0^{o-} = 1/2$ and $C_0^{o+} = C_0^{i-} = 0$, using $\alpha_n \approx \beta_n \approx 1/\sqrt{2}$ for $n \geqslant 1$, and $\alpha_0 = 1$ and $\beta_0 = 0$. For zero detuning, $\delta = 0$, Eq. (D.30) is exact. Also note that, strictly speaking, it should be $C_n^{\sigma-} = (C_n^{\sigma+})^*$, which is fulfilled for non-zero detuning, Eq. (D.29), only approximately, but is again strict for zero detuning, since all the coefficients Eq. (D.30) are real.

D.3 Large pulse area

In the limit of large pulse area ($\lambda = |E_2|^2 \gg 1$ in *Case 1* or $\lambda = |E_1|^2 \gg 1$ in *Case 2*), the excited system contains a large number of photons, $n_{\mathrm{ph}} \approx \lambda \gg 1$. The Poisson distribution in Eq. (D.13) then becomes Gaussian, with the mean rung number $\langle n \rangle = \lambda$ and the mean square deviation $\langle n^2 - \langle n \rangle^2 \rangle = \lambda$. To achieve this limit mathematically, we replace in Eq. (D.13)

$$n! \approx \sqrt{2\pi n} e^{-n} n^n \tag{D.31}$$

and, introducing a small quantity $\varepsilon \ll 1$, defined according to $n = \lambda(1+\varepsilon)$, we approximate

$$\begin{aligned} e^{-n}n^n &= e^{-n}\lambda^n(1+\varepsilon)^{\lambda(1+\varepsilon)} = e^{-n}\lambda^n e^{\lambda(1+\varepsilon)\ln(1+\varepsilon)} \\ &\approx e^{-n}\lambda^n e^{\lambda(1+\varepsilon)(\varepsilon-\varepsilon^2/2)} \approx e^{-\lambda-\lambda\varepsilon}\lambda^n e^{\lambda(\varepsilon+\varepsilon^2/2)} = e^{-\lambda}\lambda^n e^{\lambda\varepsilon^2/2}. \end{aligned} \tag{D.32}$$

Equation (D.13) then becomes

$$R_n = \frac{\lambda^n e^{-\lambda}}{n!\sqrt{n+1}}\tilde{R}_n \approx \frac{\lambda^n e^{-\lambda}}{\sqrt{2\pi\lambda}e^{-\lambda}\lambda^n e^{\lambda\varepsilon^2/2}\sqrt{\lambda}}\tilde{R}_n = \frac{e^{-z^2}}{\sqrt{2\pi}\lambda}\tilde{R}_n\,, \tag{D.33}$$

where we have introduced for convenience a new variable

$$z = \frac{n-\lambda}{\sqrt{2\lambda}}\,, \tag{D.34}$$

such that $\langle z\rangle = 0$ and $\langle z^2\rangle = 1/2$. The Lagguere polynomials in Eqs. (D.14) and (D.19) for $\tilde{R}_n$ are approximated as follows:

$$L_m^{n-m}(\lambda) \approx \frac{1}{m!}\left(\frac{\lambda}{2}\right)^{\frac{m}{2}} H_m(z)\,, \tag{D.35}$$

where $H_m(z)$ are Hermite polynomials. To prove Eq. (D.35), we use the following recursive relation [114]:

$$mL_m^{n-m}(\lambda) = (n-\lambda)L_{m-1}^{n-m+1}(\lambda) - nL_{m-2}^{n-m+2}(\lambda) + nL_{m-3}^{n-m+2}(\lambda)\,. \tag{D.36}$$

The first few polynomials in this sequence have the following form:

$$\begin{aligned} L_0^n(\lambda) &= 1\,, \\ L_1^{n-1}(\lambda) &= n-\lambda = \left(\frac{\lambda}{2}\right)^{\frac{1}{2}} 2z\,, \\ L_2^{n-2}(\lambda) &= \frac{1}{2}\left(-\lambda + (n-\lambda)^2\right) = \frac{1}{2}\,\frac{\lambda}{2}(4z^2-2)\,, \end{aligned} \tag{D.37}$$

demonstrating a strict validity of Eq. (D.35) for $m = 0$, 1, and 2. To prove Eq. (D.35) for higher m, we note that $L_m^{n-m}(\lambda) \sim \lambda^{\frac{m}{2}}$, which is clear from Eq. (D.37) and the recursive formula Eq. (D.36). In fact, all terms in Eq. (D.36) except the last one are of order $\lambda^{\frac{m}{2}}$, while the last term is of order $\lambda^{\frac{m-1}{2}}$ and thus can be neglected for large

λ. For the same reason, $L_m^{n-m}(\lambda) \approx L_m^{n+1-m}(\lambda)$, so that Eq. (D.35) can be used for both *Cases* in the $\mathcal{N}$WM, described by Eqs. (D.14) and (D.19). Finally, substituting Eq. (D.35) into Eq. (D.36) and dropping there the last term, in accordance with the above discussion, results in a recursive relation

$$H_m(z) = 2zH_{m-1}(z) - 2(m-1)H_{m-2}(z)\,, \tag{D.38}$$

which generates the Hermite polynomials [114], starting from $H_0(z) = 1$ and $H_1(z) = 2z$. Note that the latter are the two lowest-order polynomials which appear in Eq. (D.37).

We further approximate for large excitation pulse area ($\lambda \gg 1$) the eigenfrequencies Δ_n^σ, the damping γ_n, and the transition amplitudes $C_n^{\sigma s}$ in Eq. (D.28):

$$\begin{aligned}
&\Delta_n^o \approx 2\sqrt{\lambda}g + \sqrt{2}gz\,, && \Delta_n^i \approx \frac{g}{2\sqrt{\lambda}} - \frac{g}{2\sqrt{2}\lambda}z\,,\\
&\gamma_n \approx (2\lambda+1)\gamma + 2\sqrt{2\lambda}\gamma z\,,\\
&C_n^{o\pm} \approx \frac{1}{8\sqrt{\lambda}}\,, && C_n^{i\pm} \approx \frac{\sqrt{\lambda}}{2}\,,
\end{aligned} \tag{D.39}$$

where z is defined by Eq. (D.34). Again, the approximation is valid for relatively small ($\delta \ll \sqrt{\lambda}g$) or zero detuning ($\delta = 0$, $\gamma_x = \gamma_c = \gamma$).

Finally, switching in Eq. (D.28) from summation to integration,

$$\sum_{n=0}^{\infty} \to \sqrt{2\lambda}\int_{-\infty}^{\infty} dz\,, \tag{D.40}$$

and using the approximations Eqs. (D.33), (D.35), and (D.39), we obtain

$$P_{\sigma s}(t) \approx \frac{i^m}{2} A_\sigma^{(m)} e^{-i\omega_{\sigma s}t} \frac{1}{\sqrt{\pi}} \int_{-\infty}^{\infty} dz e^{-z^2} e^{-i\Delta\omega_{\sigma s}tz} H_m(z)\,, \tag{D.41}$$

where

$$\begin{aligned}
\omega_{os} &= s2\sqrt{\lambda}g - i(2\lambda+1)\gamma\,, & \omega_{is} &= s\frac{g}{2\sqrt{\lambda}} - i(2\lambda+1)\gamma\,,\\
\Delta\omega_{os} &= s\sqrt{2}g - i2\sqrt{2\lambda}\gamma\,, & \Delta\omega_{is} &= -s\frac{g}{2\sqrt{2}\lambda} - i2\sqrt{2\lambda}\gamma\,,\\
A_o^{(m)} &= \frac{(-i)^m}{4m!(\sqrt{2\lambda})^m}\,, & A_i^{(m)} &= 4\lambda A_o^{(m)}\,,
\end{aligned} \tag{D.42}$$

and $s = \pm 1$. The amplitudes $A_\sigma^{(m)}$ of the $\mathcal{N}$WM polarisation are given in Eq. (D.42) for *Case 2*, for which $m = \mathcal{N}/2$. Note, however, that Eqs. (D.41) and (D.42) describe also the $\mathcal{N}$WM polarisation in *Case 1*, provided that all $P_{\sigma s}(t)$ are divided by λ and $m = \mathcal{N}/2 - 1$ is used.

Now, performing the integration in Eq. (D.41) we find

$$P_{\sigma s}(t) \approx \frac{1}{2}A_\sigma^{(m)}(\Delta\omega_{\sigma s}t)^m \exp\left\{-i\omega_{\sigma s}t - (\Delta\omega_{\sigma s}t)^2/4\right\}\,, \tag{D.43}$$

with the help of the following analytic integral:

$$\begin{aligned}
I_m(p) &= \int_{-\infty}^{\infty} e^{ipz}H_m(z)e^{-z^2}dz\\
&= \int_{-\infty}^{\infty} e^{ipz}\left[2zH_{m-1}(z) - 2(m-1)H_{m-2}(z)\right]e^{-z^2}dz\\
&= \int_{-\infty}^{\infty} e^{ipz}\left[ipH_{m-1}(z) + H'_{m-1}(z) - 2(m-1)H_{m-2}(z)\right]e^{-z^2}dz\\
&= ipI_{m-1} = (ip)^m\sqrt{\pi}e^{-p^2/4}\,.
\end{aligned} \tag{D.44}$$

Note that in deriving Eq. (D.44) we have used the recursive relation Eq. (D.38), integration by parts, the following property of Hermite polynomials

$$H'_m(z) = 2mH_{m-1}(z)\,, \tag{D.45}$$

and the Fourier transform of the Gaussian function:

$$I_0(p) = \int_{-\infty}^{\infty} e^{ipz} e^{-z^2} dz = \sqrt{\pi} e^{-p^2/4} \,. \tag{D.46}$$

Finally, to obtain the $\mathcal{N}$WM spectrum, using $\bar{\Omega}$ as the zero of frequency for convenience, we Fourier transform the time-dependent optical polarisation:

$$\begin{aligned} \tilde{P}_{\sigma s}(\omega) &= \int_0^{\infty} e^{i\omega t} P_{\sigma s}(t) dt \\ &= A_\sigma^{(m)} \frac{1}{2} \int_0^{\infty} (\Delta\omega_{\sigma s} t)^m \exp\left\{ i(\omega - \omega_{\sigma s})t - (\Delta\omega_{\sigma s} t)^2/4 \right\} dt \\ &= \frac{A_\sigma^{(m)}}{\Delta\omega_{\sigma s}} w_m \left(\frac{\omega - \omega_{\sigma s}}{\Delta\omega_{\sigma s}} \right) , \end{aligned} \tag{D.47}$$

where $|\arg(\Delta\omega_{\sigma s})| < \pi/4$. If the last condition is not fulfilled, $\Delta\omega_{\sigma s}$ must be replaced with $-\Delta\omega_{\sigma s}$ and a sign factor $(-1)^m$ be added to the answer, see below for more details. This is actually the case of $o-$ and $i+$ transition, for which Re $\Delta\omega_{o-} > 0$ and $\Delta\omega_{i+} > 0$. This can be conveniently dealt with by using the spectral symmetry:

$$\tilde{P}(\omega) = \sum_{\sigma=i,o} \sum_{s=\pm} \tilde{P}_{\sigma s}(\omega) = \bar{P}(\omega) + \bar{P}^*(-\omega) \,, \tag{D.48}$$

where

$$\bar{P}(\omega) = \tilde{P}_{o+}(\omega) + \tilde{P}_{i-}(\omega) = A_o^{(m)} \left[\frac{1}{\Delta\omega_{o+}} w_m \left(\frac{\omega - \omega_{o+}}{\Delta\omega_{o+}} \right) + \frac{4\lambda}{\Delta\omega_{i-}} w_m \left(\frac{\omega - \omega_{i-}}{\Delta\omega_{i-}} \right) \right] . \tag{D.49}$$

Function $w_m(z)$ in Eqs. (D.47) and (D.49) is defined as

$$w_m(z) = \frac{1}{2} \int_0^{\infty} t^m e^{izt} e^{-t^2/4} dt \,, \tag{D.50}$$

and can be easily expressed in terms of the Faddeeva function, $w(z) = 2w_0(z)/\sqrt{\pi}$,

via its m-th derivative:

$$w_m(z) = (-i)^m \frac{d^m}{dz^m} w_0(z)\,. \tag{D.51}$$

It is, however, more practical to use a recursive formula which can be obtained integrating Eq. (D.50) by parts, which gives

$$w_m(z) = 2izw_{m-1}(z) + 2(m-1)w_{m-2}(z) \tag{D.52}$$

for $m \geqslant 2$,

$$w_1(z) = 1 + 2izw_0(z) \tag{D.53}$$

for $m = 1$, and

$$w_0(z) = G(z) + iD(z) = \frac{\sqrt{\pi}}{2} w(z) \tag{D.54}$$

for $m = 0$. Here, $G(z)$ is the Gaussian function,

$$G(z) = \frac{\sqrt{\pi}}{2} e^{-z^2}\,, \tag{D.55}$$

$D(z)$ is the standard Dawson's integral,

$$D(z) = \frac{1}{2}\int_0^\infty e^{-t^2/4}\sin(zt)dt = e^{-z^2}\int_0^z e^{t^2}dt\,, \tag{D.56}$$

and $w(z)$ is the Faddeeva function. The latter is well-know due to its real part, describing a Voigt (Gaussian) profile for complex (real) z.

The integral $w_m(z)$ in Eq. (D.50) can also be written explicitly using the Faddeeva function, Hermite polynomials and associated polynomials $Q_m(z)$ satisfying the recursive relation Eq. (D.38) of Hermite polynomials,

$$Q_m(z) = 2zQ_{m-1}(z) - 2(m-1)Q_{m-2}(z)\,, \tag{D.57}$$

but starting from $Q_1(z) = 1$ and $Q_2(z) = 2z$ instead. Functions $w_m(z)$ take the form

$$w_m(z) = i^m H_m(z) w_0(z) + i^{m-1} Q_m(z) \tag{D.58}$$

with $w_0(z)$ given by Eq. (D.54) and

$$\begin{aligned}
&H_0(z) = 1\,, && Q_0(z) = 0\,,\\
&H_1(z) = 2z\,, && Q_1(z) = 1\,,\\
&H_2(z) = 4z^2 - 2\,, && Q_2(z) = 2z\,,\\
&H_3(z) = 8z^3 - 12z\,, && Q_3(z) = 4z^2 - 4\,,\\
&H_4(z) = 16z^4 - 48z^2 + 12\,, && Q_4(z) = 8z^3 - 20z\,,\\
&H_5(z) = 32z^5 - 160z^3 + 120z\,, && Q_5(z) = 16z^4 - 72z^2 + 32\,,
\end{aligned} \tag{D.59}$$

listed above for the first few m.

Note also that we have reduced the integral in Eq. (D.47) to Faddeeva function in the following way

$$\begin{aligned}
\int_0^\infty e^{iat} e^{-(bt)^2/4} dt &= e^{-(a/b)^2} \int_0^\infty e^{-b^2(t-t_0)^2/4} dt \\
&= e^{-(a/b)^2} \left[\int_0^{t_0} e^{-b^2 t^2/4} dt + \int_0^\infty e^{-b^2 t^2/4} dt \right] \\
&= e^{-(a/b)^2} \left[\frac{2i}{b} \int_0^{a/b} e^{t^2} dt + \frac{\sqrt{\pi}}{b} \right] = \frac{2}{b} w_0(a/b)\,,
\end{aligned} \tag{D.60}$$

where $t_0 = 2ia/b$. While the initial integral is invariant with respect to the sign change of b and only requires that $\mathrm{Re}\,(b^2) > 0$, necessary for convergence, the Gaussian term in the last line of Eq. (D.60), containing the factor $\sqrt{\pi}/b$, is valid only if $|\arg(b)| < \pi/4$. This leads to the requirement introduced above that $|\arg(\Delta\omega_{\sigma s})| < \pi/4$, and if not, $\Delta\omega_{\sigma s}$ should be taken with the opposite sign.

Figure D.1 illustrates a comparison of FWM spectra, calculated using the exact

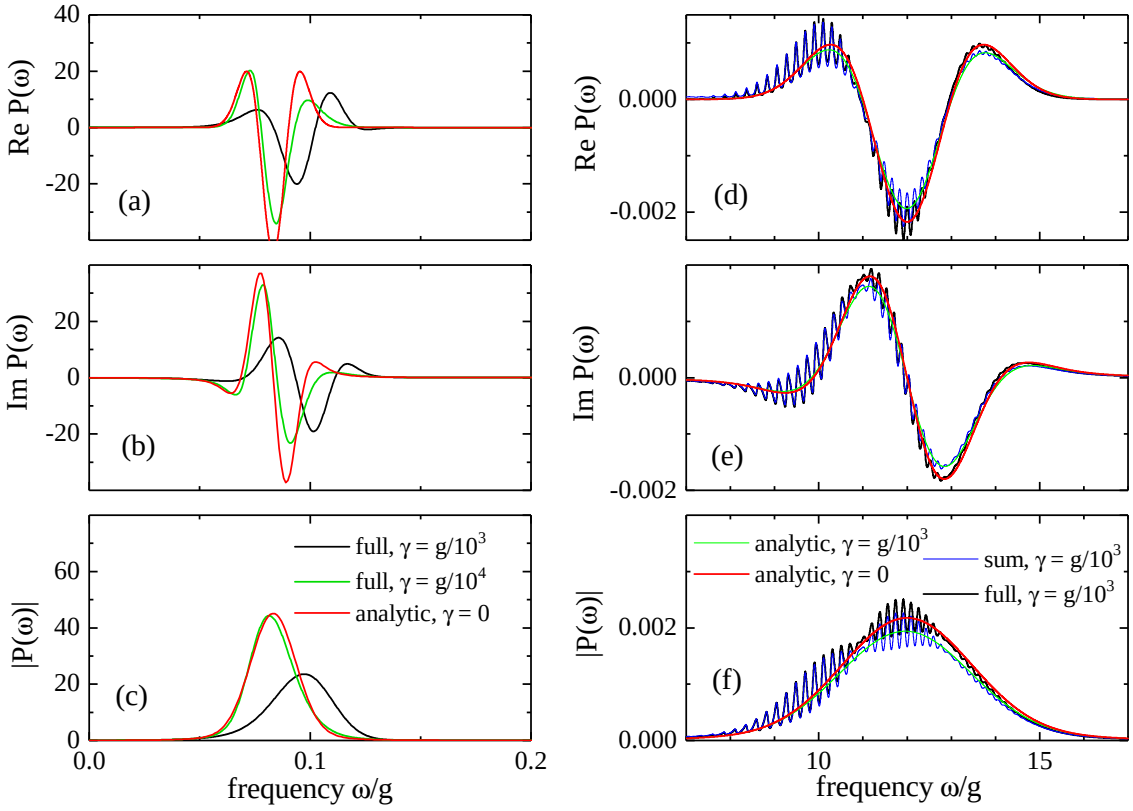

Figure D.1: Exact FWM spectrum (black and green lines) for $|E_1| = 6$, $|E_2| = 0.001$, zero detuning, and $\gamma_C = \gamma_X = \gamma$ with the values of γ as given, in comparison with the analytic approximation Eqs. (D.48) and (D.49) (red lines), and the full sum Eq. (D.28) (blue lines). Left and right panels show the spectral regions of, respectively, inner and outer transitions (for positive frequencies). The spectra are shown without the factor Eq. (D.21).

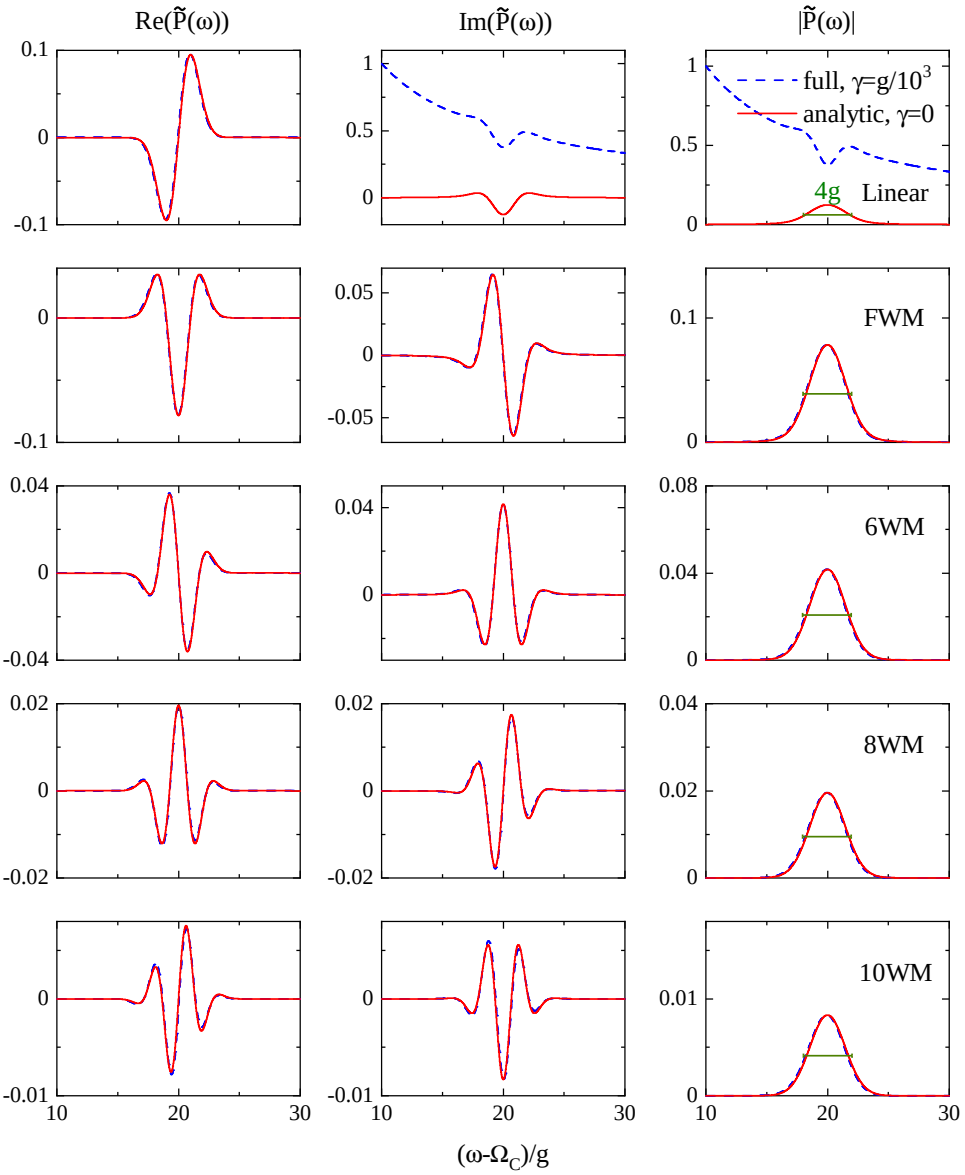

Figure D.2: Analytic approximation Eqs. (D.48) and (D.49) (red lines) for the outer-transition sideband of the $\mathcal{N}$WM spectrum with $\mathcal{N} = 2$, 4, 6, 8, 10, and 12, $|E_1| = 10$, $|E_2| = 0.001$, zero detuning, and $\gamma_C = \gamma_X = \gamma = 0$, in comparison with the exact calculation with $\gamma = 0.001g$ (blue lines). The horizontal bars show the spectral linewidth of $4g$. The left, middle, and right panels show, respectively the real, imaginary part, and the absolute value of $\tilde{P}(\omega)$. All spectra are shown without the factor Eq. (D.21) and are multiplied with $|E_1|^{\mathcal{N}/2}$.

solution, the analytic formulas Eqs. (D.48) and (D.49), and the sum Eq. (D.28) without converting it to an integral, with coefficients taken in the form of Eq. (D.30). For the damping $\gamma = 0.001g$, the sideband (right panels) shows individual outer transitions contributing to it, both in the sum and in the full spectrum. This is happening because the difference between the transition frequencies, $g/\sqrt{n}$ [see Eq. (C.13)], is larger than the damping $\gamma_n = (2n+1)\gamma$ (here $n \sim 36$). The pattern of oscillations seen in the spectral profile can be understood from the modulation of the Poisson distribution with Lagguere polynomial $L_2^{n-1}(\lambda)$ specific to this nonlinearity channel, see Eq. (D.20). In fact, $L_2^{n-1}(\lambda)$ presents a parabola which is clearly seen in the amplitude of oscillations, having naughts at around $\omega/g = 11$ and 13. The frequency difference between the neighboring inner transitions, $-g/(4n\sqrt{n})$, is in turn much smaller than the damping, so that similar oscillations in the peak of the central band (left panel) are not seen even for a 10 times smaller damping. The analytic approximation (red curves) shows no oscillations, since the conversion of a sum into an integral used in its derivation effectively introduces a spectral damping covering the distance between neighboring transitions. Interestingly, the analytic approximation shows the best agreement with the full calculation when it is taken with zero damping, while for the same damping ($\gamma = 0.001g$) the agreement is worse.

We further look at the spectral profile for higher non-linearities, concentrating on the positive-frequency sideband of the Mollow triplet. Figure D.2 shows the real, imaginary part and the absolute value of the $\mathcal{N}$WM spectrum, for all even $\mathcal{N}$ from 2 to 12. The number of oscillations in the real an imaginary parts grows linearly with $\mathcal{N}$, and the real and imaginary parts are lookng very similar for the neighboring $\mathcal{N}$, which is the property of the generalized Faddeeva function w_m determining the spectra. The absolute value, however, shows no oscillations and the same linewidth of around $4g$, practically independent of $\mathcal{N}$. The right panels demonstrate a very good agreement between the analytic approximation and the exact calculation, for

all spectra.

E | Supplementary Figures

E.1 Complex number map to HSV colour space

For each coloured plot including 2D and bubble plots using colour to distinguish phases of complex values z, the hsv value channel is given by the absolute value $|z|$ raised to some gamma correction γ to make darker regions clearer to see, and phase $angle(z)$ maps to the hsv hue channel. "scale" is the maximum absolute value of a 2D plot. If scale is not stated, assume the plot has been normalised.

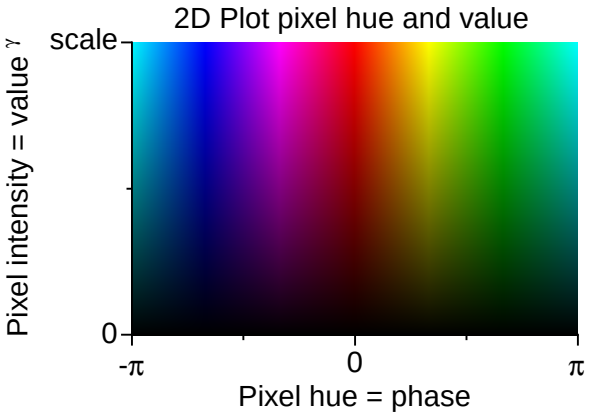

Figure E.1: Hue-Value Map for plotting complex numbers.

E.2 Two-Level QD coupled to a MC

2L QDMC Polarisation figures.

a) 2D plot of polarisation curve at each value of E listed along the y axis.

b) Integrated power (normalised to have $max = 1$) calculated by integrating a) at a single value of E.

c) single absolute polarisation curve extracted from a), at the values below c).

d),**e)**,**f)** bubble diagrams showing the transition contributions to $\tilde{P}(\omega)$ at the values of E used in c). Per bubble, the size is determined by $|A|$ with colour $angle(A)$, and position in x and y axis directions are the real and imaginary parts of the associated eigenvalue ω All figures use the HSV map described above, with the same colour map applied to the bubble plots.

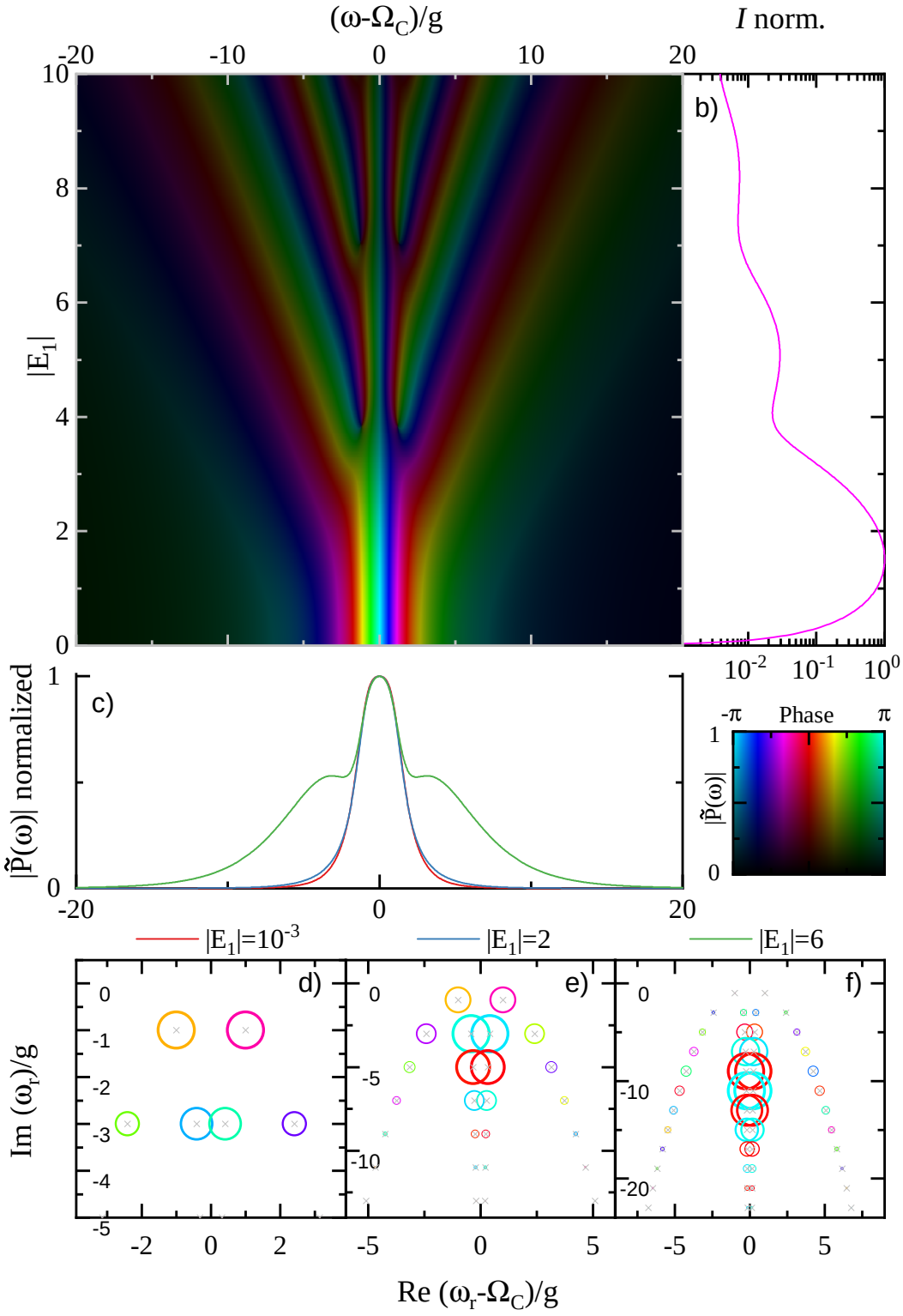

Figure E.2: E_1 changing, $\delta = 0$, $\gamma_c = \gamma_x = g$.

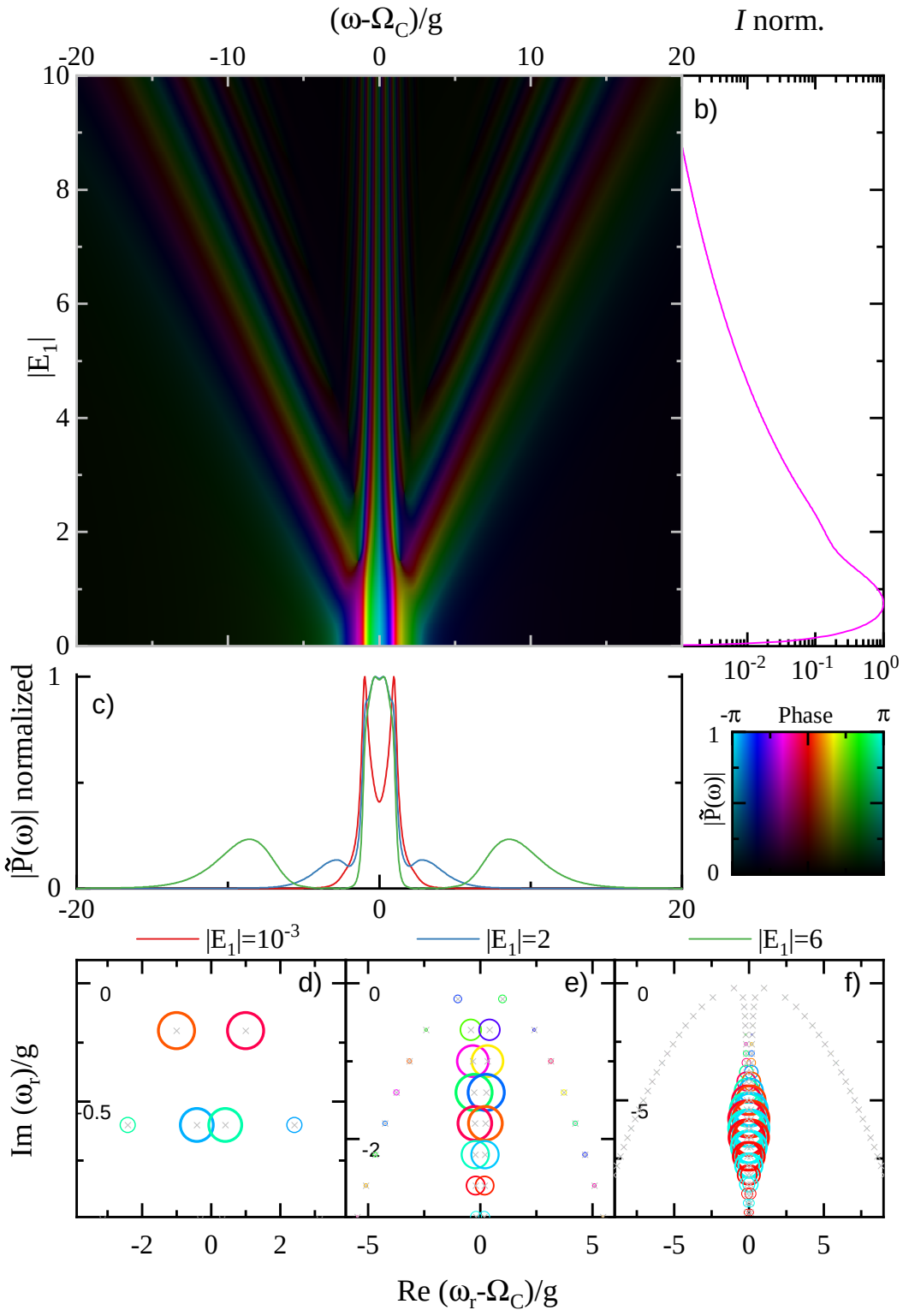

Figure E.3: E_1 changing, $\delta = 0$, $\gamma_c = \gamma_x = g/5$.

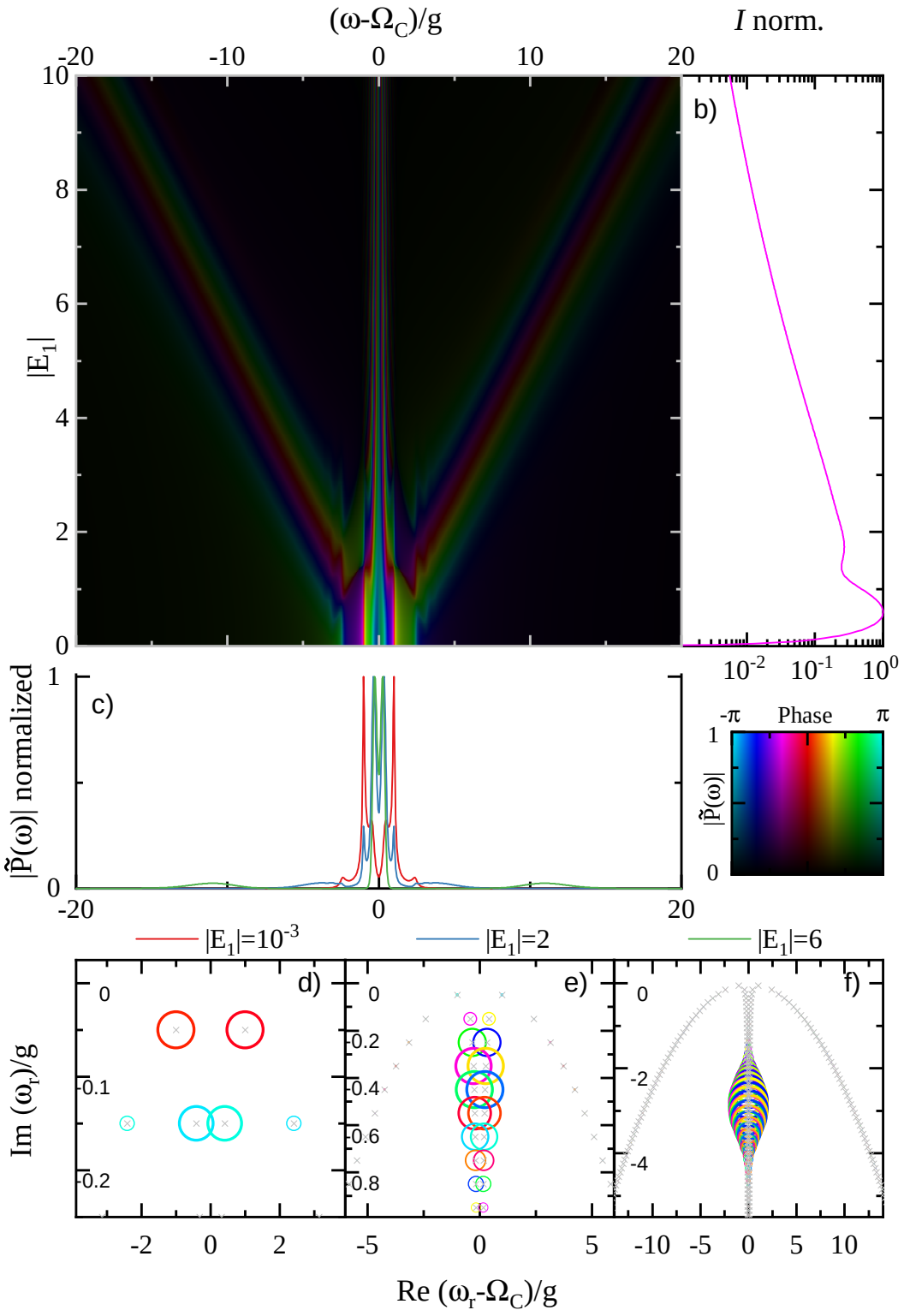

Figure E.4: E_1 changing, $\delta = 0$, $\gamma_c = \gamma_x = g/20$.

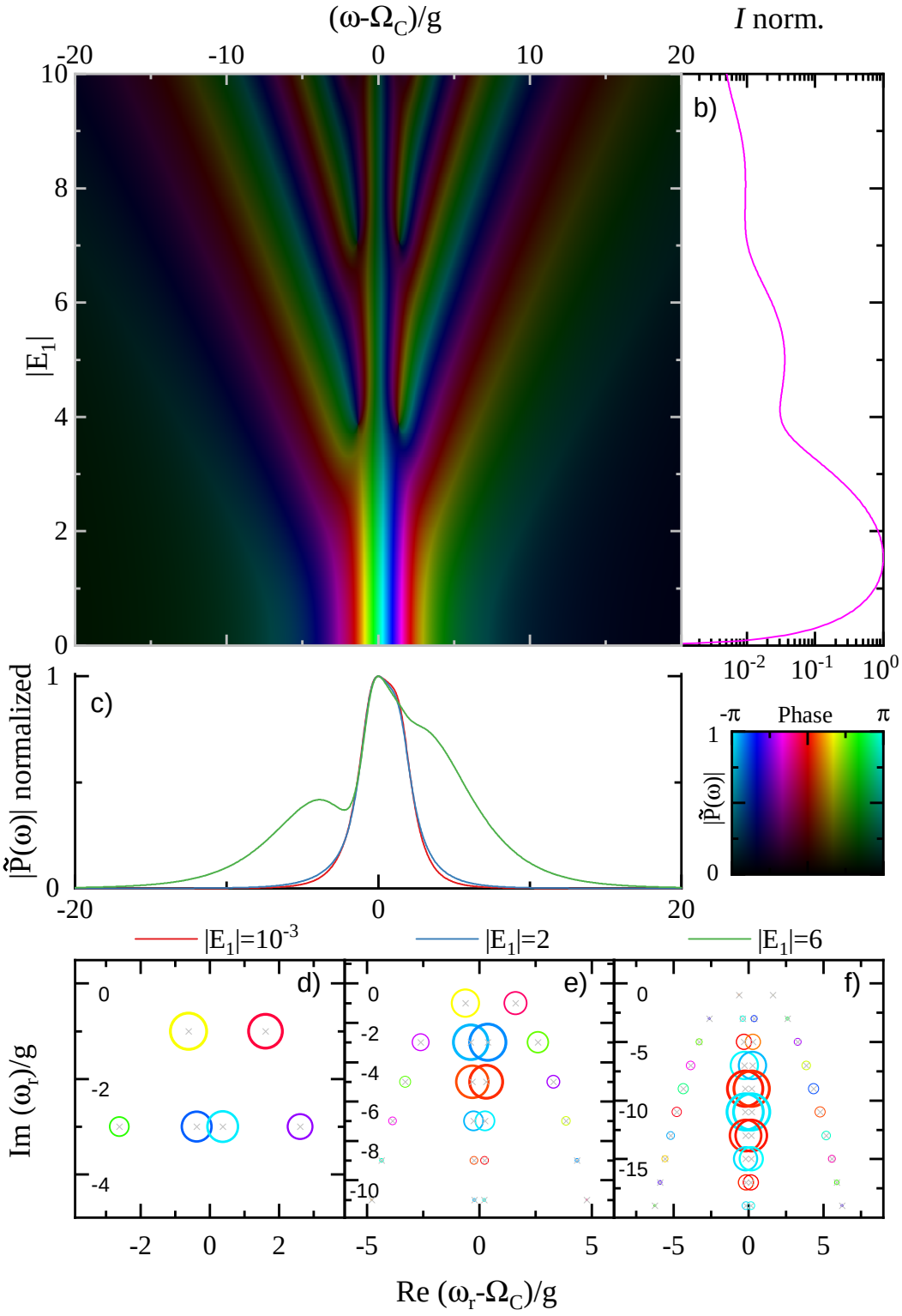

Figure E.5: E_1 changing, $\delta = g$, $\gamma_c = \gamma_x = g$.

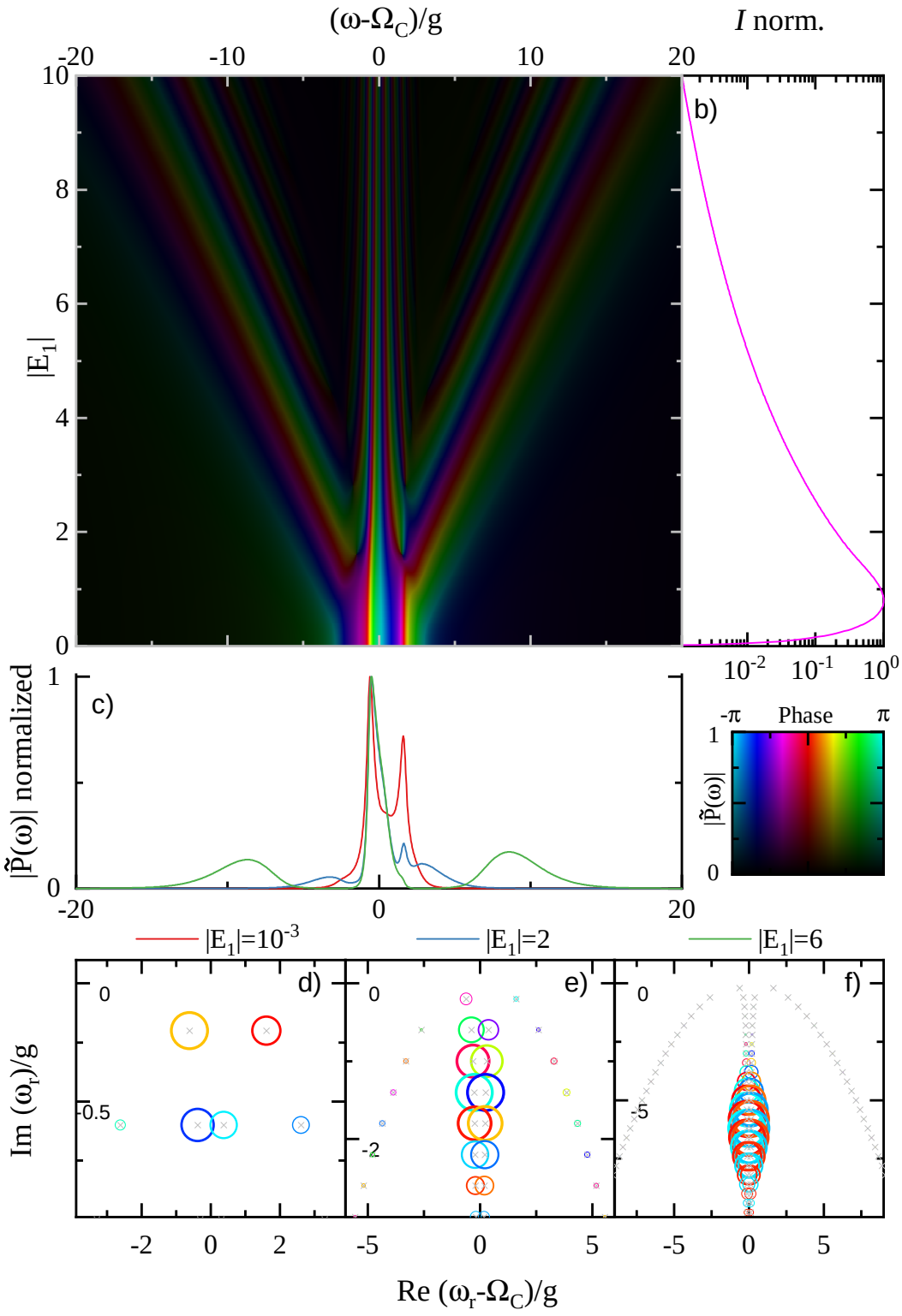

Figure E.6: E_1 changing, $\delta = g$, $\gamma_c = \gamma_x = g/5$.

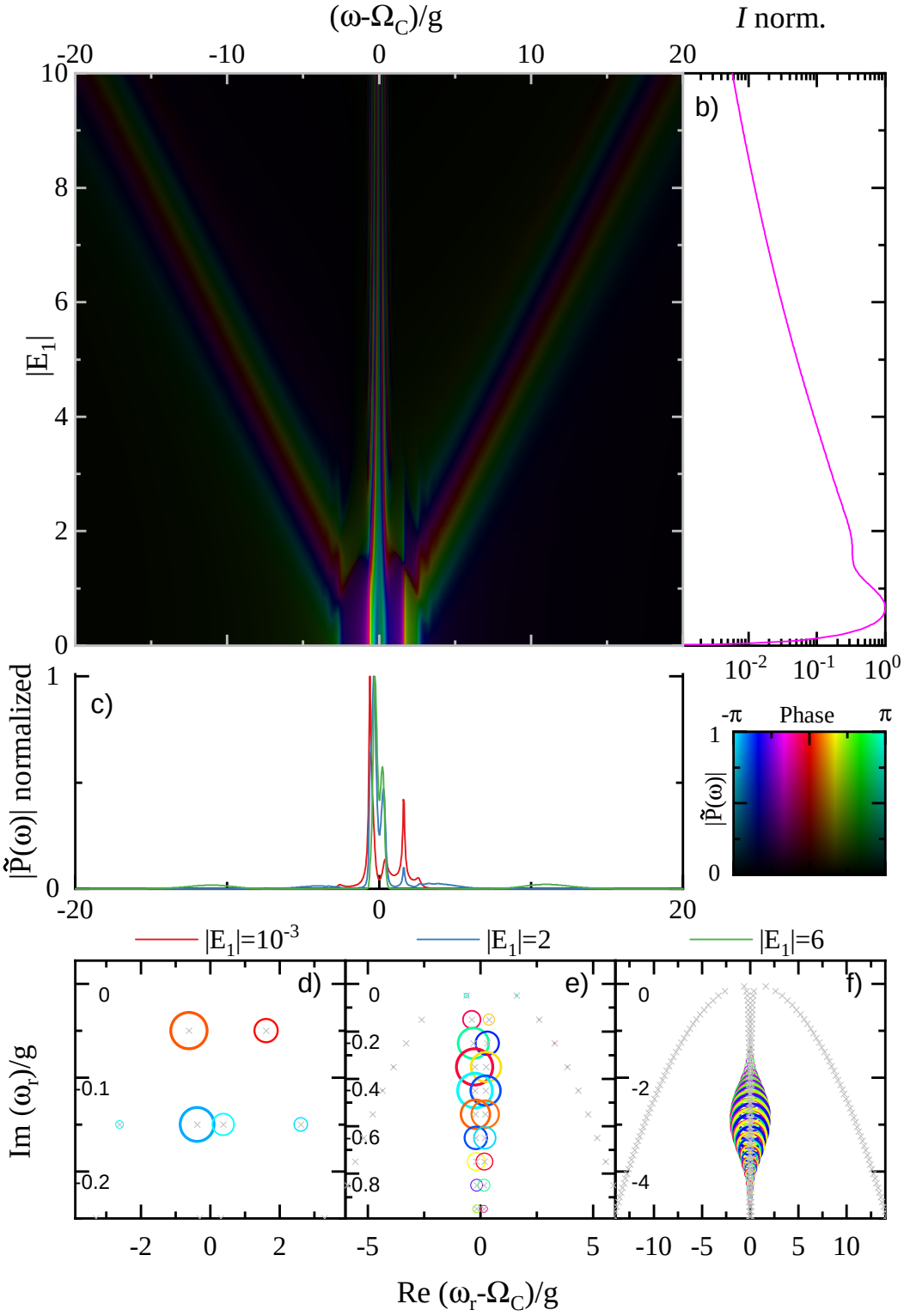

Figure E.7: E_1 changing, $\delta = g$, $\gamma_c = \gamma_x = g/20$.

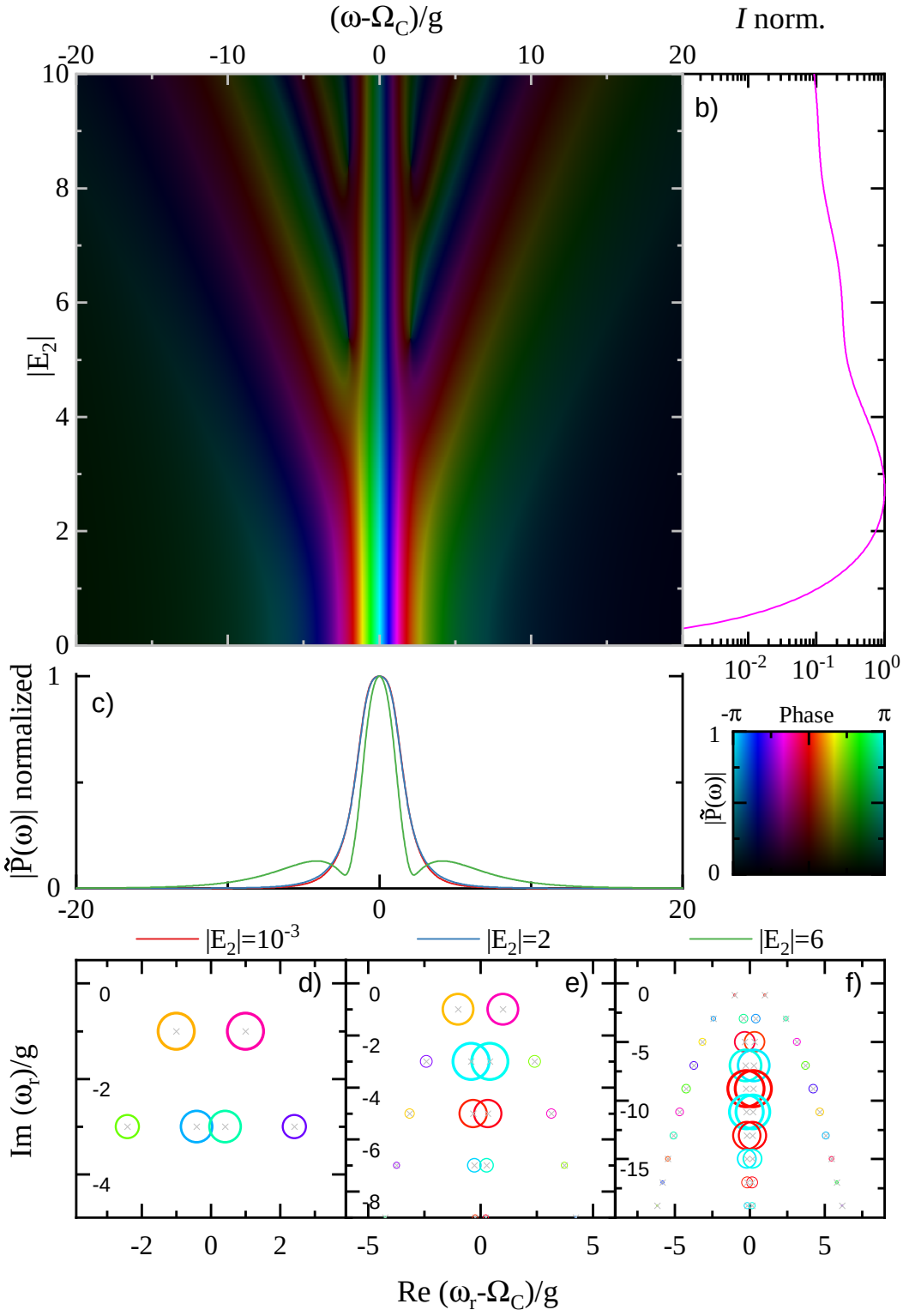

Figure E.8: E_2 changing, $\delta = 0$, $\gamma_c = \gamma_x = g$.

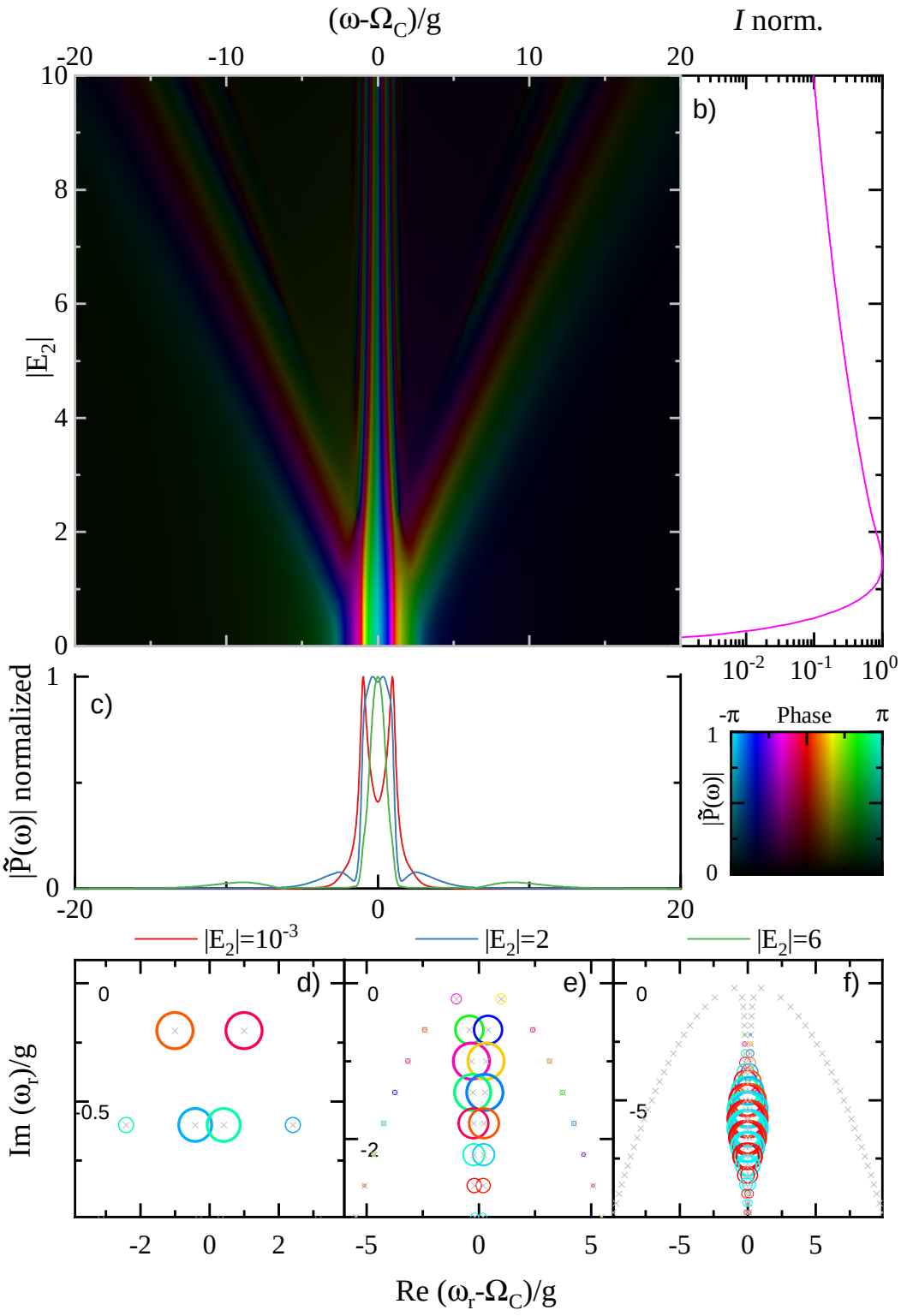

Figure E.9: E_2 changing, $\delta = 0$, $\gamma_c = \gamma_x = g/5$.

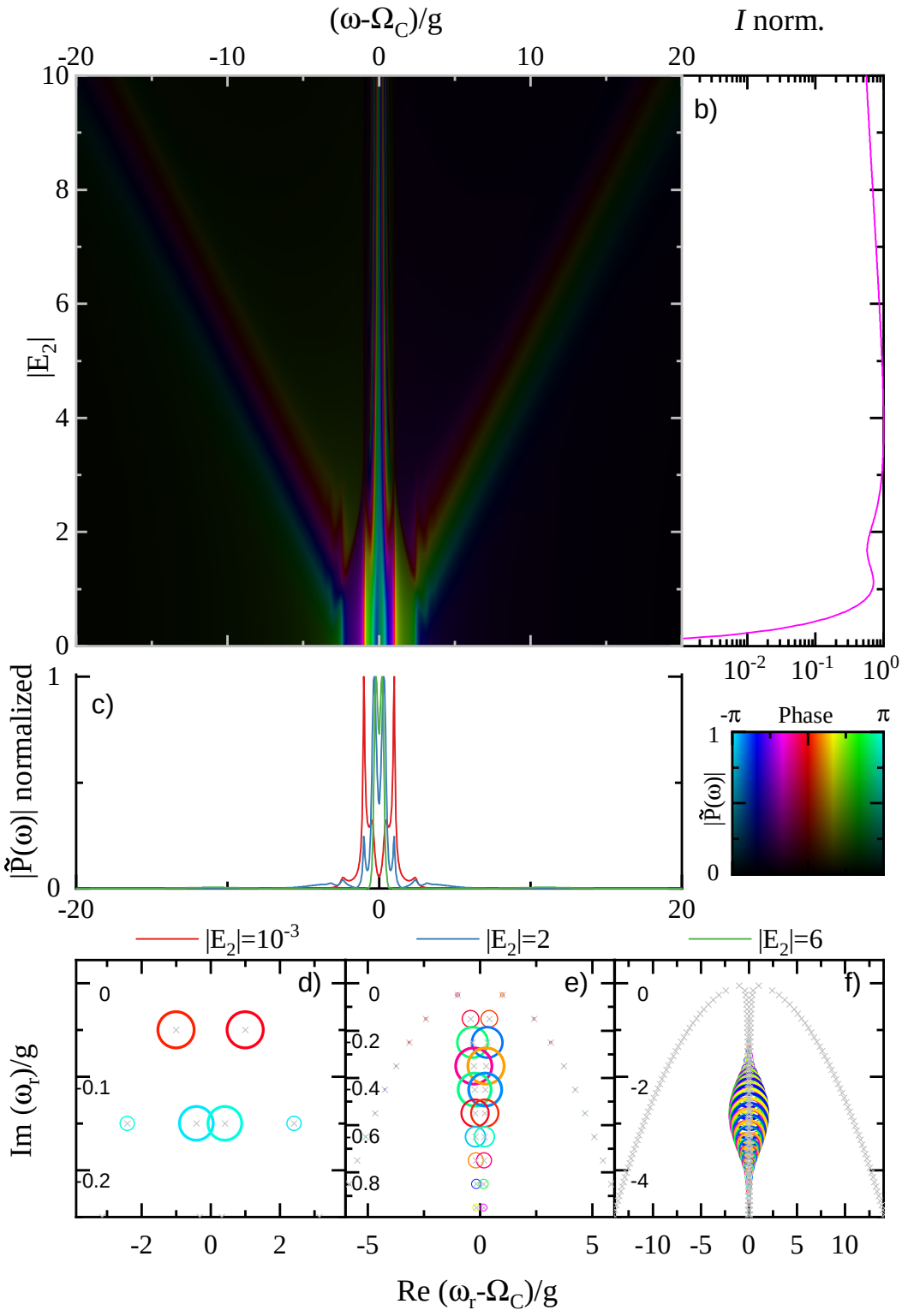

Figure E.10: E_2 changing, $\delta = 0$, $\gamma_c = \gamma_x = g/20$.

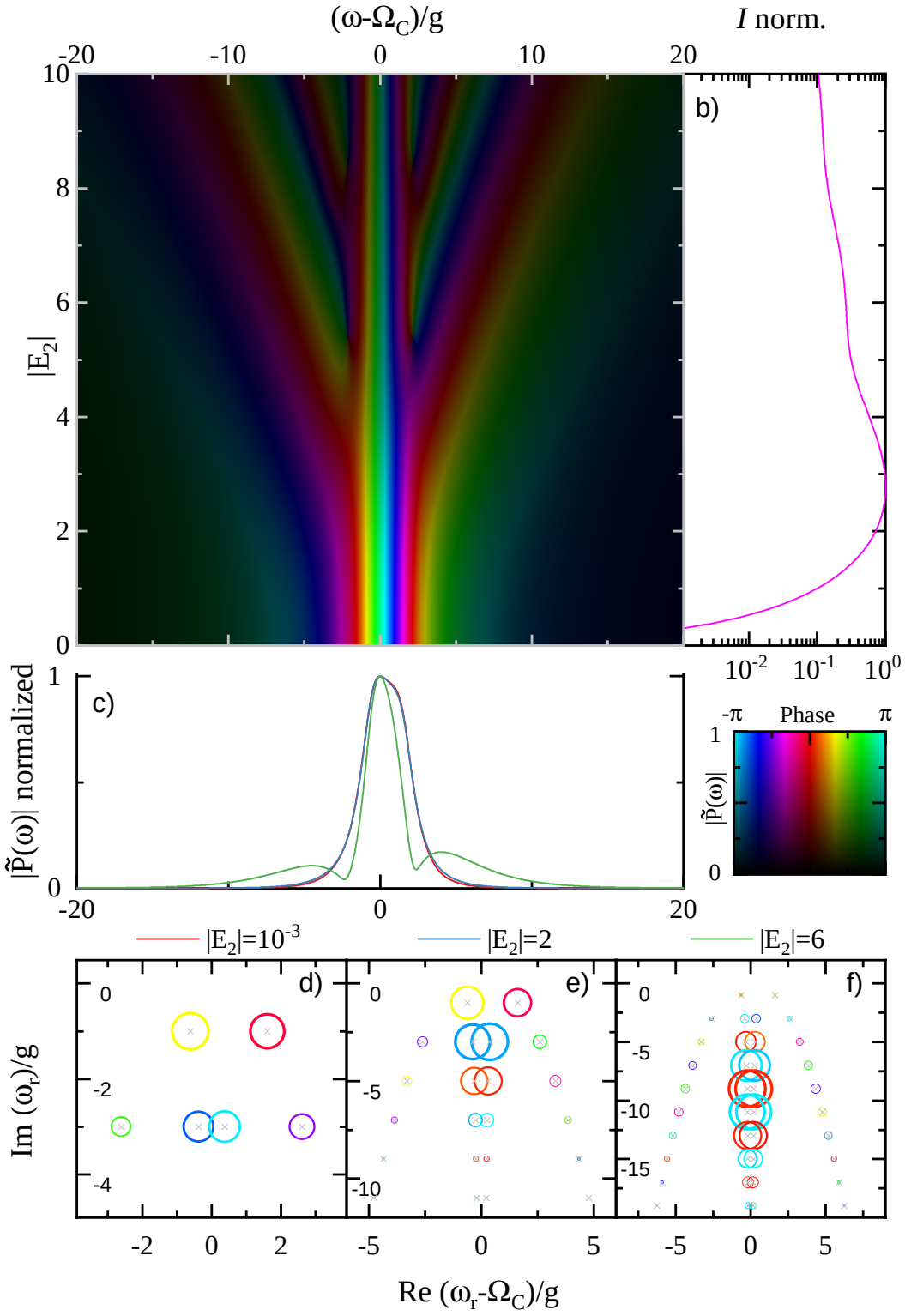

Figure E.11: E_2 changing, $\delta = g$, $\gamma_c = \gamma_x = g$.

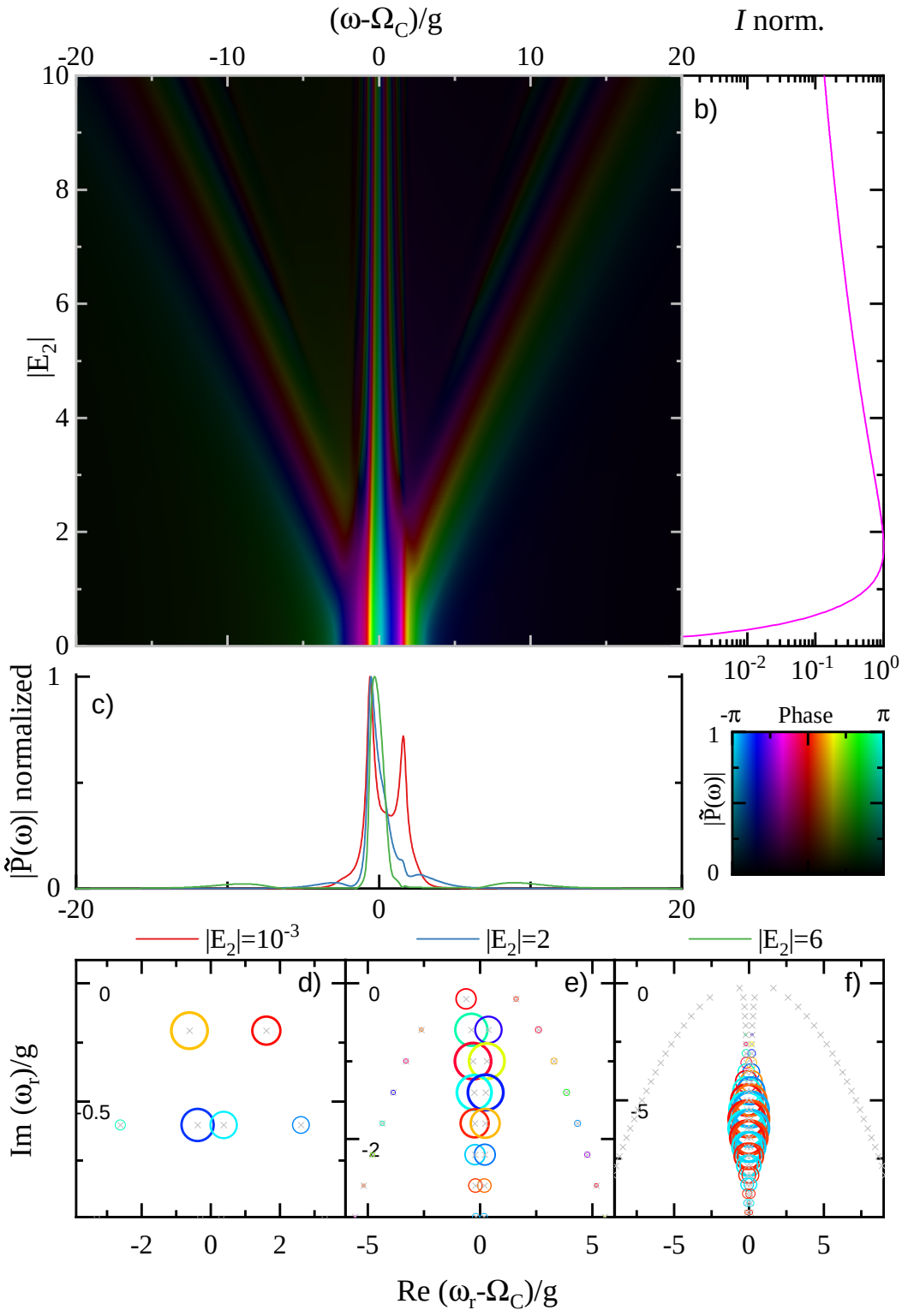

Figure E.12: E_2 changing, $\delta = g$, $\gamma_c = \gamma_x = g/5$.

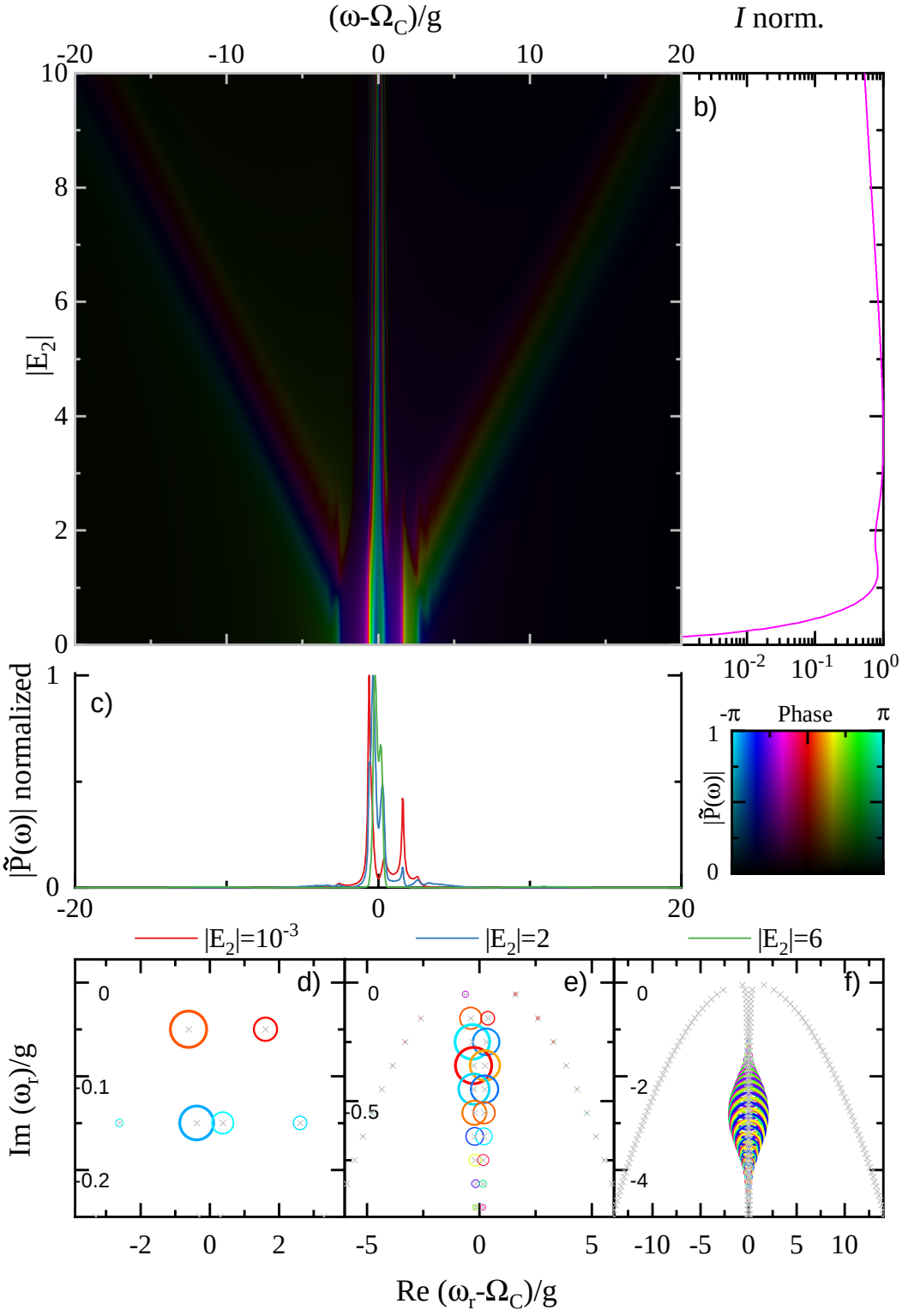

Figure E.13: E_2 changing, $\delta = g$, $\gamma_c = \gamma_x = g/20$.

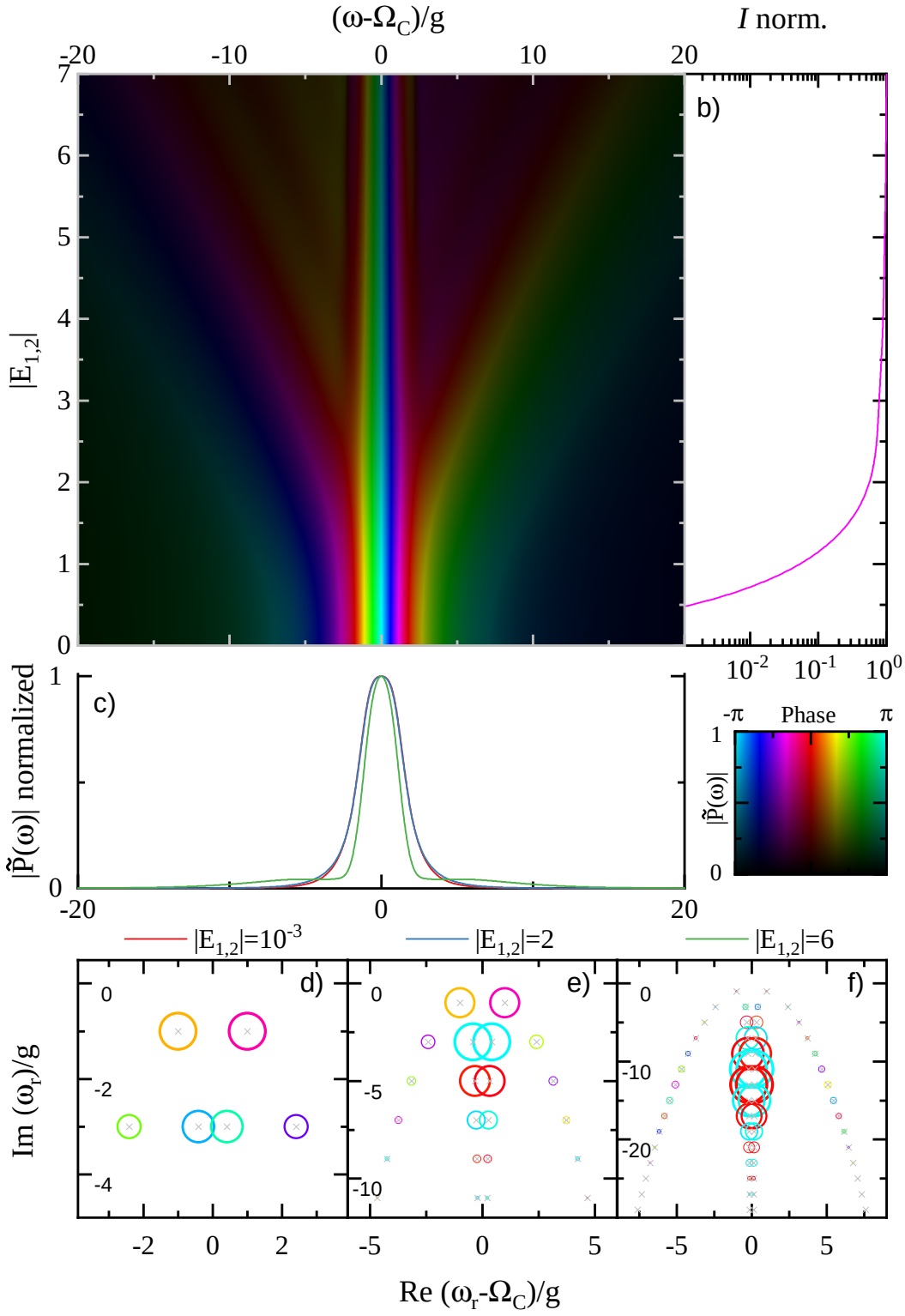

Figure E.14: $E_1 = E_2$ changing, $\delta = 0$, $\gamma_c = \gamma_x = g$.

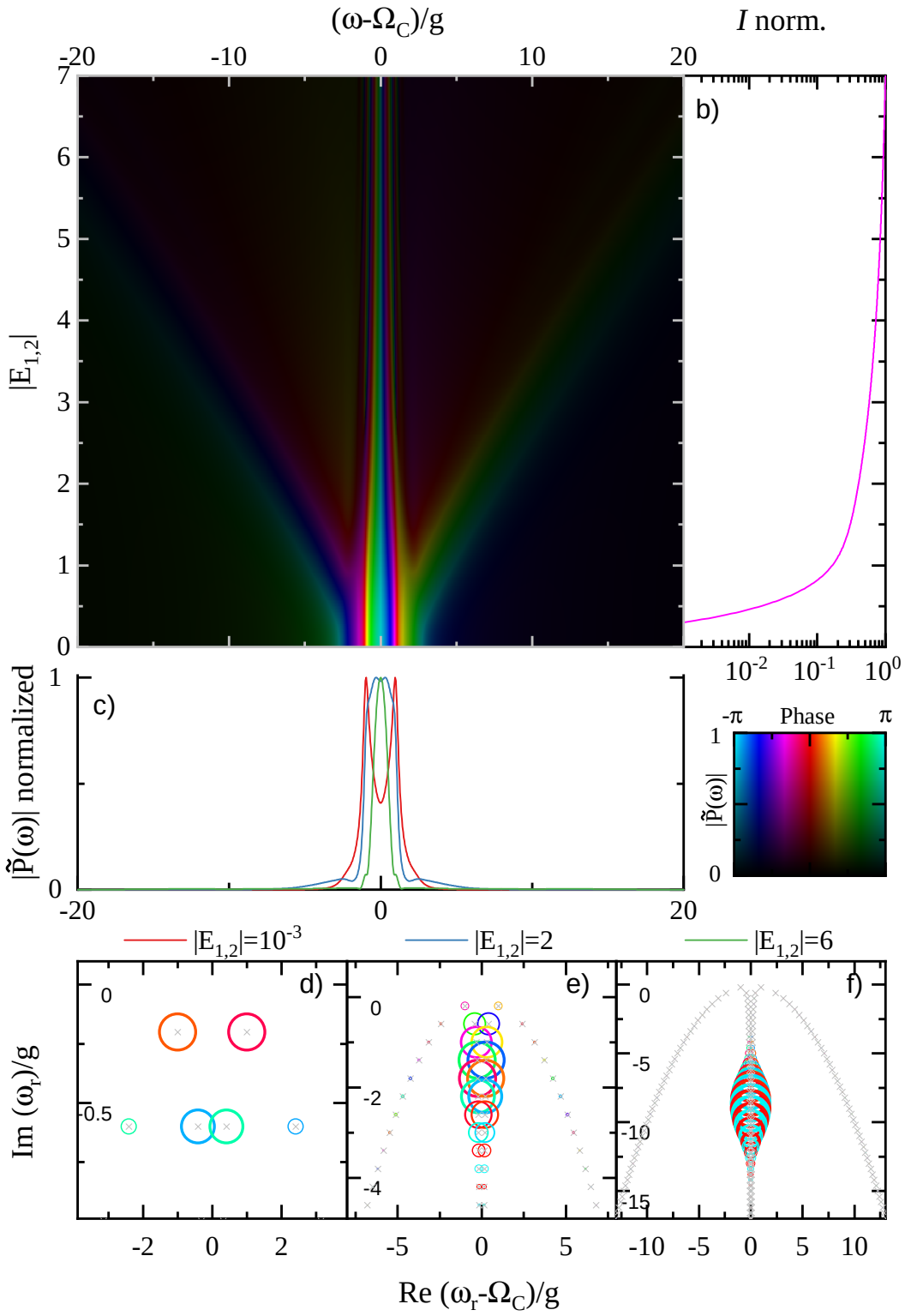

Figure E.15: $E_1 = E_2$ changing, $\delta = 0$, $\gamma_c = \gamma_x = g/5$.

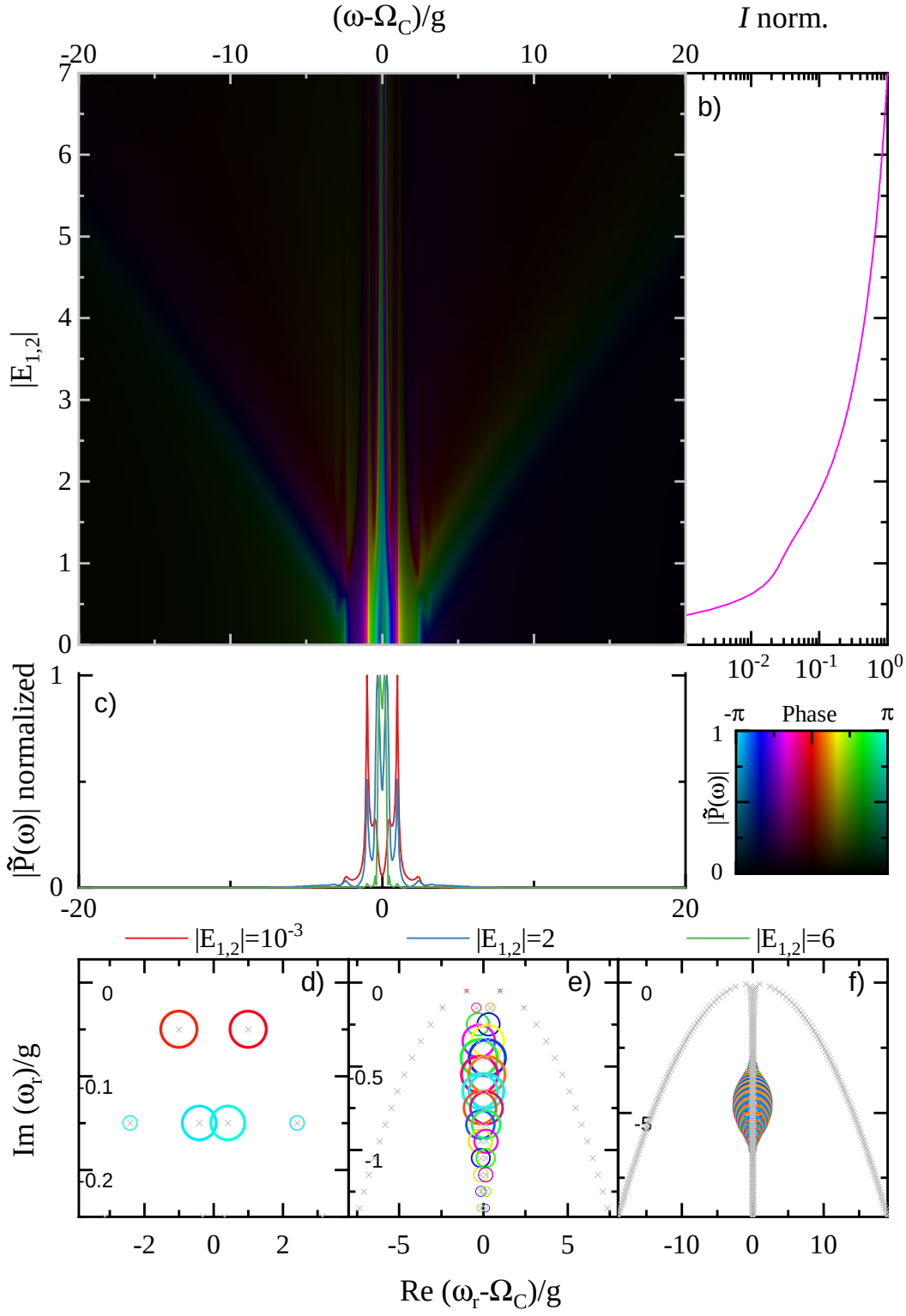

Figure E.16: $E_1 = E_2$ changing, $\delta = 0$, $\gamma_c = \gamma_x = g/20$.

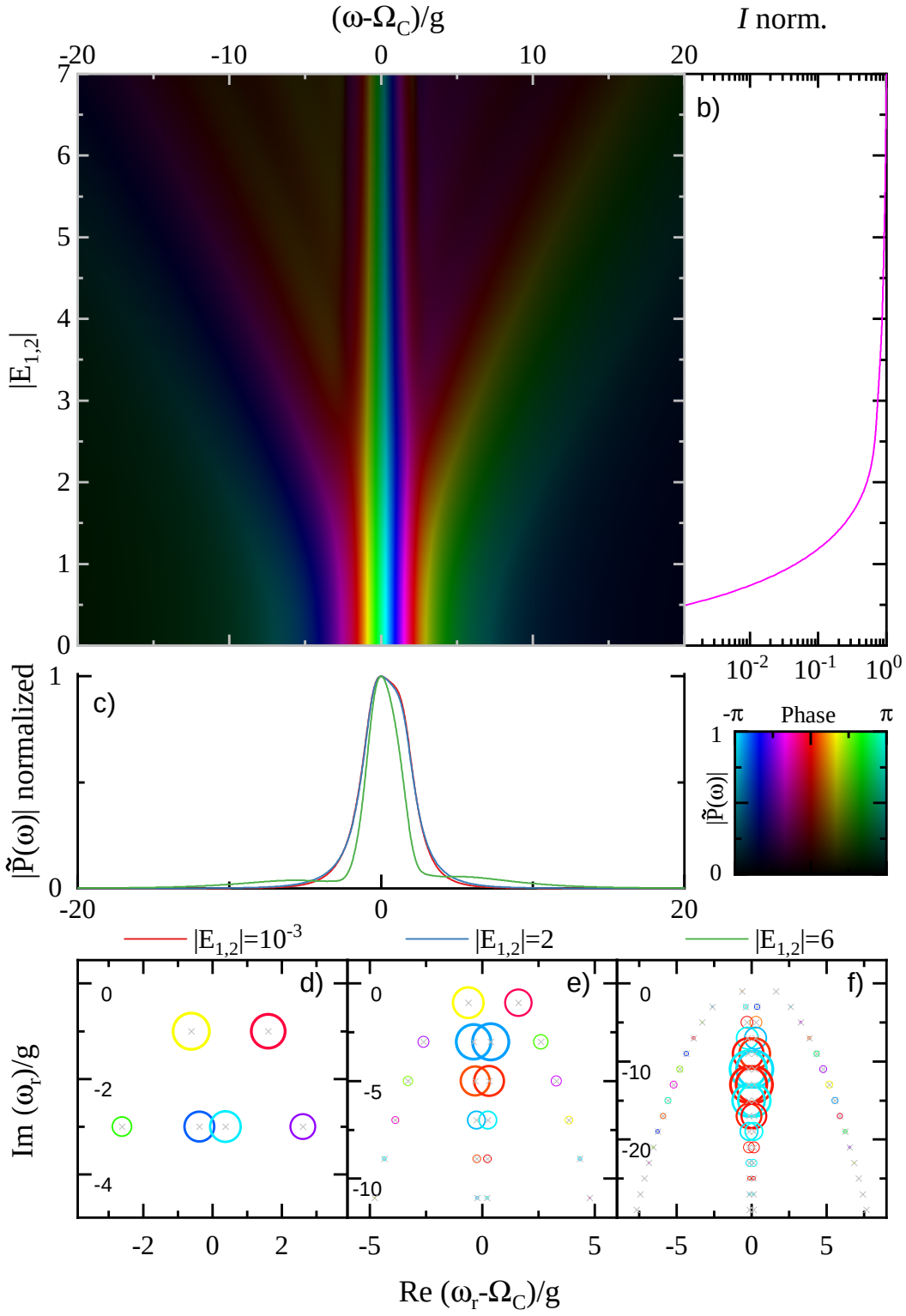

Figure E.17: $E_1 = E_2$ changing, $\delta = g$, $\gamma_c = \gamma_x = g$.

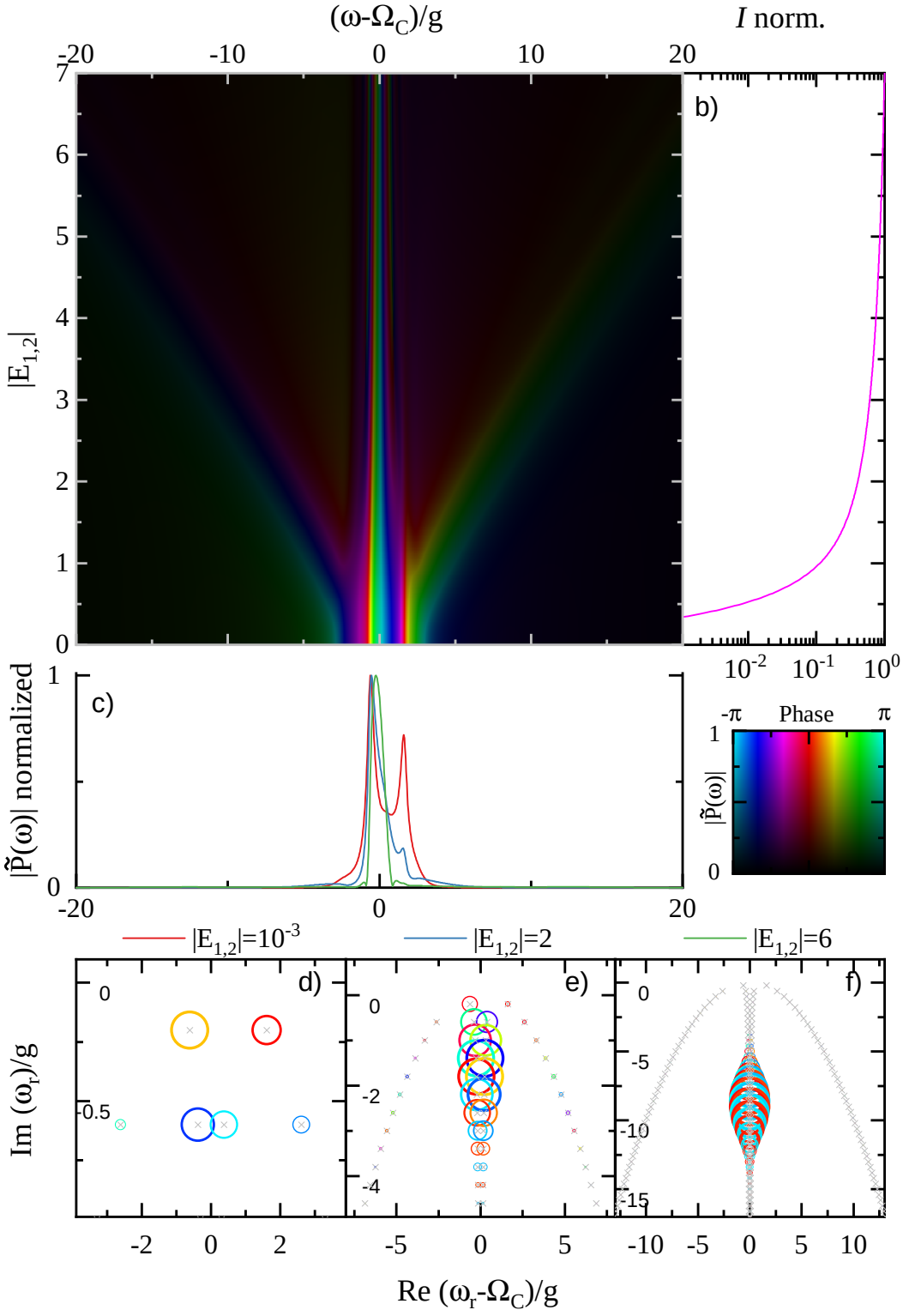

Figure E.18: $E_1 = E_2$ changing, $\delta = g$, $\gamma_c = \gamma_x = g/5$.

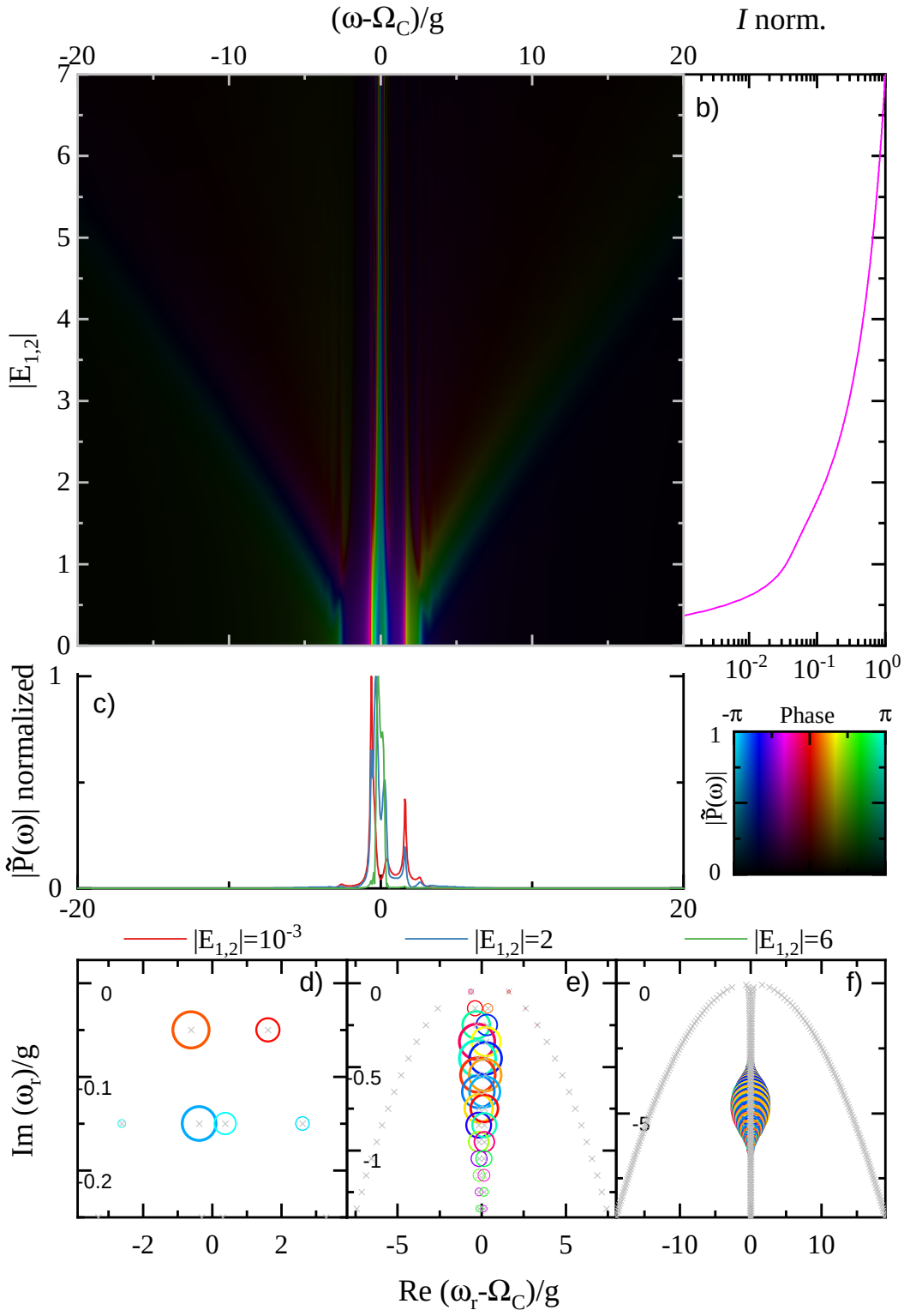

Figure E.19: $E_1 = E_2$ changing, $\delta = g$, $\gamma_c = \gamma_x = g/20$.

E.3 3-level

This section comprises a list of 3-level plots, varying the biexciton-cavity coupling constant, dampings and excitation strengths of the two pulses. All data divided by $i|E_1|^{|\Delta N_1|}|E_2|^{|\Delta N_2|}$ where $|E_n|$ is the magnitude and $|\Delta N_n|$ is the pulse phase channel of pulse n,

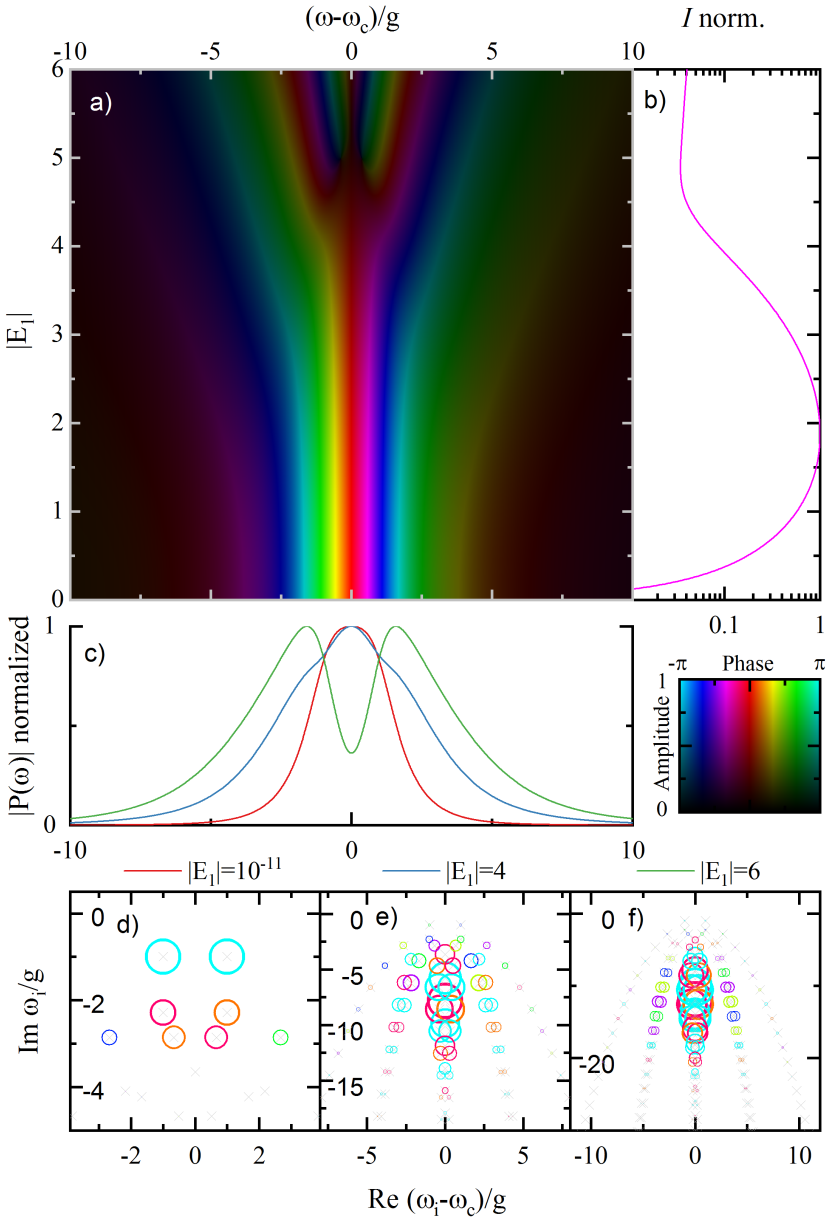

Figure E.20: E_1 changing, $\delta = 0$, $\gamma_c = \gamma_x = g$, $g_b/g_x = 1$.

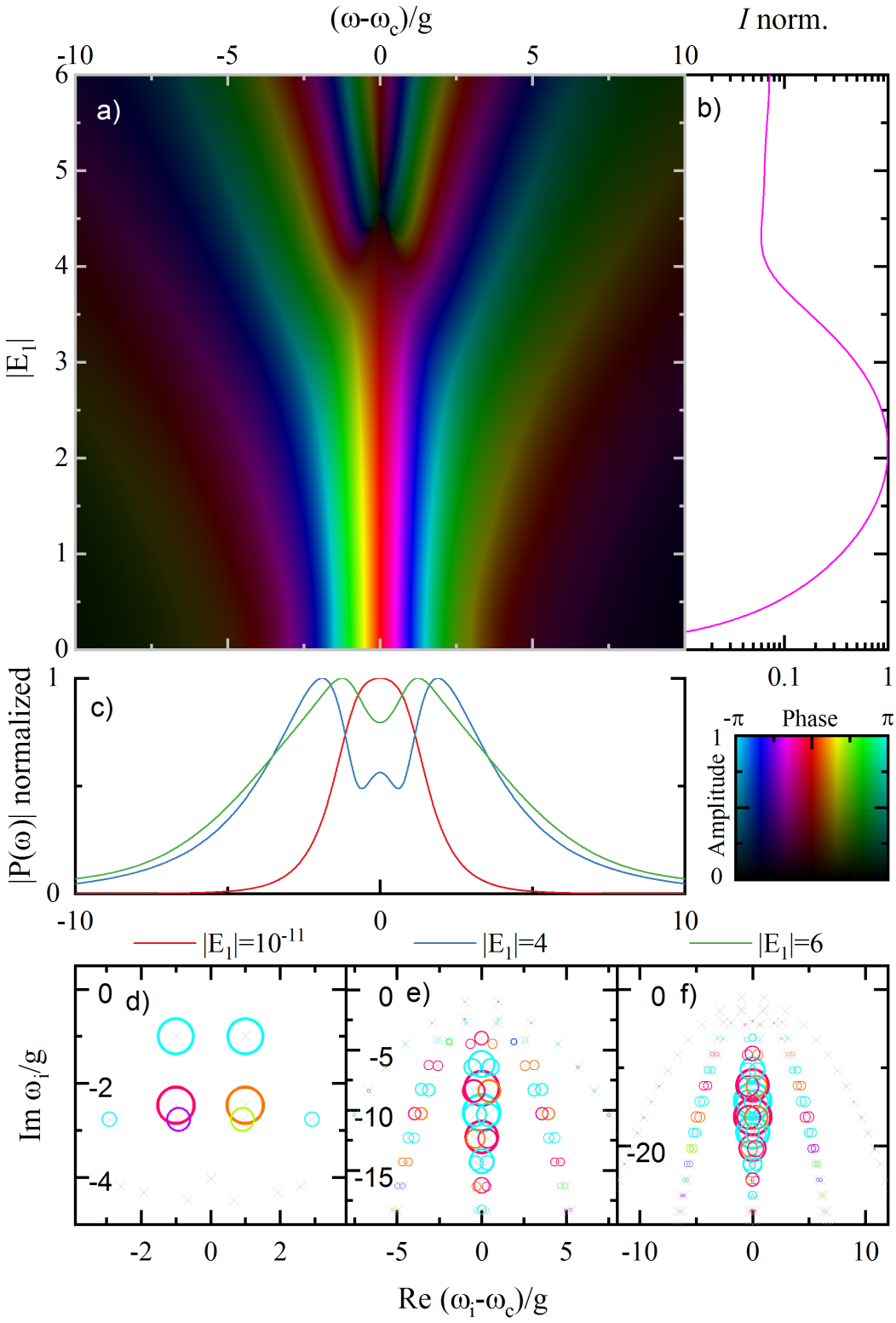

Figure E.21: E_1 changing, $\delta = 0$, $\gamma_c = \gamma_x = g$, $g_b/g_x = \sqrt{2}$.

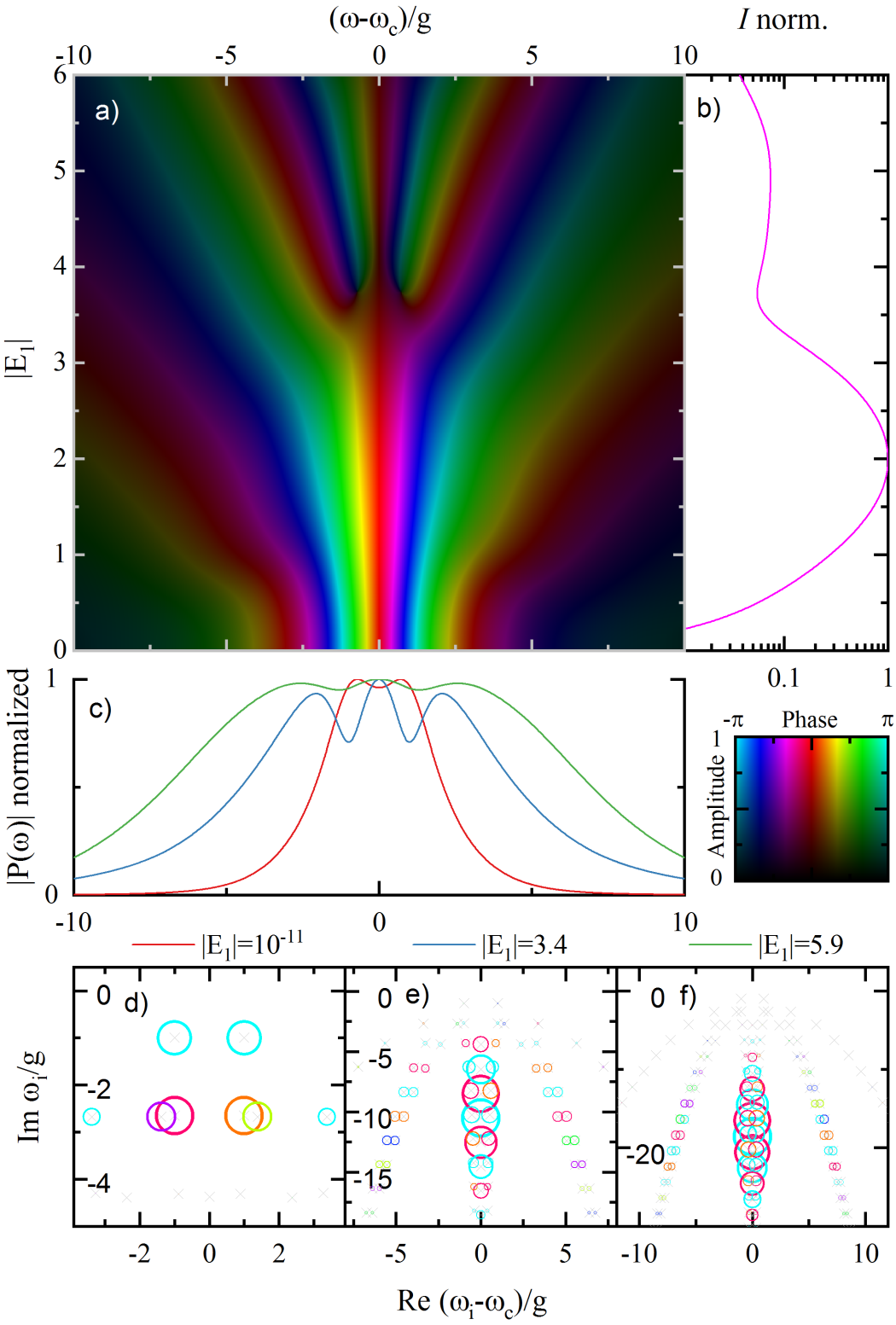

Figure E.22: E_1 changing, $\delta = 0$, $\gamma_c = \gamma_x = g$, $g_b/g_x = 1$.

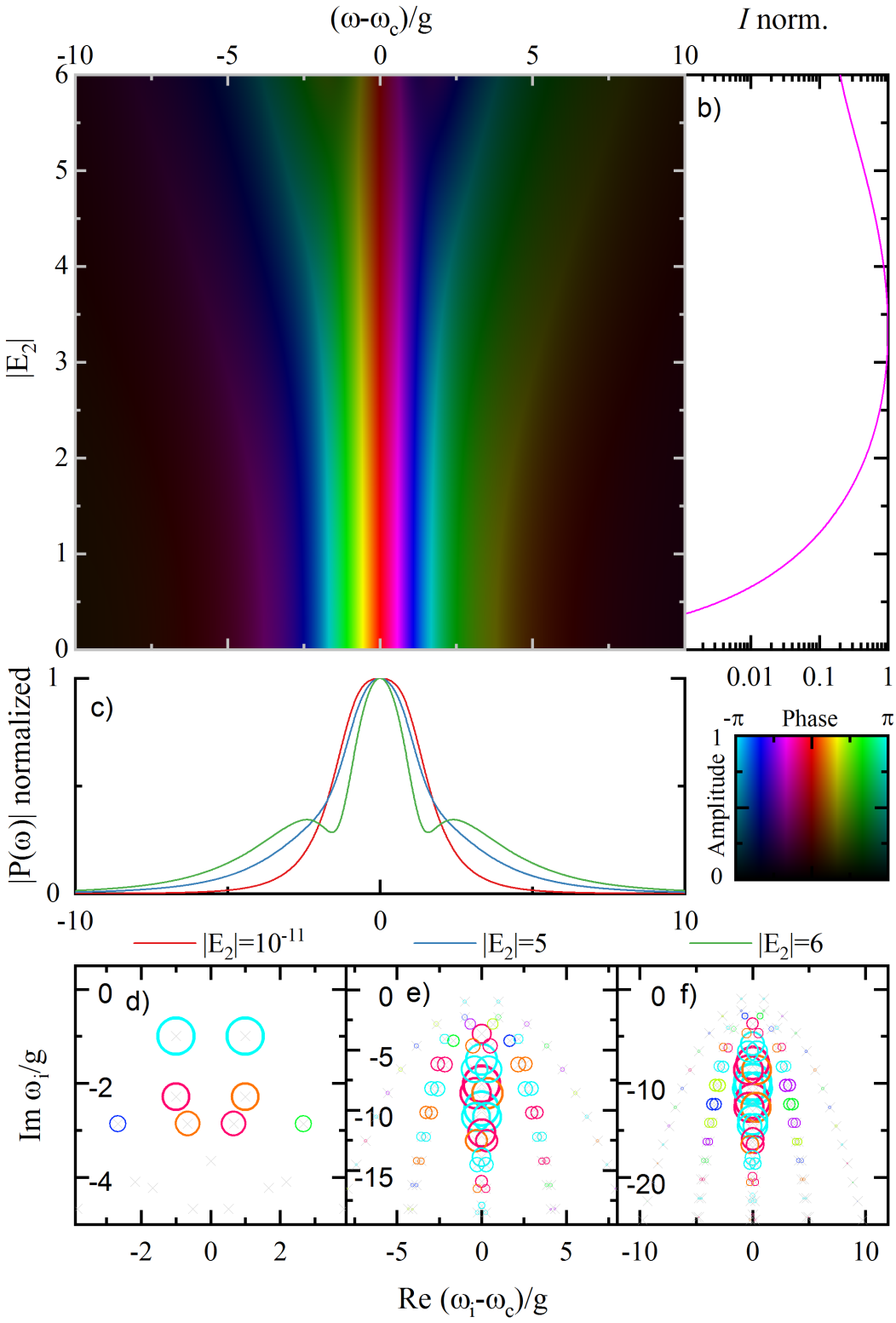

Figure E.23: E_2 changing, $\delta = 0$, $\gamma_c = \gamma_x = g$, $g_b/g_x = 1$.

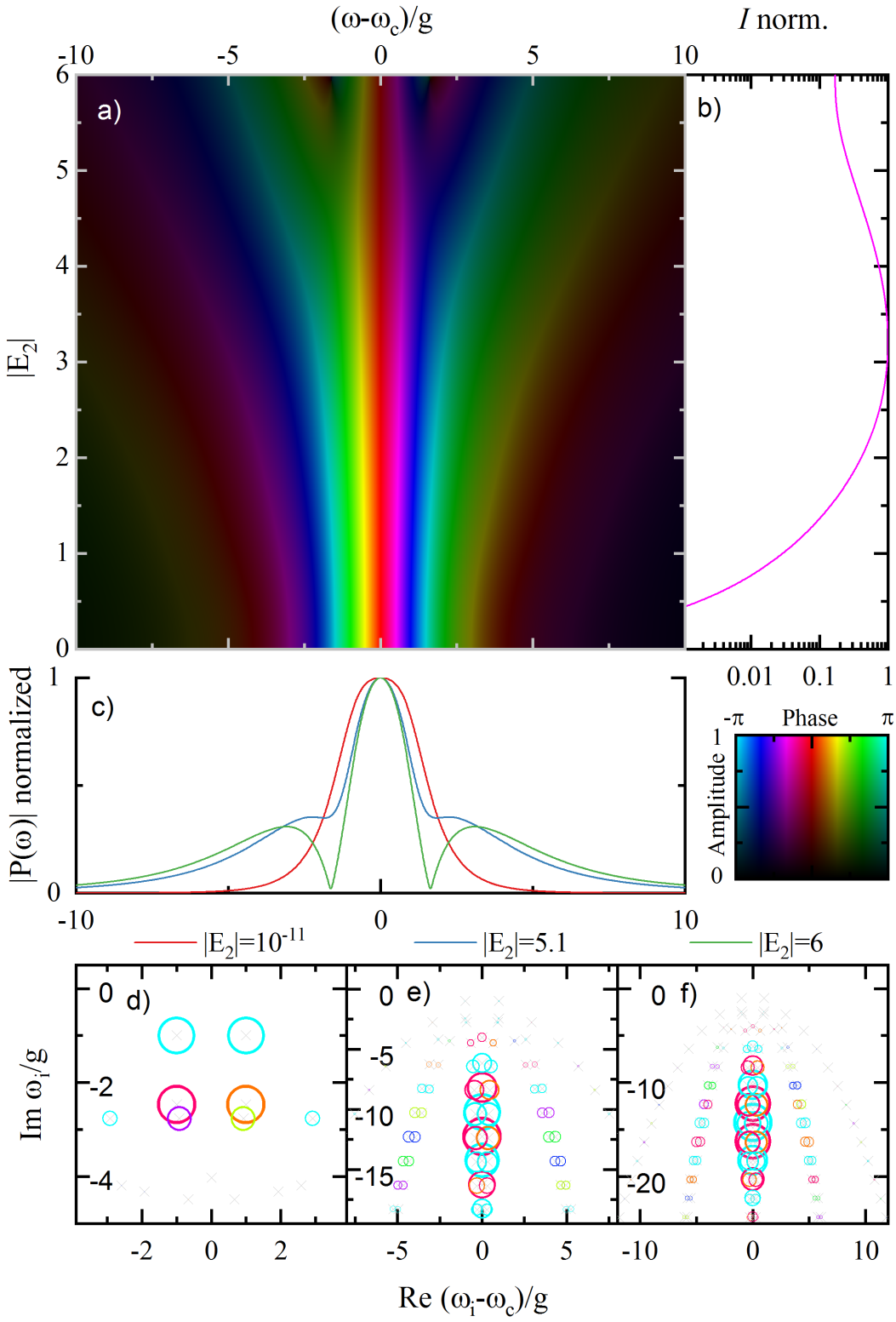

Figure E.24: E_2 changing, $\delta = 0$, $\gamma_c = \gamma_x = g$, $g_b/g_x = \sqrt{2}$.

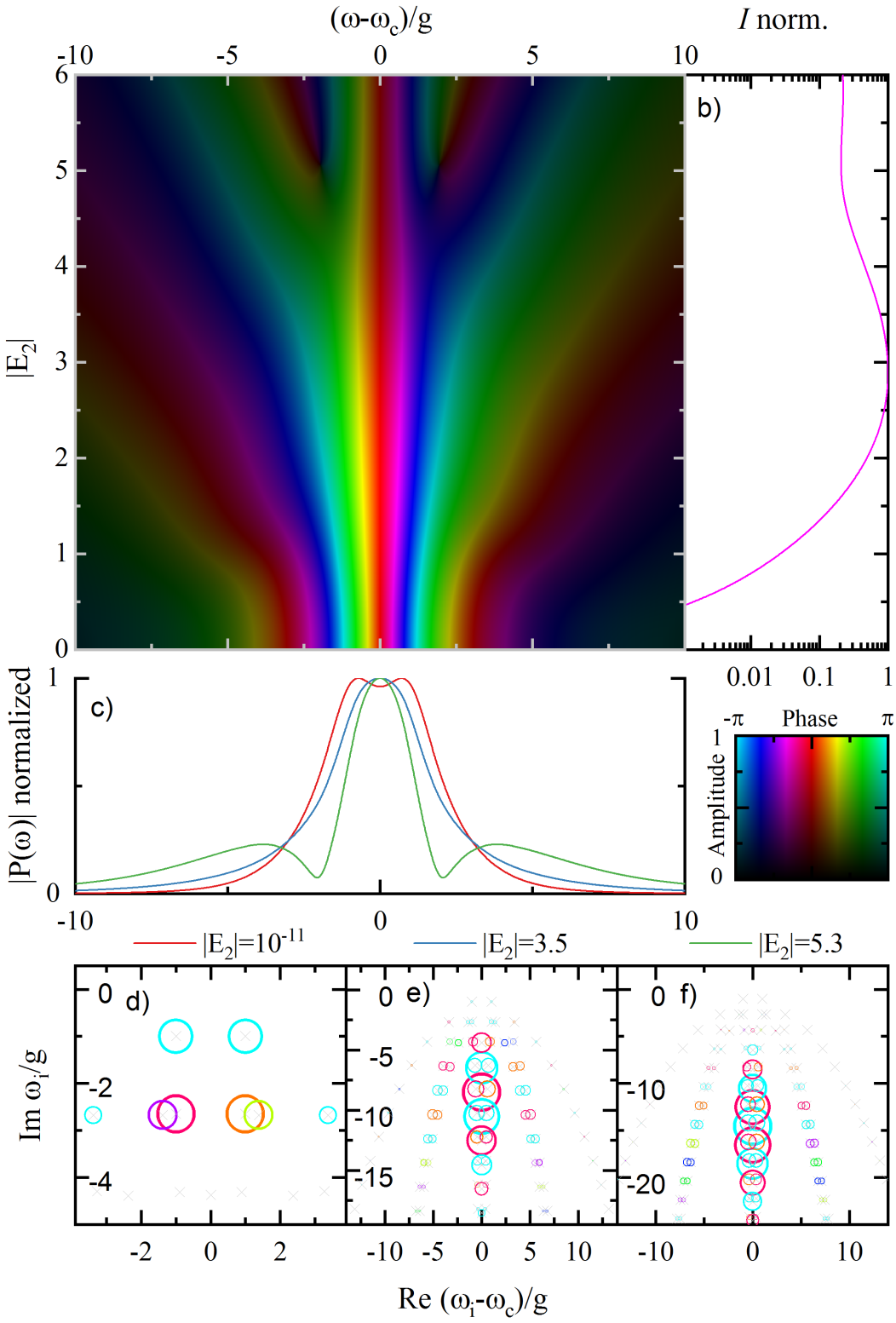

Figure E.25: E_2 changing, $\delta = 0$, $\gamma_c = \gamma_x = g$, $g_b/g_x = 1$.

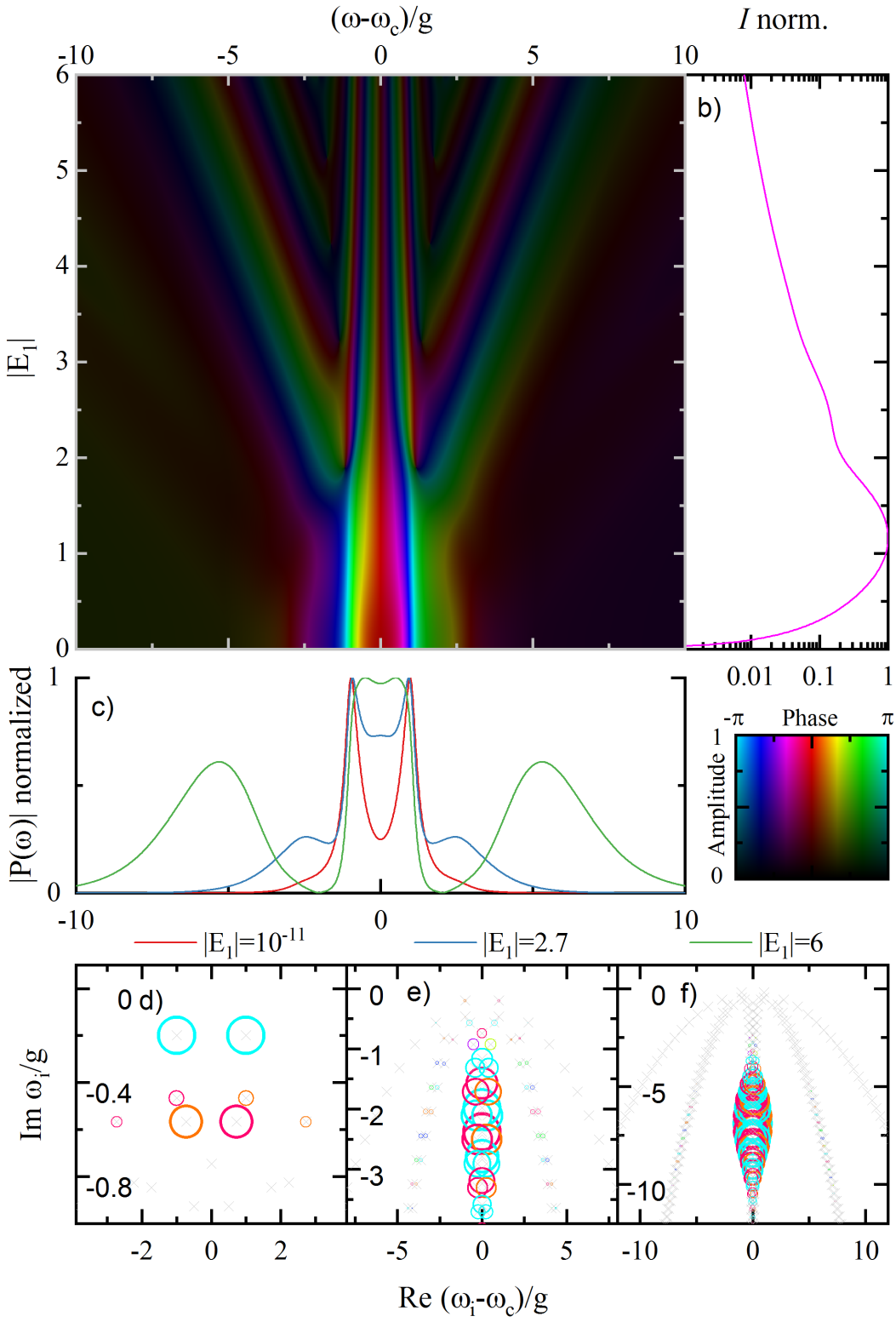

Figure E.26: E_1 changing, $\delta = 0$, $\gamma_c = \gamma_x = g/5$, $g_b/g_x = 1$.

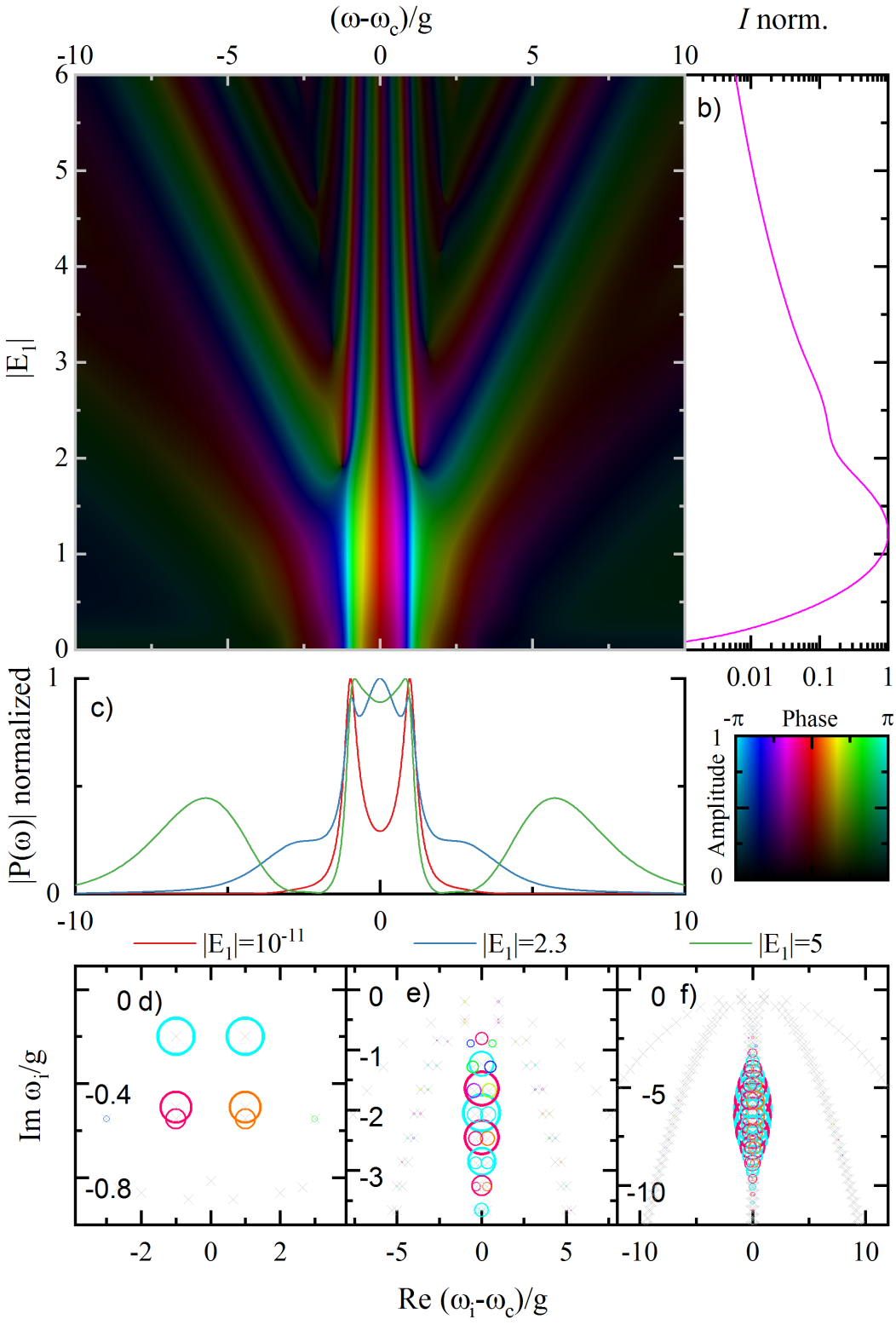

Figure E.27: E_1 changing, $\delta = 0$, $\gamma_c = \gamma_x = g/5$, $g_b/g_x = \sqrt{2}$.

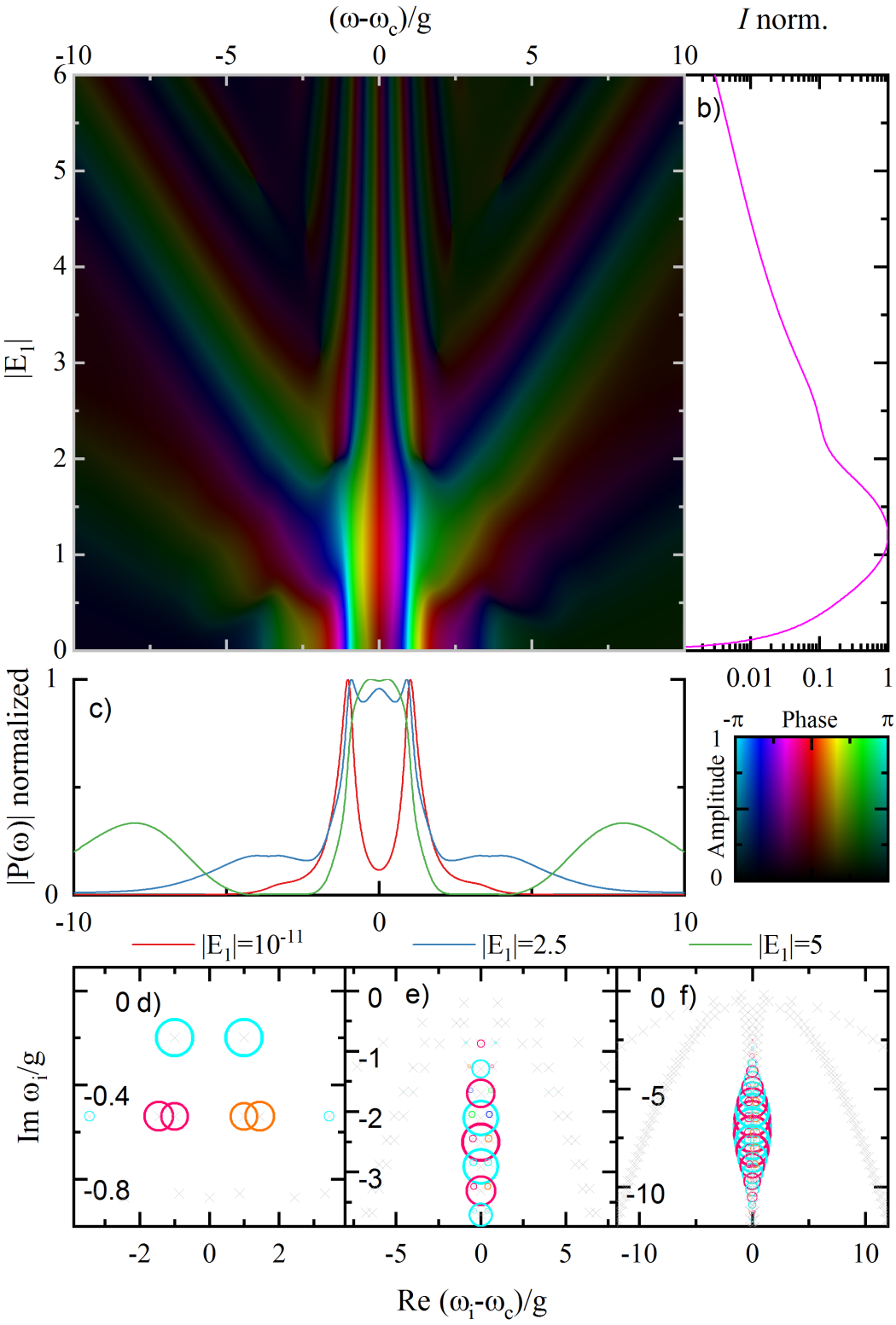

Figure E.28: E_1 changing, $\delta = 0$, $\gamma_c = \gamma_x = g/5$, $g_b/g_x = 1$.

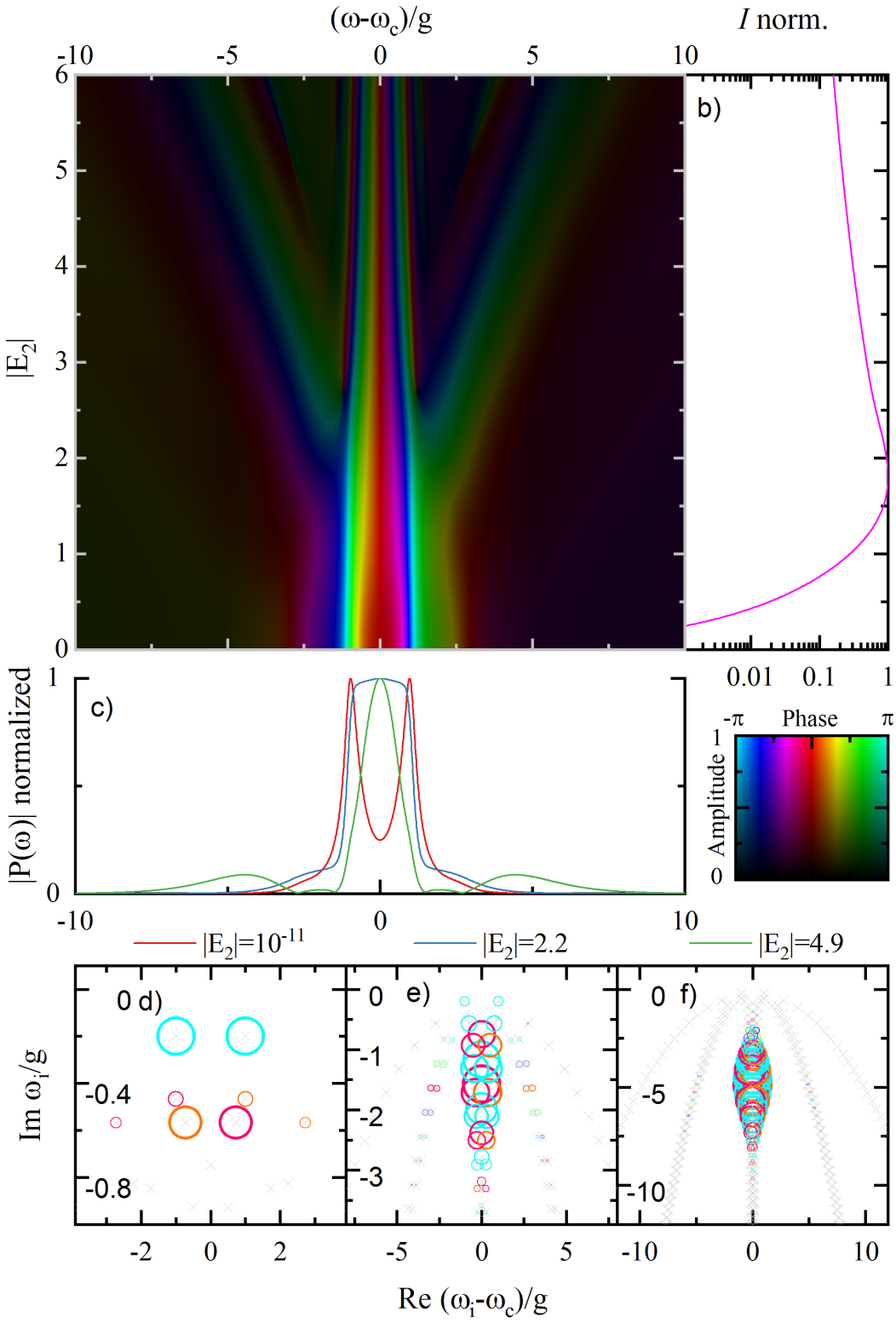

Figure E.29: E_2 changing, $\delta = 0$, $\gamma_c = \gamma_x = g/5$, $g_b/g_x = 1$.

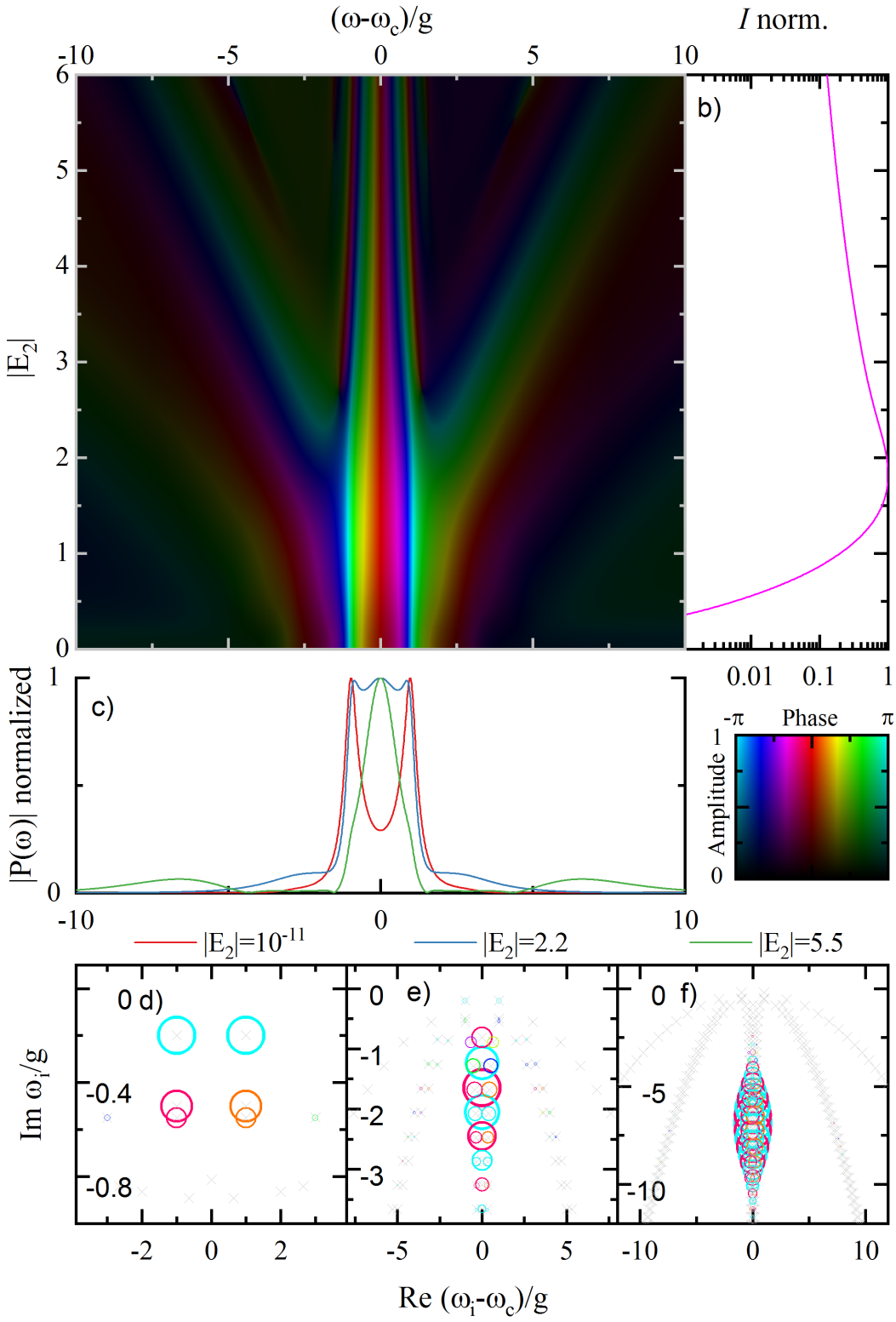

Figure E.30: E_2 changing, $\delta = 0$, $\gamma_c = \gamma_x = g/5$, $g_b/g_x = \sqrt{2}$.

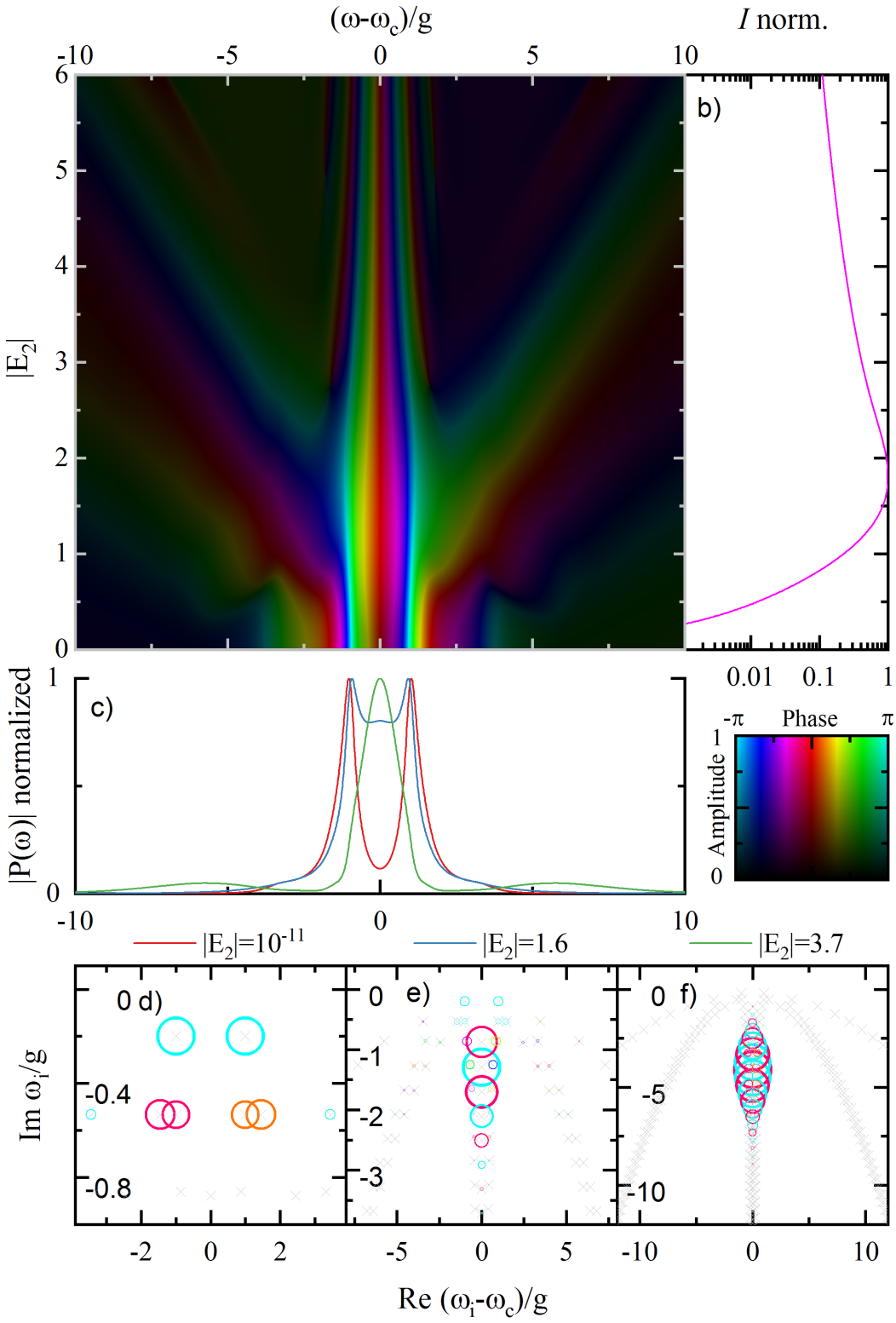

Figure E.31: E_2 changing, $\delta = 0$, $\gamma_c = \gamma_x = g/5$, $g_b/g_x = 1$.

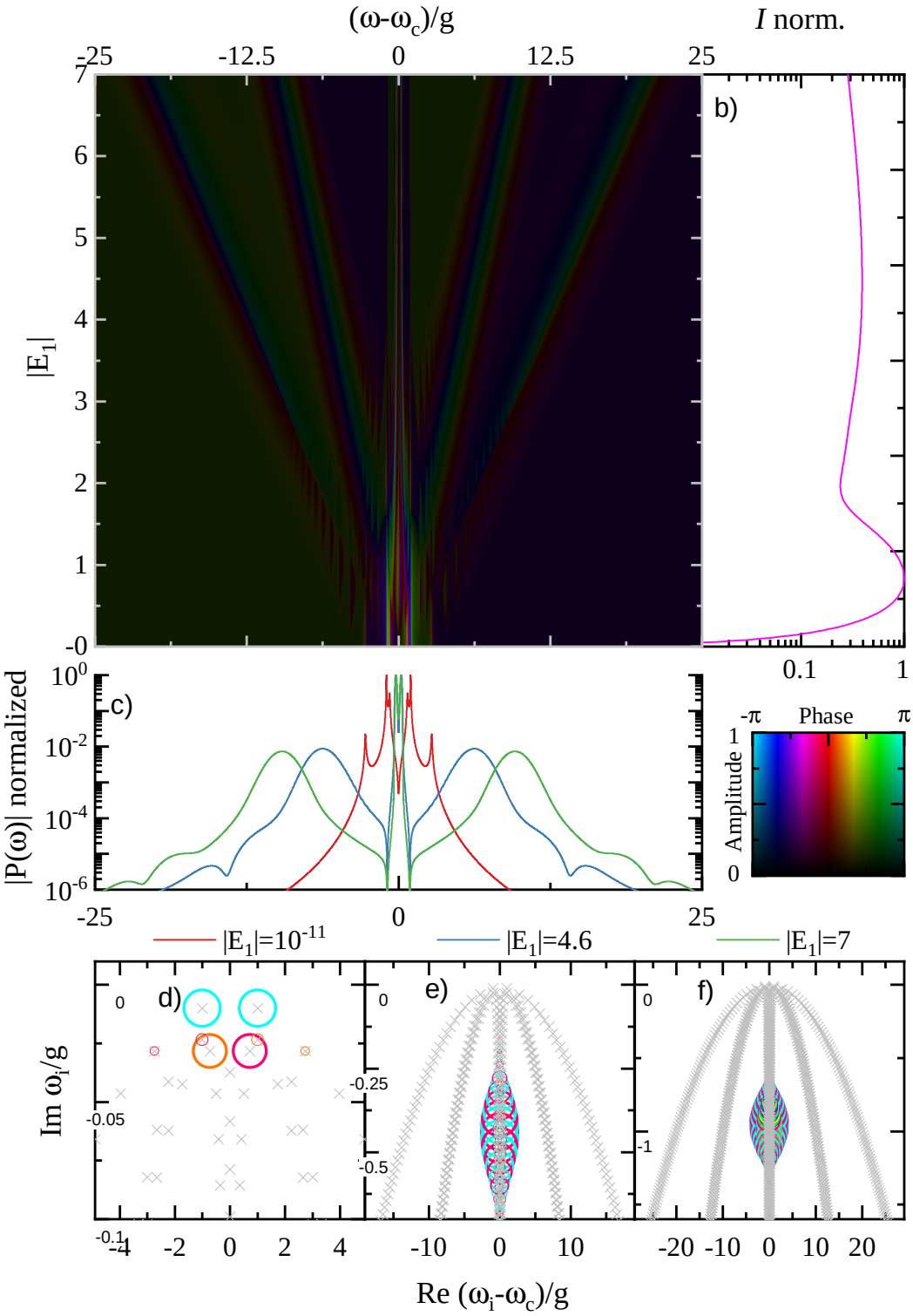

Figure E.32: E_1 changing, $\delta = 0$, $\gamma_c = \gamma_x = g/100$, $g_b/g_x = 1$.

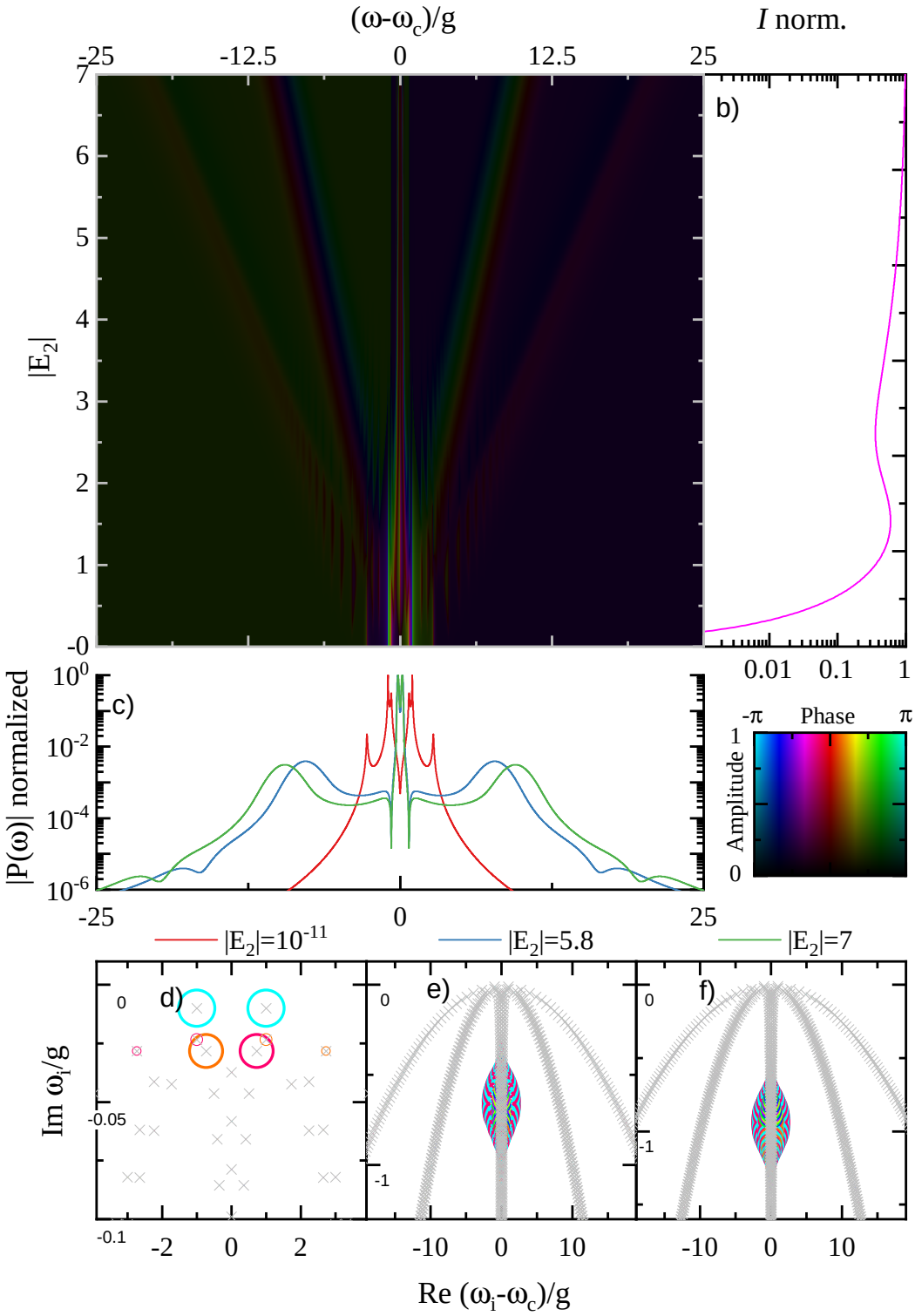

Figure E.33: E_2 changing, $\delta = 0$, $\gamma_c = \gamma_x = g/100$, $g_b/g_x = 1$.

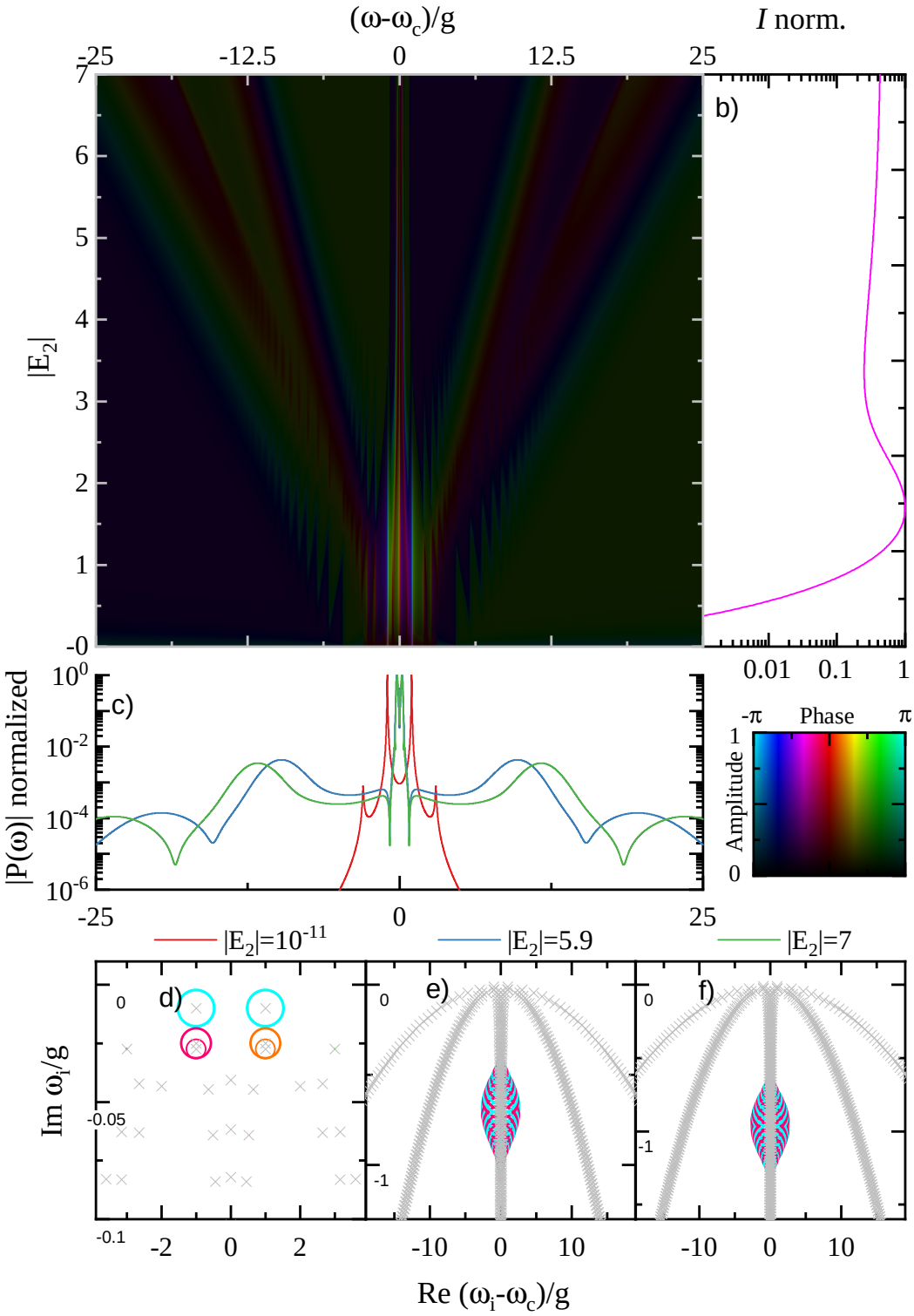

Figure E.34: E_2 changing, $\delta = 0$, $\gamma_c = \gamma_x = g/100$, $g_b/g_x = \sqrt{2}$.

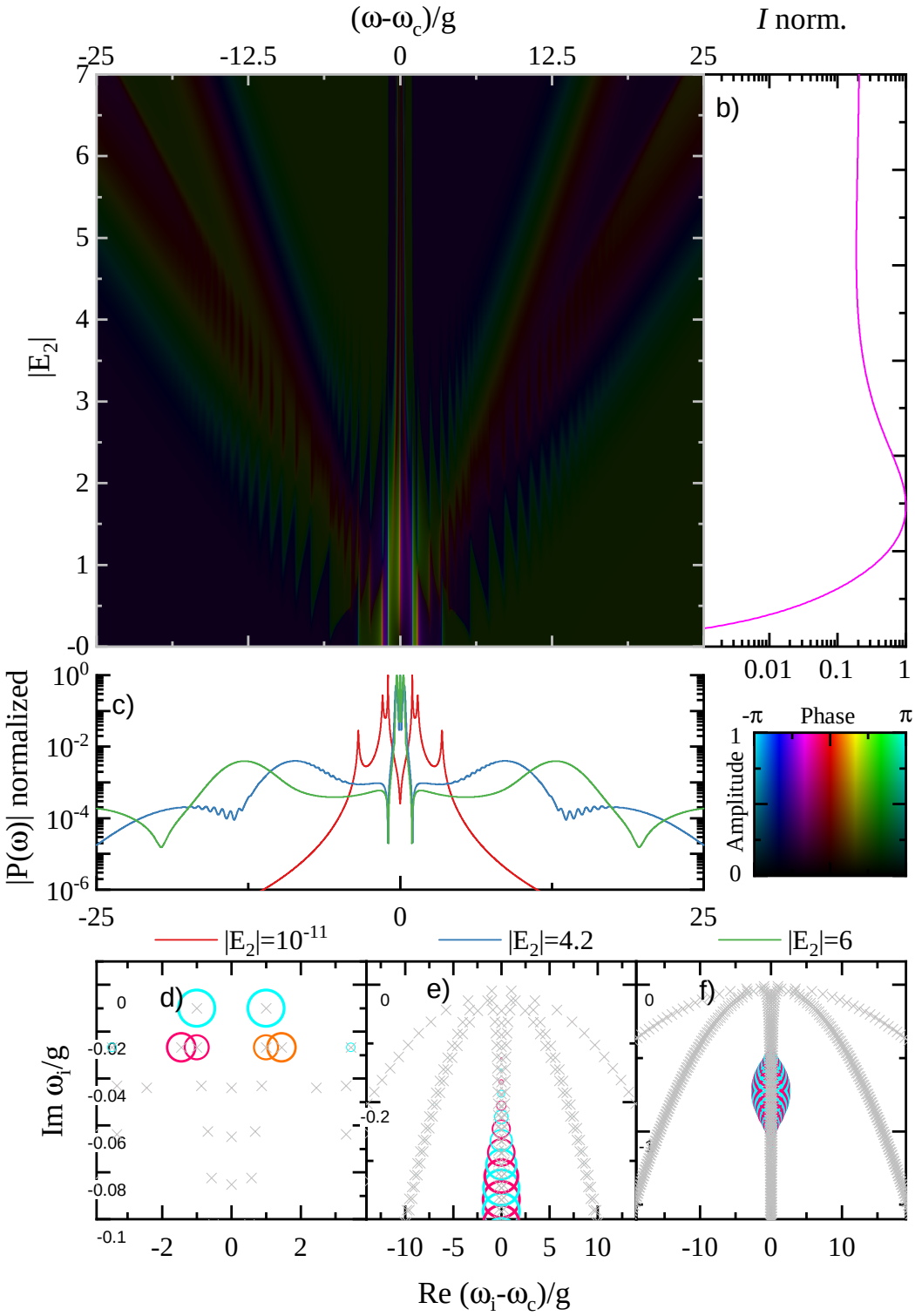

Figure E.35: E_2 changing, $\delta = 0$, $\gamma_c = \gamma_x = g/100$, $g_b/g_x = 1$.

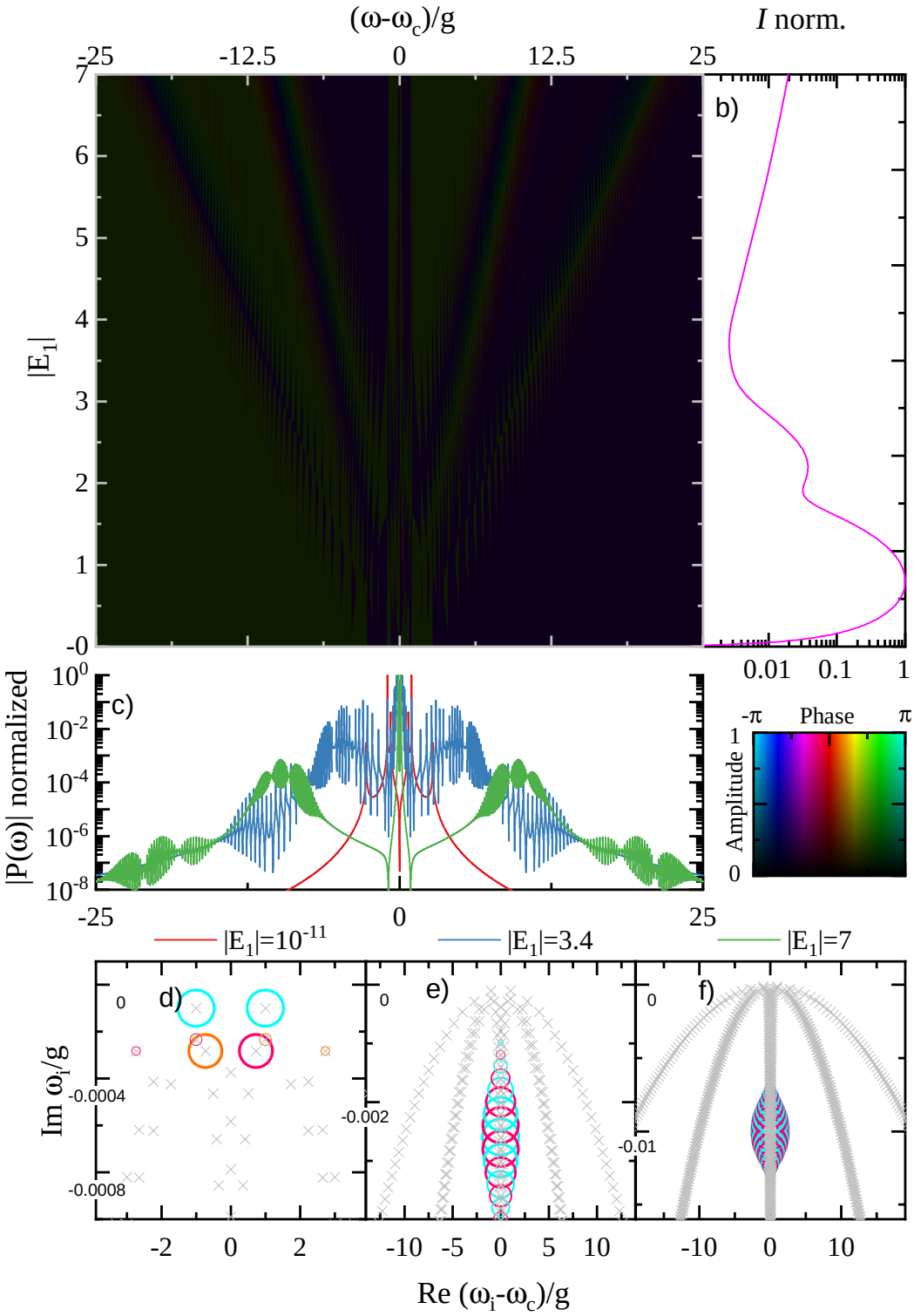

Figure E.36: E_1 changing, $\delta = 0$, $\gamma_c = \gamma_x = g/10000$, $g_b/g_x = 1$.

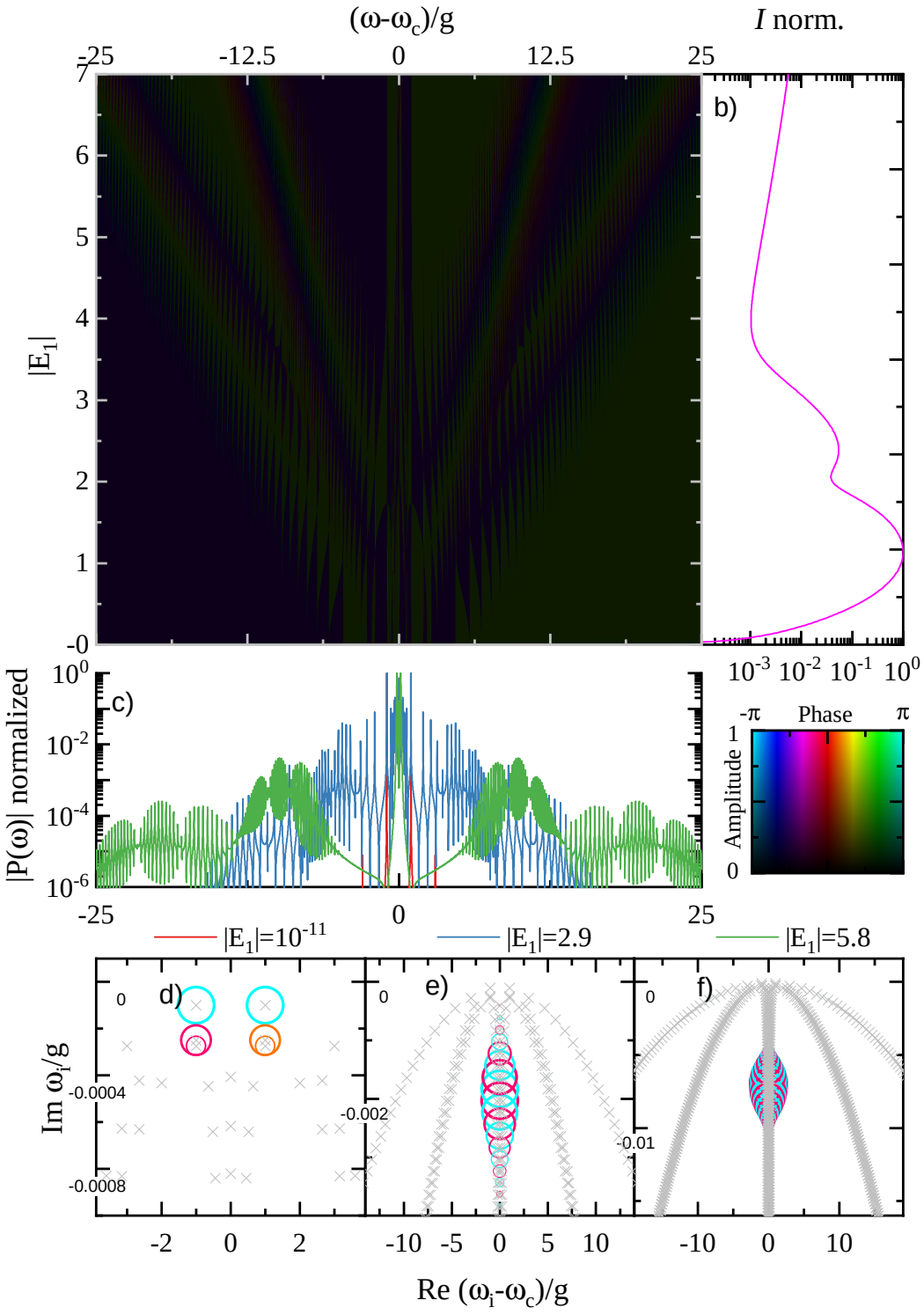

Figure E.37: E_1 changing, $\delta = 0$, $\gamma_c = \gamma_x = g/10000$, $g_b/g_x = \sqrt{2}$.

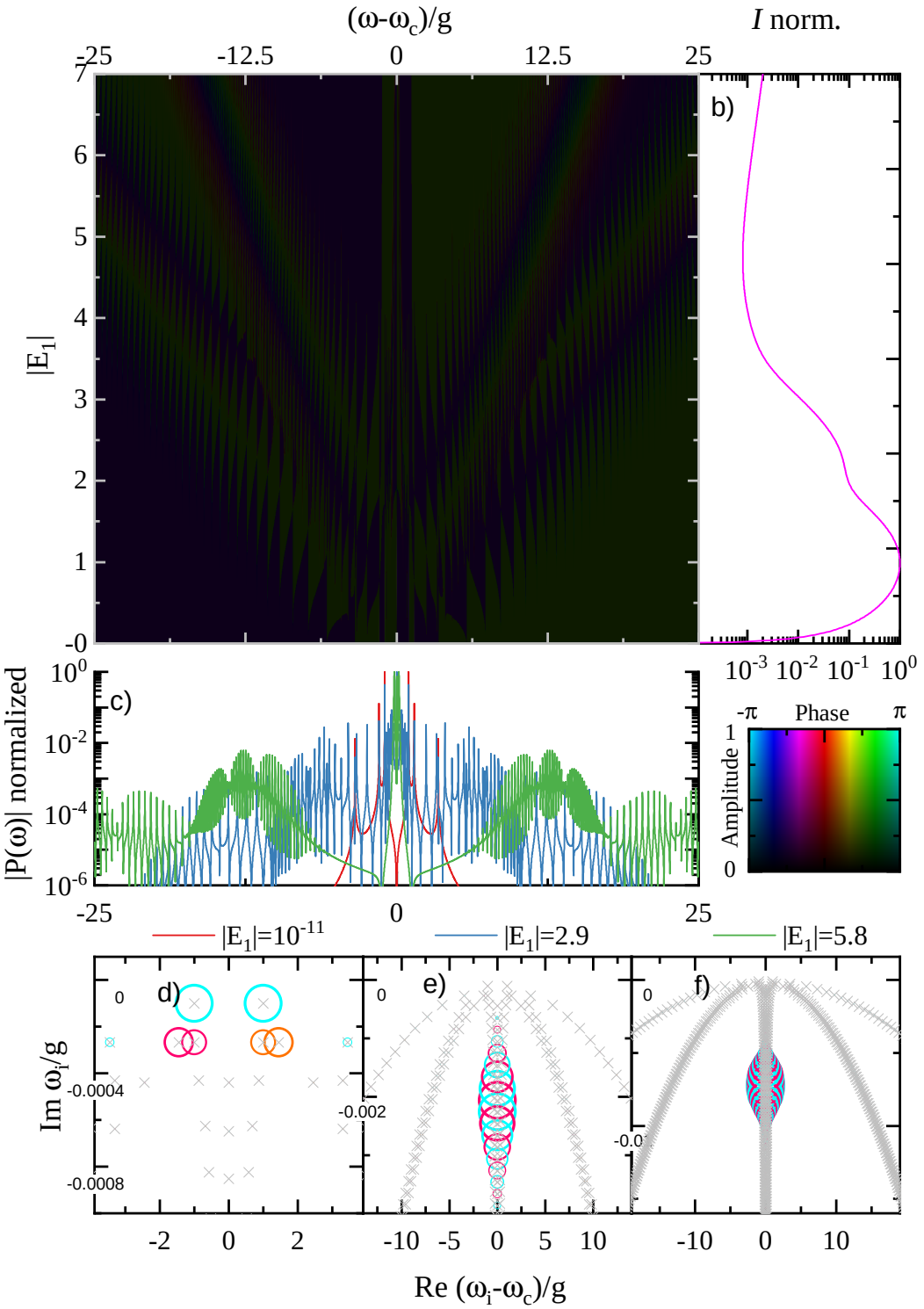

Figure E.38: E_1 changing, $\delta = 0$, $\gamma_c = \gamma_x = g/10000$, $g_b/g_x = 1$.

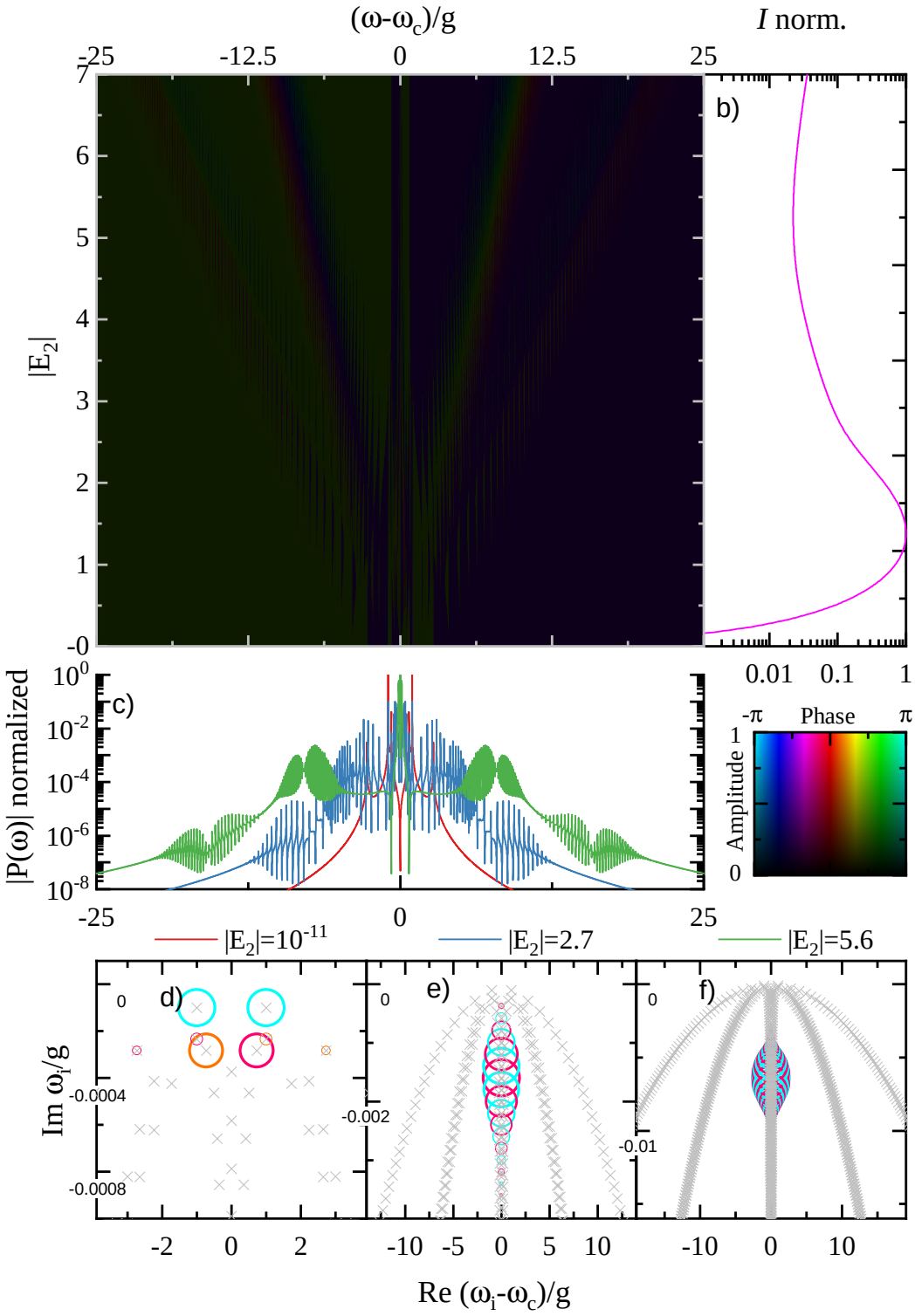

Figure E.39: E_2 changing, $\delta = 0$, $\gamma_c = \gamma_x = g/10000$, $g_b/g_x = 1$.

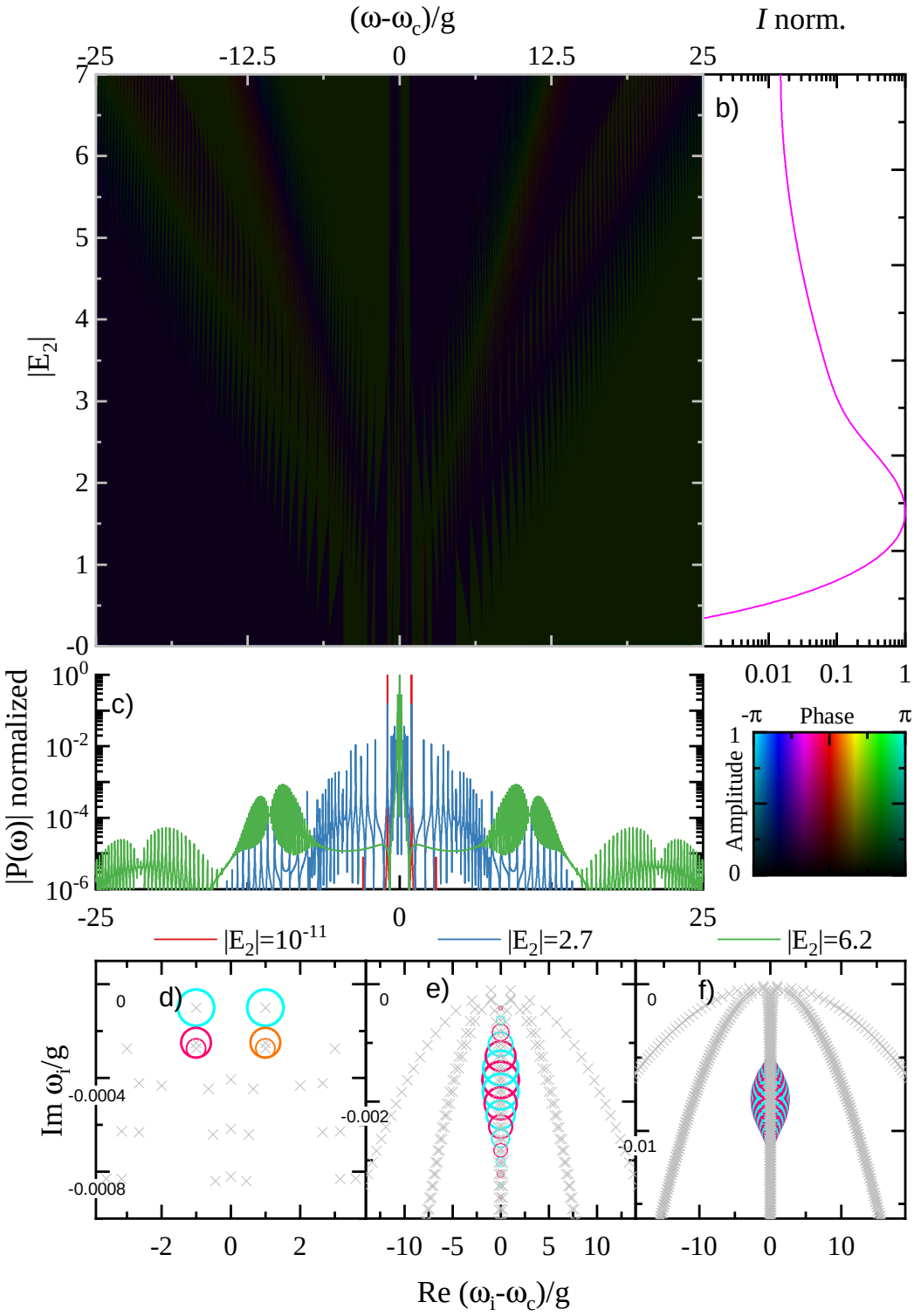

Figure E.40: E_2 changing, $\delta = 0$, $\gamma_c = \gamma_x = g/10000$, $g_b/g_x = \sqrt{2}$.

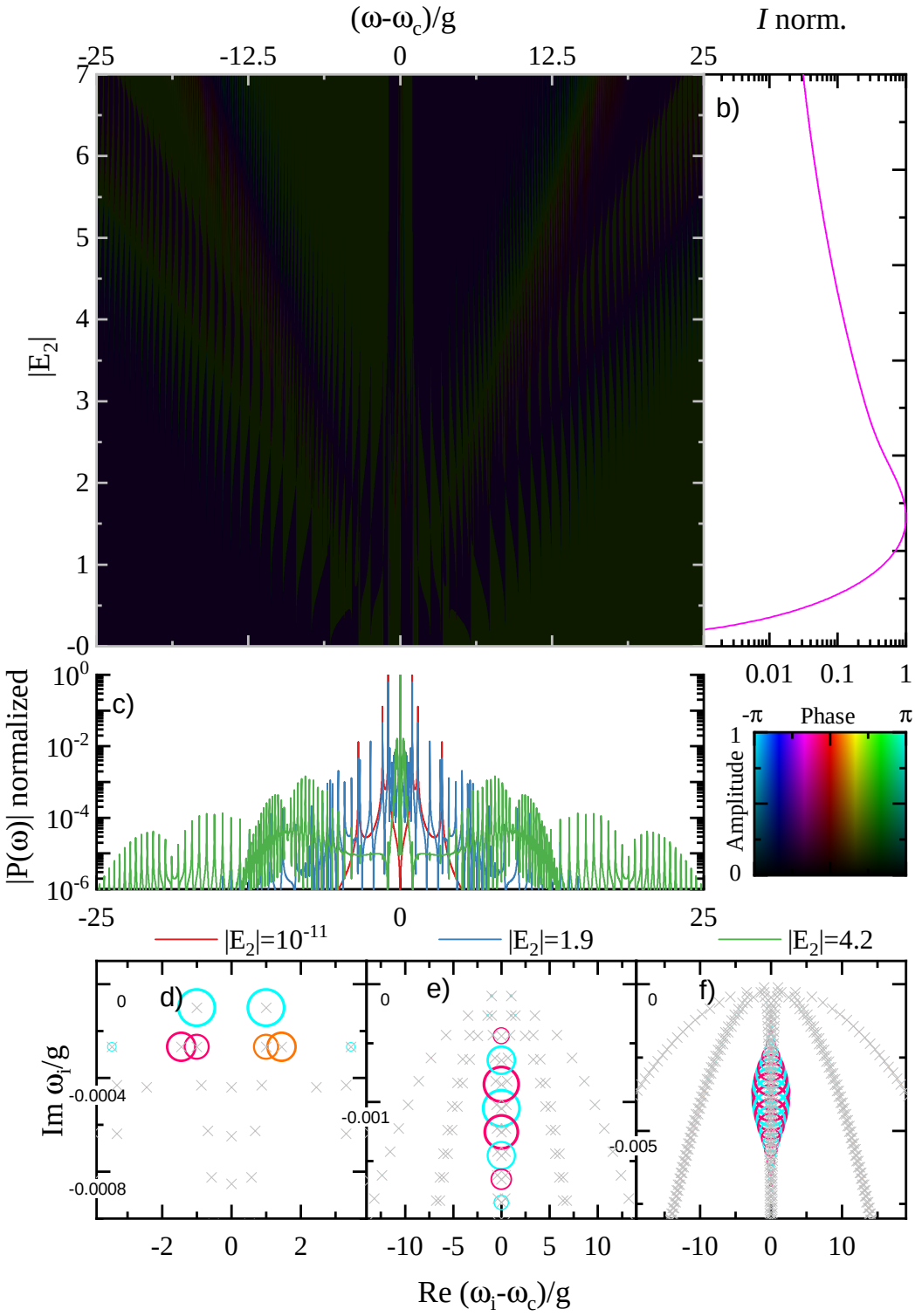

Figure E.41: E_2 changing, $\delta = 0$, $\gamma_c = \gamma_x = g/10000$, $g_b/g_x = 1$.

E.4 Functions

Functions can be plotted by colouring a pixel based on their complex output. Pixel hue is scaled map of output phase between 0 and 1, then mapped to the hue channel in HSV colour space. Pixel saturation is nominally 1, and sharply transisions to 1/2 around when the complex output has a phase of 0 (red area), $\pi/2$ (lime area), π (cyan area) or $3\pi/2$ (purple area). Pixel value is a periodic sawtooth function in log scale, log base 10 of the complex output absolute value, mod 1. This means an output absolute values which have ratios of integer powers of 10 take the same pixel value, eg: 12 and 1.2 have the same value. It also means that the function magnitude is increasing when going from a light-to-dark barrier and when the pixel value is slowly increasing, and vice versa. Figure E.42 gives an example of the colouring system. Phase increases from red to green, in the y direction, and amplitude (exponential of a real number) increases with the x axis. The barrier at $Re(z) = 0$ shows where e^z has a magnitude of 1, and the white region at $Im(z) = 0$ shows where the function has a purely real output.

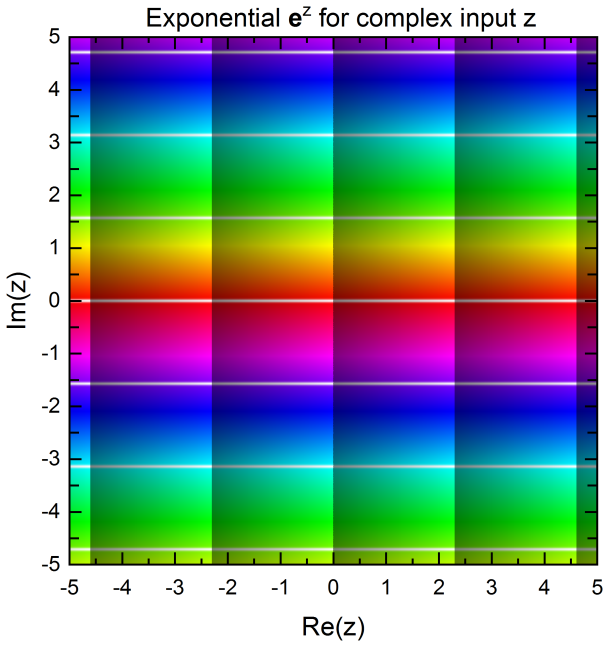

Figure E.42: Complex output diagram for the Exponential function

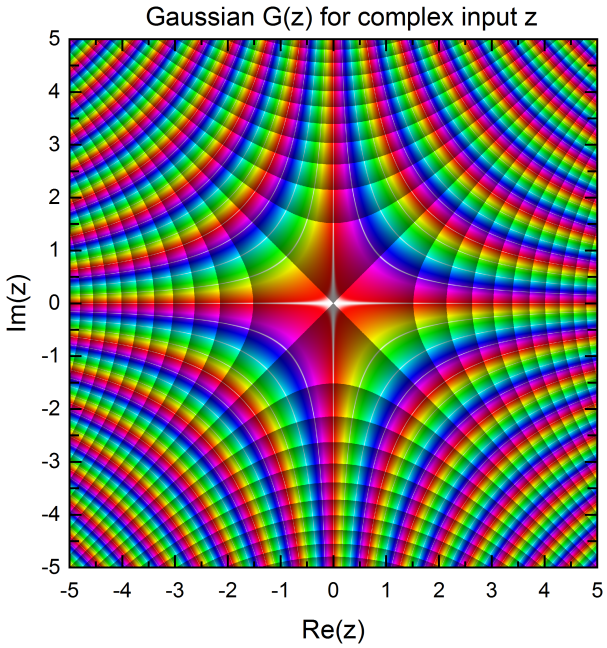

Figure E.43: Complex output diagram for the Gaussian function

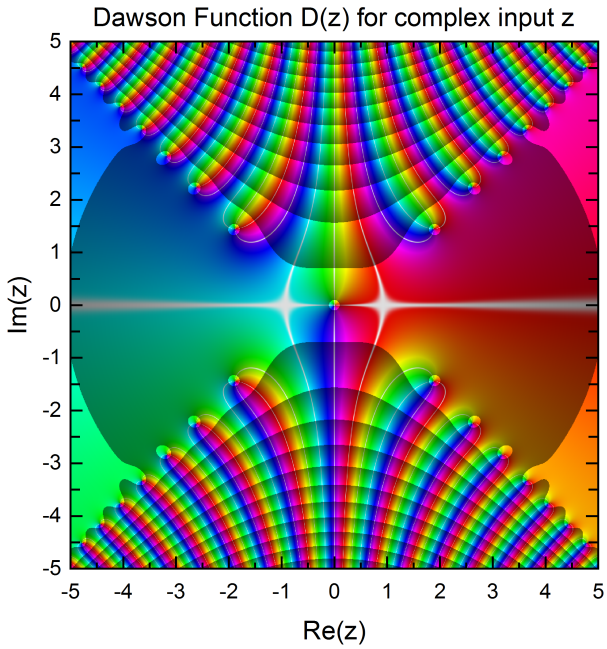

Figure E.44: Complex output diagram for the Dawson function (sometimes called Dawson integral)

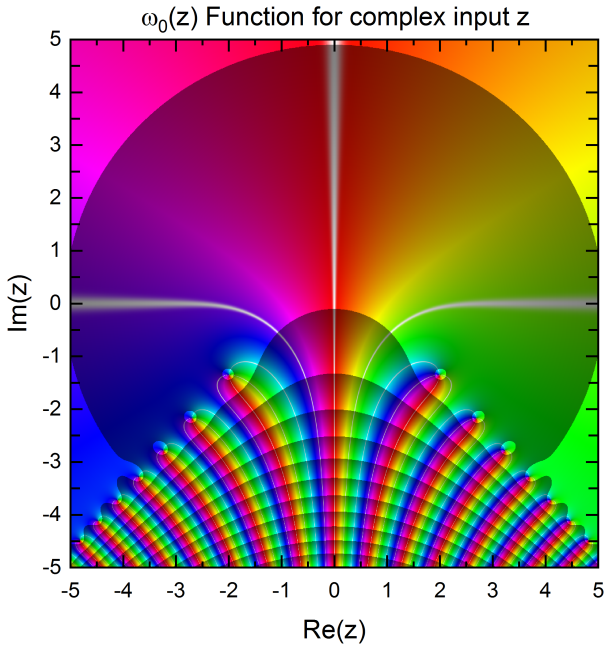

Figure E.45: Complex output diagram for the scaled faddeeva function ω_0

F | Video data

Data in this section supplements figures in Sec. E.3. Video data is used to represent more parameter space than is available in a 2D graph. By varying one more parameter over the video frame count we can have up to three variables changing over the same axes, while keeping each frame filled (unlike pseudo-3D plots where data can potentially be underneath other data). Youtube video descriptions contain information on each data set presented in this section.

F.1 2-level QDMC system | High excitation regime

https://youtu.be/w03czcn7ec8 Four-wave mixing response of the 2-level QDMC system. Plotted as colour diagrams, in each frame we vary a number of variables analysed in multiple plots, increasing pulse excitation strength over video frame.

F.2 3-level QDMC system | Low excitation regime N-wave mixing

https://youtu.be/nfY6YX-ybHg

N-wave mixing dynamics plotted as colour diagrams with E_1 varying along the y axis and $(\omega - \Omega_c)/g$ along the x axis.

F.3 3-level QDMC system | High excitation regime

https://youtu.be/q3aCUtowMDM

Four wave mixing dynamics plotted as colour diagrams with E_1 or E_2 varying along the y axis and $(\omega - \Omega_c)/g$ varying over the x axis.

G | Code for QDMC simulations and visualisation routines

This section is a log of code which was developed during the thesis period. Code will be released for public access 1 year after submission of this thesis.

G.1 2-level quantum dot coupled to a microcavity

Main 2L C program

https://github.com/SpicyPhysics/2L-QDMC-Dynamics

Inputting a parameter file, produce analytic eigendecomposition of L into a list of eigenfrequencies and amplitudes (output to file), followed by spectral and time domain NWM polarisation curves (output to file)

G.2 3-level quantum dot coupled to a microcavity

Main 3L C++ program

https://github.com/SpicyPhysics/3L-QDMC-Dynamics

Inputting a parameter file, produce eigendecomposition of L into a list of eigenfrequencies and amplitudes (output to file), followed by spectral NWM polarisation (output to file). Requires MPFR and GMP libraries, along with our modified Eigen

library, be present in order to compile/run.

G.2.1 Computational time order

Time dependence of the main parts of the program, excluding matrix exponential component

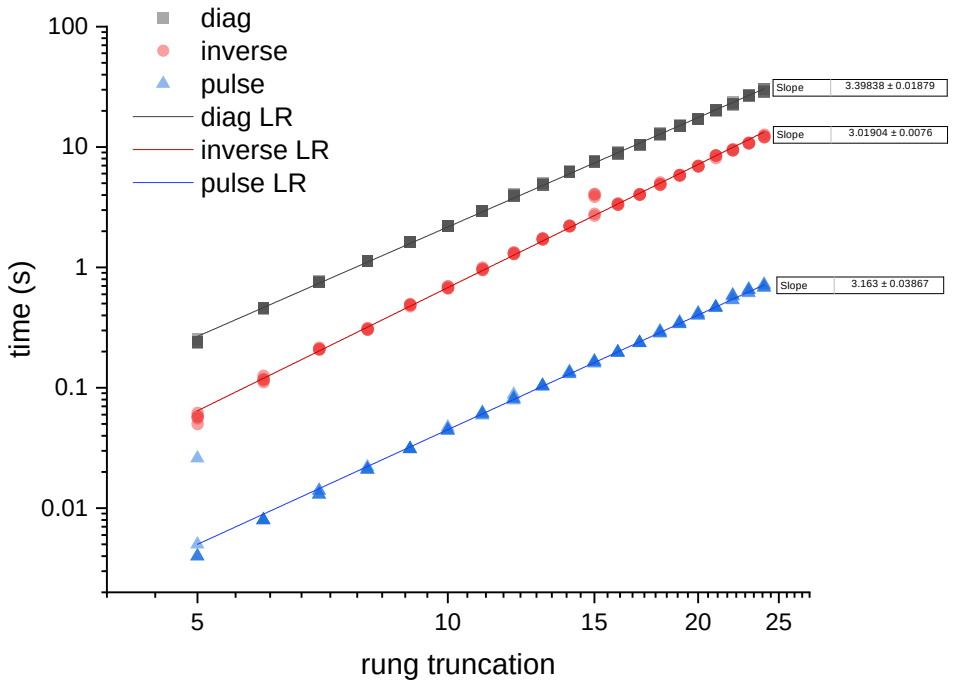

Figure G.1: Fit of code run duration over rung count. Increasing by one rung increases matrix size by 9. Fits show cubic time for all sections, but slightly higher for diagonalisation using the Eigen library. During optimisation, Eigen orders the input matrix during optimisation, which may change the time order depending on the actual matrix's values. Pulses contain sets of linear time for all elements which equals quadratic time, but repetitive matrix multiplication requires cubic time. Run on stock Intel 4690k @ 3.9GHz.

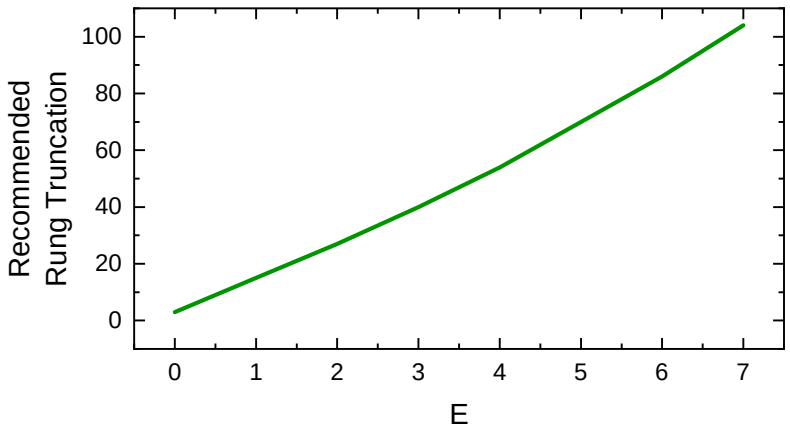

Figure G.2: Recommended rung truncation in the 3-level code for optimal speed for given input pulse field amplitude. Undercutting these values will result in production of unreliable data.

G.2.2 Eigen Extension Functions Demo

Demo for Eigen modification

https://github.com/SpicyPhysics/Eigen-Multiprecision-Diagonalisation

Code base used to produce the 3-level code, using the Eigen and Boost multiprecision libraries with a few tweaks to the Eigen library. After compilation, produces an example of multiprecision linear solve, diagonalisation and matrix exponential. The latest version of this demo is included in the 3-level code repository.

H | Eigenvalues of the 3-level QDMC System

In this section the eigenvalues of the 3-level QDMC system are found.

The 3-level QDMC Hamiltonian is as Eq. (H.1)

$$H_n = \begin{bmatrix} (n-2)\omega_c + \omega_b & \sqrt{n-1}g_b & \cdot \\ \sqrt{n-1}g_b & (n-1)\omega_c + \omega_x & \sqrt{n}g_x \\ \cdot & \sqrt{n}g_x & n\omega_c \end{bmatrix} \tag{H.1}$$

From the third order characteristic polynomial p_{H_n} of H_n an expression for its eigenvalues λ_n of the nth rung Hamiltonian can be found. As this matrix is by no means as simple as the 2-level QDMC Hamiltonian, none of the expressions in this section are in any way convenient or easy to digest. As a test check we can import these values into code, and compare directly with numerical diagonalisation as a

test check.

$$p_{H_n} = \begin{cases} & \lambda^3 \\ + & \lambda^2 \quad (3\omega_c - \omega_b - \omega_x - 3n\omega_c) \\ + & \lambda \quad \begin{pmatrix} 3n^2{\omega_c}^2 - \omega_b\omega_c + \omega_b\omega_x - 2\omega_c\omega_x - {g_b}^2 n - {g_x}^2 n \\ - 6n{\omega_c}^2 + {g_b}^2 + 2{\omega_c}^2 + 2n\omega_b\omega_c + 2n\omega_c\omega_x \end{pmatrix} \\ + & \begin{pmatrix} 3n^2{\omega_c}^3 - n^3{\omega_c}^3 - 2n{\omega_c}^3 - {g_b}^2 n\omega_c + {g_x}^2 n\omega_b - 2{g_x}^2 n\omega_c + n\omega_b{\omega_c}^2 \\ +2n{\omega_c}^2\omega_x + {g_b}^2 n^2\omega_c + {g_x}^2 n^2\omega_c - n^2\omega_b{\omega_c}^2 - n^2{\omega_c}^2\omega_x - n\omega_b\omega_c\omega_x \end{pmatrix} \end{cases} \tag{H.2}$$

Three eigenvaules with lower bias λ_n^-, central bias λ_n° and upper bias λ_n^+ are found from diagonalisation, with an exact albeit ugly expression

$$\begin{aligned} \lambda_n^- = \beta + \tfrac{b-a}{2} - \kappa \qquad \lambda_n^\circ = \beta + a - b \qquad \lambda_n^+ = \beta + \tfrac{b-a}{2} + \kappa \\ \beta = \tfrac{\omega_b+\omega_x}{3} + (n-1)\omega_c \\ \kappa = \tfrac{\sqrt{3}}{2} i(a+b) \\ a = \frac{2^{2/3}\left[\sqrt{[a_0]^2 - 4\,[a_1]^3} + a_0\right]^{1/3}}{6} \\ a_0 = 27{g_b}^2\omega_c - 9{g_b}^2\omega_b - 9{g_b}^2\omega_x + 9\omega_b{\omega_c}^2 - 9{\omega_b}^2\omega_c \\ - 3\omega_b{\omega_x}^2 - 3{\omega_b}^2\omega_x - 18{\omega_c}^2\omega_x + 2{\omega_b}^3 + 18\omega_b\omega_c\omega_x + 2{\omega_x}^3 \\ + n(+9{g_b}^2\omega_b - 27{g_b}^2\omega_c + 9{g_b}^2\omega_x - 18{g_x}^2\omega_b + 27{g_x}^2\omega_c + 9{g_x}^2\omega_x) \\ a_1 = 3{g_b}^2\, n - \omega_b\omega_x - 3\omega_b\omega_c + 3{g_x}^2\, n - 3{g_b}^2 + {\omega_b}^2 + 3{\omega_c}^2 + {\omega_x}^2 \\ b = -\tfrac{3{g_b}^2\, n - \omega_b\omega_x - 3\omega_b\omega_c + 3{g_x}^2\, n - 3{g_b}^2 + {\omega_b}^2 + 3{\omega_c}^2 + {\omega_x}^2}{9\,a} \end{aligned} \tag{H.3}$$

This reveals a list of eigenvalues ω_j for any arbitrary rung n of the three-level QDMC Lindblad operator, with j an index ranging from 0 to the size of L at rung n. For rungs 1,2,3, j has a range of 0 to 1,7,16, and increases by 9 for every additional rung. For numeric multiplication this implies an increase in computation time by a

factor of $(9/4)^3 \approx 11.4$ (as multiplication is $\mathcal{O}(n^3)$).

$n=0$	λ_0^-	λ_0°	
$n=1$	$\lambda_1^- - \lambda_0^-$	$\lambda_1^\circ - \lambda_0^-$	$\lambda_1^+ - \lambda_0^-$
	$\lambda_1^- - \lambda_0^\circ$	$\lambda_1^\circ - \lambda_0^\circ$	$\lambda_1^+ - \lambda_0^\circ$
$n \geq 2$	$\lambda_n^- - \lambda_{n-1}^-$	$\lambda_n^\circ - \lambda_{n-1}^-$	$\lambda_n^+ - \lambda_{n-1}^-$
	$\lambda_n^- - \lambda_{n-1}^\circ$	$\lambda_n^\circ - \lambda_{n-1}^\circ$	$\lambda_n^+ - \lambda_{n-1}^\circ$
	$\lambda_n^- - \lambda_{n-1}^+$	$\lambda_n^\circ - \lambda_{n-1}^+$	$\lambda_n^+ - \lambda_{n-1}^+$

(H.4)

Where lower orders of the hamiltonian H_0 and H_1 are diagonalised the same as Appendix. B. The eigenvectors U of the three-level Lindblad matrix are found numerically either by finding the eigenvalues listed here then finding the kernel, or nullspace, of $L - \omega I$ (with ω representing a stacked list of all eigenvalues ω_n up to the nth truncation of L), or by numerically diagonalising L using a general complex matrix algorithm like QR which produces eigenvalues and eigenvectors as pairs but not in rung order.

"What do you mean I leave everything until the last minute? there's at least a quarter of an hour left."